

**Experimental investigations on vortex-induced
fluid-structure interaction benchmarks and
corresponding numerical RANS predictions**

Von der Fakultät für Maschinenbau
der Helmut-Schmidt-Universität / Universität der Bundeswehr Hamburg
zur Erlangung des akademischen Grades eines Doktor-Ingenieurs
genehmigte

Dissertation
vorgelegt von

Andreas Kalmbach

aus Oranienburg

Hamburg, Juni 2015

Referent: Univ.-Prof. Dr.-Ing. habil. Michael Breuer

Koreferent: Univ.-Prof. Dr. rer. nat. habil. Christian Joachim Kähler

Tag der mündlichen Prüfung: 19. Juni 2015

Abstract

In the last decade, the demand for the prediction of complex multi-physics problems such as fluid-structure interaction (FSI) has strongly increased. These FSI phenomena can be found in many industry-related applications, e.g., in the design of aircrafts, wind turbines or heart valves to mention only a few. In present and future applications with complex multi-physics couplings, the numerical prediction of FSI problems is an important and valuable engineering tool in the design, life cycle analysis and prototyping.

Due to enhanced numerical algorithms and the strong increase of the computational power in the last decades, it is now feasible to simulate real-world FSI problems. Thus, a variety of numerical models are available or are currently in development to predict FSI applications. To evaluate and improve these complex non-linear computations, experimental studies are highly necessary. In order to provide reliable data for the validation and evaluation of coupled Computational Fluid Dynamics (CFD) and Computational Structure Dynamics (CSD) tools, different experimental test configurations (benchmarks) were developed and studied.

In the present thesis four series of test configurations exposed to turbulent flows are investigated using precise experimental measurement techniques and complementary numerical predictions. In each case the flexible structures are excited by vortex shedding. The shed vortices move downstream and start to interact with the flexible structures leading to a bidirectional self-excited fluid-structure interaction. Due to the oscillating behavior of this flow phenomenon and the resulting pressure distribution along the fluid-structure interface, the flexible structures start to deflect. To provide reliable data for the evaluation of numerical predictions, extensive preliminary studies are carried out to examine proper operating conditions in terms of e.g., the geometry and properties of the structures, the inflow velocity of the flow, the order of the structural deflections and the reproducibility of the coupled system response.

The experimental investigations are performed in a water channel (Göttingen type) allowing contactless data acquisition systems for the flow (2D particle image velocimetry and 3D particle tracking techniques) and structural measurements (2D laser line triangulation). Due to cycle-to-cycle variations of the structural deflections owing to chaotic irregular fluctuations of the turbulent flow field, the flow measurements are phase-averaged to obtain representative data. For all test configurations the system response as a function of the inflow velocities is analyzed. Different swiveling states of the flexible structures are identified and assigned to already known excitation mechanisms. Furthermore, for each test case the flow and structural behavior at a well-chosen inflow velocity is extensively investigated. Here, the coupled system is experimentally determined in form of two-dimensional flow fields and two-dimensional structural deformations representing the data base for the validation purpose.

The first test case series FSI-PfS-1*x* consists of a fixed rigid cylinder with an attached flexible plate. Three different elastic materials are applied to similar working conditions producing deflections in the order of the front cylinder diameter in the first and second swiveling mode. The second series FSI-PfS-2*x* uses the same configuration but applies an additional steel weight attached at the trailing edge of the flexible plate and a fixed or rotational mount of the front cylinder. This modification increases the inertia of the system and enables even larger structural deformations in the second swiveling mode. Regarding these first two test cases, both

configurations are generating almost two-dimensional structural system responses. To develop a three-dimensional test case, the third benchmark FSI-PfS-3*x* replaces the circular cylinder by a tapered cylinder. As a consequence the flow and the resulting structural responses are of three-dimensional kind in the first swiveling mode. The last test series FSI-PfS-4*x* is application-oriented and addresses well-known vortex-induced vibrations which are common in technical applications like heat exchangers consisting of tube bundles. Here, a long circular cylinder is fixed at one channel wall and is free at the opposite site. Two different configurations, a single flexible cylinder and a 3×3 arrangement are studied. The crossflow configuration causes large deflections of the free cylinder tip and high swiveling frequencies.

The complementary numerical studies are carried out with the multi-physics software environment of ANSYS[®] 14.0 using the FSI coupling interface between ANSYS[®] CFX for the fluid flow and ANSYS[®] Mechanical for the structure deformation. Due to the turbulent flow conditions a RANS turbulence model (SST) is used to predict the vortex shedding from the cylinder and the fluid flow in the wake of the structure.

The numerical predictions lead to satisfactory results for the two-dimensional test cases and less reasonable results for the three-dimensional test configurations. For the three dimensional numerical simulations limitations of the cell numbers and difficult boundary conditions for the structure lead to non-physical results.

In summary, this thesis carried out an extensive experimental investigation concerning several FSI-benchmark configurations in the turbulent flow regime. While the first test case FSI-PfS-1*x* is rather simple to predict, the simulations of the test cases FSI-PfS-2*x*, 3*x* and 4*x* are more difficult due to their increased physical complexity.

The test cases were published in international journals and the data sets of FSI-PfS-1*a* and FSI-PfS-2*a* are available on the ERCOFTAC/QNET wiki website (<http://qnet-ercoftac.cfms.org.uk>).

Kurzfassung

In den letzten Jahren stieg die Nachfrage nach verlässlichen Vorhersagemodellen für die numerische Simulation von Fluid-Struktur-Wechselwirkungen (FSI) stark an. Diese komplexen physikalischen Wechselwirkungen sind in vielen industrie-relevanten Anwendungen zu finden, beispielsweise in der Entwicklung von Tragflügeln, Windkraftanlagen oder künstlichen Herzklappen. Schon heute ist die numerische Simulation von diesen multi-physikalischen Vorgängen ein immer wichtiger werdendes Werkzeug in der Produktentwicklung für Lebensdaueranalysen sowie im Prototyping.

Durch die Entwicklung von verbesserten numerischen Algorithmen und den starken Anstieg der Rechenleistung ist es nun möglich, auch anwendungsnahe gekoppelte Fluid- (CFD) und Struktur- (CSM) Simulationen durchzuführen. Für die Verbesserung und Weiterentwicklung der numerischen Modelle sind Vergleiche mit experimentellen Daten unerlässlich. Zu diesem Zweck wurden in der Vergangenheit verschiedene Testkonfigurationen (Benchmarks) entwickelt und untersucht.

In der vorliegenden Arbeit werden vier unterschiedliche Testkonfigurationen mit präzisen experimentellen Messmethoden und komplementären numerischen Simulationen untersucht. In jedem Testfall wird eine flexible Struktur einer turbulenten Strömung ausgesetzt und die Strukturantwort analysiert. Durch die entstehenden Wirbelablösungen an der Struktur und die daraus resultierenden quasi-periodisch wechselnden Druckkräfte auf der Fluid-Struktur-Grenzfläche wird diese zum Schwingen angeregt. Für die Bereitstellung von verlässlichen experimentellen Daten zur Validierung numerischer Modelle wurden umfangreiche Vorstudien durchgeführt, um die besten Betriebszustände der einzelnen Testfälle zu identifizieren. Im einzelnen sind dies die einfache Geometrie und Materialeigenschaften der Struktur, die Einströmgeschwindigkeit des Fluids, die Auslenkungen der Struktur sowie die Reproduzierbarkeit der Systemantwort (Strömung und Struktur).

Die experimentellen Untersuchungen wurden in einem Wasserkanal Göttinger Bauart durchgeführt. Der eingesetzte Versuchsstand ermöglicht die Nutzung kontaktloser Lasermesstechniken für die Untersuchung der Strömung (2D-Particle-Image-Velocimetry sowie 3D-Particle-Tracking) und der Strukturbewegung (2D-Laser-Line-Triangulation). Aufgrund der zyklischen Schwankung der Strukturauslenkung innerhalb einer Periode, welche wiederum durch die turbulenten Fluktuationen in der Strömung hervorgerufen wird, wurden die Messdaten für Struktur und Strömung nachträglich phasengemittelt. Für alle Testfälle wurde die Strukturantwort als Funktion der Einströmgeschwindigkeit analysiert. Dabei wurden verschiedene Schwingungszustände identifiziert und bekannten Anregungsmechanismen zugeordnet. Weiterhin wurden für alle Testfälle bei einer bestimmten Einströmgeschwindigkeit detailliertere Untersuchungen durchgeführt. Dazu wurde der Systemzustand innerhalb einer quasi-periodischen Schwingung für die Strömung sowie die Strukturbewegung experimentell ermittelt. Gleichzeitig ermöglichen diese Daten den späteren Vergleich mit numerischen Ergebnissen.

Die Testreihe FSI-PfS-1x besteht aus einem starren Zylinder, an welchem eine elastische Platte befestigt ist. Drei unterschiedliche elastische Materialien wurden unter ähnlichen Betriebsbedingungen untersucht. Für diese Testfälle wurden Strukturauslenkungen im Bereich des Zylinderdurchmessers im ersten und zweiten Schwingungsmodus ermittelt. Die zweite Testreihe

FSI-PfS-2*x* benutzt eine ähnliche jedoch leicht veränderte Konfiguration wie FSI-PfS-1*x*. Um größere Verformungen zu ermöglichen, wurde die Trägheit der Struktur mithilfe eines zusätzlichen Gewichts am Ende der elastischen Platte erhöht. Weiterhin wurde der Einfluss der Zylinderlagerung untersucht. Für beide Konfigurationen (fixierter Zylinder und drehbar gelagerter Zylinder) wurden große Strukturverformungen im zweiten Schwingungsmodus festgestellt. Die ersten beiden Testreihen FSI-PfS-1*x* und 2 *x* sind vornehmlich auf zweidimensionale Struktur- und Strömungsbewegungen beschränkt. Um eine dreidimensionale Testkonfiguration zu entwickeln, wurde der starre Zylinder durch einen starren Kegelstumpf ersetzt (FSI-PfS-3*x*). Wiederum wurde eine elastische Platte hinten am Kegel befestigt. Für die Strömung und die Strukturbewegung wurden quasi-periodische dreidimensionale Bewegungszustände im ersten Schwingungsmodus ermittelt. Die letzte Testreihe befasst sich mit einem anwendungsbezogenen Aufbau und orientiert sich an bekannten Untersuchungen wirbelinduzierter Schwingungen (VIV). Dieses Phänomen tritt in sehr vielen technischen Anwendungen auf, beispielsweise in Rohrbündelwärmetauschern. Der Aufbau von FSI-PfS-4*x* besteht aus einem langen elastischen Zylinder, welcher an einer Seite fest fixiert und an der gegenüberliegenden Seite freibeweglich ist. Optional wird der elastische Zylinder in einer Anordnung von starren Zylindern begrenzt. Die Querströmung verursacht große Strukturverformungen mit hohen Schwingungsfrequenzen des elastischen Zylinders.

Die komplementären numerischen Untersuchungen wurden mit der Multi-Physik-Softwareumgebung von ANSYS® 14.0 durchgeführt. Dabei wurde der Strömungslöser ANSYS® CFX mit dem Strukturlöser ANSYS® Mechanical gekoppelt. Aufgrund der vorliegenden turbulenten Strömung wurde ein RANS Turbulenzmodell (SST) verwendet. Die numerischen Untersuchungen konnten teilweise die experimentellen Systemzustände reproduzieren. Gerade die Simulation der zweidimensionalen Testfälle ergab gute Übereinstimmungen mit den experimentellen Daten. Für die dreidimensionalen Testfälle wurden aufgrund von Beschränkungen der Zellanzahl und unpassenden Randbedingungen für die Struktur teilweise unphysikalische Ergebnisse produziert.

Zusammenfassend enthält die vorliegende Arbeit ausführliche Beschreibungen und Analysen verschiedener Fluid-Struktur-Wechselwirkungs-Testfälle. Während die Testreihe FSI-PfS-1*x* noch eher einfach numerisch reproduzierbar ist, steigt der Aufwand der Berechnung für die Testfälle FSI-PfS-2*x*, 3*x* und 4*x* erheblich an. Verantwortlich dafür sind die deutlich komplexeren physikalischen Kopplungsmechanismen zwischen dem strömenden Medium und der schwingenden Struktur.

Die Testfälle wurden in internationalen Journalen publiziert und die Datensätze der Testfälle FSI-PfS-1*a* und FSI-PfS-2*a* sind über die ERCOFTAC/QNET Wiki Website (<http://qnet-ercoftac.cfms.org.uk>) verfügbar.

Contents

Nomenclature	VIII
1 Introduction	1
1.1 Motivation	1
1.2 Literature review	2
1.3 Objectives of the present work	14
1.4 Outline	15
2 Fundamentals of structure and fluid dynamics	17
2.1 Governing equations of structure dynamics	17
2.1.1 Kinematics	17
2.1.2 Dynamics	19
2.1.3 Constitutive relations	20
2.1.4 Initial and boundary value problem of non-linear elastodynamics	22
2.1.5 Weak formulation	22
2.2 Governing equations of fluid dynamics	23
2.3 Turbulent flows	24
2.4 Turbulent flows near walls	29
2.5 Governing equations of fluid dynamics on moving grids	30
3 Fluid-structure interaction mechanisms	33
4 Experimental measuring techniques and test facility	39
4.1 Description of the test facility	39
4.2 Planar particle-image velocimetry	41
4.2.1 Particle follow behavior	42
4.2.2 Optical requirements	44
4.2.3 Velocity processing	46
4.3 Volumetric particle tracking	47
4.4 Laser triangulation	52
5 Numerical simulation techniques	55
5.1 Computational structure dynamics	55
5.1.1 Element formulations	60
5.1.2 Temporal discretization	60
5.2 Computational fluid dynamics	61
5.2.1 Spatial discretization	61
5.2.2 Temporal discretization	63
5.2.3 Discretization of grid movement	64
5.2.4 Flow modeling near the wall	65
5.3 Coupling method	66
5.4 Mesh movement	67

5.5	Validation of the coupling scheme	68
6	Definition of the benchmark cases	71
6.1	Flow phenomena past bluff bodies	71
6.2	Classification of the test cases	73
6.3	General definitions of the test cases FSI-PfS-1x – FSI-PfS-3x	74
6.3.1	Two-dimensional geometry without rear mass - FSI-PfS-1x	75
6.3.2	Two-dimensional geometry with rear mass - FSI-PfS-2x	76
6.3.3	Three-dimensional geometry - FSI-PfS-3x	77
6.3.4	Application-based test cases - FSI-PfS-4x	79
7	Experimental set-up	83
7.1	Measurement set-ups	83
7.1.1	Mono PIV measurement set-up	84
7.1.2	V3V measurement set-up	85
7.1.3	LLT measurement set-up	90
7.1.4	Illustration of the entire measurement set-up	90
7.1.5	Comparison of the applied flow measurement techniques	92
7.2	Measurement errors	95
7.2.1	PIV measurement errors	95
7.2.2	V3V measurement errors	101
7.2.3	LLT measurement errors	101
7.3	Flow conditions	102
7.4	Post-processing procedures	102
7.4.1	Generation of phase-resolved data	102
7.4.2	Proper orthogonal decomposition	105
8	Preliminary studies	109
8.1	Flow measurements around rigid structures	109
8.1.1	FSI-PfS-1x/2x	109
8.1.2	FSI-PfS-3x	111
8.1.3	FSI-PfS-4x	115
8.2	Structural tests	120
8.2.1	Structural tests for FSI-PfS-1x, 2x and 3x	120
8.2.1.1	Static tests	120
8.2.1.2	Dynamic tests	123
8.2.1.3	Decay tests	126
8.2.2	Structural tests for FSI-PfS-4x	129
8.3	Modal analysis	130
9	Numerical setup	133
9.1	Grids and boundary conditions of FSI-PfS-1x and 2x	133
9.1.1	CFD	133
9.1.2	CSD	136

9.1.3	Coupling conditions	137
9.2	Grids and boundary conditions of FSI-PfS-3x	138
9.2.1	CFD	138
9.2.2	CSD	140
9.2.3	Coupling conditions	140
9.3	Grids and boundary conditions of FSI-PfS-4x	140
9.3.1	CFD	140
9.3.2	CSD	143
9.3.3	Coupling conditions	143
10	Results and Discussion	145
10.1	Experimental results and analysis	146
10.1.1	FSI-PfS-1x (Two-dimensional geometry without rear mass)	146
10.1.2	FSI-PfS-2x (Two-dimensional geometry with rear mass)	178
10.1.3	FSI-PfS-3x (Three-dimensional geometry)	203
10.1.4	FSI-PfS-4x (Application-based test cases)	229
10.2	Numerical results	254
10.2.1	FSI-PfS-1x (Two-dimensional geometry without rear mass)	254
10.2.2	FSI-PfS-2x (Two-dimensional geometry with rear mass)	269
10.2.3	FSI-PfS-3x (Three-dimensional geometry)	278
10.2.4	FSI-PfS-4x (Application-based test cases)	286
11	Conclusions and Outlook	292
11.1	Conclusions	293
11.2	Outlook	301
	References	314

Nomenclature

Latin symbols

Symbol	Unit	Description
a_1	-	SST model constant
A	-	POD temporal coefficients
A	m^2	area
a, b	m	cell length
a_o, a_1	-	polynomial coefficients
A	m	added mass
B	-	derived shape functions
b	m	cylinder distance
B	Ns/m	added damping
c	-	coupling iteration
C	-	logarithmic boundary layer constant
C	-	POD auto-covariance matrix
c	-	sensitivity factor
c	-	shape coefficients
c	-	stiffness model exponent
C	N/m	material elasticity tensor
c	N/m	stiffness constant
c^T	-	tangent stiffness
C_μ	-	SST model constant
$c_{p,f}$	$m^2 / (s^2 K)$	specific heat capacity
C_d, C_l	-	force coefficient
C	N/m	added stiffness
$CD_{k\omega}$	-	SST cross diffusion term
d	-	assemblage vector of nodal unknowns
D	-	modal damping value
d	m	deformation vector
d	m	diameter
D	m	diameter
d	m	displacement vector
d	Ns/m	damping constant
d_{beam}	m	laser beam diameter
D_{ij}	-	diffusion tensor
d_e	m	nodal displacements
D_k	-	diffusion
d_l	m	lens diameter
d_p	m	particle diameter
e	m	laser lens distance
E	m^2/s^2	energy content

E	N/m ²	GREEN-LAGRANGIAN strain tensor
<i>E</i>	N/m ²	YOUNG's modulus
F	-	deformation gradient tensor
<i>f</i>	1/s	frequency
\bar{f}	N	mean force
<i>f'</i>	N	force fluctuation
<i>f</i>	m	focal length
F	N	assemblage vectors of force unknowns
<i>f</i>	N	external forces
f	N	force vector
<i>f</i>	N	volume forces
<i>F, f</i>	-	diffusive fluxes
<i>f_{ext}</i>	N	external force
<i>F₂</i>	-	SST blending function
<i>F_d</i>	N	drag force
<i>F_l</i>	N	lift force
<i>f_N</i>	1/s	natural frequency
<i>f_p</i>	N	particle force
<i>f_s</i>	1/s	vortex shedding frequency
<i>G</i>	-	shear modulus
<i>g</i>	m/s ²	gravitational acceleration
<i>h</i>	m	wall distance
<i>H, h</i>	m	height
<i>h_{lightsheet}</i>	m	laser light sheet thickness
<i>H_c</i>	m	cylinder center <i>y</i> -position
I	N/m ²	identity tensor
<i>I₁, I₂</i>	-	image record
K	-	assemblage property matrix
<i>k</i>	m ² /s ²	kinetic energy
<i>k</i>	m ² /s ²	turbulent kinetic energy
<i>K_B</i>	-	bending stiffness
<i>k_e</i>	N/m	element stiffness
<i>l</i>	m	characteristic length
<i>L, l</i>	m	length
<i>L_c</i>	m	cylinder center <i>x</i> -position
<i>l_d</i>	m	calibration dot distance
<i>l_k</i>	m	Kolmogorov length
<i>L_T</i>	m	characteristic length scale
<i>m</i>	kg	mass
<i>M, m, N, n</i>	pixel	image/grid size
<i>n</i>	-	measurement segment
<i>n</i>	-	nodal number
n	-	normal vector

N	-	shape function
n	-	amount of elements
\mathbf{n}_k	-	normal vector
\bar{p}	N/m ²	mean pressure
p	N/m ²	pressure
P_{ij}	-	production tensor
p_0	N/m ²	initial pressure
P_k	-	production
p'	N/m ²	pressure fluctuations
q_Φ	-	integrand
r	-	residual
\mathbf{r}	m	mesh displacement
r, s	-	normalized coordinates
Re	-	Reynolds number
Re _p	-	particle Reynolds number
s	m	lens sensor distance
S	m ²	surface
\mathbf{S}	N/m ²	PIOLA-KIRCHHOFF stress tensor
Sk	-	Stokes number
St	-	Strouhal number
T	K	temperature
\mathbf{t}	N/m ²	stress tensor
T	s	period length
Δt	s	time interval
t	s	time
t	s	measurement segment length
t_0	s	initial time
t_e	N	element forces
Tu	-	turbulence level
TR	-	taper ratio
\bar{u}	m/s	mean velocity
\mathbf{u}	m/s	velocity vector
u, v, w	m/s	velocity components
u^+	m/s	dimensionless velocity
u_∞	m/s	inflow velocity
u_τ	m/s	shear stress velocity
u_{inflow}	m/s	inflow velocity
$u_{p,\text{lag}}$	m/s	particle lag velocity
u_p	m/s	particle velocity
u_s	m/s	sedimentation velocity
U_T	m/s	characteristic velocity scale
U_t	m/s	tangential velocity
u'	m/s	velocity fluctuations

V	m^3	volume
V_p	m^3	particle volume
W	Nm	deformation work
W, w	m	width
\mathbf{x}, \mathbf{X}	m	displacement vector
x, y, z	m	coordinate components
x, y, z	m	displacement components
x/D	-	dimensionless x -coordinate
y^+	-	dimensionless wall distance
y_0	m	initial displacement

Greek symbols

Symbol	Unit	Description
α	-	angle
α	-	Rayleigh damping constant
α	-	underrelaxation factor
α_1, α_2	-	SST model constant
β	-	Rayleigh damping constant
β	-	scheme coefficient
β, β^*	-	SST model constant
γ	-	magnification factor
Γ	-	angle dislocation
Γ_s	m^2	structure surface
Γ_f	m^2	fluid surface
δ	-	delay constant
δ_{ij}	-	Kronecker delta
ϵ_{ij}	-	dissipation tensor
ϵ	m^2/s^3	dissipation
ζ	-	mesh stiffness
Θ	-	angle dislocation
κ	-	von Kàrmàn constant
λ	-	POD eigenvalues
λ	m	wave length
λ_2	-	vortex criterion
λ_s	-	LAMÈ constant
λ_f	$\text{W}/(\text{m K})$	heat conductivity
Λ	-	logarithmic decrement
μ_s	-	LAMÈ constant
μ_f	Ns/m^2	dynamic viscosity
μ_T	$(\text{m kg})/\text{s}$	eddy viscosity
ν_f	m^2/s	kinematic viscosity
ν	-	POISSON ratio
π	-	Pi
Π_{ij}	-	pressure shear correlation tensor
ρ_f	kg/m^3	fluid density
$\rho_{k1}, \rho_{k2}, \rho_{\omega1}, \rho_{\omega2}$	-	SST model constants
ρ_p	kg/m^3	particle density
ρ_s	kg/m^3	structure density
σ	-	standard deviation
σ	N/m^2	stress tensor
τ_f	s	fluid response time
τ_p	s	particle response time

τ_w	N/m^2	wall shear stress
τ	N/m^2	shear stress
$\tau_{ij,\text{RANS}}$	N/m^2	Reynolds stress tensor
$\tau_{ij,\text{mol}}$	N/m^2	molecular viscous stress tensor
Φ	-	arbitrary flow quantity
Φ_c	-	cross correlation function
Φ_d	-	drag phase shift
Φ_l	-	lift phase shift
χ	-	measurement quantities
ω_s	$1/\text{s}$	angular frequency
ω	$1/\text{s}$	vorticity vector
$\omega_x, \omega_y, \omega_z$	$1/\text{s}$	vorticity components
Ω_0	-	initial deformation state
Ω_s	-	deformed state
Ω_s	m^3	structure volume
Ω_f	m^3	fluid volume

Abbreviation

Abbreviation	Description
ALE	Arbitrary Lagrangian-Eulerian
CCD	Coupled conductive device
CFD	Computational Fluid Dynamics
CSD	Computational Structure Dynamics
CSM	Computational Structure Mechanics
CTA	Constant temperature anemometry
CV	Control volume
DES	Detached-eddy simulation
DNS	Direct numerical simulation
EIE	Extraneous-induced excitation
EPDM	Ethylene propylene diene monomer
FE	Finite element
FEM	Finite-element method
FPGA	Field programmable gate array
FIE	Fluctuation-induced excitation
FSI	Fluid-Structure interaction
IIE	Instability-induced excitation
LDV	Laser-Doppler velocimetry
LES	Large-eddy simulation
LLT	Laser-line triangulation
Nd:YAG	Neodymium-doped yttrium aluminum garnet
MIE	Movement-induced excitation
MFX	ANSYS [®] Multifield solver
PA	Polyamide
PE	Polyethylene
PIV	Particle-image velocimetry
POD	Proper orthogonal decomposition
RANS	Reynolds-averaged Navier-Stokes equations
SHGS	Silver hollow glass spheres
SST	shear stress transport model
URANS	Unsteady Reynolds-averaged Navier-Stokes equations
V3V	Volumetric three-dimensional velocimetry
VIV	Vortex-induced vibrations

1. Introduction

1.1. Motivation

Nowadays, common problems in the field of engineering are of multi-physical nature. Two or more physical phenomena act together within one system, which can not or only in a limited manner described separately. In the past, these coupled problems were simplified by appropriate methods. With the ongoing research in, for example, fluid and structure mechanics or thermodynamics an enormous disciplinary knowledge is available. Complex individual problems are described by empirical studies, mathematical models and computational methods. In terms of better physical understanding or technical requirements like optimization or risk prevention, the investigation of coupled problems moves into the focus in research and development. The understanding and modeling of interactions between those physical disciplines is the challenge in modern engineering.

A very common physical interaction is the coupling between an (unsteady) fluid flow and the motion or deformation of a solid structure. Shear stresses and pressure forces are acting on the interface between the fluid and the solid. The forces induce a motion and/or deformation of the structure which affects again the surrounding fluid. This fluid-structure interaction (FSI) is related to many natural phenomena and technical applications. From micro-scaled up to large structures fluid-structure interactions are wide-spread. Examples of the natural appearances are the micro-scaled FSI of insects which use the deformation of small hairs or antennas to monitor environmental conditions like their flight velocity or the macro-scaled FSI of trees which are exposed to unsteady wind loads and react with oscillations of the treetop on this physical coupling. Similar to the natural presence of FSI, many technical applications use or are confronted with the FSI effect. Several engineering fields like civil engineering (wind-load induced oscillations of buildings), aeroelasticity (vibrations of airfoils), process engineering (membrane pumps, flow-induced vibrations of heat exchangers, turbo machines) and biology (extending and contracting arteries, artificial heart valves) are connected with FSI effects. A well-known FSI application is a wind turbine for producing renewable power. The wind load on the rotor blade induces a rotatory movement of the rotor which is transformed into electrical power by a generator. But beside this positive side, the FSI coupling can also have fatal consequences under certain conditions. With increasing wind velocities the forces on the rotor blades also rise and potentially lead to structural failures of the blades. Therefore, also in fields of safety and risk prevention these problems have to be taken into account. In very new engineering fields fluid-structure interactions are used for product innovations. For example, biologically inspired sensors use the FSI effect on micro-cantilevers to measure velocities (Su et al., 2002; Liu et al., 2012) similar to the insects mentioned.

The increasing demand of complex engineering solutions of products and constructions raised the necessity for predictions of multi-field processes. Reasons are the increased efficiency of simulation-supported developments and the substitution of expensive experimental studies. In both, structure and fluid mechanics, the predictions of various problems by analytical and numerical methods are possible for a long time. On the other hand, especially the numerical prediction of eventually turbulent flows is computationally expensive. The coupling of a computational fluid dynamic (CFD) prediction with a computational structure dynamic (CSD)

prediction multiplies these costs. Due to this circumstance the numerical prediction of FSI problems was not effectively possible for a long time. With the ongoing research of enhanced numerical algorithms in science and industry and the strong advancement in computational power, more complex problems can be predicted now. Therefore, many numerical methods for the FSI coupling were and are currently developed and it is now feasible to simulate real-world FSI problems. To evaluate and improve these complex non-linear computations, complementary experimental studies under clearly defined operating conditions (benchmark cases) are highly necessary and the main topic of this thesis.

1.2. Literature review

FSI benchmarks

A variety of numerical models for FSI predictions are currently developed, see, e.g., Heil (2004); Farhat et al. (2006); Menter et al. (2006); Förster et al. (2007); Degroote et al. (2008); Küttler and Wall (2009); Turek et al. (2010); Vierendeels et al. (2010); Bungartz et al. (2010); Gomes et al. (2011); Breuer et al. (2012); De Nayer et al. (2012). To evaluate and improve these algorithms the comparison with experimental studies is used to validate, verify and enhance the computational solution. Therefore, experimental test cases under clearly defined operating conditions are developed. By direct comparison of the results the numerical method can be validated regarding its physical integrity and precision. With that information a further improvement of the FSI method is possible. In most cases relative simple FSI problems are chosen to form a validation test case. With the restriction to simple geometries and well-known flow conditions the sources of uncertainties of the benchmark should be kept on an acceptable level. During the last decade a lot of FSI benchmarks were published. Most of them are restricted either to numerical or experimental investigations. Experimentally examined test cases are of course limited by the physical feasibility. As already mentioned these studies are often focused on simple geometric structures and controllable boundary conditions and moderate, predictable structural responses. Very common are purely numerical benchmarks to prove numerical properties like stability, efficiency and precision of a FSI algorithm. In these test cases the attention is paid to a precise description of the applied coupling method and the employed computational meshes to produce reference data on a well-chosen coupled problem. In contrast to the experimental investigations these cases are not bound to the laboratory scale and the limitations of the measurement techniques. Thereby, different numerical methods or parameter studies can be compared and support the validation process. Some of these studies are presented in the following ¹:

In 2001 Glück et al. (2001) published two numerical FSI benchmarks consisting of a simple two-dimensional flexible plate oscillating in a channel (Fig. 1) and a three-dimensional flexible

¹All figures in this section are schematically illustrated to give an impression of the specific FSI problem. Due to the complex and numerous deformation states, these illustrations are no exact reproductions of the test case definitions and measured or predicted results.

L-shaped plate (Fig. 2). Both configurations are exposed to a laminar flow ($Re = 50 - 500$). The benchmarks provide numerical results on the decay motion of the two-dimensional structure and the quasi-static structural deformation for the three-dimensional test case.

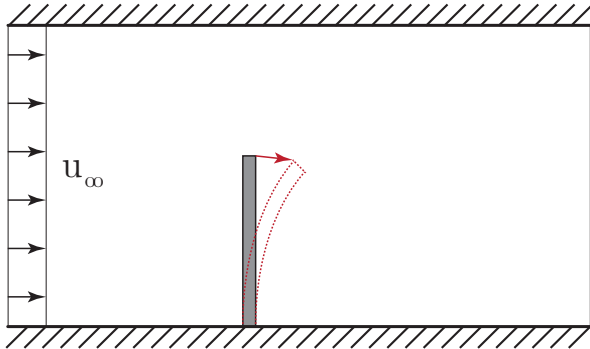


Figure 1: Flexible plate FSI benchmark by Glück et al. (2001).

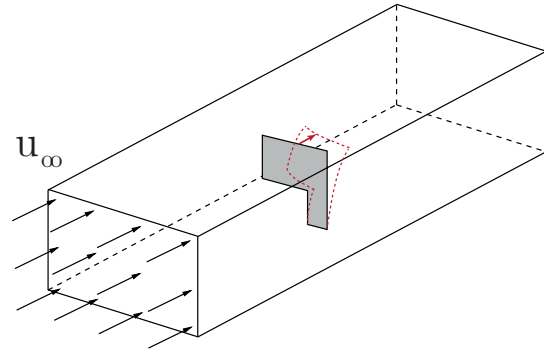


Figure 2: L-shaped plate FSI benchmark by Glück et al. (2001).

Another numerical test case is published by Wall (1999) and Mok (2001) and provides a two-dimensional channel with a contraction behind a vertical flexible rubber-plate (Fig. 3). The flexible plate reduces the cross-section of the channel of which only the half is modeled (symmetry boundary conditions are set on the symmetry axis). This configuration is exposed to a laminar flow ($Re = 100$) and results in a static deformation of the plate in the flow direction and a large recirculation area behind it. Unsteady effects (increase and decrease of the pressure force on the structure, formation of large and small-scaled eddies behind the plate and a transient deformation of the structure) behind the plate are observed during the first 25 s of the simulation time. After 25 s a steady state is reached. As a consequence of the channel contraction the recirculation area behind the flexible rubber plate is restricted. Nobile (2001) and Formaggia et al. (2001) set up a three-dimensional numerical FSI test case of an artificial artery (Fig. 4) at $Re = 40$. Through this straight tube a given pressure pulse propagates which extends the flexible artery structure and delivers a fully three-dimensional and unsteady deformation state.

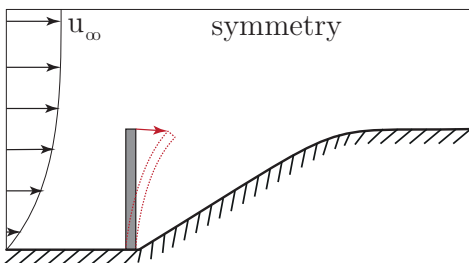


Figure 3: Contracting channel FSI benchmark by Wall (1999).

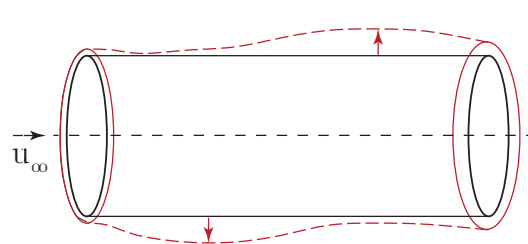


Figure 4: Flexible pipe FSI benchmark by Nobile (2001).

Similar to this test case is the setup of Sieber (2001) which describes a laminar flow ($Re = 100$) in an elastic pipe with supported ends and two unsteady pinching forces (Fig. 5). This study investigates the fluid response while the structure is being deformed by external forces. As a consequence of the force excitation the pipe contracts and the fluid velocity and pressure

reacts on this change. The alteration of the fluid quantities changes the fluid forces on the pipe walls which again results in a modified deformation state. A second test case by Sieber (2001) is related to the common phenomenon of vortex-induced vibrations (VIV) of an elastically mounted rigid circular cylinder (free in the xy -plane, Fig. 6) in a laminar flows ($Re = 20 - 100$). Due to the alternating shedding of vortices on the cylinder surface the pressure forces oscillate and result in a periodic displacement of the cylinder mainly in cross-flow direction.

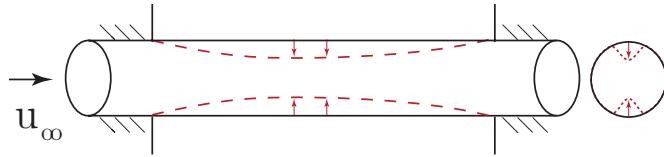


Figure 5: Contracting pipe FSI benchmark by Sieber (2001).

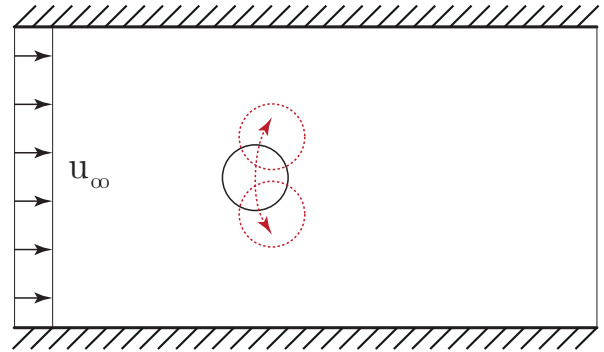


Figure 6: Vortex-induced vibration of an elastically mounted cylinder, FSI benchmark by Sieber (2001).

A third test case is performed by Sieber (2001) on a three-dimensional FSI problem. Here, the cylinder is slightly asymmetrically fixed on the channel walls but is fully elastic between them (Fig. 7). Due to the narrow channel (channel width to cylinder diameter: $w/d = 4.1$) the walls (no-slip) have a stabilizing effect on the flow around the cylinder ($Re = 150$). This leads to a suppression of the vortex shedding which is rather typical for flows around circular cylinders in free flow. The deformation of the cylinder shape occurs due to the high pressure at the stagnation point at the front of the cylinder. Remarkable is that despite the laminar flow conditions and the absence of the formation of large eddies, small oscillations of the structure deformation are predicted. Responsible for these structure deflections is the asymmetric wake behind the cylinder and generally the three-dimensional effects in the flow due to the asymmetric geometry.

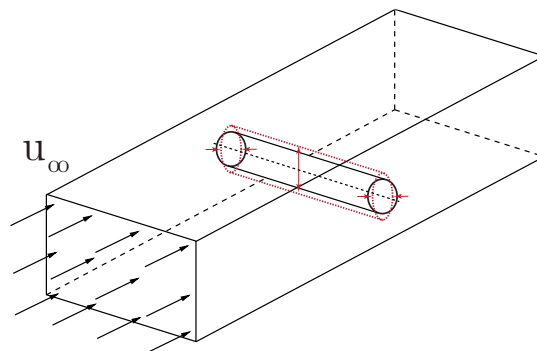


Figure 7: Elastic cylinder FSI benchmark by Sieber (2001).

Lee et al. (2013) present two further benchmarks related to cylinder oscillations. The first case consists of a rigid cylinder in a quiescent fluid (Fig. 8). In contrast to the previously introduced

benchmarks here the fluid motion is not the excitation source of the structure motion. In this case, the cylinder is continuously excited by a harmonic horizontal oscillation within the fluid at rest. Therefore, the physics is limited to a one-way fluid-structure interaction. That means that the streamwise displacement of the cylinder is prescribed and only the fluid reacts on the physical changes in the system. According to the mount of the cylinder the motion in the transverse direction is prohibited. Lee et al. (2013) are interested in the reaction of the surrounding water to the cylinder vibration which is examined by two-dimensional numerical FSI predictions of the laminar flow using the immersed boundary technique. The usage of one-way coupled prescribed structure motion cases is a common preliminary study for the fluid and mesh motion solver. The results achieved are in a good agreement with previous investigations by Dütsch et al. (1998) based on LDV flow measurements and complementary 2D numerical predictions.

The second case of Lee et al. (2013) is directly related to VIV and uses a similar set-up as the first benchmark. Now, the cylinder is mounted elastically in both streamwise and transverse directions with two spring-damper systems which allow motions in the xy -plane. Furthermore, a constant inflow velocity is set to establish a periodic vortex shedding from the cylinder. Due to the oscillating fluid forces on the cylinder periodic sinusoidal displacements in both x - and y -directions are predicted. Thereby, the y -displacements of the rigid cylinder are much larger than its x -displacements, while the x -directional frequency is twice the y -directional frequency as expected. For the sake of completeness, it has to be mentioned that a lot of numerical and also experimental investigations concerning similar VIV configurations are carried out over the last three decades. The broad range of different setups (elastically-mounted rigid cylinders with x - or y -motion, elastically mounted rigid cylinders with xy -motion, forced oscillations of cylinders) is summarized in Williamson and Govardhan (2004) and will therefore not be mentioned here. The general outcome is that the strong interaction between the fluid flow and the structural deflection is responsible for several different excitation and response modes. These modes depend on the free degrees of freedom of the structure, the material properties and the flow conditions and experimentally observed and computationally reproduced in many studies as summarized in Williamson and Govardhan (2004).

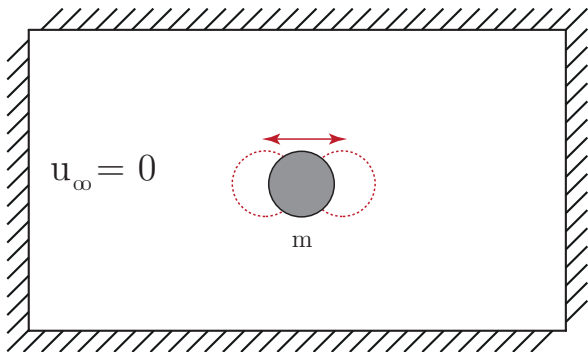


Figure 8: Forced cylinder oscillation, FSI benchmark by Lee et al. (2013).

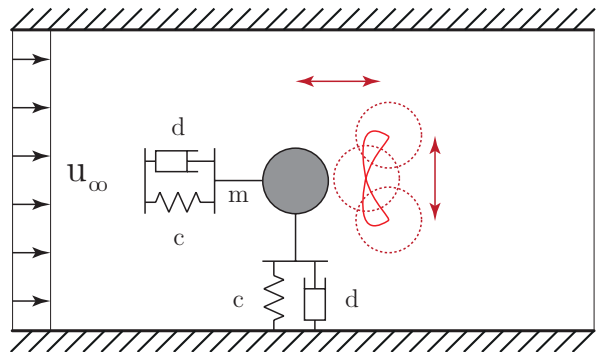


Figure 9: Elastically mounted rigid cylinder (xy -plane), FSI benchmark by Lee et al. (2013).

Another numerical FSI investigation is presented by Balint and Lucey (2005). Here, a can-

tilivered flexible plate is placed into a viscous channel flow (Fig. 10) as a representation of the dynamics of the human upper airway. The focus of the study is the instability mechanism of the flexible plate that cause airway blockage during sleep. Therefore, different scenarios are computed with free or blocked inflow conditions on the two inflows (airways) at Reynolds numbers up to 1512. When both upper and lower airways are free, the plate is found to loose its stability through a flutter mechanism beyond a critical Reynolds number. In this configuration several bending modes are present according to the inflow velocity. When one airway is closed, the plate principally looses its stability through a separation mechanism and again a critical flow speed exists. For this case it is stated that the structural damping is essential for the plate deflection and leads to potential constrictions of the channel.

Two other FSI problems are presented by Hübner et al. (2004). The first problem is a laminar fluid flow ($Re = 1700$) around a two-dimensional building interacting with a thin membrane on the roof of the building (Fig. 11). A separation area develops starting at the leading edge of the building, whereas vortex shedding occurs at the trailing edge. The pressure fluctuations caused by the unsteady separation area at the leading edge induce a small-scaled quasi-periodic oscillation of the membrane.

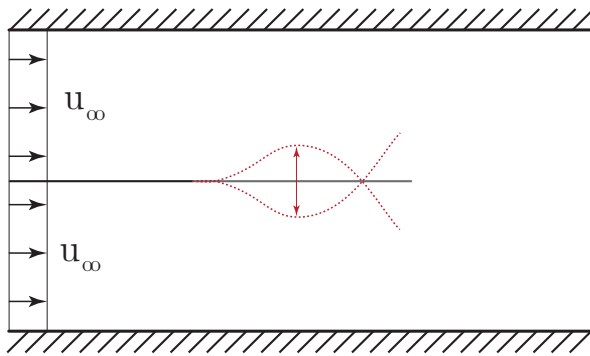


Figure 10: Cantilevered flexible plate FSI benchmark by Balint and Lucey (2005).

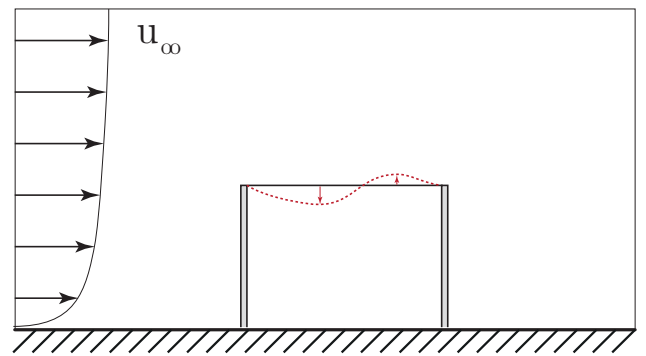


Figure 11: Thin membrane FSI benchmark by Hübner et al. (2004).

The second test case is a modified configuration of a test case published by Wall and Ramm (1998). Both numerical studies consist of a thin elastic cantilever plate which is situated in the wake of a rigid square cylinder (Fig. 12). However, Hübner et al. (2004) reduced the inflow velocity used by Wall and Ramm (1998) which leads to a smaller Reynolds number of $Re = 204$ (compared to $Re = 332$ by Wall and Ramm (1998)). Based on the coupled unsteady FSI simulations of Hübner et al. (2004) a periodic vortex shedding occurs at the edges of the square cylinder. Due to the pressure forces acting on the plate, a high-amplitude periodic plate vibration is predicted. Another outcome of this study is that the FSI coupling is strongly influenced by the initial conditions. The FSI system behavior changes significantly, if the simulation starts with a large initial tip deflection which may represent a temporary load. This change leads to a much lower oscillation frequency but more than doubled displacements at the tip of the structure. Also Wall and Ramm (1998) state that two stable solutions of the FSI problem coexist depending on the initial conditions.

In 2003, the DFG Research Unit 493 "Fluid-Structure Interaction: Modeling, Simulation,

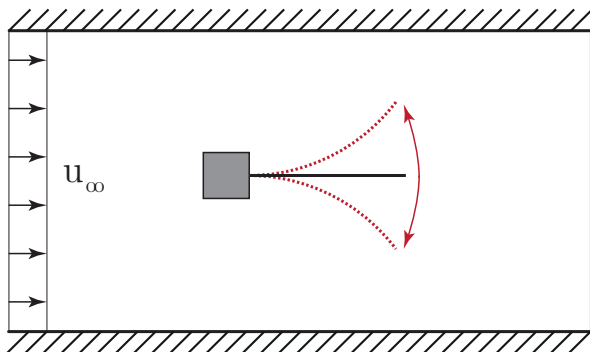


Figure 12: Square cylinder with an elastic splitter plate, FSI benchmark by Wall and Ramm (1998).

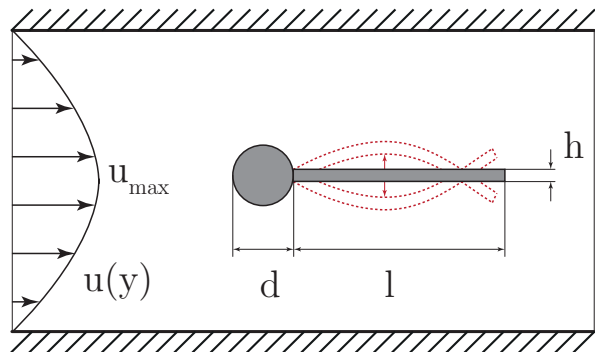


Figure 13: Circular cylinder with an elastic splitter plate, FSI benchmark by Turek and Hron (2006).

Optimization” was founded to investigate FSI effects using a variety of different numerical methods (Bungartz and Schäfer, 2006; Bungartz et al., 2010). The primary objective of the research group was the systematic and coordinated development of numerical methods for the robust and efficient simulation of fluid-structure interactions. One part of this project was the proposal of the well-known numerical benchmark by Turek and Hron (2006). This benchmark is based on the two-dimensional version of the widely-used CFD benchmark ”Confined Flow around a Cylinder” (Schäfer et al., 1996) and attaches a thick and elastic plate consisting of an artificial material to this fixed rigid cylinder (Fig. 13). The geometric setting of the test case consists of a long narrow channel with an asymmetric fixation of the structure in the vicinity of the inlet. The position of the structure is intentionally slightly non-symmetric to prevent the dependence of the onset of any possible oscillation on the precision of the computation. The ratio between the plate length and the cylinder diameter is set to $l/d = 3.5$ and the relation of the plate thickness to the cylinder diameter is $h/d = 0.2$, respectively. Similar to the already mentioned second test case of Hübner et al. (2004) the laminar flow ($Re = 10 - 200$) generates a vortex-induced oscillation of the flexible structure in the second swiveling mode and deflections in the order of the cylinder diameter. In addition to the FSI simulations this benchmark also provides fluid-only and structure-only predictions which are useful for the validation of uncoupled solvers. Because of the broad provision of comparative data and the simple geometry and boundary conditions, this benchmark is well-known and often used for validating numerical FSI methods. The computations are based on extensive studies on highly resolved grids to ensure a high quality of the results. Unfortunately, only numerical investigations are available as a consequence of the more or less artificial material properties and physical dimensions of the structure and the fluid which were chosen purely based on numerical issues without taking into account how to implement the benchmark case into an experimental test facility.

Lee et al. (2012) present the FSI prediction of a flapping flexible plate in a quiescent fluid (Fig. 14) to investigate the effect of flexibility on the generation of effective propulsion for different operating conditions between rotation and translation. The flapping plate is translated in the y -direction and propelled in the x -direction. Translational velocities are composed of three portions: the constant velocity portion with a constant angle of attack, deceleration at the end of the constant velocity portion, and acceleration at the beginning of the constant

velocity portion. Furthermore, three types of rotation are applied: advanced, symmetrical and delayed rotation. For the symmetrical rotation, half of the rotation took place at the end of the translational movement and the other half took place at the beginning of the translation. For the advanced rotation, rotation took place in advance before the translational reverse. For the delayed rotation, rotation occurred after the reverse translation (for detailed information of the different motion phases, refer to Lee et al. (2012)). The numerical results of this study show that the behavior of the FSI coupling on the different phases is rather important for the creation of propulsion. The predicted elasticity effects of the deformed plate are analyzed and show that the major role of the flexible plate is to reduce the drag in the flow in comparison to complementary studies with a rigid plate. It is stated that the flexibility effectively reduces the propulsion losses in the rotation process (especially in the advanced rotation case), which improves the efficiency of propulsion and underlines the importance of flexible structures exposed to FSI in technical processes.

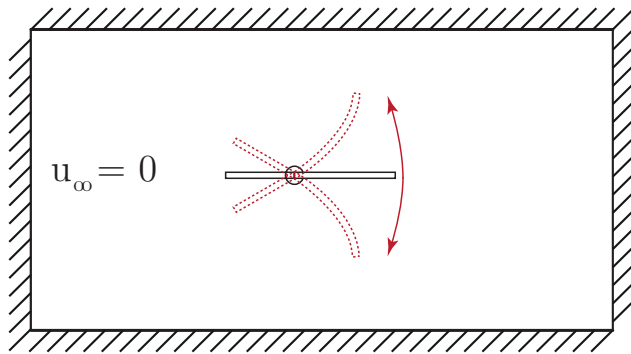


Figure 14: Rotationally mounted flexible plate, FSI benchmark by Lee et al. (2012).

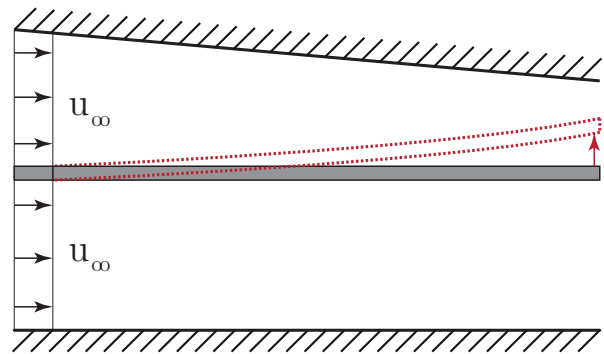


Figure 15: Flexible wall between two disconnected flows, FSI benchmark by Menter et al. (2006).

Another validation test case is developed by Menter et al. (2006) and consists of two channels separated by a flexible wall ($Re = 200$, Fig. 15). Due to the channel geometry a different pressure distribution in both channels results in an asymmetric load on the flexible wall. The flexible inner wall reacts with a deformation to the lower pressure side. The predictions show a good agreement for three different grid resolutions in comparison to the analytical solutions of Wang (1999).

A test case in the turbulent regime is presented by Bunge et al. (2003). Here, a rectangular rigid body is mounted elastically by a spring-damper system that only allows cross-flow oscillations. With the exposure to turbulent flows ($Re = 2 \cdot 10^4 - 12 \cdot 10^4$) a vortex-induced oscillation behavior is expected. The numerical predictions are performed on two- and three-dimensional grids and with the usage of two-equation RANS-based turbulence models. The results are compared to the experimental data of Ikenouchi et al. (1982) and show a qualitatively correct behavior. The reproduction of the first experimentally determined resonance velocity caused by vortex impingement on the trailing edge of the body is not achieved by the two-dimensional computations. The results of the three-dimensional predictions indicate a better representation of the swiveling frequencies of the body.

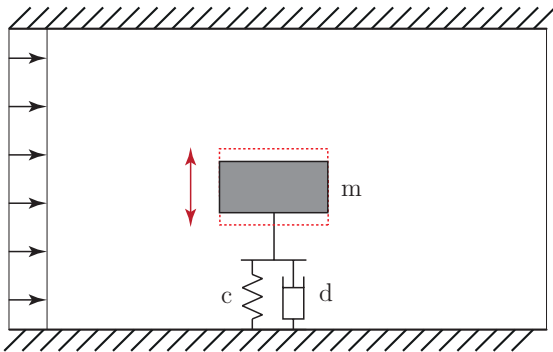


Figure 16: Elastically mounted (y -motion) rigid rectangular body, FSI benchmark by Bunge et al. (2003).

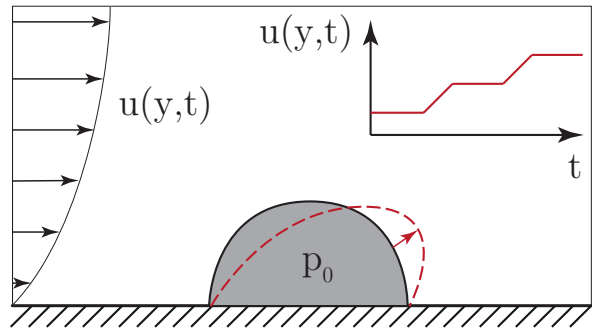


Figure 17: Semi-cylindrical flexible membrane, FSI benchmark by Teixeira and Awruch (2005).

Another numerical study in the turbulent regime is published by Teixeira and Awruch (2005). A semi-cylindrical flexible membrane is placed in a turbulent and compressible air flow at $Re = 1.9 \cdot 10^7$ (Fig. 17). The internal pressure p_0 within the structure keeps the membrane inflated but also allows deformations. The two-dimensional simulations use an algebraic turbulence model and an exponential spatial and time-dependent velocity profile at the inflow as illustrated in Fig. 17. The results reveal large unsteady deformations of the membrane including a rebounding of the structure, while a vortex is being generated downstream of it. The inflow is divided into constant and increasing velocity intervals. Therefore, stronger unsteady effects are observed during the increasing inflow velocities and nearly steady-state responses are reported during the constant inflow conditions. Furthermore, a periodic development and detachment of vortices in correspondence with the structural movement of the membrane is observable.

In summary, there are a lot of different FSI benchmarks that have been investigated numerically. Most of these studies are developed for the purpose of testing and improving a specific coupling method. The only known test case which has been used so far by many different research groups for validation purposes is the "Confined Circular Cylinder with an Elastic Splitter Plate" FSI benchmark by Turek and Hron (2006). Definitely, the main reason for this choice is the broad and reliable data base available for this benchmark. Critically seen can be the issue to validate a numerical prediction method based on another numerical computation. Generally, all the mentioned numerical benchmarks are artificial and partly only of academic interest with no direct practical application (i.e., due to the restriction to the laminar flow regime in most cases). In the following paragraphs some experimental FSI test cases will be presented. Due to the often high effort of these investigations only a limited amount of experimental FSI benchmarks is available.

To fill the gap of reliable experimental data on a specific FSI phenomenon once more the DFG Research Unit 493 (Bungartz and Schäfer, 2006; Bungartz et al., 2010) developed a test facility with special care on controllable boundary and working conditions to allow an accurate comparison between experimental measurements and numerical simulations. A lot of publications

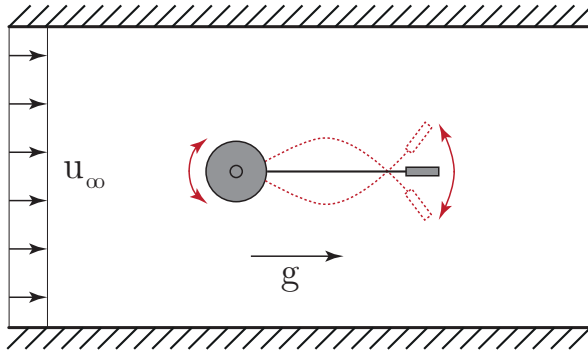


Figure 18: Rotationally mounted cylinder with steel sheet and weight, FSI benchmark by Gomes and Lienhart (2006).

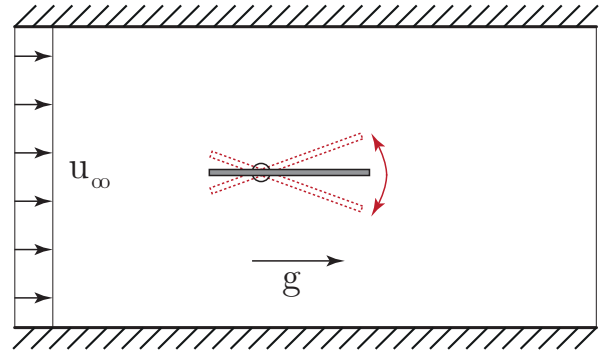


Figure 19: Rotationally mounted rigid plate, FSI benchmark by Gomes et al. (2010).

related to these studies are available by Gomes and Lienhart (2006, 2010, 2013), Gomes et al. (2011) and Gomes (2012) and contain several experimental and numerical investigations of the FSI coupling in laminar and turbulent flows.

The first experiments are performed under laminar flow conditions by using a highly viscous fluid (polyethylene glycol). The structure consists of a rigid rotatable circular cylinder with a thin steel plate attached to it (Fig. 18). At the trailing edge of the thin sheet a rectangular mass is attached to guarantee two-dimensional structure deflections and to add inertia to the system, which results in larger structural displacements. The structure is aligned with the gravitational acceleration to avoid asymmetric effects on the flow and the structural motion. Due to the two-dimensional behavior of the structure the same optical measurement system (2D-PIV) is used to obtain the structural deformation and the fluid motion in addition to the separate measurement of the front-body angle. Later on the fluid is replaced by water to further develop several fully turbulent benchmarks (Gomes and Lienhart, 2010, 2013) based on the same structures as applied in the laminar case. It is proved that the response of the structure is strongly dependent on the flow conditions in both laminar and turbulent regimes. Similarities in both regimes are found for low inflow velocities which result in structure deformations in the first swiveling mode and for high inflow velocities which leads to structural deflections in the second swiveling mode. Furthermore, the studies (Gomes, 2012; Gomes and Lienhart, 2013) analyze the excitation mechanisms according to Naudascher and Rockwell (1994) (see Section 5.3). It is stated that mainly the instability-induced excitation is responsible for the FSI coupling at low Reynolds numbers $Re < 47$. Here, the natural frequency of the structure strongly influences the FSI mechanism towards larger deformations. At higher Reynolds numbers the movement-induced excitation becomes dominant for this specific set-up and the deformations once more increases.

In addition to the experimental data, numerical simulations of the laminar flow are performed at two discrete inflow velocities $u_{\text{inflow}} = 1.07$ m/s and $u_{\text{inflow}} = 1.45$ m/s (Schäfer et al., 2010). The predicted displacements of the structure and the swiveling frequencies are in a good agreement for both inflow velocities showing the first ($u_{\text{inflow}} = 1.07$ m/s) and the second swiveling mode ($u_{\text{inflow}} = 1.45$ m/s) of the structure. These different structural bending responses are

also well-reproduced in this study. Despite the good agreement between the measured and calculated results, the numerical values for the swiveling frequencies and the structural deflection are slightly over-predicted for both cases. This tendency is also confirmed by Geller et al. (2010) who also performed simulations of the laminar test case at the inflow velocity of $u_{\text{inflow}} = 1.07$ m/s. In contrary to the laminar cases, simulations of the turbulent benchmarks ($\text{Re} = 14,960 - 26,840$) are to the best knowledge of the author not available up to now.

In general, all cases of the "Rotationally Mounted Cylinder with Steel Sheet and Weight" benchmarks of Gomes and Lienhart (2013) are found to be very challenging from the point of view of modeling and simulation. Especially the mesh deformation with respect to the free z -rotation degree of freedom (DOF) of the rigid front cylinder in addition to the attached thin steel sheet and its sharp connection to the steel weight is found to be difficult to compute. In the turbulent cases these problems concerning stability, mesh deformation and convergence are amplified. Another fully complementary study related to the same test facility with direct experimental and numerical comparisons is carried out by Gomes et al. (2010). This designated FSI benchmark consists of a rigid plate with a single rotational degree of freedom put into a water channel flow under turbulent flow conditions at $\text{Re} = 68,000$ (Fig. 19). This work contributed both, structural (angle of attack) and fluid flow measurements (velocity field). The coupled simulations are performed with an eddy-resolving turbulence model (LES) and showed some disagreements in the predicted maximum deflection angle and also in the predicted frequency which are both larger in the simulation than in the experiments (Gomes et al., 2010). The already mentioned test cases refer to academic settings with no direct application. In contrast, the following two experimental benchmarks belong to the development of marine and offshore structures. The experiments of Chaplin et al. (2005a,b) investigate the multi-modal and multi-frequency vortex-induced vibrations of a tension riser. Tension risers are applied at oil rigs or ships for the oil production and are sensitive to the ambient conditions like the flow and seawater conditions. According to the complicated access to those structures and the high costs in the case of damage, industry is interested on corresponding studies. The experiments of Chaplin et al. (2005a,b) are performed in a water channel with a towing carriage which delivers turbulent conditions at $\text{Re} = 2500 - 25,000$. Unfortunately, the study is only concentrated on the structural deformations (Fig. 20). Furthermore, the different swiveling modes found in the experiments are depending on the flow conditions and are also related to the initial conditions. Similar to the tension riser configurations are the purely experimental FSI studies of Fujarra et al. (2001) and Pesce and Fujarra (2002). They studied the vortex-induced vibrations of elastically mounted rigid and cantilevered cylinders in a turbulent water flow ($\text{Re} = 5700 - 95,000$), focusing on the hydro-elastic modal coupling in two different planes of vibration (Fig. 21). These experiments again include only structural measurements for the subharmonic couplings in in-line and cross-flow directions. Yamamoto et al. (2004) carried out complementary simulations of this test case stating that the general trend of the experimentally observed deflection is reproduced by the predictions. Disagreements are found in the lower maximum amplitude of the structure oscillation and the lack of a hysteresis observed in the experiments.

Summarizing the available experimental data on FSI benchmarks it is obvious that there is a

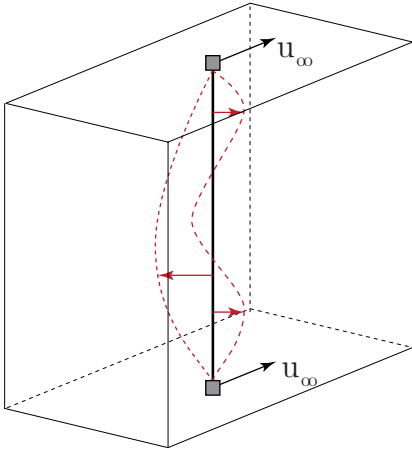


Figure 20: Two-sided mounted tension riser, FSI experiment by Chaplin et al. (2005a,b).

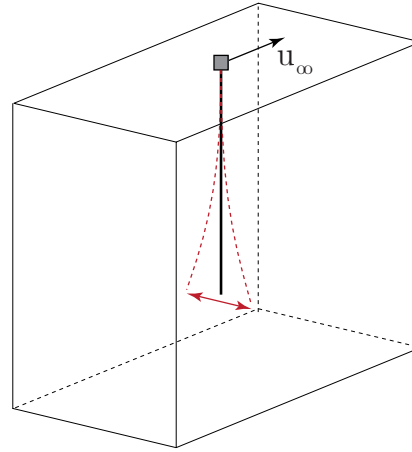


Figure 21: One-sided mounted tension riser, FSI experiment by Fujarra et al. (2001).

further need of geometrically simple test cases especially for turbulent flows. Extensive experiments were performed on the mechanism of vortex-induced vibrations on variously mounted rigid cylinders as explained in Williamson and Govardhan (2004). Here, a considerable amount of data is available. Nevertheless, these test cases include no structural deformations and therefore no complete data on bidirectional fluid-structure interactions. Gomes et al. (2010) and Gomes and Lienhart (2013) delivered reliable experimental data on several bidirectionally coupled FSI test cases in the laminar and turbulent regime. According to the challenging demands of these cases mentioned above they are up to now not widely used for the validation of FSI algorithms. In contrast to the above mentioned more academic FSI benchmarks the tension riser experiments of Chaplin et al. (2005a,b) and Pesce and Fujarra (2002) are more application-oriented. Unfortunately, only structural measurements are performed. Thus the validation of a FSI coupling method is highly limited. Furthermore, the dependence of the structural response on the initial condition is not conducive towards a validation test case.

In conclusion, the presented benchmarks are not sufficient to offer a complete, reliable and computationally feasible data basis for FSI validation in the turbulent regime. Furthermore, the only complete experimental FSI benchmarks of Gomes et al. (2010) and Gomes and Lienhart (2013) are restricted to geometrically two-dimensional problems while FSI application are often of three-dimensional kind.

Measurement techniques

In this thesis a particle-image velocimetry (PIV) system for two-dimensional flow studies, a volumetric three-dimensional velocimetry (V3V) system for three-dimensional flow fields and a laser distance triangulation sensor for two-dimensional structural deformation measurements are applied. The PIV principle is a standard method in fluid mechanics to obtain two-dimensional flow fields with two velocity components. The roots of PIV go back to the

laser-speckle velocimetry (Barker and Fourney, 1977; Dudderar and Simpkins, 1977), a technique that uses random speckle patterns to visualize fluid motions in highly concentrated particle flows in the late 1970s. With the further development of this measurement technique it was found that it is advantageous to decrease the particle concentration down to levels where individual particles or particle groups are observable (Pickering and Halliwell, 1984; Adrian, 1984). Based on these low particle densities it is noticed that the analysis of the flow is easier if the flow domain is split into many small 'interrogation' areas, which could be analyzed individually to generate one velocity for each area. The images are originally recorded using analog cameras and need an immense amount of computing power to be analyzed. With the development of high-resolution digital cameras and double-pulsed lasers this technique is now wide-spread in experimental fluid mechanics (Adrian, 1991, 2005) and offers several advantages (field and time-resolved methods, contactless operation; for a detailed description see Section 4.2) compared to other flow measurement methods like laser-Doppler velocimetry (LDV), constant temperature anemometry (CTA) or pressure-based techniques like the Pitot tube. In terms of FSI investigations the PIV technique is applied in the already mentioned FSI studies of Gomes and Lienhart (2006, 2010, 2013) and in several application-oriented investigations especially in connection with biological FSI phenomena. For instance, Kaminsky et al. (2007) validate a two-dimensional numerical prediction of a FSI-driven heart valve by PIV measurements. Another example related to the human organ research with the help of the PIV principle was recently presented by Kabinejadian et al. (2013) who applied the PIV technique to improve the design of a carotid stent for the treatment of artery bifurcations.

In contrast to the well-documented PIV method the V3V technique for volumetric flow investigations is rather new. The development of the defocused volumetric particle tracking method of the V3V is going back to the work of Willert and Gharib (1992). In this study a single camera system is defocused using a mask of three pin holes (Fig. 22). Based on this set-up the three-dimensional position of a point source of light (i.e., illuminated tracer particles as used in PIV) is projected on a single image. The sizes and locations of the particle image patterns on the image plane relate directly to the three-dimensional position of the individual particles. Thus, based on double-straddled picture sets the particles are tracked in space and time, yielding the field velocity information (example of a vortex ring in Fig. 22). Pereira and Gharib (2002) use this concept for the three-dimensional characterization of a two-phase flow. After identifying the third spatial position of the particles in the defocused particle reflection sets, a modified PIV cross-correlation algorithm is applied to obtain the three velocity components of a particle group within a specified voxel. Since in 2008 the first commercial realization of this technique was presented by the instrumentation manufacturer TSI, there are several studies available which utilize this method to investigate three-dimensional flow problems. For instance, Hill et al. (2008) measure the three-dimensional and highly unsteady flow field in the vicinity of a RUSHTON turbine in a stirred tank reactor and identify a strong radial jet, large tank-scale ring vortices, and small-scale blade tip vortices with the help of the V3V system. Another study is carried out by Troolin and Longmire (2008) who revisit an experiment on vortex rings generated from a pipe with an inclined exit. Earlier 2D-PIV studies on the same system by Webster and Longmire (1998) deliver two-dimensional results at several planes in

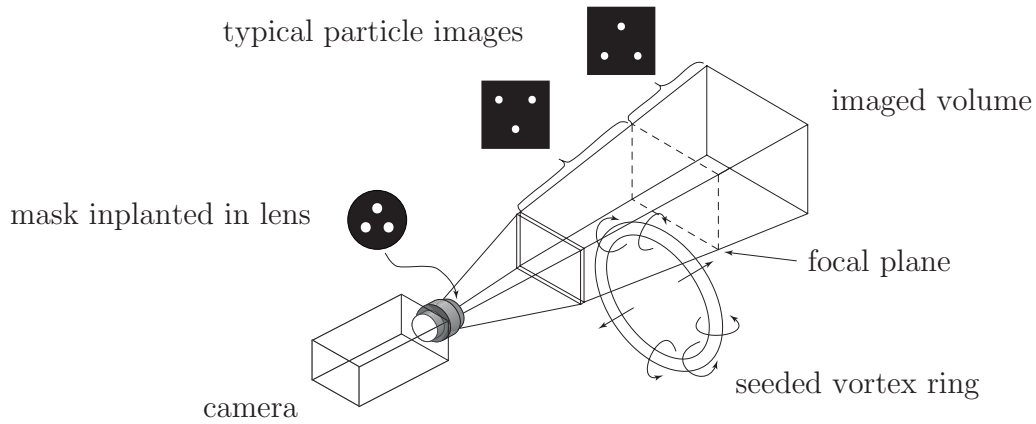


Figure 22: Single camera setup for imaging a seeded vortex ring according to Willert and Gharib (1992).

the flow domain. With the three-dimensional flow volume of the V3V-system the flow features of the complex-structured vortex ring could be captured at once and allow the analysis of particular flow structures in time. In the time-resolved volumetric measurements of Wolf et al. (2009) the laminar separation bubble at an airfoil is examined. In this study vortical structures are identified with the help of the λ_2 criterion (Jeong and Hussain, 1995). It is verified, that these structures have a regular "chessboard"-like order and correspond to a regular distribution of sinks and sources. Another study concerning the V3V technique is presented by Amatya et al. (2009). Related to fluid-structure interactions this study carried out measurements of the volumetric velocity fields behind a mechanical heart valve and upstream and downstream of a transparent deformable heart valve. Pulsed jets moving through the leaflets are identified using an ensemble-averaging as a post processing step to enhance the spatial resolution of the volumetric flow field.

Finally, some remarks about the measurement of structural displacements should be added. Single point laser triangulation is a standard method for distance measurements in science and industry since several decades (Clarke et al., 1991; Dorsch et al., 1994). The principle is based on the known geometric dependencies of the transmitting (laser) and the receiving part (CCD line/array) of the sensor (a more detailed description is found in Section 4.4.). The laser triangulation technique is different from other distance measuring principles such as laser phase-shifting or laser interferometry regarding the high data rate, the small measurement range and the higher accuracy as summarized in Amann et al. (2001) and Berkovic and Shafir (2012). With the ongoing research on temporally-resolved large CCD arrays in connection with in-time data processing the single point triangulation is further developed to multiple-point triangulation sensors. Beside the wide-spread application in industry this laser line triangulation (LLT) method is also applied in scientific research to deliver structural position information along a projected laser line. For example, Klimanov (2009) measures the surface of a rotating turbine blades with the LLT technique and uses their high spatial and temporal resolution for this dynamic application. Furthermore, Özcan (2011) utilizes the LLT method for determining the seam profile of narrow weldings and in Bouffard et al. (2013) it is used for detecting the effect of particle cohesion for the fluid dynamics in a spheronizer.

1.3. Objectives of the present work

This thesis describes and analyzes several newly developed self-exciting multi-DOF FSI test cases based on experimental and numerical methods. These test cases are developed in reference to previous studies and are modified in geometry, material properties and working conditions. The coupled flow and structure responses of the different test cases investigated are chosen with respect to the predictability of corresponding numerical simulations, the requirements of well-defined and controllable boundary conditions, the reproducibility of the results and the feasibility of precise fluid and structure measurements. With the provision of an extensive experimental data base, reliable measurement data for the validation of FSI methods are available to fill the gap of information as explained in the literature review (Section 1.2). A further investigation of the FSI coupling mechanisms analyzes the different geometrical and structural dependencies on the FSI phenomenon. Based on corresponding numerical simulations of each test case their predictability is examined and comparisons between the measurements and calculations are performed. In summary, the defined objectives of this work are focusing on the following issues:

- Development of two- and three-dimensional test cases applying appropriate simple geometries, reliable inflow conditions and commonly used materials.
- Generation of (quasi-) periodic FSI benchmark cases with (quasi-) two- and three-dimensional deformation behavior in the turbulent flow regime.
- Determination of the material properties based on suitable structural tests with a similar deformation behavior as observed in the FSI test cases.
- Set-up of adequate measurement techniques to investigate the fluid flow and the structural motions in detail for the FSI and the structural test cases.
- Development of an evaluation method to identify the mean characteristics of the FSI phenomenon at certain representative conditions.
- Analysis of dominant physical effects leading to the FSI phenomenon.
- Comparison of the different test cases to identify major FSI dependencies (e.g. material properties or inflow velocity).
- Provision and documentation of the experimental data.
- Modeling and computation of complementary FSI predictions with minor computational effort.
- Comparison between the experimental and numerical results.

The first test cases (denoted as FSI-PfS-1*x*) are developed with reference to the numerical benchmark of Turek and Hron (2006) and adapt the geometry and working conditions of the applied water channel of Gomes and Lienhart (2006, 2010, 2013). Different elastic materials are tested under several working conditions in the turbulent regime to analyze the response of the

structures with moderate deformations. Here, the focus is on quasi-two-dimensional and periodic structural deformations. The second benchmark called FSI-PfS-2 x is more closely related to the test cases of Gomes and Lienhart (2006, 2010, 2013). Based on this configuration, larger deflections and higher swiveling modes but again two-dimensional deflections are achieved. The further evolution of these nominally two-dimensional test cases are a three-dimensional geometry (cone) and the resulting three-dimensional structural deformations presented as FSI-PfS-3 x . Finally with FSI-PfS-4 x a more application-related test case scenario is developed.

The investigations presented in this thesis are partially published in reviewed journals or conference proceedings². Coupled two-dimensional flow and structure measurements of the benchmarks FSI-PfS-1 a and 1 b are reported in Breuer and Kalmbach (2011). Further contributions related to FSI-PfS-1 a with extensive comparisons to numerical predictions are presented in De Nayer et al. (2012, 2014). The detailed study of the test case FSI-PfS-2 a with coupled two- and three-dimensional flow and structural measurements is published in Kalmbach and Breuer (2012, 2013b). Furthermore, first comparisons to numerical predictions on FSI-PfS-2 a are presented in Kalmbach and Breuer (2013a). Finally, the first investigations on the three-dimensional test case FSI-PfS-3 a are described in Kalmbach et al. (2013).

1.4. *Outline*

The thesis is organized as follows: At first the governing equations of fluid and structure dynamics and the mechanisms of fluid-structure interactions are presented. The measuring techniques applied for fluid and structure investigations and the experimental setup used is shown in Section 4. The basics of computational fluid dynamics (CFD) and computational structure dynamics (CSD) and the coupling method of both solvers are presented in Section 5. Section 6 describes the investigated test cases with respect to the geometry, structure properties and flow conditions. The application of the measurement techniques to the previously defined FSI benchmarks, the evaluation of measurement errors, the flow conditions and the principle of the generation of phase-resolved data are presented in Section 7. Several preliminary studies concerning the flow and structure parameters are carried out in Section 8. Section 9 explains in detail the fluid and structure meshes used and the boundary conditions applied for the numerical predictions. Both, experimental and numerical results will be described, analyzed, discussed and compared in Section 10. Finally, the conclusions of this thesis and a short outlook to further investigations are given in Section 11.

²Only full-paper contributions are mentioned.

2. Fundamentals of structure and fluid dynamics

Fluid-structure interaction phenomena depend on the physics of the flow field and the structural movement and/or deformation. Both domains are parts of the continuum mechanics and are mathematically describable. The governing equations of the structure and the fluid mechanics, the applied approach of turbulence modeling and the fundamentals of the FSI kinematics are presented in this section.

2.1. Governing equations of structure dynamics

To understand the physical behavior of complex structural movements or deformations, the structure is divided into small control elements. Depending on this spatial discretization and the corresponding temporal discretization different scales of physical effects are describable. To explain the fundamentals of macroscopic structure dynamics a small finite element (FE) in its respective physical space is chosen. On this representative element the resulting physical changes due to its inner and external loads are considered in the following paragraphs in reference to the theoretical considerations of Oertel and Ruck (2012) and Parisch (2012).

2.1.1. Kinematics

According to an external or an inner load the stress tensor $\boldsymbol{\sigma}$ which consists of the normal stresses (in the direction of the unit normal vector \mathbf{n}) and the shear stresses (perpendicular to the unit normal vector \mathbf{n}) act on the area $d\mathbf{A} = dy \cdot dz$ (Fig. 23) at one side of the structure element.

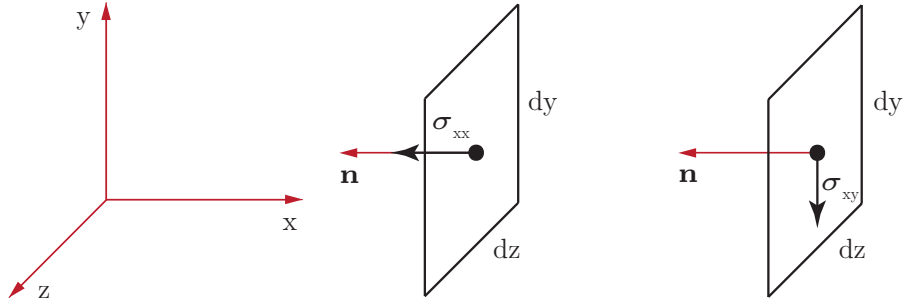


Figure 23: Normal and shear stresses.

The forces on the plane $dA_x = dy \cdot dz$ are given by $df_{xx} = \sigma_{xx} \cdot dy \cdot dz$ and $df_{xy} = \sigma_{xy} \cdot dy \cdot dz$. As illustrated in Fig. 24, on the entire control volume $dV = dx \cdot dy \cdot dz$ the three normal stresses (σ_{11} , σ_{22} , σ_{33}) and the six shear stresses (σ_{12} , σ_{13} , σ_{21} , σ_{23} , σ_{31} , σ_{32}) are acting and provoke the deformation of the volume. The CAUCHY stress tensor $\boldsymbol{\sigma}$ is symmetric with $\sigma_{12} = \sigma_{21}$, $\sigma_{13} = \sigma_{31}$ and $\sigma_{23} = \sigma_{32}$ and is written as follows:

$$\boldsymbol{\sigma} = \begin{pmatrix} \sigma_{11} & \sigma_{12} & \sigma_{13} \\ \sigma_{21} & \sigma_{22} & \sigma_{23} \\ \sigma_{31} & \sigma_{32} & \sigma_{33} \end{pmatrix} = \begin{pmatrix} \sigma_{xx} & \sigma_{xy} & \sigma_{xz} \\ \sigma_{yx} & \sigma_{yy} & \sigma_{yz} \\ \sigma_{zx} & \sigma_{zy} & \sigma_{zz} \end{pmatrix} \quad (1)$$

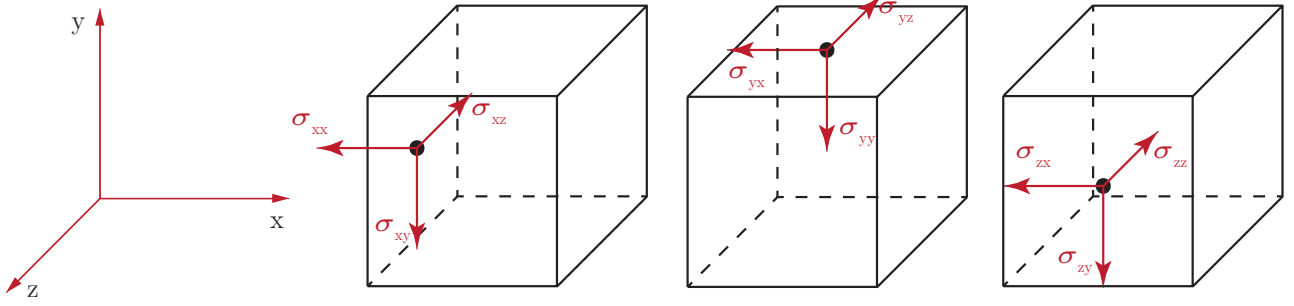


Figure 24: Stress tensor.

Fluid-structure interactions cause the deformation of a structure due to the induced forces by the flow. The deformation vector $\mathbf{d} = \mathbf{x} - \mathbf{X}$ describes a limited elastic structural response as illustrated in Fig. 25.

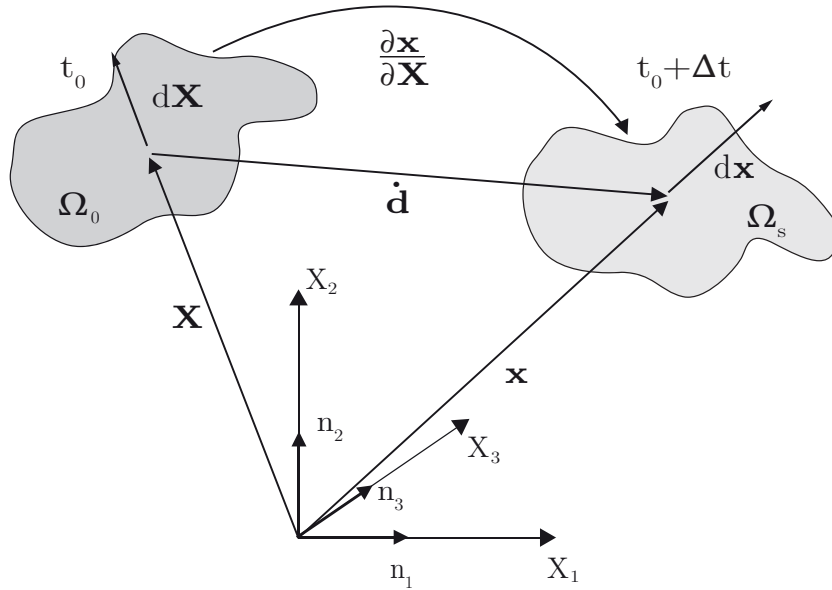


Figure 25: Reference configuration Ω_0 of the initial deformation state ($d\mathbf{X}$) and the deformed state Ω_s ($d\mathbf{x}$) (according to Parisch (2012)).

Here, the initial state Ω_0 of the undeformed structure is marked by the elemental material vector \mathbf{X} at t_0 . The deformed state Ω_s ($t_0 + \Delta t$) is described by the spatial vector \mathbf{x} . Both states are related to each other by the deformation gradient tensor \mathbf{F} which describes the change of \mathbf{X} from the initial configuration to the deformed configuration \mathbf{x} of the element as follows:

$$\mathbf{F} = \frac{\partial \mathbf{x}}{\partial \mathbf{X}}. \quad (2)$$

The motion of the element is divided into rigid-body translations and rotations and strains. The rigid-body motions result in a global change of the position but induces no additional stresses into the system. Therefore, these motions should not be considered in the following stress-strain relation. The material deformation gradient \mathbf{F} is not invariant to the mentioned rigid-body motion and therefore not an appropriate quantity for the description of the strain in a material law. Instead, the square of the differential line element $d\mathbf{X}$ in the undeformed

configuration and $d\mathbf{x}$ in the deformed configuration is employed:

$$(d\mathbf{X})^2 = d\mathbf{X} \cdot d\mathbf{X} \quad \text{and} \quad (d\mathbf{x})^2 = d\mathbf{x} \cdot d\mathbf{x}. \quad (3)$$

Eq. (2) substituted in Eq. (3):

$$(d\mathbf{x})^2 = (\mathbf{F} d\mathbf{X}) \cdot (\mathbf{F} d\mathbf{X}). \quad (4)$$

The difference between the squares of $(d\mathbf{x})^2$ and $(d\mathbf{X})^2$ leads to an appropriate strain quantity:

$$(d\mathbf{x})^2 - (d\mathbf{X})^2 = (\mathbf{F} d\mathbf{X}) \cdot (\mathbf{F} d\mathbf{X}) - d\mathbf{X} \cdot d\mathbf{X} = (\mathbf{F} (\mathbf{F} - \mathbf{I})) \cdot d\mathbf{X} \cdot d\mathbf{X} = 2\mathbf{E} \cdot d\mathbf{X} \cdot d\mathbf{X}. \quad (5)$$

Here, \mathbf{E} is denoted as the GREEN-LAGRANGIAN strain tensor, which is invariant towards rigid-body motions and valid for large, non-linear deformations. Transformed and related to the deformation vector \mathbf{d} it is expressed by:

$$\mathbf{E} = \frac{1}{2} (\mathbf{F}^T \mathbf{F} - \mathbf{I}) = \frac{1}{2} \cdot \left(\left(\frac{\partial \mathbf{x}}{\partial \mathbf{X}} \right)^T \frac{\partial \mathbf{x}}{\partial \mathbf{X}} - \mathbf{I} \right) = \frac{1}{2} \cdot \left(\frac{\partial \mathbf{d}}{\partial \mathbf{X}} + \left(\frac{\partial \mathbf{d}}{\partial \mathbf{X}} \right)^T + \left(\frac{\partial \mathbf{d}}{\partial \mathbf{X}} \right)^T \frac{\partial \mathbf{d}}{\partial \mathbf{X}} \right). \quad (6)$$

In case of small deformations ($\mathbf{x} \approx \mathbf{X}$) the non-linear terms are negligible and the GREEN-LAGRANGIAN strain tensor \mathbf{E} can be re-written as:

$$\mathbf{E} = \frac{1}{2} \left(\frac{\partial \mathbf{d}}{\partial \mathbf{X}} + \left(\frac{\partial \mathbf{d}}{\partial \mathbf{X}} \right)^T + \left(\frac{\partial \mathbf{d}}{\partial \mathbf{X}} \right)^T \frac{\partial \mathbf{d}}{\partial \mathbf{X}} \right) \approx \frac{1}{2} \left(\frac{\partial \mathbf{d}}{\partial \mathbf{X}} + \left(\frac{\partial \mathbf{d}}{\partial \mathbf{X}} \right)^T \right) \quad (7)$$

2.1.2. Dynamics

The local momentum conservation equation guarantees the equilibrium of the inner, external and inertia forces of a moving system. It is derived from the global momentum equation according to NEWTON's second law. It expresses that the total variation of the momentum is equal to the sum of all forces on the structure and its surface:

$$\frac{D}{Dt} \int_{\Omega_s} \rho_s \dot{\mathbf{d}} d\Omega_s = \int_{\Gamma_s} \mathbf{t} d\Gamma_s + \int_{\Omega_s} \rho_s \mathbf{f} d\Omega_s. \quad (8)$$

Here, Ω_s and $\Gamma_s = \partial\Omega_s$ describe the volume and the surface of the structure, ρ_s the density, \mathbf{t} expresses the stress vector on the element surface and \mathbf{f} the volume forces. Based on the theorem of CAUCHY $\mathbf{t} = \boldsymbol{\sigma} \cdot \mathbf{n}$ the stress vector \mathbf{t} can be divided into the stress components in normal direction (\mathbf{n}). The physical stress tensor in the deformed state is related to the second PIOLA-KIRCHHOFF stress tensor \mathbf{S} :

$$\mathbf{S} = \det(\mathbf{F}) \mathbf{F}^{-1} \boldsymbol{\sigma} (\mathbf{F}^T)^{-1}. \quad (9)$$

\mathbf{S} relates the forces and surfaces on the reference configuration and forms the conjugated stress quantity towards the GREEN-LAGRANGIAN strain tensor \mathbf{E} . The resulting force on the surface

of an element $d\mathbf{f} = \mathbf{t} d\Gamma_s$ is transformed into:

$$\mathbf{t} d\Gamma_s = \mathbf{F} \mathbf{S} \mathbf{n} d\Gamma_s. \quad (10)$$

By applying the GAUSS's theorem to Eq. (8), the surface integral is converted into a volume integral, which leads to:

$$\frac{D}{Dt} \int_{\Omega_s} \rho_s \dot{\mathbf{d}} d\Omega_s = \int_{\Omega_s} (\nabla \mathbf{F} \mathbf{S} + \rho_s \mathbf{f}) d\Omega_s. \quad (11)$$

Since Eq. (11) is valid for any $d\Omega_s$ it can be rewritten as the local momentum equation (first CAUCHY motion equation) which is used in the finite-element method:

$$\rho_s \ddot{\mathbf{d}} = \nabla(\mathbf{F} \mathbf{S}) + \rho_s \mathbf{f}. \quad (12)$$

2.1.3. Constitutive relations

To relate the geometrical descriptions of the element with its static or dynamic behavior, material models are formulated. In this thesis the deformation of thin elastic structures due to the surrounding flow is investigated. Therefore, the description of the stress-strain relation for isotropic structures and large elastic deformations is given by the ST.-VENANT-KIRCHHOFF material model with the coupling of the GREEN-LAGRANGIAN strain tensor \mathbf{E} and the second PIOLA-KIRCHHOFF stress tensor \mathbf{S} .

For the GREEN elasticity a specific inner strain or deformation work $W_{\text{int}}(\mathbf{E})$ is postulated. Related to the second PIOLA-KIRCHHOFF stress tensor \mathbf{S} this describes a potential function. In comparison to its time derivative

$$\dot{W}_{\text{int}} = \frac{\partial W_{\text{int}}}{\partial \mathbf{E}} : \dot{\mathbf{E}} \quad (13)$$

with the inner strain work $\dot{W}_{\text{int}} = \mathbf{S} : \dot{\mathbf{E}}$ the constitutive relation in its general form is derived:

$$\mathbf{S} = \frac{\partial W_{\text{int}}}{\partial \mathbf{E}}. \quad (14)$$

This stress-strain relation and the restriction to homogeneous, isotropic, elastic materials results in

$$\mathbf{S} = \mathbf{C} : \mathbf{E}. \quad (15)$$

In this general formulation of the HOOKE's law the fourth-order material elasticity tensor \mathbf{C} is depending on the properties of the material but not on the induced loads.

The characteristic properties of a material plays an important role for the interactions between fluid and solid domains. For example, a rubber material will respond with another deformation as steel under the same load induced by the flow. Material models are based on stress-strain curves to take the behavior of different materials under external loads into account.

In Fig. 26 the stress-strain curves for a metal and a rubber material are schematically shown illustrating the difference between a linear and non-linear material behavior up to their specific elastic deformation limit. Elastics are characterized by materials that return to its initial state

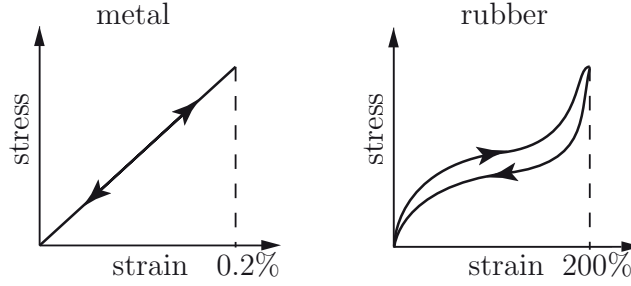


Figure 26: Comparison of stress-strain curves of metal and rubber material.

when removing the load without any irreversible deformations or stresses. As an example, metal has a linear-elastic behavior till the elastic proportional limit, where the non-linear region starts and plastic structure deformations appear. In contrast to metal, rubber provides a nearly non-linear pseudo-elastic stress-strain behavior and a far higher elastic proportional limit. Pseudo-elastic means that the structure passes different stress-strain curves during the load and the load removal. With this deformation behavior the rubber dissipates energy and possesses a stress-strain curve with a characteristic hysteresis. As already mentioned, materials are classified to be homogeneous/isotropic or inhomogeneous/anisotropic. Especially the microstructure of rubber materials is depending on the applied loads. For instances, large inner strains result in a more anisotropic material behavior and are more difficult to describe. As a consequence, in this thesis the elastics are assumed to be isotropic with the restrictions to small strains.

For isotropic materials there are only two independent elastic material constants left to describe the material properties. With the mentioned simplifications Eq. (15) is reduced to

$$\mathbf{S} = \lambda_s \operatorname{tr}(\mathbf{E}) \mathbf{I} + 2 \cdot \mu_s \cdot \mathbf{E} \quad (16)$$

where λ_s and μ_s (μ_s is also known as the shear modulus G) are denoted as the LAMÈ constants. The properties of an isotropic material are often described with the YOUNG'S modulus E and the POISSON'S ratio ν . Both material parameters can be expressed by the LAMÈ constants:

$$\lambda_s = \frac{\nu E}{(1 + \nu)(1 - 2\nu)} \quad \text{and} \quad \mu_s = \frac{E}{2(1 + \nu)}. \quad (17)$$

The YOUNG'S modulus E describes the stiffness of a material and plays an important role in the choice of a material with respect to its elasticity properties. Stress-strain measurements in the linear elastic material range allow the determination of the YOUNG'S modulus E . In addition, the POISSON'S ratio ν is also assignable. In detail, when a sample object is stretched (or compressed) the extension (or contraction) in the direction of the applied load corresponds to a contraction (or extension) in a direction perpendicular to the applied load. The ratio between these two quantities (negative ratio of relative contraction to relative extension) is defined as the POISSON'S ratio ν and represents the strain load capacity of a material. In contrast, the shear modulus G is a quantity for the deformation resistance of a material under shear loads.

2.1.4. Initial and boundary value problem of non-linear elastodynamics

Based on the previous considerations the following summary of the initial value and boundary value problem of the non-linear elastodynamics in its local or strong formulation is presented. This non-linear system of hyperbolic, partial differential equations consists of the dynamic momentum equation (Eq. (12)), the kinematic relation (Eq. (6)) and the material law (Eq. (16)) and are completed by the initial and boundary conditions of the structural domain:

dynamic equation - local momentum equation (first CAUCHY motion equation):

$$\rho_s \ddot{\mathbf{d}} = \nabla (\mathbf{F} \mathbf{S}) + \rho_s \mathbf{f}$$

kinematic equation - GREEN-LAGRANGIAN strain tensor \mathbf{E} :

$$\mathbf{E} = \frac{1}{2} (\mathbf{F}^T \mathbf{F} - \mathbf{I})$$

material law - ST.-VENANT-KIRCHHOFF material model:

$$\mathbf{S} = \mathbf{C} : \mathbf{E} = \lambda_s \text{tr}(\mathbf{E}) \mathbf{I} + 2 \cdot \mu_s \cdot \mathbf{E}. \quad (18)$$

initial conditions:

$$\mathbf{d} = \mathbf{d}_0 \quad \text{and} \quad \dot{\mathbf{d}} = \dot{\mathbf{d}}_0 \quad \text{in } \Omega_s \quad \text{at } t_0.$$

Dirichlet boundary conditions:

$$\hat{\mathbf{d}} = \hat{\mathbf{d}} \quad \text{on } \Gamma_s$$

Neumann boundary conditions:

$$\hat{\mathbf{t}} = \hat{\mathbf{t}} \quad \text{on } \Gamma_s$$

Here, the initial conditions are the displacements \mathbf{d}_0 and the deformation velocities $\dot{\mathbf{d}}_0$ in the entire structural domain Ω_s at the initial time t_0 . The boundary conditions of the structure $\Gamma_s = \partial\Omega_s$ are either defined by the Dirichlet conditions Γ_s with prescribed displacements $\hat{\mathbf{d}}$ or the Neumann conditions Γ_s with prescribed stresses $\hat{\mathbf{t}}$.

2.1.5. Weak formulation

For the solution of this system, its weak formulation is necessary. Therefore, the equations are transformed from the local differential to the integral weak form. Its derivation employs the principle of virtual work which is based on the assumption that the sum of the external and internal work disappears for a small virtual displacement of the structure. These virtual displacements employ the variation of the deformation vector $\delta\mathbf{d}$ and are infinitesimal small, kinematically valid but otherwise arbitrary. Similarly, the variation of the GREEN-LAGRANGIAN strain tensor $\delta\mathbf{E}$ is derived. Based on these test functions the weak formulation of the initial and boundary value problem of the geometrically non-linear motion equation (8) is given by:

$$\int_{\Omega_s} \rho_s \ddot{\mathbf{d}} \cdot \delta\mathbf{d} \, d\Omega_s + \int_{\Omega_s} \delta\mathbf{E} : \mathbf{S} \, d\Omega_s = \int_{\Gamma_s} \hat{\mathbf{t}} \cdot \delta\mathbf{d} \, d\Gamma_s + \int_{\Omega_s} \rho_s \mathbf{f} \cdot \delta\mathbf{d} \, d\Omega_s \quad (19)$$

While in the strong formulation the equilibrium and the boundary conditions have to be locally valid, the weak form only needs to be integrally fulfilled. The other equations of the system as well as the initial and boundary conditions remain in their strong formulation.

With the principle of virtual work the terms in Eq. (19) correspond to the virtual work of the inertia forces δW_{dyn} , the inner work δW_{in} and the external work δW_{ext} on the structure:

$$\delta W = \delta W_{\text{dyn}} + \delta W_{\text{in}} + \delta W_{\text{ext}} = 0. \quad (20)$$

The single terms are given by Eq. (19):

$$\begin{aligned} -\delta W_{\text{dyn}} &= \int_{\Omega_s} \rho_s \ddot{\mathbf{d}} \cdot \delta \mathbf{d} \, d\Omega_s \\ -\delta W_{\text{in}} &= \int_{\Omega_s} \delta \mathbf{E} : \mathbf{S} \, d\Omega_s \\ \delta W_{\text{ext}} &= \int_{\Gamma_s} \hat{\mathbf{t}} \cdot \delta \mathbf{d} \, d\Gamma_s + \int_{\Omega_s} \rho_s \mathbf{f} \cdot \delta \mathbf{d} \, d\Omega_s \end{aligned} \quad (21)$$

This theoretical consideration is applied to predict structural motions and deformations. The implementation of the principle of virtual work in the numerical solution of the finite-element method (FEM) is described in Section 5.1.

2.2. Governing equations of fluid dynamics

In the following section the equations of the motion for a fluid volume element $dV = dx \cdot dy \cdot dz$ are presented. This motion is described with the fluid velocity vector \mathbf{u} consisting of the CARTESIAN flow velocity components $(u, v, w) = (u_1, u_2, u_3)$. Similar to the stress tensor \mathbf{S} (Eq. (1)) of the structure mechanics the STOKES hypothesis of the stress tensor $\boldsymbol{\sigma}$ for a NEWTONIAN fluid is applied to describe the shear stresses and normal stresses in a flow. The momentum conservation equations for an incompressible fluid read:

$$\rho_f \cdot \frac{d\mathbf{u}}{dt} = \rho_f \cdot \left(\frac{\partial \mathbf{u}}{\partial t} + \mathbf{u} \frac{\partial \mathbf{u}}{\partial \mathbf{x}} \right) = \frac{\partial \boldsymbol{\sigma}}{\partial \mathbf{x}} + \rho_f \mathbf{g} + \mathbf{f}. \quad (22)$$

Here, ρ_f marks the density of the fluid, \mathbf{g} the gravitational acceleration and \mathbf{f} describes the external forces acting on the volume element. To obtain the general momentum conservation equation of the NAVIER-STOKES equations the stress tensor $\boldsymbol{\sigma}$ is separated into the shear stresses $\boldsymbol{\tau}$ and the normal stresses (pressure p). The pressure is acting normal to the surfaces of the volume element dV and is given by the stress tensor components $\sigma_{11}, \sigma_{22}, \sigma_{33}$. Accordingly, the shear stresses are acting tangential to the surfaces of the volume element dV and are given by the stress tensor components $\sigma_{12}, \sigma_{13}, \sigma_{21}, \sigma_{23}, \sigma_{31}, \sigma_{32}$. The viscous term $\boldsymbol{\tau}$ determines the momentum exchange in relation to the gradients of the velocity vector \mathbf{u} . The general formulation of HOOKE's law (Eq. 15) in structural mechanics corresponds to the STOKES hypothesis for NEWTONIAN fluids in fluid mechanics:

$$\boldsymbol{\sigma} = -p \cdot \mathbf{I} - \frac{2}{3} \mu_f (\nabla \cdot \mathbf{u}) \mathbf{I} + \mu_f \cdot \left(\frac{\partial \mathbf{u}}{\partial \mathbf{x}} + \left(\frac{\partial \mathbf{u}}{\partial \mathbf{x}} \right)^T \right). \quad (23)$$

With the mass conservation equation of an incompressible fluid (Eq. (26)) the viscous term is simplified according to $\nabla \cdot \mathbf{u} = 0$ and results in:

$$\boldsymbol{\sigma} = -p \cdot \mathbf{I} + \mu_f \cdot \left(\frac{\partial \mathbf{u}}{\partial \mathbf{x}} + \left(\frac{\partial \mathbf{u}}{\partial \mathbf{x}} \right)^T \right). \quad (24)$$

Applied in Eq. (22) the momentum conservation equations are formed:

$$\rho_f \cdot \frac{d\mathbf{u}}{dt} = \rho_f \cdot \left(\frac{\partial \mathbf{u}}{\partial t} + \mathbf{u} \frac{\partial \mathbf{u}}{\partial \mathbf{x}} \right) = -\frac{\partial p}{\partial \mathbf{x}} + \mu_f \cdot \frac{\partial}{\partial \mathbf{x}} \left(\frac{\partial \mathbf{u}}{\partial \mathbf{x}} + \left(\frac{\partial \mathbf{u}}{\partial \mathbf{x}} \right)^T \right) + \rho_f \mathbf{g} + \mathbf{f}. \quad (25)$$

In general, viscous flows can be described by three velocity components $\mathbf{u} = (u, v, w)$ of the CARTESIAN coordinate system $\mathbf{x} = (x, y, z)$, the density of the medium ρ_f , the pressure p and the temperature T . All quantities are functions of time and space. Furthermore, the material properties are characterized by the viscosity (dynamic viscosity μ_f , kinematic viscosity $\nu_f = \mu_f/\rho_f$), the heat conductivity λ_f and the specific heat capacity $c_{p,f}$. With the fundamental conservation equations of mass, momentum and energy and the thermodynamic constitutive equations these variables are connected to each other. This system of governing equations are known as the NAVIER-STOKES equations. The investigations in this thesis are restricted to chemical non-reactive, isothermal, incompressible, NEWTONIAN fluids, which leads to the neglect of the energy equation in the general formulation of the NAVIER-STOKES equations (Breuer, 2002). With these simplifications and a fixed spatial coordinate system the NAVIER-STOKES equations are expressed by one mass conservation equation (Eq. (26)) and three momentum conservation equations (Eq. (27)):

$$\nabla \cdot \mathbf{u} = 0 \quad (26)$$

$$\underbrace{\rho_f \frac{\partial \mathbf{u}}{\partial t}}_{\text{local acceleration}} + \underbrace{\rho_f \mathbf{u} \frac{\partial \mathbf{u}}{\partial \mathbf{x}}}_{\text{convective acceleration}} = \underbrace{-\frac{\partial p}{\partial \mathbf{x}}}_{\text{pressure forces}} + \underbrace{\mu_f \cdot \frac{\partial}{\partial \mathbf{x}} \left(\frac{\partial \mathbf{u}}{\partial \mathbf{x}} + \left(\frac{\partial \mathbf{u}}{\partial \mathbf{x}} \right)^T \right)}_{\text{viscous forces}} + \underbrace{\rho_f \mathbf{g}}_{\text{mass forces}} + \underbrace{\mathbf{f}}_{\text{external forces}} \quad (27)$$

Flows are fully described by this set of equations (under the restriction due to the mentioned simplifications). Since the benchmark test cases presented in this thesis are focused on turbulent flows, some issues on the theory of turbulence are discussed in the following section.

2.3. Turbulent flows

Flows are classified into laminar, transitional and turbulent physical states. Laminar flows have a high degree of order, contain only molecular diffusion processes and absorb external disturbances. Above a certain level of external perturbations the flow changes into the turbulent flow regime (transition). In contrast to the laminar behavior turbulent flows are always unsteady and highly irregular. Turbulence contains three-dimensional vortical structures of different length scales and can be described by stochastic fluctuations of the flow variables which are superimposed on the average flow. In turbulent flows the viscous damping is not sufficient enough to lessen external disturbances. Contrarily, the disturbances are amplified and the flow

becomes even more chaotic under certain conditions. Figure 27 illustrates a velocity signal

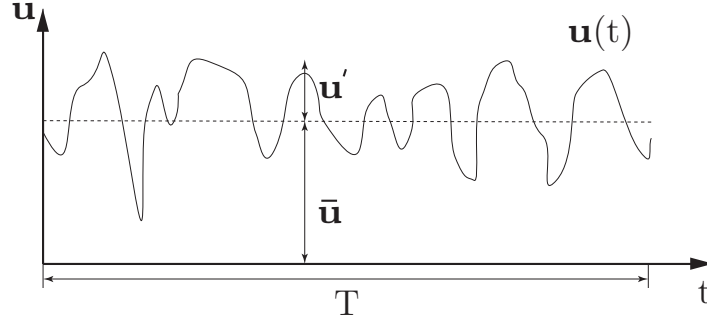


Figure 27: Velocity signal $\mathbf{u}(t)$ in a turbulent flow containing the global mean part $\bar{\mathbf{u}}$ and the random turbulence-related fluctuating part \mathbf{u}' .

$\mathbf{u}(t)$ at a fixed point \mathbf{x} in a turbulent flow. The history of the velocity profile \mathbf{u} consists of the global mean part $\bar{\mathbf{u}}$ and a random turbulence-related fluctuating part \mathbf{u}' (Reynolds and Hussain, 1972; Cantwell and Coles, 1983). This decomposition is called Reynolds approach and is described by:

$$\mathbf{u} = \bar{\mathbf{u}} + \mathbf{u}' \quad \text{and} \quad p = \bar{p} + p'. \quad (28)$$

The average velocity $\bar{\mathbf{u}}$ over the time interval T is given by:

$$\bar{\mathbf{u}}(\mathbf{x}) = \lim_{T \rightarrow \infty} \frac{1}{T} \int_0^T \mathbf{u}(\mathbf{x}, t) dt. \quad (29)$$

It is common to classify flows with the aid of dimensionless numbers. First, the Reynolds number describes the relation of inertia forces to viscous forces and depends on a characteristic velocity u , a characteristic length l and the kinematic viscosity ν_f of the fluid:

$$\text{Re} = \frac{u \cdot l}{\nu_f}. \quad (30)$$

As mentioned above viscous forces have the property to damp disturbances. Higher Reynolds numbers ($\text{Re}_{\text{turbulent}} \gg \text{Re}_{\text{laminar}}$) describe turbulent flows where the inertia prevails the viscous forces for several orders of magnitude. In every case the Reynolds number refers to the specific flow problem which is expressed by the characteristic length l and the characteristic velocity u . Therefore, a general critical Reynolds number is not available for the transition from a laminar to a turbulent flow.

Another characteristic number to classify flows is the turbulence level Tu :

$$\text{Tu} = \frac{1}{\bar{\mathbf{u}}} \cdot \sqrt{\frac{1}{3} \cdot (\overline{u'^2} + \overline{v'^2} + \overline{w'^2})}. \quad (31)$$

This number describes the fluctuation level within the flow and is formed with the mean flow velocity $\bar{\mathbf{u}}$ in the main flow direction and the averaged velocity fluctuations $\overline{\mathbf{u}'^2}$:

$$\overline{\mathbf{u}'^2} = \frac{1}{n} \cdot \sum_{j=1}^n (\bar{\mathbf{u}} - \mathbf{u}_j)^2. \quad (32)$$

Turbulence levels below 5% indicate mildly fluctuating flows. Levels of about 10% and higher are connected with highly turbulent flows.

The majority of technical flow applications are concerned with turbulent flows. Therefore, a detailed description of this physical flow state is necessary and is the object of many investigations in the last century. For the mathematical description of turbulence the considerations of Osborne Reynolds (Eq. (28)) are introduced into the NAVIER-STOKES equations (26) and (27) to obtain the governing equations of the average flow field of an incompressible, isothermal turbulent flow:

$$\nabla \cdot \mathbf{u} = 0 \quad (33)$$

$$\rho_f \frac{\partial (\bar{\mathbf{u}})}{\partial t} + \rho_f \frac{\partial (\bar{\mathbf{u}} \bar{\mathbf{u}})}{\partial \mathbf{x}} = -\frac{\partial \bar{p}}{\partial \mathbf{x}} + \mu_f \cdot \frac{\partial}{\partial \mathbf{x}} \left(\frac{\partial \bar{\mathbf{u}}}{\partial \mathbf{x}} + \left(\frac{\partial \bar{\mathbf{u}}}{\partial \mathbf{x}} \right)^T \right) + \rho_f \mathbf{g} + \mathbf{f}. \quad (34)$$

The decomposition of the non-linear term $\rho_f \bar{\mathbf{u}} \bar{\mathbf{u}}$ based on the approach of Reynolds (Eq. (28)) in a mean value and a fluctuating value results in the Reynolds stress tensor $\boldsymbol{\tau}^{RANS}$:

$$\rho_f \bar{\mathbf{u}} \bar{\mathbf{u}} = \rho_f \left(\overline{(\bar{\mathbf{u}} + \mathbf{u}') (\bar{\mathbf{u}} + \mathbf{u}')} \right) = \rho_f (\bar{\mathbf{u}} \bar{\mathbf{u}} + \overline{\mathbf{u}' \mathbf{u}'}) \quad (35)$$

$$\boldsymbol{\tau}^{RANS} = \rho_f \overline{\mathbf{u}' \mathbf{u}'}. \quad (36)$$

With the help of these relations and the averaged governing equations the Reynolds-averaged Navier-Stokes equations (RANS) are obtained:

$$\nabla \cdot \bar{\mathbf{u}} = 0 \quad (37)$$

$$\rho_f \frac{\partial (\bar{\mathbf{u}})}{\partial t} + \rho_f \frac{\partial (\bar{\mathbf{u}} \bar{\mathbf{u}})}{\partial \mathbf{x}} = -\frac{\partial \bar{p}}{\partial \mathbf{x}} + \mu_f \cdot \frac{\partial}{\partial \mathbf{x}} \left(\frac{\partial \bar{\mathbf{u}}}{\partial \mathbf{x}} + \left(\frac{\partial \bar{\mathbf{u}}}{\partial \mathbf{x}} \right)^T \right) - \frac{\partial}{\partial \mathbf{x}} (\rho_f \overline{\mathbf{u}' \mathbf{u}'}) + \rho_f \mathbf{g} + \mathbf{f}. \quad (38)$$

The set of equations contains the Reynolds stress tensor $\boldsymbol{\tau}^{RANS} = \rho_f \overline{\mathbf{u}' \mathbf{u}'}$ as an additional unknown. The term describes the influence of the turbulent fluctuations which have to be considered in the averaged Navier-Stokes equations. This issue is commonly known as "The Closure Problem" of turbulence. To solve this system of equations additional empirical relations or additional transport equations (turbulence models) are necessary. The most common kind of turbulence models is based on the principle of eddy viscosity. These models use the Boussinesq approximation, which handles the Reynolds stresses similar to the molecular viscous stresses τ^{mol} . The eddy viscosity μ_T is used as a proportionality factor in order to couple the Reynolds stresses to the gradients of the average flow velocities. Thereby, μ_T is not a material parameter. The eddy viscosity depends only on the flow characteristics (such as the

Reynolds number or other turbulence properties) and the average flow field. The Reynolds stress tensor $\boldsymbol{\tau}^{RANS}$ can now be expressed as follows:

$$\boldsymbol{\tau}^{RANS} = -\mu_T \left(\frac{\partial \bar{\mathbf{u}}}{\partial \mathbf{x}} + \left(\frac{\partial \bar{\mathbf{u}}}{\partial \mathbf{x}} \right)^T \right) + \frac{2}{3} \rho_f \mathbf{I} k \quad (39)$$

Here, k denotes the specific turbulent kinetic energy and μ_T describes the eddy viscosity. The identity matrix \mathbf{I} in Eq. (39) is equal to unity on the diagonal, otherwise zero. The term containing \mathbf{I} in Eq. (39) ensures that the sum of the normal stresses is consistent with twice the turbulent kinetic energy k . The eddy viscosity model allows to reduce the number of unknowns to one, i.e., the eddy viscosity requiring the assumption of isotropic turbulence.

In the last decades a lot of different approaches were developed to model turbulence leading to different resolution requirements and computational effort. One-equation models solve the transport equation of a single quantity such as the turbulent kinetic energy k or the eddy viscosity μ_T to model turbulence. Frequently used are so-called two-equation turbulence models which solve two additional partial differential equations, one for a characteristic velocity and one for a characteristic length scale. The more advanced Reynolds-stress models are also based on the approach of Reynolds, but solve six additional partial differential equations for each component of the Reynolds stress tensor and one partial differential equation for the characteristic length scale (Breuer, 2002). However, these Reynolds stress models are computationally more expensive than two-equation models. Eddy resolving approaches such as the large-eddy simulation (LES) or the direct numerical simulation (DNS) provide a detailed look into the irregular structures within a turbulent flow but are even more computationally expensive and require an increased effort in spatial and temporal discretization (Breuer, 2002).

In this thesis a two-equation turbulence model based on the RANS approach is used for the numerical predictions of the turbulent flow field. As already mentioned, turbulence models add further mathematical formulations to the RANS equations for the unknown Reynolds stresses based on the known flow quantities. The exact transport equations of the Reynolds stresses according to Breuer (2013) are given in index notation by:

$$\begin{aligned} \frac{\partial \tau_{ij}^{RANS}}{\partial t} + \bar{u}_k \frac{\tau_{ij}^{RANS}}{\partial x_k} &= \underbrace{-\tau_{ik}^{RANS} \frac{\partial \bar{u}_j}{\partial x_k} + \tau_{jk}^{RANS} \frac{\partial \bar{u}_i}{\partial x_k}}_{P_{ij}} + \underbrace{p' \left(\frac{\partial u'_i}{\partial x_j} + \frac{\partial u'_j}{\partial x_i} \right)}_{\Pi_{ij}} - \underbrace{2 \mu_f \left(\frac{\partial u'_i}{\partial x_k} \frac{\partial u'_j}{\partial x_k} \right)}_{\epsilon_{ij}} + \\ &\underbrace{\mu_f \left(\frac{\partial^2 \overline{u'_i u'_j}}{\partial x_k \partial x_k} - \frac{\partial \overline{u'_i u'_j u'_k}}{\partial x_k} - \frac{\partial}{\partial x_k} (p' (\delta_{kj} u'_i + \delta_{ki} u'_j)) \right)}_{D_{ij}}. \end{aligned} \quad (40)$$

The sources of the Reynolds stresses consist of the production tensor P_{ij} , the pressure-shear correlation tensor Π_{ij} , the dissipation tensor ϵ_{ij} and the diffusion tensor D_{ij} . Only the production tensor is directly calculable based on the known flow quantities. All other terms include unknown correlations such as $\overline{p' u'_i}$ which need additional modeling assumptions for their approximation. The exact transport equation of the turbulent kinetic energy derived by

contracting Eq. (40) is again given in index notation by:

$$\frac{\partial k}{\partial t} + \bar{u}_k \frac{\partial k}{\partial x_k} = \underbrace{-\tau_{ik}^{RANS} \frac{\partial \bar{u}_i}{\partial x_k}}_{P_k} - \underbrace{\mu_f \left(\frac{\partial u'_i}{\partial x_k} \frac{\partial u'_i}{\partial x_k} \right)}_{\epsilon} + \underbrace{\mu_f \left(\frac{\partial^2 k}{\partial x_k \partial x_k} \right) - \frac{1}{2} \frac{\partial \overline{u'_i u'_j u'_k}}{\partial x_k} - \frac{\partial}{\partial x_k} (\overline{p' (\delta_{ki} u'_i)})}_{D_k}. \quad (41)$$

Again the source terms contain the production P_k , the dissipation ϵ and the diffusion D_k and again only the production is directly calculable. Both, Eq. (40) and Eq. (41), are used to develop turbulence models. In the eddy-viscosity approach the six unknown Reynolds stress components are now only dependent on the two unknowns, k and μ_T . For a two-equation model these unknowns are determined by the solution of the transport equation of the turbulent kinetic energy k and the transport equation of the dissipation rate ϵ or a comparable quantity. Then the eddy-viscosity μ_T can be approximated by the characteristic scales of the major turbulence elements U_T and L_T , which are expressed by k and ϵ .

In this thesis the two-equation shear stress transport (SST) turbulence model of Menter et al. (2003) is used. The SST model delivers improved results for the majority of turbulent flow applications by combining two existing turbulence models ($k-\epsilon$ and $k-\omega$ model). Experiences with the $k-\omega$ model (Wilcox, 1988) turned out to be substantially more accurate than the $k-\epsilon$ model (Jones and Launder, 1972) in the near-wall layers and has therefore been successful for flows with moderate adverse pressure gradients, but fails for flows with pressure-induced separation (Menter, 1993). In addition, the ω -equation shows a strong sensitivity to the values of ω in the freestream outside the boundary layer (Menter, 1992). The freestream sensitivity has largely prevented the ω -equation from replacing the ϵ -equation as the standard scale-equation in turbulence modeling, despite its superior performance in the near-wall region (Menter et al., 2003). Therefore, the both models are coupled by a wall-distance based blending function to use their individual advantages and lessen their handicaps. The main additional complexity in the model formulation compared to standard models lies in the necessity to compute the distance from the wall. This is achieved by the solution of a POISSON equation (Tucker et al., 2005) and is therefore compatible with modern CFD codes. Thus, the SST model (Menter et al., 2003) solves the transport equations of the kinetic turbulent energy k and the characteristic turbulent frequency ω or the dissipation rate ϵ depending on the wall distance. For this purpose the $k-\epsilon$ model is transformed into a ω -formulation by:

$$\epsilon = C_\mu k \omega \quad (42)$$

Accordingly, the transport equations of k and ω are given by:

$$\frac{\partial k}{\partial t} + u_i \frac{\partial k}{\partial x_i} = \tilde{P}_k - \beta^* k \omega + \frac{1}{\rho_f} \frac{\partial}{\partial x_i} \left[(\mu_f + \sigma_{k1} \mu_T) \frac{\partial k}{\partial x_i} \right]. \quad (43)$$

$$\frac{\partial \omega}{\partial t} + u_i \frac{\partial \omega}{\partial x_i} = \alpha_1 \tilde{P}_k \mu_T - \beta k \omega^2 + \frac{1}{\rho_f} \frac{\partial}{\partial x_i} \left[(\mu_f + \sigma_{\omega 1} \mu_T) \frac{\partial \omega}{\partial x_i} \right] + 2(1 - F_1) \sigma_{\omega 2} \frac{1}{\omega} \frac{\partial k}{\partial x_i} \frac{\partial \omega}{\partial x_i} \quad (44)$$

The blending function F_1 between the $k-\epsilon$ model and the $k-\omega$ model is given with:

$$F_1 = \tanh \left[\left[\min \left(\max \left(\frac{\sqrt{k}}{\beta^* \omega y}, \frac{500 \nu_f}{y^2 \omega} \right), \frac{4 \rho_f \sigma_{\omega 2} k}{CD_{k\omega} y^2} \right) \right]^4 \right]. \quad (45)$$

Here y is the distance to the nearest wall and $CD_{k\omega}$ is denoted as the ‘cross-diffusion term’:

$$CD_{k\omega} = \max \left(2 \rho_f \sigma_{\omega 2} \frac{1}{\omega} \frac{\partial k}{\partial x_i} \frac{\partial \omega}{\partial x_i}, 10^{-10} \right). \quad (46)$$

F_1 is equal to zero far away from the surface ($k - \epsilon$ model), and switches over to one inside the boundary layer ($k - \omega$ model). The turbulent eddy viscosity is defined as follows:

$$\mu_T = \frac{a_1 k}{\max(a_1 \omega, S F_2)}. \quad (47)$$

Here $S = \sqrt{2 S_{ij} S_{ij}}$ is the invariant measure of the strain rate and F_2 is a second blending function defined by:

$$F_2 = \tanh \left[\left[\max \left(\frac{2\sqrt{k}}{\beta^* \omega y}, \frac{500 \nu_f}{y^2 \omega} \right) \right]^2 \right]. \quad (48)$$

A production limiter is used in the SST model to prevent the build-up of turbulence in stagnation regions:

$$P_k = \mu_T \frac{\partial u_i}{\partial x_j} \left(\frac{\partial u_i}{\partial x_j} + \frac{\partial u_j}{\partial x_i} \right) \rightarrow \tilde{P}_k = \min(P_k, 10 \cdot \beta^* \rho_f k \omega) \quad (49)$$

All constants are derived by the blending from $\alpha = \alpha_1 F + \alpha_2 (1 - F)$ from the corresponding constants of the $k - \epsilon$ and the $k - \omega$ model. The included empirical model constants are set to $C_\mu = 0.09$, $\alpha_1 = 5/9$, $\alpha_2 = 0.44$, $a_1 = 0.31$, $\beta = 3/40$, $\beta^* = 0.09$, $\sigma_{k1} = 0.85$, $\sigma_{k2} = 1$, $\sigma_{\omega 1} = 0.50$ and $\sigma_{\omega 2} = 0.856$ according to Menter et al. (2003).

2.4. Turbulent flows near walls

In fluid dynamics flows are divided into bulk flows and wall-bounded flows near solid or flexible surfaces/bodies. In the near-wall region (denoted as boundary layer) the friction effects of the flow with the solid or flexible body has a significant influence on the whole flow. For instance, the alternating vortex shedding, responsible for the fluid-structure interaction phenomena studied in the present work, is partly a result of the complex physical effects near the walls of the front body. In the following paragraphs only a brief summary of this complex topic is given to describe the flow modeling of the applied fluid solver near the walls. A detailed description of the boundary layer theory including the simplification of the Navier-Stokes equations to the boundary layer equations are given in Schlichting and Gersten (2004).

For low Reynolds numbers the flow conditions in the boundary layer are described as laminar. In the common case of a flow over a flat plate, the flow in the boundary layer is almost aligned with the outer flow. On the surface of the plate the fluid velocity is zero and denoted no-slip condition ($\mathbf{u}(y = 0) = 0$). With increasing wall distance the flow velocity increases towards the outer free-stream velocity u_∞ . The distance of the interface between the boundary layer and

the bulk flow to the solid/flexible surface is called boundary layer thickness δ and is defined as the distance to the wall where the flow velocity in the boundary layer reaches 99% of the free-stream velocity u_∞ . Mathematically the velocity profile $u(y)$ from the wall ($y = 0$) up to the boundary layer thickness ($y = \delta$) can be approximated, e.g., by a quadratic function or the solution of Blasius (1908).

For higher Reynolds numbers the flow within the boundary layer becomes turbulent. Here, the flow is highly irregular and contains chaotic vortical structures of different sizes. Due to the increased fluctuations in the near-wall region the velocity profile in the boundary layer changes with respect to the laminar situation. Now, the velocity profile can be approximated by logarithmic functions to mention only one approximation method. Despite the high momentum exchange in the turbulent boundary layers a thin viscous sub-layer exists close to the surface. This thin layer occurs due to molecular motion in the proximity of the wall where the turbulent velocity fluctuations become almost zero.

The applied boundary layer modeling approach based on the logarithmic law of the wall will be given in Section 5.2.4.

2.5. Governing equations of fluid dynamics on moving grids

As explained in the previous sections fluid and structure motions are described by separate sets of equations. In the following section the definition of the physical interface conditions and the ARBITRARY LAGRANGIAN-EULERIAN (ALE) formulation of the conservation equations are presented.

The entire physical domain of a FSI phenomenon consists of the fluid domain $\Omega_f(t)$ and the structural domain $\Omega_s(t)$. Both regions are coupled at the interface $I(t)$ between the fluid and the structural domain as illustrated in Fig. 28. The boundaries are defined by $\Gamma_f(t)$ for the fluid domain and $\Gamma_s(t)$ for the solid domain.

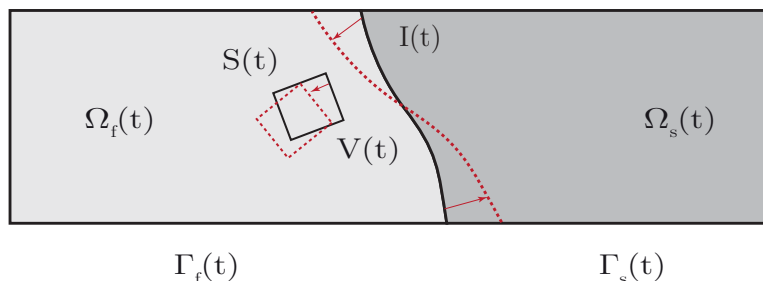


Figure 28: Definition of the geometry of surface-coupled FSI phenomena.

At the moving surface $I(t)$ of the structure the deformation velocity $\dot{\mathbf{d}}$ of the structure is equal to the flow velocity \mathbf{u} in the fluid domain (STOKES no-slip condition):

$$\dot{\mathbf{d}}|_I = \begin{pmatrix} \dot{d}_1 \\ \dot{d}_2 \\ \dot{d}_3 \end{pmatrix} \longleftrightarrow \mathbf{u}|_I = \begin{pmatrix} u \\ v \\ w \end{pmatrix}. \quad (50)$$

The mathematical description of the deformable structure is related to the LAGRANGIAN approach which is expressed for a moving reference system. It can also be described in a fluid

dynamic context as a fluid parcel following the fluid flow along its path line. In contrary, the EULERIAN approach describes the fluid variables in a fixed spatial reference system like a measuring probe which detects the fluid velocity at a fixed point as a function of the time. Both formulations are combined in the ARBITRARY LAGRANGIAN-EULERIAN (ALE) approach at the time-dependent interface between both domains. Furthermore, this approach is also applied to take the deformation of the computational grid of the fluid domain into account (illustrated in Fig. 28 on an arbitrarily chosen moving control volume $V(t)$ with the surface $S(t)$). The ALE formulation of the conservation equations (26) and (27) are introduced. First the mass conservation for incompressible flows (Eq. (26)) is now expressed by:

$$\frac{d}{dt} \int_{V(t)} \rho_f dV + \int_{S(t)} \rho_f (\mathbf{u} - \mathbf{u}|_S) dS = 0 \quad (51)$$

Here, $\mathbf{u}|_S$ refers to the velocity of the time-dependent surface $S(t)$ of the control volume. As a result of the moving faces of the CV there are additional mass fluxes. This additional mass flux is further illustrated by the example of a quiescent fluid with a moving CV within the fluid domain. Here, the motion of the control volume generates a mass flux over the boundary faces without any physical flow motion. To determine the unknown grid velocity $\mathbf{u}|_S$ while preserving the mass conservation, the space conservation law (SCL, Demirdžić and Perić (1988, 1990)) is applied:

$$\frac{d}{dt} \int_{V(t)} \rho_f dV + \int_{S(t)} \mathbf{u}|_S \mathbf{n} dS = 0 \quad (52)$$

These considerations are also applied to the conservation equation of the momentum:

$$\begin{aligned} \frac{d}{dt} \int_{V(t)} \rho_f \mathbf{u} dV + \int_{S(t)} \rho_f (\mathbf{u} - \mathbf{u}|_S) \mathbf{u} \mathbf{n} dS = & - \int_{S(t)} p \mathbf{n} dS + \int_{V(t)} \mu_f (\nabla \mathbf{u} + (\nabla \mathbf{u})^T) dV + \\ & \int_{V(t)} \rho_f \mathbf{g} dV + \int_{V(t)} \mathbf{f} dV \end{aligned} \quad (53)$$

The first term describes the local change of the momentum in the time-dependent control volume $V(t)$. Analog to the ALE formulation of the mass conservation equation, the additional momentum fluxes over the boundaries $S(t)$ are similar to the convective fluxes and are therefore summarized in the second term. The right side of the equation integrates all sources over the moving control volume $V(t)$. With these three equations (space, mass and momentum conservation), the ALE formulation allows the numerical solution of the NAVIER-STOKES equations on time-dependent (moving) computational grids and will be used for the numerical predictions in this thesis.

3. Fluid-structure interaction mechanisms

Fluid-structure interactions describe the dynamic bidirectional response of a flow with a deformable structure. The motions and/or deformations of the structure are induced by the surrounding flow. The instantaneous forces $\mathbf{f} = \bar{\mathbf{f}} + \mathbf{f}'$ acting on the incremental area dA of the structure are related to the instantaneous flow velocity $\mathbf{u} = \bar{\mathbf{u}}|_I + \mathbf{u}'|_I$ and their corresponding pressure $p = \bar{p} + p'$. The behavior of these flow quantities prescribe the excitation of the structure and thereby the entire characteristic of the FSI coupling. In the following paragraphs the excitation mechanisms of FSI phenomena are summarized.

The sources of the excitation characterized by Naudascher and Rockwell (1994) are presented in Fig. 29 by Gomes (2012). Here, the classification of FSI mechanisms into steady hydrodynamic loads, unsteady hydrodynamic loads as a result of the fluctuating flow (fluctuation-induced excitation (FIE)) and unsteady hydrodynamic loads as a result of the structural movement (movement-induced excitation (MIE)) is made.

The steady excitation case is rather simple compared to the transient FSI phenomena. This FSI system is described by a mean time-independent fluid load on the structure. Under the neglect of initial effects, the structural response can be assumed as static. The benchmark case "Flexible Plate" by Glück et al. (2001) is an example of this excitation state. Here, the flexible structure is exposed to a laminar almost steady flow. After a short unsteady initial phase both flow and structure reach a static equilibrium.

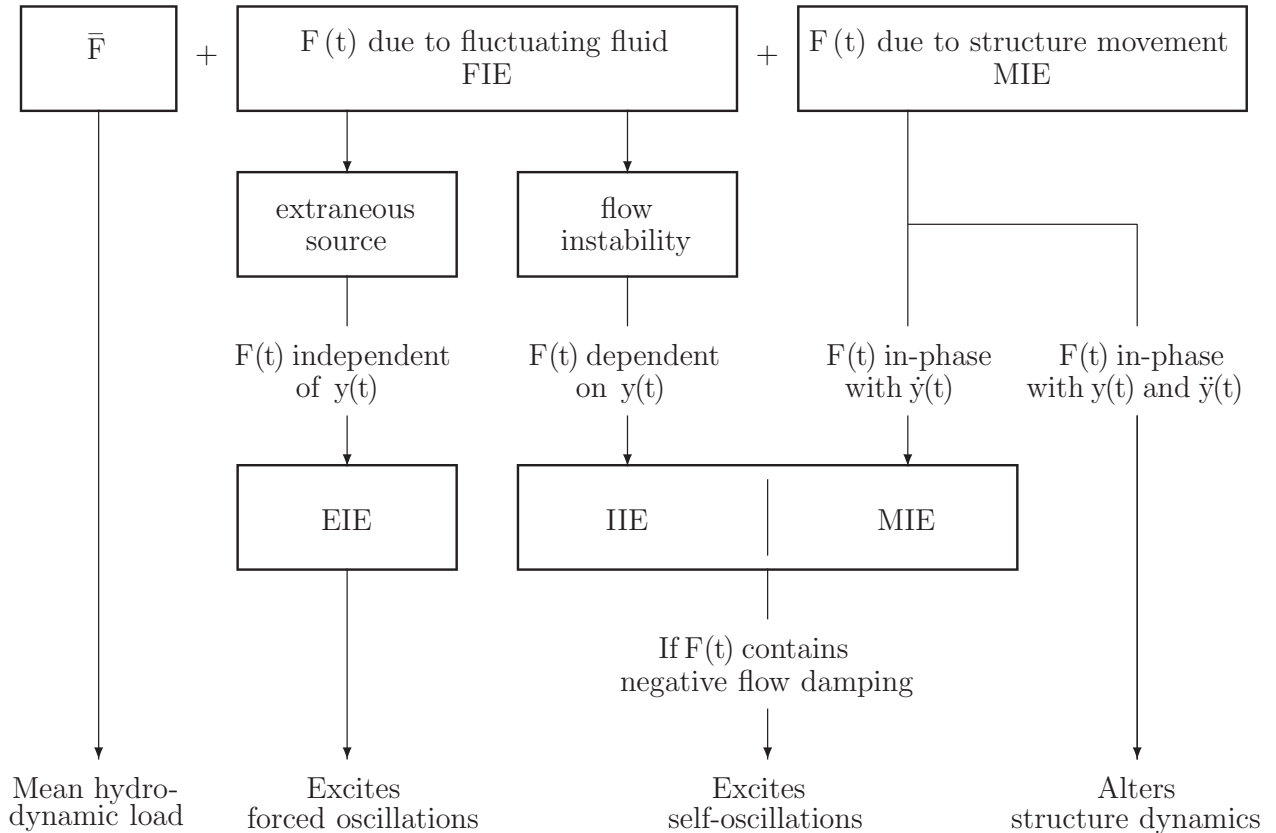


Figure 29: FSI mechanisms characterized by the excitation source (Gomes, 2012).

In the case of an unsteady flow the fluctuation-induced excitation mechanism (FIE) is introduced. Two distinctions are made according to the dependency of the flow on the structural motion. As a first case, the extraneously induced excitation (EIE) is not induced by potential instabilities related to the structure or its motion. EIE is the result of fluctuations in the field variables (velocity or pressure) itself. Reasons for EIE are, e.g., turbulence, cavitation or pulsating flows. The most typical reasons are turbulence effects produced by different types of free-shear flows such as wakes of other structures further upstream of the excited body, mixing layers, jets or boundary layers. In general, EIE is characterized by a structural displacement which is sustained by an extraneous energy source. This mostly results in a random excitation force on the surface of the structure in the case that the fluctuations are produced by turbulence (often in direction of the main flow direction). For instance, EIE is present at turbine runner vanes while passing the static guide vanes. Here, the flow is highly affected by the passage of the rotating vane along the static vane and induces a temporary load peak on both structures. Therefore, each passage a small structural response is noticed (Dhopade et al., 2010).

In contrast to EIE the instability-induced excitations (IIE) are caused by flow instabilities. Flow instabilities which may result in IIE are interface instabilities, impinging shear layers or vortex shedding. In the case of vortex shedding on a bluff body the structure induces the flow instability and the resulting forces yield the deflection of the structure. Due to amplification mechanisms (fluid-elastic and fluid-resonance effects) in flows the exciting forces on the structure get so intense, well correlated and concentrated close to a dominant frequency (e.g., the vortex shedding frequency f_s) that the forces can lead to larger structural deflections in comparison to EIE. Here, resonances between the dominant frequency f_s and the natural frequency of the structure f_N are possible and often result in even larger structural motions and deformations. In the fluid resonance case the flow and structure characteristics generate a quasi-periodic state, where the frequency of the flow instability and the structural response reach a similar level. This state called "lock-in" is highly influenced by the amplifications of the structural response (fluid-elastic response, fluid-resonance response) and the phase conditions ($F(t)$ to d , \dot{d} and \ddot{d}) between both domains. IIE is highly correlated with the excited vibrations and therefore clearly distinguished from the forced vibrations of the extraneously induced excitations (EIE) mentioned before.

In case of IIE the motion of the structure through the flowing medium alters the fluid loads by itself. Whenever, this alternation of the fluid forces results in a negative damping or in other words in an energy transfer from the flow to the structure the excitation is self-induced. In the case of EIE the excitation frequency is independent of the structure motion and indicates the frequency of the resulting structure oscillation. For IIE the elasticity of the structure modulates the oscillation frequency that alters the whole system response with respect to the specific structural eigenmodes and eigenfrequencies.

Closely connected to the IIE is the movement-induced excitation (MIE). Here the motion of the structure and the thereby occurring forces on their surface amplifies the structural response and thus are again self-induced. In contrast to IIE, MIE are inherently linked to the body movement and disappears if the structure comes to rest. MIE are characterized by large periodic structural motions and are highly affected by the surrounding flow. In the literature MIE

is sub-classified by the phase difference of the movement-induced excitation force $F(t)$ to the position d , the velocity \dot{d} and the acceleration \ddot{d} of the moving structure. If $F(t)$ is in-phase with \dot{d} minor resonances due to the induced motion are reported. In contrast, an in-phase of d and \ddot{d} with $F(t)$ amplifies the excitation once more and leads to a significant change in the system coupling and their dependent properties (i.e., oscillation frequency, swiveling mode, maximum and minimum deflections). An example of this alternation is the locked-in oscillation frequency of the structure with the vortex shedding frequency. Both frequencies are still equal but are altered (in contrast to IIE) due to the strong influence of the interaction of the coupled system. Another common example for MIE are flutter effects on airfoils. The flow around the structure creates IIE of the airfoil and these small motions amplify the excitation state (MIE) to larger displacements and altered deflection frequencies.

In general, all three types of flow-induced excitations (EIE, IIE, MIE) are often present simultaneously and affect each other to a more complex FSI phenomenon. As a consequence, the classification of a FSI phenomenon to a single excitation state is only feasible for simple geometries.

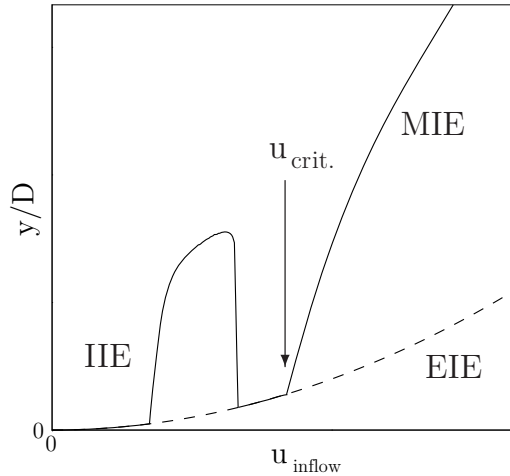


Figure 30: General character of the transverse FSI excitation of a cylinder in cross-flow (Gomes, 2012).

In Fig. 30 the general oscillation behavior y/D of an elastically supported rigid cylinder in cross-flow direction is illustrated as a function of the inflow velocity u_{inflow} . First, the EIE starts to excite the cylinder with small deflections. With increasing inflow velocities the excitation changes into the IIE mode. Here, much larger and periodic displacements are present increasing with the inflow velocity. At a certain critical inflow velocity the crossover to MIE is reached. This inflow velocity is related to the eigenfrequencies of the structure and the oscillation frequency of the present coupled system. The following strong increase of the deflection amplitudes with the inflow velocity is characteristic for MIE.

In the following paragraph the acting forces on this exemplary structure and their response to the main excitation sources are described based on the consideration of Naudascher and Rockwell (1994). As already mentioned, the interaction can lead to irregular (EIE) or (quasi-) periodic (IIE, MIE) structural deflections. In Fig. 31 the main excitation mechanisms for the already mentioned example of an elastically supported rigid cylinder in a flow are illustrated.

Since the EIE act especially in the main flow direction, the cylinder is restricted to motions in x -direction in this case. The turbulent flow acts on the surface of the rigid body and as a consequence the forces on the cylinder are also irregular and cause a corresponding non-periodic motion of the cylinder.

For the IIE and MIE mechanisms in Fig. 31 the cylinder is exemplarily allowed to move in cross-flow direction similar to Fig. 30. In the case of a laminar flow around the cylinder this configuration can result in a harmonic excitation force according to the lack of turbulent flow fluctuations and the shedding of vortices from the cylinder surface. This force can be described mathematically by a sinusoidal function, which also characterizes the behavior of a simple oscillator:

$$F(t) = F_0 \cos(\omega_s t) \quad \text{and} \quad \omega_s = 2\pi f_s. \quad (54)$$

An oscillator is defined as a solid or fluid mass which deflects out of its equilibrium state and oscillates due to an exciting force. Fluid oscillators are described as discrete (e.g., fluid oscillations due to an impinging shear layer) or distributed (e.g., fluid oscillations due to gravity waves). A solid oscillator consists of a rigid body that is elastically supported and can translate or rotate. Furthermore, elastic structures can also be oscillators due to flexible or torsional deformations.

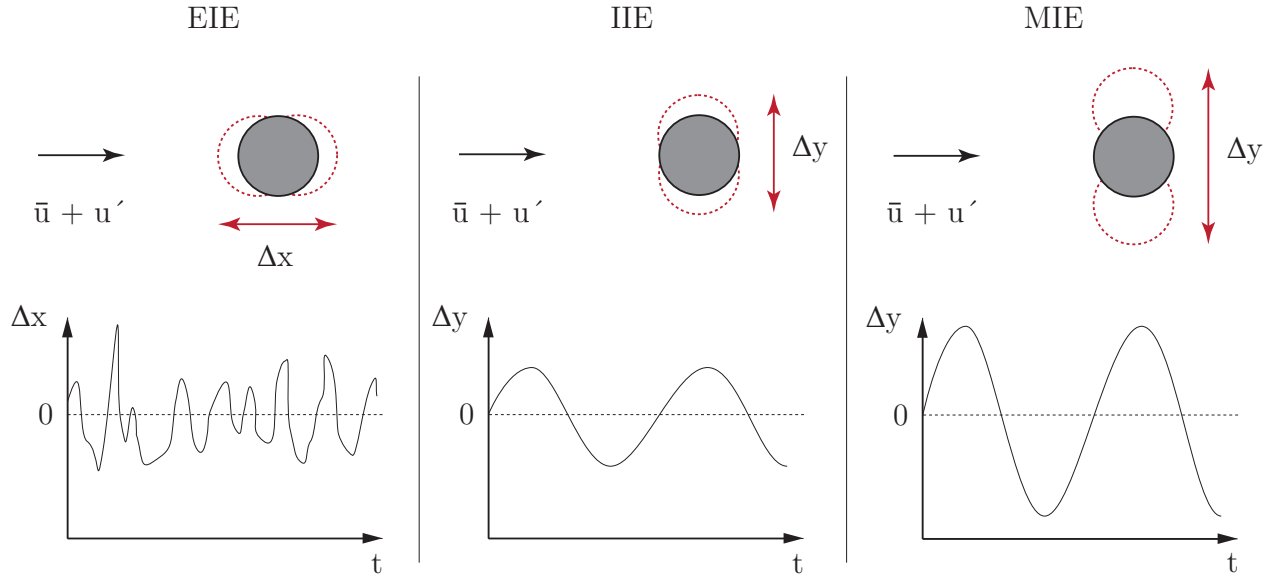


Figure 31: Examples of the different excitation mechanisms (EIE, IIE, MIE).

In Fig. 31 a common example of a simple solid oscillator in terms of fluid-structure interactions is presented. Due to the alternating shedding of vortices from the surface of the cylinder the oscillations in the lift force F_l occur at the vortex shedding frequency f_s and the oscillations in the drag force F_d appear with twice the vortex shedding frequency.

$$\begin{aligned} F_l(t) &= F_{l,0} \cos(\omega_s t + \Phi_l) \\ F_d(t) &= F_{d,0} \cos(2 \omega_s t + \Phi_d) \end{aligned} \quad (55)$$

Here, the angular frequency ω is expressed by $\omega = 2 \pi f_s$ and Φ_l and Φ_d represent the initial phase shift of the oscillations of the lift and the drag and are set to zero in the following

considerations. Due to the respective forces acting on the structure the self-induced excitation leads to (quasi-) periodic oscillations of the cylinder in cross-flow direction. For the IIE and MIE mechanisms the harmonic structural motion, e.g., the displacement, velocity and acceleration of the cylinder can be described by:

$$\begin{aligned} y(t) &= y_0 \cos(\omega_s t) \\ \dot{y}(t) &= -y_0 \omega_s \sin(\omega_s t) \\ \ddot{y}(t) &= -y_0 \omega_s^2 \cos(\omega_s t). \end{aligned} \quad (56)$$

The equation of motion for the cylinder is given relying on the mass m , the damping coefficient d and the stiffness c (referring to the structure alone):

$$m \ddot{y}(t) + d \dot{y}(t) + c y(t) = F_y(t) \quad (57)$$

The fluid force $F_y(t)$ acting on the projected surface (length \cdot diameter) of the cylinder $L \cdot D$ is related to the unsteady force coefficient $c_y(t)$ and is expressed by:

$$F_y(t) = \cdot c_y(t) \cdot \frac{\rho_f}{2} \cdot \bar{u}_x^2 \cdot L \cdot D. \quad (58)$$

Furthermore, this force can be split into three components, which are in-phase with the body acceleration \ddot{y} , the body velocity \dot{y} and the body displacement y , respectively:

$$F_y(t) = -A' \ddot{y}(t) - B' \dot{y}(t) - C' y(t). \quad (59)$$

This equation indicates that the system behaves like a solid oscillator with an added mass A' , an added damping B' and an added stiffness C' . The added mass effect describes the inertia added to the system by an accelerating or decelerating fluid mass. The structure suppresses (or deflects) some volume of the surrounding fluid as it moves through it and transfers energy into the fluid. The opposite effect appears by the added damping and the added stiffness. Here, the added or fluid damping can become negative because of the vibration of the structure. This effect occurs due to energy which is transferred from the flow into the structure. Basically, this is the reason for self-excited fluid-structure interactions. All three effects rely on the geometry (here the diameter D), the fluid properties (especially the density ρ_f), the interaction of both domains (y_0, f) and the flow conditions ($u_{\text{inflow}}, \text{Re}, \text{Tu}$). Equation (59) substituted in Eq. (57) results in:

$$m \ddot{y}(t) + d \dot{y}(t) + c y(t) = -A' \ddot{y}(t) - B' \dot{y}(t) - C' y(t) \quad (60)$$

and leads to:

$$(m + A') \ddot{y}(t) + (d + B') \dot{y}(t) + (c + C') y(t) = 0. \quad (61)$$

Due to the absence of a closed theoretical model for FSI couplings, the added stiffness cannot be distinguished from the added mass as the structure acceleration is in-phase with the displacements. Therefore, the added stiffness is included in a modified added mass term A'' :

$$F_y(t) = -A'' \ddot{y}(t) - B' \dot{y}(t) \quad (62)$$

$$(m + A'') \ddot{y}(t) + (b + B') \dot{y}(t) + c y(t) = 0. \quad (63)$$

As a consequence of these added quantities the structures dynamics is changed. This includes for instance the modification of the natural frequency of a structure surrounded by a vacuum $f_{n,\text{vacuum}}$ or by a fluid $f_{n,\text{fluid}}$:

$$f_{n,\text{vacuum}} = \frac{1}{2 \pi} \sqrt{\frac{c}{m}} \quad (64)$$

$$f_{n,\text{fluid}} = \frac{1}{2 \pi} \sqrt{\frac{c}{m + A''}} \quad (65)$$

These considerations should give a short impression how strong the different dependencies influence each other in terms of this theoretical model. At this time, only the numerical solution of complex FSI problems based on monolithic or partitioned approaches is feasible. The numerical FSI coupling method applied in this thesis is described in Section 5.3.

4. Experimental measuring techniques and test facility

Experimental FSI investigations contain fluid and structure measurements for a full description of the physical process. For both physical domains the same requirements on the measurement techniques are relevant. Important are a sufficient spatial and temporal resolution and an adequate post-processing approach to obtain all important physical information of the measured object. In general, all measurement techniques are restricted to ascertainable quantities. In fluid mechanics velocities, pressures, temperatures and fluid densities/concentrations within a flow are detectable with mostly indirect methods. Equivalent quantities are also measurable in structure mechanics with the advantage of direct measurement methods especially for position-based quantities like the velocity or the acceleration.

Ideally, the same measurement technique for both physical domains are employed for the investigations of a FSI phenomenon. The reference for the present thesis are the benchmark measurements performed by Gomes and Lienhart (2013). They applied the same optical measurement system for the simultaneous acquisition of the velocity fields and the structural deflections. This is applicable if the structural deflections are supposed to be two-dimensional and the optical axis of the measurement system coincides with the deflection plane. To allow the measurement of general three-dimensional deformations of structures, other solutions are necessary. Reasons for the limitations of image-based in-line techniques are the optical blockage of structural parts through three-dimensional deformations. Despite the different techniques applied, the measured quantities used in the present work remain the same as in Gomes and Lienhart (2010, 2013).

The fluid velocity fields are captured by a two-dimensional particle-image velocimetry (PIV) set-up and the structural deflections are measured by a separate laser line triangulation (LLT) technique. In addition to the two-dimensional flow measurements, three-dimensional flow measurements with a volumetric particle tracking system (V3V) are performed to investigate the behavior of the flow in spanwise direction. The separation of the structural measurements into a stand-alone system is also necessary due to the reduced measurement volume of the V3V system, which does not include the structure within the recorded images and the three-dimensional structure deformations observed in the test cases FSI-PfS-3x and 4x. In the following section the applied test facility and the employed measurement techniques are presented in detail. The specific experimental set-up, including the alignment of the measurement devices, specific test conditions etc. are explained in Section 7.

4.1. Description of the test facility

As already mentioned in Section 1.2, the DFG Research Unit 493 "Fluid-Structure Interaction: Modeling, Simulation, Optimization" was founded to investigate FSI effects under the usage of numerical and experimental methods (Bungartz and Schäfer, 2006; Bungartz et al., 2010). The primary objective was the systematic and coordinated development of numerical methods for the robust and efficient simulation of fluid-structure interactions. Moreover, the development of an experimental reference FSI benchmark aimed at the validation and evaluation of newly developed and already existing calculation methods. According to experimental as well as numerical requirements a water channel for the study of FSI effects was designed and constructed at LSTM Erlangen by Gomes and Lienhart (2006). With this Göttingen-type tunnel depicted

in Fig. 32 it is possible to generate laminar and turbulent flows ($5 \cdot 10^1 < Re < 10^5$). The studies in the laminar regime of Gomes and Lienhart (2010) were performed with polyethylene glycol (PEG) as working fluid. Similar to the turbulent studies of Gomes and Lienhart (2013), the present study uses water as the working fluid. The construction of the flow channel allows the implementation of small structure models in the test section. Due to different types of bearings applied on the backplate and the transparent front glass of the test section the rotational degree of freedom in spanwise direction of the structure model can be released or disabled. The test section has a length of $L = 0.338$ m, a height of $H = 0.240$ m and a width of $W = 0.180$ m. The blocking ratio of the channel for the structure models defined in Section 6 ranges from 3.2% to 11.3%. In the test section inlet velocities up to 6 m/s can be provided by a 24 kW axial pump. In Fig. 33 the linear performance curve of the axial pump and the resulting turbulence level Tu within the channel are shown. Further information on the properties of the channel are given in Section 7.3.

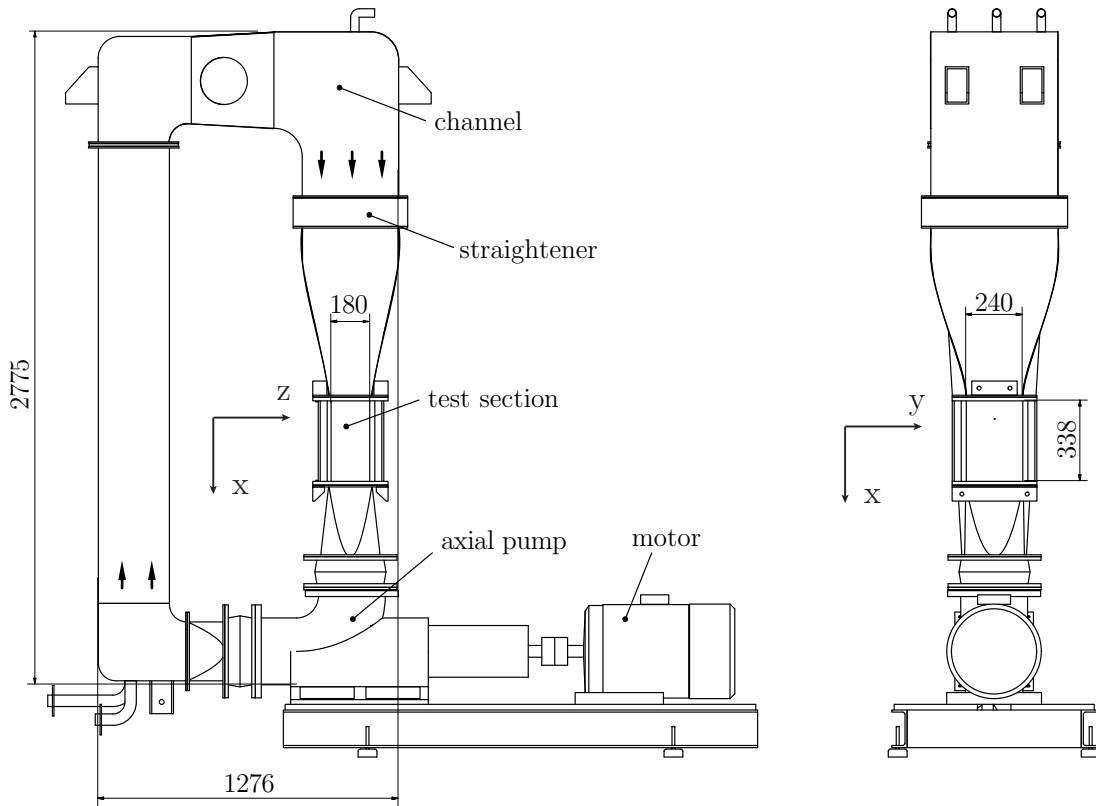


Figure 32: Sketch of the flow channel (dimensions given in mm).

During the design of the flow tunnel, special concern was put on controllable and precise boundary and working conditions, in order to provide reliable data which allow to achieve a good agreement between experimental and numerical results. Therefore, the channel includes several rectifiers and straighteners to guarantee a uniform inflow into the test section. To prevent asymmetries in the structural deflection and the flow the gravity force is aligned with the x -axis in the main flow direction within the test section. The test section is optically accessible on three sides to allow optical measurement systems like LLT, PIV and V3V. The

measurement techniques employed are the object of the following paragraphs.

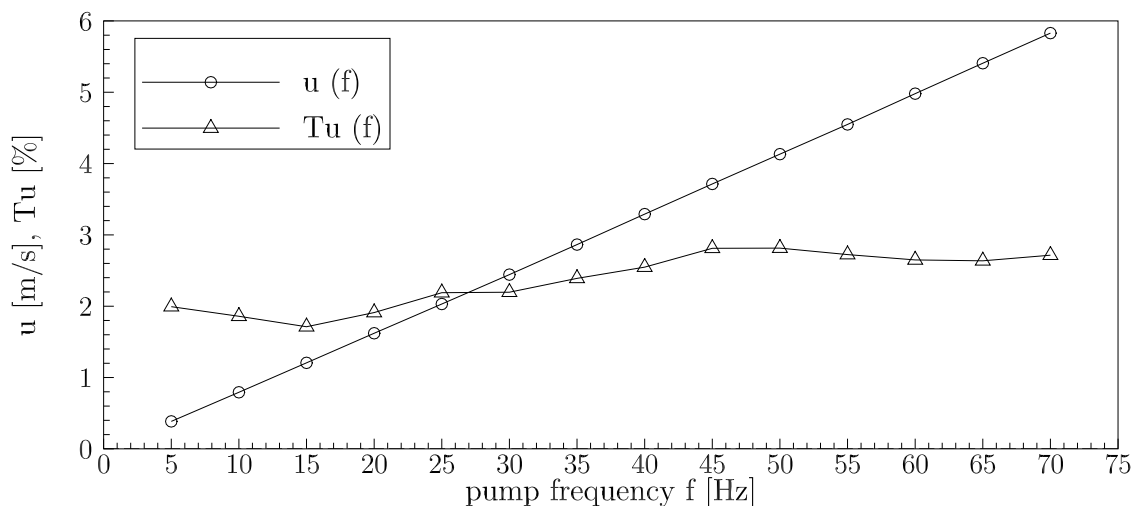


Figure 33: Pump calibration curve for water.

4.2. Planar particle-image velocimetry

The particle-image velocimetry (PIV) is a non-invasive measuring technique, which is able to quantify velocities of a flowing medium in a single illuminated two-dimensional plane. With over 30 years of development and optimization this method is well-established and also broadly used in science and industry (Adrian, 2005). Numerous set-ups and configurations for different flow applications are used. Small-scale flow phenomena, e.g., microfluidics in cells (Santiago et al., 1998; Shinohara et al., 2004) or large-scale experiments in wind tunnels for airplane aerodynamics (Kompenhans et al., 2000; Watanabe and Kato, 2003) define the wide area of different applications of this flexible measuring technique. Pressure-based techniques like the Pitot tube, or thermal anemometry like hot-wire probes are invasive measuring techniques, which interact with the flow. In contrast, the PIV method is an optical measurement method that works contactless and therefore hardly affects the flow. Further characteristics of a common PIV-system are the complete coverage of the flow field (at least within a 2D plane) with a high spatial and temporal resolution usually in the order of 10 Hz. With the ongoing development in opto-electronics high-speed cameras with a higher temporal resolution in the order of 10 kHz are employed for PIV applications, especially for highly turbulent flows.

A classic particle-image velocimetry (Adrian, 1991) set-up depicted in Fig. 34 consists of a single camera obtaining two components of the fluid velocity in a plane illuminated by a thin laser light sheet. Tiny particles dispersed into the fluid are following the preferably transparent fluid and reflecting the light during the passage through the light sheet. By taking two reflection fields in a short time interval Δt with high-resolution digital cameras, the displacements of the particles between those pictures is calculable.

The most common technique used for this purpose is the cross-correlation method that estimates the most likely displacements of several particle groups on an equidistant grid which subdivides the recorded PIV image. Based on a precise preliminary spatial calibration and the known time interval Δt between the two recordings, the velocity components u and v in all

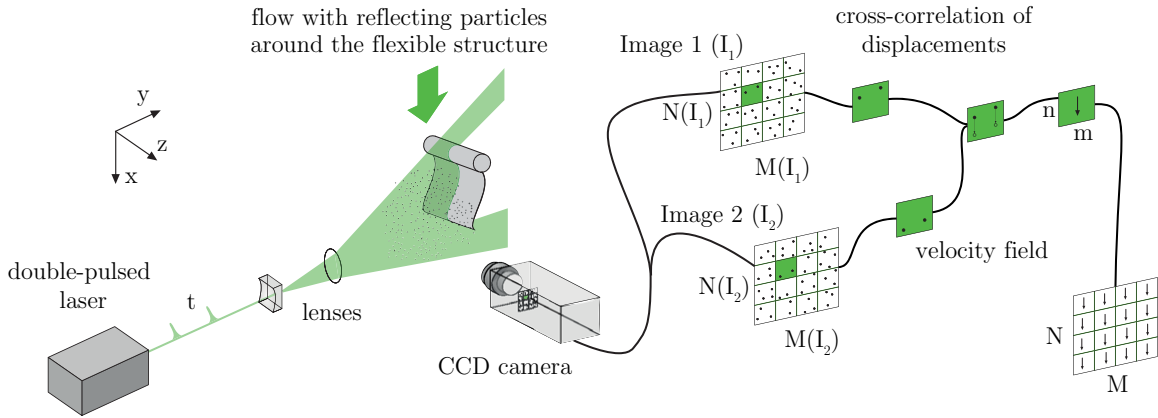


Figure 34: Measuring principle of the particle-image velocimetry.

correlated particle groups can be calculated.

The application and precision of the PIV method depends on several factors which are partly connected to each other. Relevant parameters are the state of matter of the fluid (liquids or gases), the flow conditions (laminar or turbulent flows), the geometry (size of the measuring field and structures in the flow), energy density (reflection level of the particles, laser power, laser pulse frequency, uniform illumination of the flow field), the tracer particles (state of matter, size, shape, material density ratio of the particle to the fluid, surface coatings, particle density in the flow) and the velocity procession method. In the following paragraphs the most important parameters of the PIV method are discussed.

4.2.1. Particle follow behavior

The size of a tracer particle (including its follow behavior) is in conflict with the amount of reflected laser light which increases with the square of the particle diameter. The tracers should be sufficiently small to guarantee an accurate follow behavior in the fluid and not alter the fluid properties or the flow characteristics. Small particle diameters result in a low reflection level and low light intensities on the CCD image sensor. Despite highly reflective coatings on the tracer surface, the selection of a tracer is often a compromise between its follow behavior and its light emission. Furthermore, the obtained light on the camera sensor of a reflective particle relies on the particle density in the flow. A distinction is made in low, medium and high density images (see Fig. 35).

A low particle image density such as illustrated in Fig. 35a refers to the particle tracking velocimetry (PTV). In this case individual particles in a series of images can be detected and tracked over the time. Medium density (Fig. 35b) reflection fields are used for the PIV method, which uses particle groups instead of individual particles to identify their displacement within two images. Therefore, a higher amount of particles compared to PTV is injected into the flow. In the case of high density particle images (Fig. 35c) no individual particles or groups can be identified as they overlap and form speckles. The deformation of the speckles between two illuminations can be used for the reconstruction of the flow motion and is denoted laser-speckle velocimetry (LSV).

Since the principle of the PIV method applied in the present thesis is based on the motion

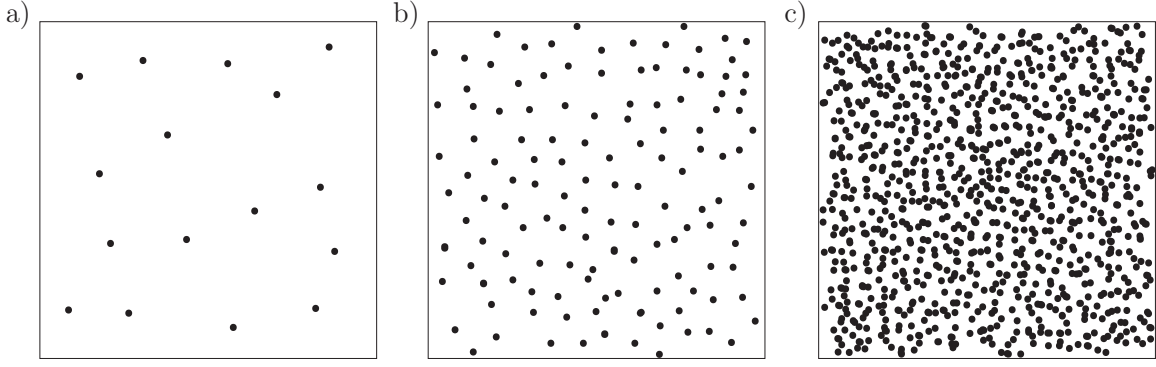


Figure 35: Different particle image densities: a) low (PTV), b) medium (PIV), and c) high image density (LSV).

of the particles, it is important to ensure their exact follow behavior to the fluid. The follow behavior depends on the particle shape which is usually assumed as spherical with the diameter d_p , the particle density ρ_p and the fluid properties (density ρ_f , dynamic viscosity μ_f , Re). The flow-driven motion of a single particle is governed by NEWTON's law:

$$\rho_p \frac{\pi d_p^3}{6} \frac{d\mathbf{u}_p}{dt} = \sum \mathbf{f}_p. \quad (66)$$

The main forces \mathbf{f}_p acting on a particle are expressed by the following terms according to Thomas (1992) and Melling (1997):

$$\begin{aligned} \sum \mathbf{f}_p = & \underbrace{\rho_f \frac{\pi d_p^2}{8} c_D (\mathbf{u}_f - \mathbf{u}_p)^2}_{\text{I}} - \underbrace{\nabla p V_p}_{\text{II}} + \underbrace{\frac{1}{2} \rho_f \frac{\pi d_p^3}{6} \left(\frac{D\mathbf{u}_f}{dt} - \frac{d\mathbf{u}_p}{dt} \right)}_{\text{III}} - \\ & \underbrace{\frac{3}{2} d_p^2 (\pi \mu_f \rho_f)^{\frac{1}{2}} \cdot \int_{t_0}^t \left(\frac{D\mathbf{u}_f}{dt} - \frac{d\mathbf{u}_p}{dt} \right) \frac{d\tau}{\sqrt{t - \tau}}}_{\text{IV}} + \underbrace{f_{\text{ext}}}_{\text{V}}. \end{aligned} \quad (67)$$

The first term I describes the viscous drag according to the assumption of STOKES flow. Term II refers to the pressure gradient in the vicinity of the particle. Term III is related to the already mentioned added-mass effect which describes the resistance of an inviscid fluid to the acceleration of the particle. Term IV is known as the BASSET history integral, which is related to drag fluctuations due to acceleration processes like unsteady flow effects. Finally, the last term V denotes the external forces such as gravity and buoyancy. In most cases of PIV measurements, many terms in this equation can be neglected except the term of STOKES's drag law and the external forces (Thomas, 1992). The STOKES's law is applied when the particle's Reynolds number Re_p is in the order of unity, where Re_p is defined as:

$$\text{Re}_p = \frac{\rho_f |\mathbf{u}_f - \mathbf{u}_p| d_p}{\mu_f}. \quad (68)$$

In addition to this requirement, a couple of other quantities can be used for the evaluation of the follow behavior. The major error on the follow behavior is related to the inertia and drag forces acting on the moving particle. Based on the balance between these forces a small

spherical particle follows a viscous, continuously accelerated medium with the lag velocity $\mathbf{u}_{p,\text{lag}}$:

$$\mathbf{u}_{p,\text{lag}} = \mathbf{u}_f - \mathbf{u}_p = \frac{\rho_p d_p^2}{18\mu_f} \frac{d\mathbf{u}_p}{dt} = \tau_p \frac{d\mathbf{u}_p}{dt}. \quad (69)$$

In case of an optimal follow behavior the lag velocity tends to zero. In practice, often heavier tracers are used for PIV measurements. The particle velocity response behavior to the fluid velocity for heavy particles with a much higher density ($\rho_p \gg \rho_f$, e.g. gas flows) in a continuously accelerating flow is described for the one-dimensional case by:

$$u_p(t) = u_f \left[1 - \exp\left(-\frac{t}{\tau_p}\right) \right]. \quad (70)$$

Here, the particle response time τ_p is a characteristic quantity of the particle inertia and is defined by:

$$\tau_p = \frac{\rho_p d_p^2}{18 \mu_f}. \quad (71)$$

Especially for the measurement of small-scaled flow structures in turbulent flows τ_p has to be necessarily small. The STOKES number is a dimensionless quantity, which expresses the relation between the response time of the particle τ_p (Eq. (71)) and the characteristic time scale of the fluid τ_f :

$$\text{Sk} = \frac{\tau_p}{\tau_f} = \frac{\rho_p d_p^2}{18 \mu_f} \frac{u_f}{d_p}, \quad (72)$$

where τ_f is determined by:

$$\tau_f = \frac{u_f}{d_p}. \quad (73)$$

As already mentioned, for an acceptable tracing accuracy, the particle response time τ_p should be much smaller than the smallest time scale of the flow τ_f . Therefore, smaller STOKES numbers represent a better tracing accuracy. For $\text{Sk} \rightarrow 0$ the particles will perfectly follow the flow, while for $\text{Sk} \rightarrow \infty$ the particles are completely unresponsive to the fluid flow like a bullet. In this case the particles fully decouple from the flow especially where the flow decelerates abruptly. For turbulent flows the seeding particles need to be smaller than the smallest fluid length scale (KOLMOGOROV length l_k) if all flow structures should be detected.

Another good reference for the follow behavior is based on the balance between the drag and the buoyancy forces to the gravitational force. From this balance, the sedimentation velocity u_s of the particle can be derived. The sedimentation velocity is given by:

$$u_s = \frac{d_p^2 g (\rho_p - \rho_f)}{18\mu_f}. \quad (74)$$

In the case of a quiescent flow it refers to the settling velocity of a particle. With low sedimentation velocities (floating particle) an almost independent behavior to the gravitational force can be proven.

4.2.2. Optical requirements

To quantify the particle motion, scattered light on their surfaces are captured by digital cameras within a short time interval. The light source of these reflections is in most cases a monochromatic laser which emits high-energy laser pulses. Between the laser head and the measuring section a light sheet optic consisting of two spherical and one cylindrical lenses is placed (see Fig. 36).

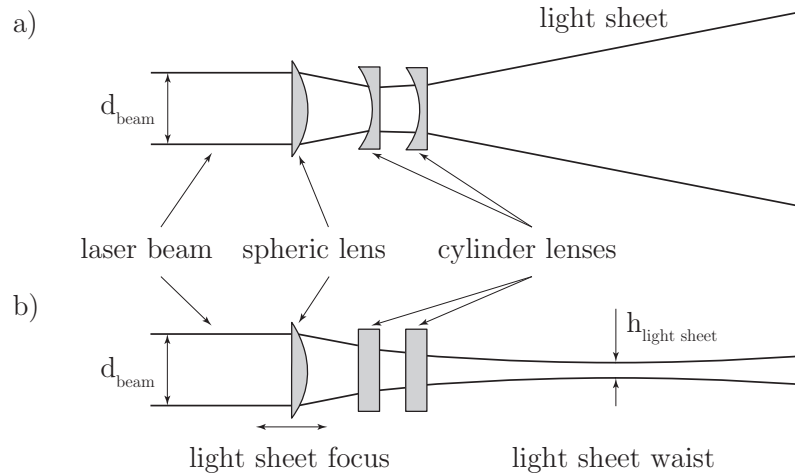


Figure 36: Illustration of the laser beam extension to a light sheet a) side view; b) top view.

With the resulting transformation of the circular laser beam to a thin laser sheet a planar area within the flow is illuminated. The obtained particle image intensity and therefore the contrast of the PIV images is proportional to the scattered light power on the particle surface. The light scattered by small particles is a function of the ratio of the refractive index of the particles to the surrounding medium, the particles shape, their size and orientation.

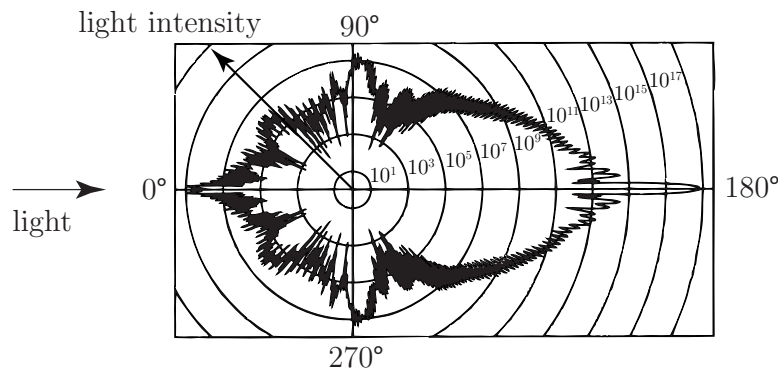


Figure 37: Light scattering by a 10 μm glass particle (Raffel et al., 1998).

Figure 37 illustrates the polar distribution of the scattered light intensity of a 10 μm glass particle in water according to the Mie theory (Mie, 1908) at a wavelength of $\lambda = 532 \text{ nm}$ which refers to a frequency-doubled Neodymium-doped Yttrium Aluminum Garnet (Nd:YAG) laser used in common PIV set-ups (and also in this thesis). The light intensity is not blocked by the particle itself but spread in all directions. In case of a mono-PIV set-up a charge-coupled device (CCD) camera is placed normal to a laser light sheet. There, the recorded light intensity is much lower than in the forward or backward scatter direction.

4.2.3. Velocity processing

The recorded images are typically stored with a 12bit gray-scale color resolution (4096 gray-scales, from black to white according to their registered light intensity on the CCD chip). To obtain the velocity vectors the image-pair is divided into an equidistant grid with the size $M \times N$. Each grid cell or interrogation spot (IS) with the size $m \times n$ pixels contains a variable amount of particle images. The specific amount depends on the interrogation size and the tracer density. Smaller interrogation spots result in a higher grid resolution and finally more velocity vectors within a PIV result, but require increased seeding densities and/or higher resolving CCD cameras.

Based on the particle image motions a representative displacement vector between the two recordings (I_1, I_2) is determined for each interrogation spot (see Fig. 34). Since statistical correlation methods are used for this image analysis, a minimum number of particle images within the interrogation spot are necessary. Due to the contrast of the bright particle reflections to the darkened background, the position (x, y) of each particle image is determined. Often a particle image diameter between 2 and 3 pixels is recommended. The exact position of the single particle image is obtained by a sub-pixel determination of its center of mass based on its gray-scale distribution. Usually the pixel with the largest light intensity denotes the center of the particle image.

With the assumption that a small group of particle images in the interrogation spot IS in I_1 is excited by the same flow motion, the particle image group with its specific particle image positions is found again in I_2 . Due to the possibility that not only one displacement is calculated, the spatial (two-dimensional) cross-correlation function Φ_c finds the most probable displacement vector (m, n) (Raffel et al., 1998; Tropea et al., 2007):

$$\Phi_c(m, n) = \sum_{i=0}^{m-1} \sum_{j=0}^{n-1} g_1(i, j) \cdot g_2(i + m, j + n). \quad (75)$$

In this context, the displacement vector (m, n) of the particle image group is determined with g_1 and g_2 as the position (i, j) in the two recordings I_1 and I_2 . Reaching the maximum value of $\Phi_c = 1$ an absolute agreement in the displacement is found. A value of $\Phi_c = 0$ represents an absolute mismatch. Figure 38 shows the principle of the cross-correlation on the displacement of a single particle image.

In Fig. 38a all possible particle image displacements in a two-dimensional domain are illustrated. Each particle image in the second image (gray) is a possible matching candidate as presented in the histogram in Fig. 38b, where each peak marks a possible particle image displacement. All peaks have equal heights as the probable displacements are not weighted yet. To find the most probable particle image displacement the cross-correlation procedure is carried out for all particle images in the same interrogation spot and the probabilities in the displacement histogram are superimposed leading to the weighted histogram. Hence, the peak for the most probable particle image displacement will be dominant over the displacement peaks for unrelated particle image pairs as shown in Fig. 38c. Typically, the possibilities of a feasible displacement is reduced to usually only one accordance.

Finally, the calculated displacement is converted with a previously maintained calibration fac-

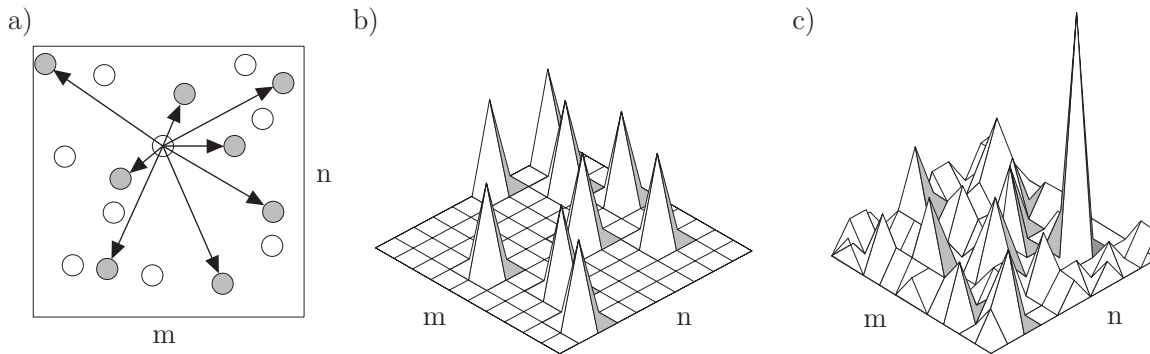


Figure 38: Illustration of the cross-correlation method applied in PIV for one arbitrary interrogation spot, a) superimposed PIV image including particles (blank particles refers to I_1 , filled particles to I_2) and possible particle displacements for a single particle image; b) unweighted histogram for all possible particle image displacements of this single particle image; c) weighted histogram for the most probable particle image displacement calculated by the cross-correlation method (Tropea et al., 2007).

tor (mm/pixel) and the time interval Δt . The direction and the value of the velocity vector is divided into the two velocity components u and v according to the main directions of the coordinate system x and y of the grid. By applying the whole procedure on all interrogation spots a two-component velocity field in the plane of the laser light sheet is obtained.

4.3. Volumetric particle tracking

In the last decade the principle of the two-dimensional particle image velocimetry (Fig. 39a) was extended to even measure the third velocity component w . This section provides a brief overview of this topic before the system used here is described in more detail. The most common technique is called stereoscopic PIV and consists of two cameras in a special angular alignment to the still used laser light sheet (Fig. 39b). Both cameras are focused on the same spot in the flow. The velocity component normal to the light sheet is indirectly calculable by a special calibration function. The extension of this technique is the dual-plane PIV, where two light sheets illuminate the flow and the reflections fields are separately recorded by two cameras (monoscopic dual-plane PIV, Fig. 39c) or four cameras (stereoscopic dual-plane PIV). The distance between the light sheets can range from almost zero up to the flow depth. The recordings are decomposed by optical methods like polarization or different laser light wavelengths. The velocity field correlation uses the same algorithms like the standard mono- or stereoscopic PIV methods. According to the use of two or four cameras and their alignment to the light sheets the third velocity component normal to the light sheets is calculable.

With the increasing demand of techniques which allow the measurement of complex flows including fully three-dimensional flow structures such as vortices, wake areas or separation bubbles, several volumetric methods (three-dimensional, three velocity components \rightarrow 3D3C) are developed. Recent methods are the multi-plane PIV (holographic PIV) and the adjustable-depth volumetric PIV (tomographic PIV, volumetric defocused PIV). Holographic PIV uses multiple light sheets of different wavelengths and corresponding multiple reference laser beams, each coherent with only one light sheet (Fig. 40a). The interference of the coherent light scattered by a tracer and the reference laser beam to encode the information of the amplitude

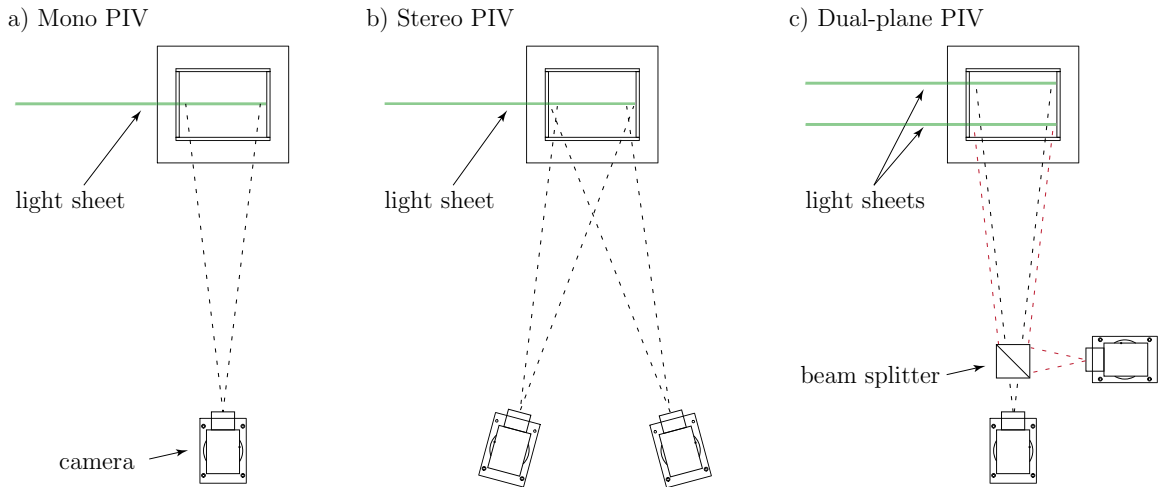


Figure 39: Alignment set-up of a) monoscopic PIV; b) stereoscopic PIV; c) monoscopic dual-plane PIV set-up.

and phase of the scattered light is received on a sensor plane which can be described as a hologram. The encoded information is used to reconstruct the original intensity field by illuminating the hologram with the original reference beam via optical methods or digital approximations. The intensity field is interrogated using 3D cross-correlation techniques to yield the velocity field (Hinsch, 2002).

In tomographic PIV the thickness of the light sheet is often expanded to one quarter of the width or length of the field of view (FOV, visible area obtained by the camera at a particular position and orientation in space). Several CCD cameras (in most cases at least four cameras) are focused under a different angle on the same point in the flow (Fig. 40b). The focal depth of the imaging system is matched with the thickness of the light sheet. The recorded image set is a quadruplet of non-collinear views of the particle reflection fields. These double-frame images are the input of the tomographic reconstruction of the particle position using the three-dimensional distribution of the light intensity. Based on the position (x, y, z) of the particles in both frames a three-dimensional particle-tracking cross-correlation is performed to obtain the three velocity components (u, v, w) (Scarano, 2013).

A similar approach is used by the volumetric defocused PIV (DFPIV) technique. Again several cameras are focused from different directions on the same point in the flow (Fig. 40c). In contrast to other PIV methods the DFPIV uses a volumetric laser illumination of the flow. This is possible due to the missing limitation of the focused range in the FOV of the cameras such as present in tomographic PIV. That means that also particles far away from the focal plane are illuminated in the laser volume and recorded by the cameras. Related to the distance of the particle to the focal plane their projections are not sharply reproduced (defocused appearance) on the camera chip. Therefore, this method is able to capture a much larger area of the flow. The applied tracer particles are often larger than in standard PIV methods due to the lower laser energy density of the illuminated measurement volume and the defocused particles. Furthermore, often the particle tracking method is performed instead of the statistical PIV algorithm. As a consequence, the tracer density is also significantly lower in DFPIV methods in comparison to normal PIV methods.

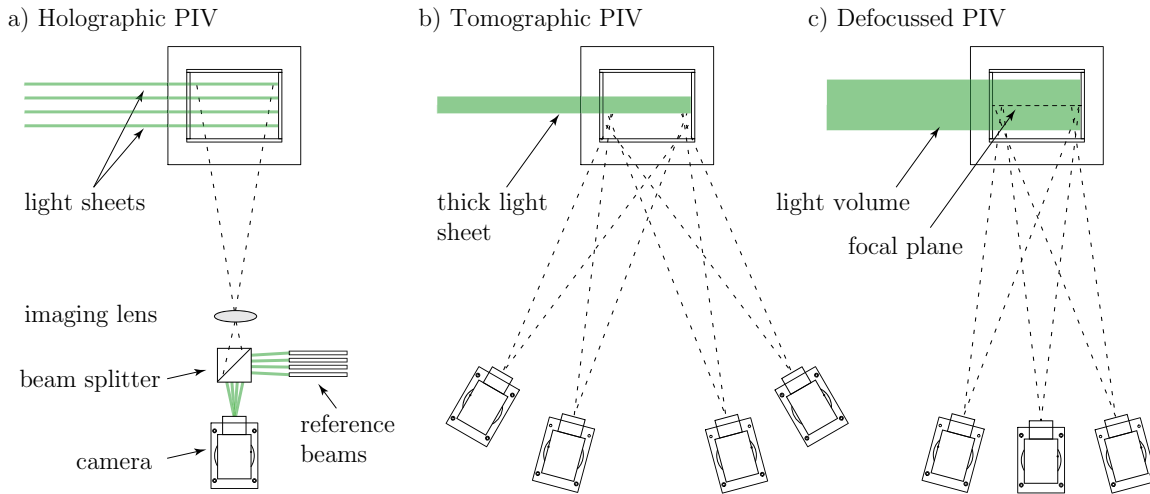


Figure 40: Alignment set-up of a) holographic PIV; b) tomographic PIV; c) defocused PIV set-up.

In this thesis the first commercially adapted system based on the DFPIV method is used. The volumetric particle-image velocimetry system (V3V) developed by TSI[®] is the further development of studies already mentioned in Section 1.2. The V3V system consists of three 4 Megapixel (MP) cameras mounted in a special optical aperture (Fig. 41a). With the triangular arrangement of these cameras (top, left, right) it is possible to analyze particle displacements in a fully three-dimensional flow volume including all three velocity components (see Fig. 41a) performing only one single measurement and calibration. The measurement procedure of the V3V system is divided into five steps (Kalmbach and Breuer, 2013b):

- Calibration (step 1)
- Particle detection (step 2)
- Triplet construction (step 3)
- Triplet tracking (step 4)
- Grid interpolation (step 5)

Step 1: Calibration

The preliminary spatial calibration of the flow volume uses an one-plane calibration target which is traversed through the measurement volume in equidistant steps (step size between 5 and 10 mm). On each position a set of pictures (including all three cameras) is taken and the analyzed pictures map one measurement plane. Using an equidistant point array on the target the perspective distortion in the images are taken into account. The points on the target are detected in the picture sets and reproduced by polynomial functions. At the end of the calibration process the whole measurement volume is mapped by functions which describe the position of each point in the volume using a triangle formed by the different camera angles. The size of the triangle is directly related to the distance from the V3V optic defining the z -direction of the measurement volume.

Step 2: Particle detection

For the determination of the two-dimensional position of each particle in the captured images an intensity threshold is set to reduce inferences in the background (i.e., light reflections on the channel walls). Any valid particle must have a peak intensity above this threshold and a high ratio between the peak intensity of the particle and the local background intensity. Afterwards, a Gaussian intensity profile is fitted to the particle image, where the peak represents the center of the particle (Troolin and Longmire, 2008).

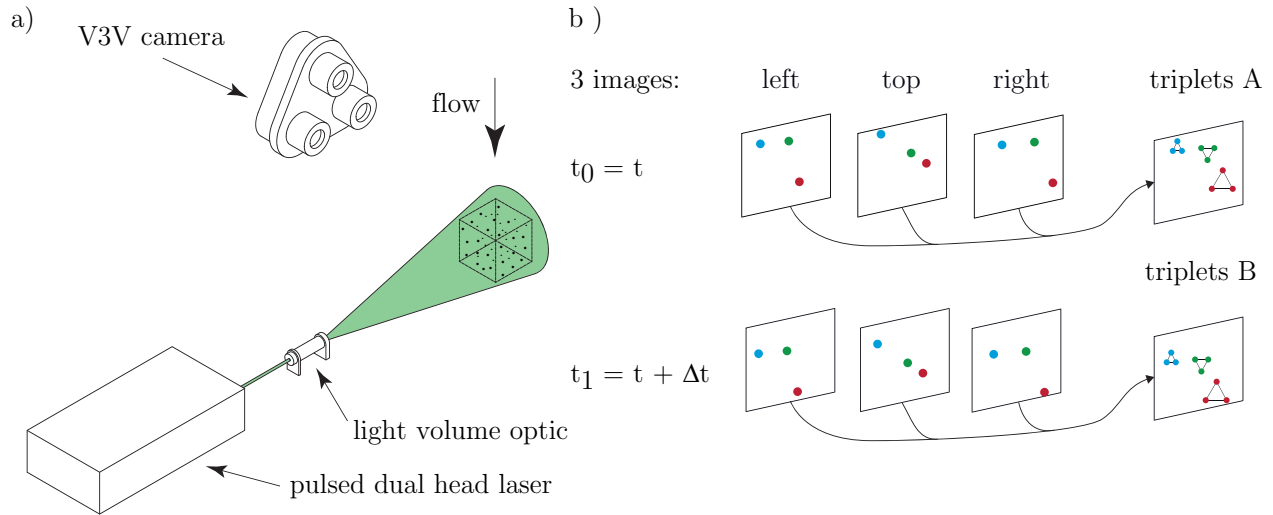


Figure 41: Particle detection procedure a) V3V set-up; b) data processing from reflection fields to 3D velocity vector cloud.

Based on the 2D positions of each particle in all six images (two images captured on each camera (top, left, right)) a three-dimensional reconstruction of their individual three-dimensional position is applied (see Fig. 42).

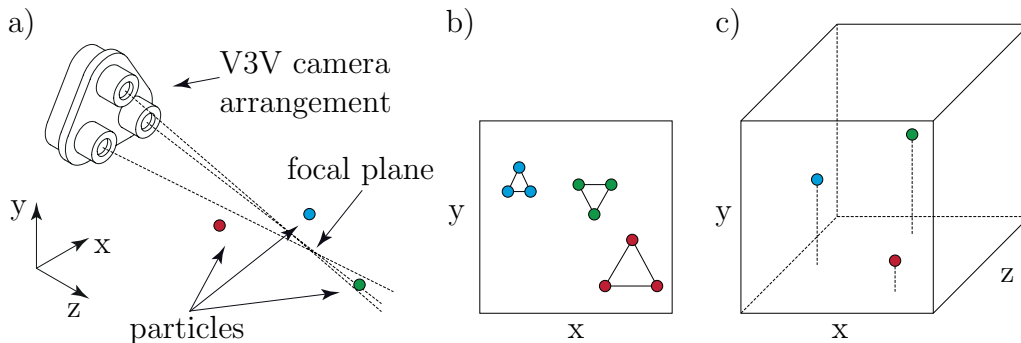


Figure 42: Spatial particle detection: a) camera alignment; b) 2D image composition including triplet detection (each triplet is formed by the specific particle position in the three different camera images (top, right, left)); c) 3D particle position based on the center of mass and the size of the triplet.

Step 3: Triplet construction

In the measurement images the position of a single particle in the top camera image defines a ray in the right camera image based on the three-dimensional calibration functions. The

position reconstruction algorithm searches along this ray in the right image for possible 2D particle matches (search step A in Fig. 43). In the case of a positive match the position of the particle found defines another ray in the left image, where the search procedure is repeated (search step B in Fig. 43). Based on a further positive finding of a particle in the left image, the third search step proves the initial particle position in the top image (search step C in Fig. 43). In the case that in each search step no match is found (gray particles in Fig. 43) that is located within a 0.5 sub-pixel tolerance of the triangle defined by the calibration, the initial particle in the top image is not used (Troolin and Longmire, 2008). A successful search algorithm with matching particles in all three images results in the formation of a triplet (step 3, Fig. 42b, Fig. 41b). This search process is sequentially repeated for all particles found in the top camera image. The size of the triplet is related to the depth position z of the particle. Since the focal plane of the V3V optic is in most cases located at the end of the measurement volume, the triplets are larger in the vicinity of the V3V optic (red triplet in Fig. 42b) and smaller (blue triplet in Fig. 42b) towards the focal plane. In the case that the focal plane is not placed at the end of the measurement volume, the triplet of a particle behind the focal plane is upside down (green triplet in Fig. 42b).

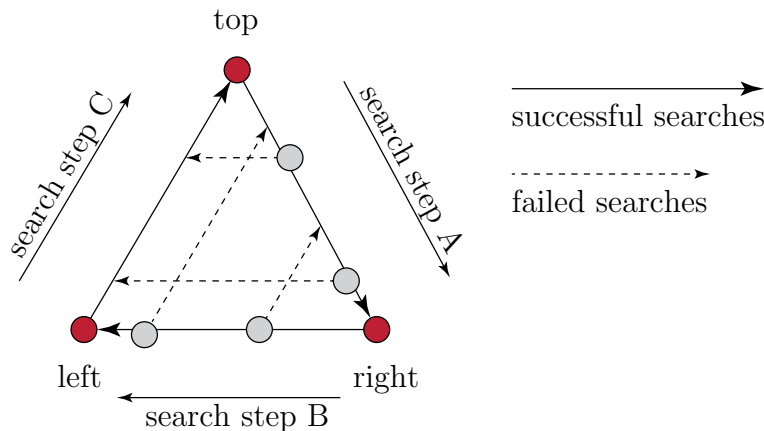


Figure 43: Illustration of the triplet reconstruction algorithm.

Step 4: Triplet tracking

After the spatial location of all particles in the flow volume within the two frames (t_0 and $t_0 + \Delta t$) a particle tracking algorithm according to Pereira et al. (2006) and Ohmi and Li (2000) is performed to obtain the specific particle displacements. To increase the correlation probability, clusters of spatially related particles are formed. These cubically shaped clusters are similar to the interrogation spots in standard PIV methods but of three-dimensional kind. The clusters in the frame t_0 are smaller in volume than the corresponding clusters in frame $t_0 + \Delta t$ (Fig. 44). This size extension is applied to follow particles which move out of the initial cluster area. By increasing the volume of the clusters in frame $t_0 + \Delta t$ more particles could be tracked and the correlation probability is increased.

Within a cluster, each pair of corresponding particles is assigned to a number of matching probabilities with feasible displacements. Initially each particle displacement has the same probability. The probability computation is based on the assumption that neighboring par-

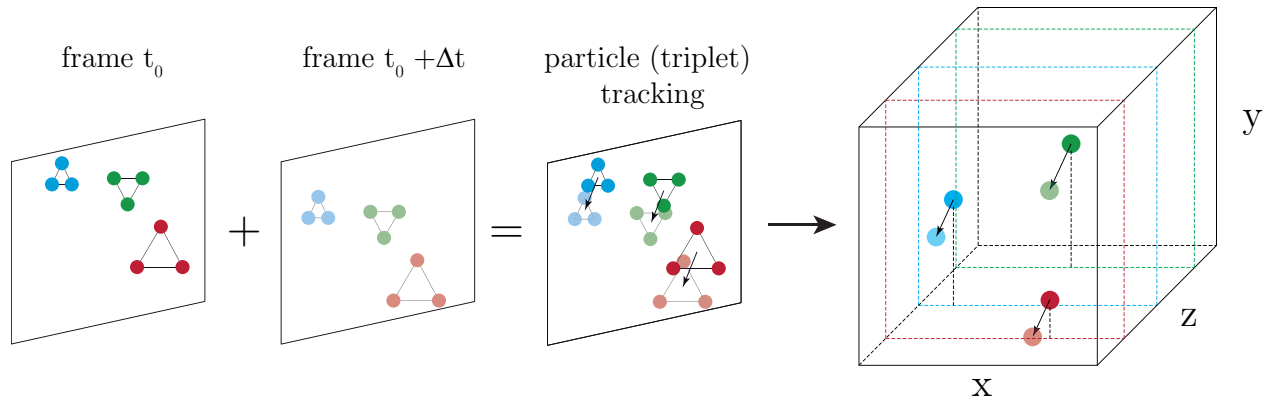


Figure 44: Particle tracking of triplets at frame t_0 and frame $t_0 + \Delta t$.

ticles move similarly. These probabilities are then iteratively recomputed for all particles in the cluster, until a convergence criterion is reached. If the maximum matching probability is calculated and larger than a specified threshold, the valid displacement for this particle (Δx , Δy , Δz) is found (Fig. 44, Troolin and Longmire, 2008). Based on the calibration and the displacement of the particles in all three dimensions and the time interval Δt , all three velocity components of each valid particle are determined.

Step 5: Grid interpolation

In the last step the randomly distributed velocity vectors are interpolated onto an equidistant grid using the Gaussian process.

4.4. Laser triangulation

The experimental FSI investigations in this thesis involves both, fluid and structure measurements. In industrial applications the non-contact structural measurements are often based on laser distance techniques, especially the laser triangulation. This technique is chosen here because of the known geometric dependencies, the high data rates, the small measurement range and the resulting higher accuracy in comparison to other techniques such as laser phase-shifting or laser interferometry.

The principle of the optical triangulation is known for centuries, e.g., the sextant in maritime navigation. The simplest set-up uses a laser beam which is focused onto an object X_1 as illustrated in Fig. 45. A one-dimensional CCD sensor is located near the laser output and detects the diffusely reflected light on the object surface. If the object moves ($X_1 \rightarrow X_2$), a change of the reflection angle occurs and thus the projection changes ($x_1 \rightarrow x_2$) on the sensor. Based on this change in position the new distance to the object is calculated using trigonometric functions (based on the known angle α between the laser beam and the optical axis of the sensor, the distance e between the optical center and the laser beam, the focal length f and the diameter d_l of the lens and its distance s to the sensor array) and an internal length calibration with respect to the applied measurement range. The measurement accuracy increases with an increasing angle between the laser and the sensor. At the same time, with increasing angles larger object areas may become shaded. A compromise is found for angles between $\alpha = 25 - 45$ degrees. This relationship between measurement resolution and observation angle

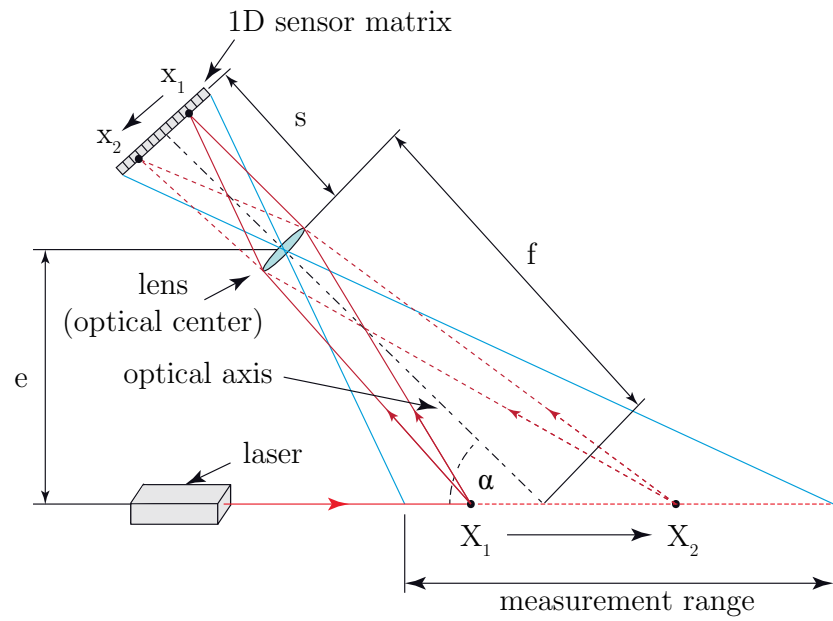


Figure 45: Measurement principle of the single-point laser triangulation.

is typical for all triangulation based methods.

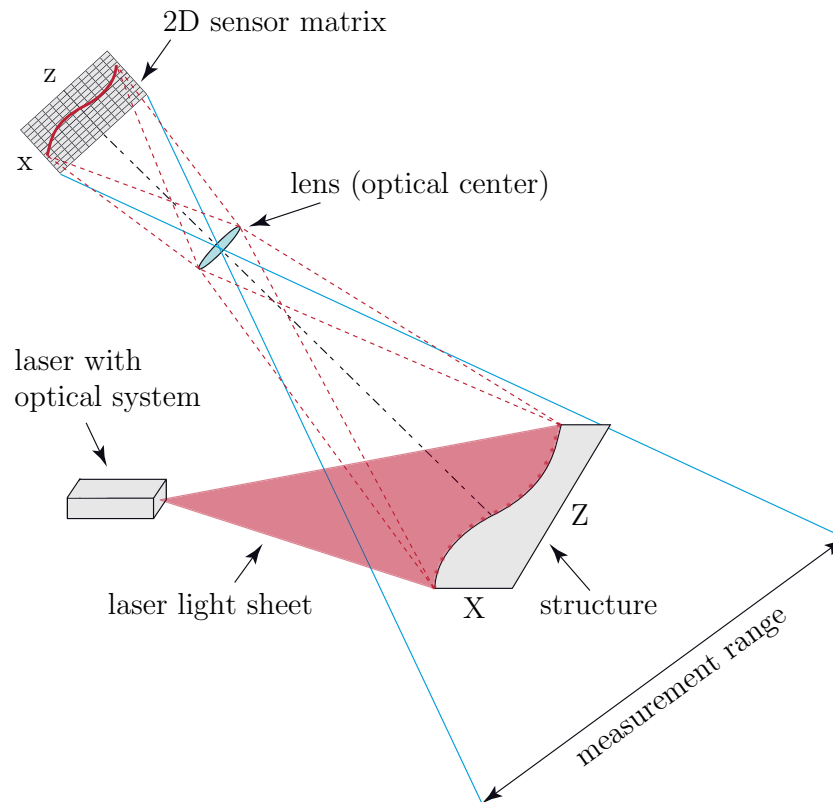


Figure 46: Measurement principle of the laser line triangulation.

To study simultaneously more than one measurement point on the structure the single point triangulation is extended to the laser line triangulation, which is used in this thesis. By use of an optical system a laser line is emitted and projected onto the target surface (Fig. 46). The one-dimensional sensor array of the single-point sensor is replaced by a two-dimensional CCD

matrix which enables to detect the two-dimensional structure position of a predefined number of points along the laser line. In addition to the calibrated distance information (x -axis) the sensor uses the matrix image to calculate the position along the laser line (z -axis). This generates precise measurements, which represent the profile of the structure contour along the projected laser line. Regardless of the position or angle the profile data are absolutely calibrated data-sets in a two-dimensional coordinate system that is fixed with respect to the sensor position.

5. Numerical simulation techniques

The numerical prediction of FSI phenomena is realized by either monolithic or partitioned approaches (Degroote et al., 2009). In the monolithic approach the governing equations of the flow and the structure motion are solved simultaneously by a single solver. Contrarily, in the partitioned approach the governing equations of the flow and structural motion are separately solved by two distinct solvers. Due to the independent development of structure and fluid solvers and the thereby related advanced levels of these algorithms, in most cases the partitioned approach is used. Taking this advantage, the modular approach is applied in this thesis and will therefore be further discussed. Both, the flow solver (CFD) and the structure solver (CSD) divide the physical space into small units. The CSD solver is based on the finite-element method (FEM) and uses a temporal and spatial discretization of the initial-boundary value problem. The CFD solver applies the finite-volume method (FVM). The computational domains are decomposed into finite elements (FEM) for the structural prediction or finite volumes (FVM) for the fluid motion, where the field quantities are interpolated by shape functions. In combination with time-stepping methods the partial differential equations are approximated by corresponding algebraic formulations for the fluid and structure dynamics, which are finally solved using high-performance computers. The numerical predictions in this thesis are carried out with the commercial multi-physics environment ANSYS[®]-CFX 14.0 (ANSYS, 2011b). Considering the well-proved applicability of the single solvers in science and industry the applied numerical simulation techniques will only be explained briefly in the following paragraphs.

5.1. Computational structure dynamics

The behavior (motion, deformation) of a structure can be represented using mathematical models (approximate models), which are derived based on the continuum mechanics conservation laws (Eq. (18)). For the formulation of the finite-element method (FEM) a lot of principles are used. According to Reddy (2004) two general distinctions are common. The first method is based on the principle of static equilibrium (also known as direct method) and is applied for structural computations which can be represented by simple governing equations. Here, the theorem of Castigliano (Castigliano, 1879) and the principle of minimum potential energy (e.g. explained in Parisch (2012)) are used for complicated elastic structural problems. The second method applies more sophisticated mathematical principles like variational approaches to formulate the finite-element analysis for phenomena governed by complex differential equations, involving derivative terms such as Ritz, Galerkin, collocation, and least-squares methods to mention only a few (Reddy, 2004). The mathematical approximation of the governing equations the structural geometry has to be discretized. As already mentioned, the physical space of the structural body is divided into small finite-elements. Due to the broad application of finite-element analysis numerous different element formulations were developed to provide the specific simulation demands in engineering. In general, linear or quadratic shape functions are applied to approximate the field functions according to the element geometry and the preferred accuracy of the results.

Based on the mathematical approximation of the governing equations and the element discretization a general equation for a single finite element can be formulated:

$$\mathbf{k} \mathbf{q} = \mathbf{Q}. \quad (76)$$

Here, \mathbf{k} describes the characteristics of the continuum, \mathbf{q} represents the column matrix nodal values (output variable of interest) and \mathbf{Q} marks the input to the continuum. In case of a stress analysis, \mathbf{k} represents the stiffness matrix, \mathbf{q} describes the vector of nodal displacements, and \mathbf{Q} denotes the vector of nodal forces. The individual formulation of each finite element is followed by the ensemble of these finite elements to a global/assemblage equation which is given in the form below:

$$\mathbf{K} \mathbf{d} = \mathbf{F}. \quad (77)$$

In this equation \mathbf{K} marks the assemblage property matrix (e.g., the stiffness matrix), \mathbf{d} gives the assemblage vector of nodal unknowns (e.g., displacements), and \mathbf{F} denotes the assemblage vector of nodal forcing parameters. Now, the nodal unknowns are determined by using high-performance computers to solve this system of equations. Afterwards, possible dependent quantities (e.g., stresses) are obtained. The solution is repeated until a prescribed convergence criterion is reached and the finite-element analysis is completed.

In the following paragraphs the finite-element method is exemplarily described for a plane structure consisting of several two-dimensional rectangular elements in the plane stress state (according to Lammering (2011)).

As already mentioned, the finite-element formulation of Eq. (76) is obtained by incorporating the governing conservation equations (Eq. (18)) into the element equations. Therefore, the element equations are derived from shape functions and the specific geometrical dependencies (e.g., node positions). In general, the number of equations for an element depends on the number of nodes used for the element. Based on this consideration, with two degrees of freedom for each node, the linear shape function for triangular or rectangular elements will consist of two unknowns (taking the two degrees of freedom into account). Therefore, the number of element equations for a triangular element is three, whereas a rectangular element would have four equations. In other words, the number of shape functions for an element depends on the total number of nodes for the particular element and the number of unknowns in each element equation is defined by the degrees of freedom of the particular node. Figure 47 illustrates an example of a rectangular element with two degrees of freedom for each node. Assuming one field variable to be analyzed, the linear shape function for this element is given in general by:

$$N(x, y) = c_0 + c_1x + c_2y + c_3xy \quad (78)$$

Here, the coefficients c_0, c_1, c_2 and c_3 are unknowns. The element equations are obtained by

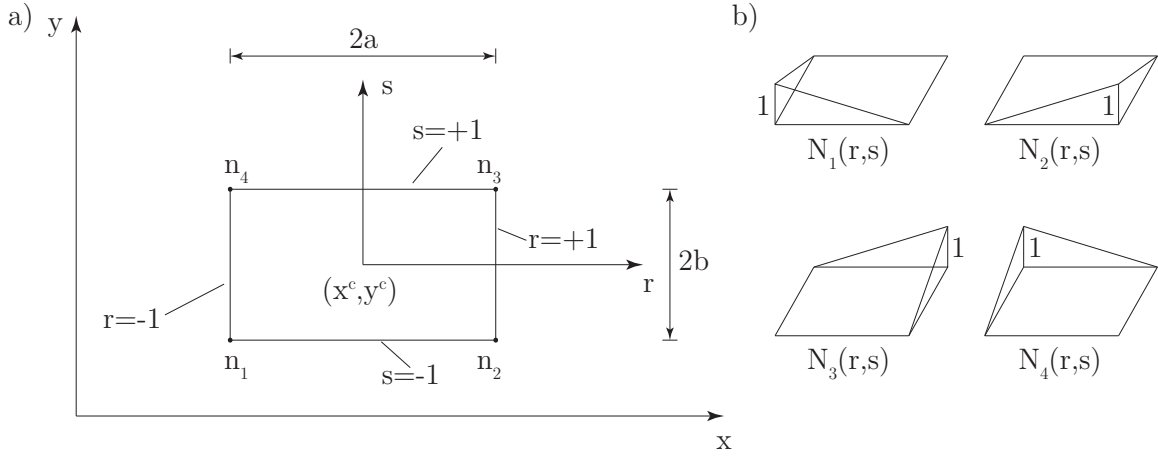


Figure 47: a) Rectangular element with four nodes; b) shape functions for each node.

incorporating the nodal conditions into the shape function leading to:

$$\begin{aligned}
 N_1(r, s) &= \frac{1}{4}(1 - r)(1 - s) \\
 N_2(r, s) &= \frac{1}{4}(1 + r)(1 - s) \\
 N_3(r, s) &= \frac{1}{4}(1 + r)(1 + s) \\
 N_4(r, s) &= \frac{1}{4}(1 - r)(1 + s)
 \end{aligned} \tag{79}$$

where r and s represent the normalized coordinate systems according to $r = (x - x^c)/a$ and $s = (y - y^c)/b$ (see Fig. 47). The displacements \mathbf{d} of the element are formulated by:

$$\begin{bmatrix} d_1(x, y) \\ d_2(x, y) \end{bmatrix} = \begin{bmatrix} N_1 & N_2 & N_3 & N_4 & 0 & 0 & 0 & 0 \\ 0 & 0 & 0 & 0 & N_1 & N_2 & N_3 & N_4 \end{bmatrix} \begin{bmatrix} d_1^1 \\ d_2^1 \\ d_3^1 \\ d_4^1 \\ d_1^2 \\ d_2^2 \\ d_3^2 \\ d_4^2 \end{bmatrix} \tag{80}$$

or

$$\mathbf{d} = \mathbf{N} \mathbf{d}_e. \tag{81}$$

The displacement field \mathbf{d} of the element is described by the nodal displacements \mathbf{d}_e (upper index: node number, lower index: displacement component) and approximated by the corresponding shape functions \mathbf{N} . These linear shape functions are valid under the following conditions:

$$\sum_{i=1}^4 N_i(r, s) = 1 \tag{82}$$

$$N_i(r_i, s_j) = \begin{cases} 1 & \text{for } i = j \\ 0 & \text{for } i \neq j \end{cases}. \quad (83)$$

Now the strains can be expressed by the nodal displacements \mathbf{d}_e . Therefore, the strains \mathbf{E} are obtained by the derivative of the displacements \mathbf{d} with respect to the coordinates \mathbf{x} (under the restriction of small deformations only the linear part of the GREEN-LAGRANGIAN strain tensor containing four strain components is used (refer to Eq. (7) in Section 2.1.1).

$$E^{\text{lin}} = \begin{bmatrix} E_{11} \\ E_{22} \\ E_{12} \\ E_{21} \end{bmatrix} = \begin{bmatrix} \frac{\partial d_1}{\partial x} \\ \frac{\partial d_2}{\partial y} \\ \frac{\partial d_1}{\partial y} \\ \frac{\partial d_2}{\partial x} \end{bmatrix} \quad (84)$$

The derivation of the shape functions Eq. (79) with respect to the coordinates \mathbf{x} results in:

$$\begin{aligned} \frac{\partial \mathbf{N}}{\partial x} &= \frac{\partial \mathbf{N}}{\partial r} \frac{\partial r}{\partial x} = \frac{1}{a} \frac{\partial \mathbf{N}}{\partial r} \\ \frac{\partial \mathbf{N}}{\partial y} &= \frac{\partial \mathbf{N}}{\partial s} \frac{\partial s}{\partial y} = \frac{1}{b} \frac{\partial \mathbf{N}}{\partial s}. \end{aligned} \quad (85)$$

Equation (85) substituted in Eq. (81) and Eq. (84) leads to the strain-displacement relation:

$$\begin{bmatrix} E_{11} \\ E_{22} \\ E_{12} \\ E_{21} \end{bmatrix} = \begin{bmatrix} \frac{1}{a} N_{1,r} & \frac{1}{a} N_{2,r} & \frac{1}{a} N_{3,r} & \frac{1}{a} N_{4,r} & 0 & 0 & 0 & 0 \\ 0 & 0 & 0 & 0 & \frac{1}{b} N_{1,s} & \frac{1}{b} N_{2,s} & \frac{1}{b} N_{3,s} & \frac{1}{b} N_{4,s} \\ \frac{1}{b} N_{1,s} & \frac{1}{b} N_{2,s} & \frac{1}{b} N_{3,s} & \frac{1}{b} N_{4,s} & 0 & 0 & 0 & 0 \\ 0 & 0 & 0 & 0 & \frac{1}{a} N_{1,r} & \frac{1}{a} N_{2,r} & \frac{1}{a} N_{3,r} & \frac{1}{a} N_{4,r} \end{bmatrix} \begin{bmatrix} d_1^1 \\ d_1^2 \\ d_1^3 \\ d_1^4 \\ d_2^1 \\ d_2^2 \\ d_2^3 \\ d_2^4 \end{bmatrix} \quad (86)$$

or

$$\mathbf{E} = \mathbf{B} \mathbf{d}_e \quad (87)$$

Here, the matrix \mathbf{B} contains the derivatives of the shape functions \mathbf{N} . To obtain the element stiffness matrix the principle of the virtual strains $\delta \mathbf{E}$ (refer to Section 2.1.5) is applied:

$$\delta \mathbf{E} = \mathbf{B} \delta \mathbf{d}_e. \quad (88)$$

Based on this principle the stiffness matrix (the second integral of Eq. (19)) together with the constitutive relations of this specific case (represented by the material elasticity tensor \mathbf{C}) is now formulated in its discretized form:

$$\int_{\Omega_s} \delta \mathbf{d}_e^T \mathbf{B}^T \mathbf{C} \mathbf{B} \mathbf{d}_e d\Omega_s. \quad (89)$$

Similar to this procedure the element load vector $\hat{\mathbf{t}}$ representing the surface loads is obtained. Therefore, the fourth integral of Eq. (19) of the principle of virtual displacements is discretized.

Here, again the shape functions \mathbf{N} already defined for the displacement field are used to obtain:

$$\hat{\mathbf{t}} = \mathbf{N} \mathbf{t}_e. \quad (90)$$

The relation of the virtual displacement field combined with the virtual nodal displacements according to Eq. (81):

$$\delta \mathbf{d} = \mathbf{N} \delta \mathbf{d}_e \quad (91)$$

define the integral of the element load vector:

$$\int_{\Gamma_s} \delta \mathbf{d}_e^T \mathbf{N}^T \mathbf{N} \mathbf{t}_e d\Gamma_s. \quad (92)$$

The discretized form of the principle of virtual displacement is now given by:

$$\bigcup_{e=1}^n \left\{ \int_{\Omega_s} \delta \mathbf{d}_e^T \mathbf{B}^T \mathbf{C} \mathbf{B} \mathbf{d}_e d\Omega_s - \int_{\Gamma_s} \delta \mathbf{d}_e^T \mathbf{N}^T \mathbf{N} \mathbf{t}_e d\Gamma_s \right\} = 0. \quad (93)$$

The two-dimensional structure is discretized into n finite elements. The sum over all elements defines the entire stiffness matrix. Due to the arbitrary components of the virtual displacement $\delta \mathbf{d}$ the linear system of equation is given by:

$$\bigcup_{e=1}^n \left\{ \int_{\Omega_s} \mathbf{B}^T \mathbf{C} \mathbf{B} d\Omega_s \right\} \mathbf{d} = \bigcup_{e=1}^n \left\{ \int_{\Gamma_s} \mathbf{N}^T \mathbf{N} d\Gamma_s \right\} \hat{\mathbf{t}}. \quad (94)$$

This equation in its simplified form is already given at the beginning of this paragraph as Eq. (77). In the present formulation \mathbf{K} denotes the stiffness matrix and is defined by:

$$\mathbf{K} = \bigcup_{e=1}^n \mathbf{k}_e = \bigcup_{e=1}^n \left\{ \int_{\Omega_s} \mathbf{B}^T \mathbf{C} \mathbf{B} d\Omega_s \right\}. \quad (95)$$

Similarly, the load vector \mathbf{F} is given by:

$$\mathbf{F} = \bigcup_{e=1}^n \left\{ \int_{\Gamma_s} \mathbf{N}^T \mathbf{N} d\Gamma_s \right\} \hat{\mathbf{t}}. \quad (96)$$

Based on the solution of the system of equations (in this thesis an iterative preconditioned conjugated gradient solver (PCG, implicit) is applied) the deformation state of the structural system is known. Now, the second PIOLA-KIRCHHOFF stress tensor \mathbf{S} is calculable based on the material law:

$$\mathbf{S} = \mathbf{C} : \mathbf{E}. \quad (97)$$

Here, \mathbf{C} denotes the already discussed fourth-order material elasticity tensor. Equation (87) substituted into Eq. (97) yields the discretized stress-deformation relation:

$$\mathbf{S} = \mathbf{C} : \mathbf{B} \mathbf{d}_e. \quad (98)$$

Similar to this simple two-dimensional example more complex finite-element analyses are performed. In these cases often three-dimensional element formulations are used and the linear shape functions are substituted by quadratic approaches to improve the accuracy of the results and to enable the computation of more complicated phenomena (e.g., non-linear problems like hyperelasticity).

5.1.1. Element formulations

In general, there are three groups of elements used in finite-element analysis (FEA). Line elements like springs, bars and flexures are used for a one-dimensional analysis, planar elements like triangular elements and rectangular elements are applied in a two-dimensional analysis such as membrane applications. Finally, a three-dimensional analysis is performed based on solids and plates formulated as pentahedral, hexahedral and tetrahedral elements. For each element group various types are formulated according to their specific application in the FEA.

For example, in the present thesis the second-order accurate SOLID186-brick-element is applied (Zienkiewicz, 1977; ANSYS, 2011c). This element is defined by 20 nodes having three degrees of freedom per node (translations in the nodal x , y , and z -directions) and uses triquadratic shape functions. The element supports plasticity, hyperelasticity, creep, stress stiffening, large deflections, and large strain capabilities. It has also capabilities for simulating deformations of nearly incompressible elastoplastic materials and fully incompressible hyperelastic materials. The geometry, node locations, and the element coordinate system for this element are shown in Fig. 48.

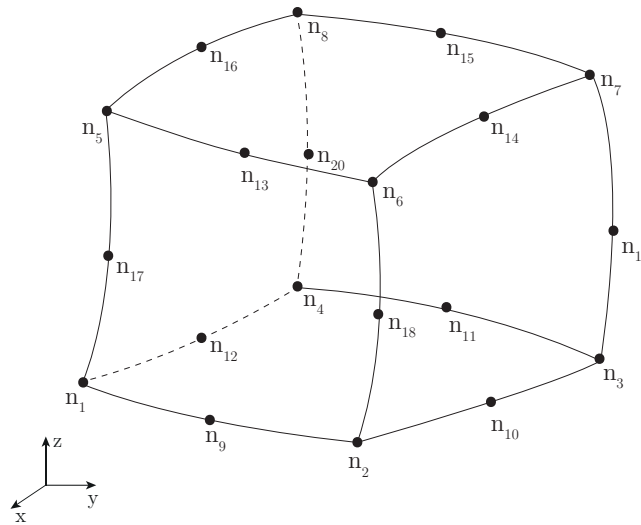


Figure 48: SOLID186 element (Zienkiewicz, 1977).

5.1.2. Temporal discretization

For the temporal discretization of the structures motion/deformation a NEWTON-RAPHSON iteration method of first-order accuracy (ANSYS, 2011c) is used in the present work. In this method an iteration procedure attempts to drive the solution to the equilibrium at each load increment l_n .

The example exhibited in Fig. 49a shows four equilibrium iterations (l_1 to l_4) in a NEWTON-RAPHSON iterative solution for one time step Δt . Based on the initial configuration of the

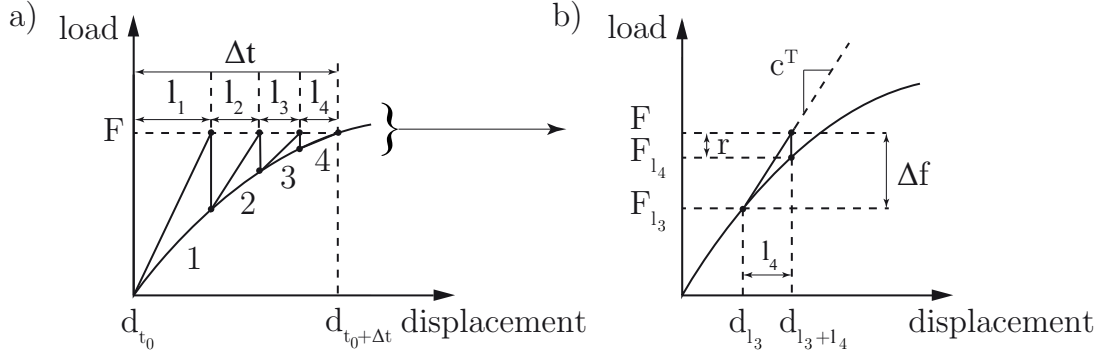


Figure 49: NEWTON-RAPHSON scheme.

structure d_{t_0} at t_0 , the tangent stiffness c^T is computed. Then the displacement increment Δd is predicted based on the load \mathbf{F} , and the structural configuration is updated to $\mathbf{d}_{t_0+l_n}$. Afterward, the internal forces (element forces) are again computed in the updated configuration in the next load increment l_n . In Fig. 49b the last load increment of this time step iteration is depicted. The residual \mathbf{r} is the termination condition for the present time step and is calculated by $\mathbf{r} = \mathbf{F}_{l_3+l_4} - \mathbf{F}_{l_3}$. If the residual \mathbf{r} drops below a predefined tolerance, the NEWTON-RAPHSON iteration is terminated and an equilibrium solution for this time step is obtained.

5.2. Computational fluid dynamics

5.2.1. Spatial discretization

For the transformation of the governing equations of fluid mechanics (Eq. (27), refer to Section 2.2) into numerically solvable equations the finite-volume method (FVM) in combination with integration rules and interpolation schemes is used. While the FEM method uses finite elements to discretize the physical space, the FVM applies finite volumes for the discretization of the fluid domain. For this purpose the aforementioned governing equations of fluid mechanics are transferred into the integral form. The formulation of the integrals is based on the predefined finite volumes (or control volumes) including volume and surface integrals. The advantage of the FVM is the automatic conformance of the conservation equations and the applicability of arbitrary finite control volumes. In general, the conservation equation of an arbitrary flow quantity Φ (e.g., the velocity $\Phi = \mathbf{u}$ or $\Phi = 1$ for mass conservation) of an incompressible flow on a time-dependent grid is given by:

$$\frac{d}{dt} \int_{V(t)} \rho \Phi dV + \int_{S(t)} \rho (\mathbf{u} - \mathbf{u}_g) \Phi dS - \int_{S(t)} \left(\Gamma_\Phi \frac{\partial \Phi}{\partial \mathbf{x}} \right) dS = \int_{V(t)} q_\Phi dV. \quad (99)$$

The volume integral on the left-hand side of Eq. (99) describes the local change of Φ within the control volume. The first surface integral marks all convective and grid-movement induced fluxes over the boundaries of the control volume, whereas the second surface integral takes all diffusive fluxes over the boundaries into account. Finally, the volume integral on the right-hand side of Eq. (99) takes the influence of possible source terms into account. As already mentioned the fluid domain is divided into small three-dimensional control volumes. This decomposition can be done using either structured or unstructured grids. In this thesis only block-structured grids are used. Thus, the following considerations are related to hexahedral cells. Every

hexahedral cell has six surfaces (north, south, west, east, top and bottom), which form the boundaries of the finite volume. Using a cell-centered variable arrangement the quantities of the flow are determined in the centroid of every cell in the fluid domain. To compute the fluid flow, the volume and surface integrals of Eq. (99) are approximated applying the cell-centered nodes. The volume integrals are approximated by the average value of the integrand q_Φ stored in the cell center and the discrete volume δV of the cell (mid-point rule). Using the known value of the integrand q_Φ at the mid-point P as an approximation for the average value \bar{q}_Φ the mid-point rule reads:

$$\bar{q}_\Phi = \frac{1}{\delta V} \int_V q_\Phi dV \quad \rightarrow \quad \int_V q_\Phi dV = \bar{q}_\Phi \delta V \approx q_{\Phi,P} \delta V. \quad (100)$$

If the integrand q_Φ shows a constant or linear behavior within the control volume, this approximation is exact. In all other cases the relation represents an approximation of second-order accuracy. The approximation of the surface integral of the hexahedron is given by the integration over each side denoted north, south, west, east, top and bottom, respectively:

$$\int_S \mathbf{f} \cdot \mathbf{n} dS = \sum_{k=(n,s,w,e,t,b)} \int_{S_k} \mathbf{f}_k \cdot \mathbf{n}_k dS_k = \sum_{k=(n,s,w,e,t,b)} \mathbf{F}_k. \quad (101)$$

The scalar product of the convective and diffusive fluxes \mathbf{f} with the normal vector \mathbf{n}_k related to the surface k results in the flux components normal to the corresponding surface. Similar to the volume integral the approximation of the surface integral is done by the mid-point rule. The application of the mid-point rule to the north side is expressed by:

$$\int_{S_n} \mathbf{f}_n \cdot \mathbf{n}_n dS_n = \bar{f}_n S_n \approx f_n S_n = F_n. \quad (102)$$

In most cases the values on the boundaries of the surfaces are not known. Therefore, an appropriate interpolation method is required. The convective and diffusive fluxes contained in the surface integral are treated separately. The convective flux over the northern side F_n^c is described by:

$$F_n^c = (\rho \mathbf{u} \Phi)_n \cdot S_n. \quad (103)$$

The variables at the mid points of the cell faces (here: n) are interpolated on this surface S_n . This approximation results in an interpolation error that occurs because the obtained values do not correspond to the exact average values on the cell faces. Starting point for a suitable interpolation method is a polynomial that approximates the distribution of the flow variable. In most methods a polynomial of first order is applied, which describes a linear distribution of the variable:

$$\Phi(x) = a_0 + a_1(x - x_p). \quad (104)$$

Based on two supporting nodes, where the variable values are known, the constants a_0 and a_1 and finally the variable value Φ_n on the northern surface is determined, respectively.

The approximation of the diffusive fluxes is done in a similar manner but also includes an

approximation of a first derivative using the polynomial approach. The polynomial of first order combined with the mid-point rule results in an overall spatial accuracy of second order.

In general, several different spatial discretization schemes (e.g., central, backward, upwind) are possible based on the alignment and amount of the applied supporting nodes. All methods show advantages and disadvantages in terms of effort, stability and accuracy.

In the present thesis the fluid computations are performed using hexahedral elements which apply linear interpolation methods for the nodes. The spatial discretization uses a high-resolution scheme. This scheme corresponds to an automatic numerical treatment of the advection terms, switching between a second-order accuracy at locations where the gradient is rather low, to a first-order scheme where the variations are getting sharper to increase the robustness of the computation.

In general, the schemes implemented in ANSYS[®] CFX can be cast in the form:

$$\Phi_f = \Phi_u + \beta \nabla \Phi \cdot \Delta \mathbf{r}. \quad (105)$$

Here, Φ_f is the unknown quantity, Φ_u its known value at the upwind node, β is a blending factor of the different advection schemes, $\nabla \Phi$ marks the gradients and $\Delta \mathbf{r}$ describes the vector from the upwind node u to node f . Based on β different discretization schemes are utilized ($\beta = 0$ yields a first-order upwind differencing scheme (UDS), $\beta = 1$ yields a central differencing scheme (CDS)). The upwind differencing scheme is very robust, but it will introduce diffusive discretization errors that tend to smear out the steep spatial gradients. The central differencing scheme is unbounded and may introduce dispersive discretization errors that tend to cause non-physical oscillations in regions of rapid solution variations. The applied high-resolution scheme (HRS) uses a nonlinear equation for the determination of β at each node (based on the boundedness principles introduced by Barth and Jespersen (1989)), computed to be as close to unity as possible without introducing new extrema. The advective flux is then evaluated using the values of β and $\nabla \Phi$ from the upwind node while the control volume gradients $\nabla \Phi$ at the nodes are calculated by using:

$$\nabla \Phi = \frac{1}{V} \sum_f (\Phi \Delta \mathbf{n})_f \quad (106)$$

where $\Delta \mathbf{n}$ is the outward surface normal vector at f and Φ is evaluated by an appropriate interpolation method. The HRS methodology involves first computing a Φ_{\max} and Φ_{\min} at each node using a stencil involving adjacent nodes (including the node itself). Next, for each integration point around the node, Eq. (105) is solved for a preliminary determination of β to ensure that the value of Φ does not undershoot Φ_{\min} or overshoot Φ_{\max} . The nodal value for β is calculated by a limiter equation (Barth and Jespersen, 1989) and is taken to be the minimum value of all integration point values surrounding the node f and is also not permitted to exceed unity (ANSYS, 2011a).

5.2.2. Temporal discretization

Due to the temporal dependency of most flow problems induced for example by turbulence effects or vortical structures, an additional time discretization is necessary. Owing to the parabolic character of the governing equations in time, a time-stepping scheme is applied. The computed solution of the flow quantity $\Phi(t_0)$ at an initial time t_0 is used to estimate the following state of $\Phi(t_0 + \Delta t) = \Phi(t_1) = \Phi^1$ after the time step Δt . Based on this solution the next time step is predicted. A general formulation of this procedure for a simple ordinary differential equation $d\Phi/dt = f$ reads as follows:

$$\int_{t_n}^{t_{n+1}} \frac{d\Phi(t)}{dt} dt = \int_{t_n}^{t_{n+1}} d\Phi(t) = \Phi^{n+1} - \Phi^n = \int_{t_n}^{t_{n+1}} f(\Phi(t), t) dt \quad (107)$$

In CFD simulations often two-level methods are used for the temporal integration. Therefore, the value of Φ^{n+1} is approximated by a linear interpolation of the function $f(t, \Phi(t))$ between the time steps t_n and t_{n+1} .

$$\Phi^{n+1} = \Phi^n + [(1 - \alpha)f(\Phi^n, t_n) + \alpha f(\Phi^{n+1}, t_{n+1})] \Delta t. \quad (108)$$

With the specification of the parameter α the integration method (e.g., explicit EULER with $\alpha = 0$, implicit EULER with $\alpha = 1$ or CRANK-NICOLSON method $\alpha = 0.5$) is determined. The unsteady computations discussed in the present work applies the implicit backward EULER method of second-order accuracy defined by:

$$\Phi^{n+1} = -\frac{1}{3}\Phi^{n-1} + \frac{4}{3}\Phi^n + \frac{2}{3}f(\Phi^{n+1}, t_{n+1})\Delta t. \quad (109)$$

Based on this method the value Φ^{n+1} to be determined is dependent on itself. Therefore, an iterative solution method is necessary. The advantage of this scheme is that the numerical stability of the implicit time integration method is almost independent on the time step size Δt .

5.2.3. Discretization of grid movement

To predict the interaction between both physical domains a precise motion of the computational grid is necessary. Here the already mentioned space conservation law (SCL) or geometric conservation law (GCL, refer to Section 2.5) assures that within a change of the position or the shape of a control volume no space is lost within the computational grid. Similar to the spatial and temporal discretization of the fluid domain also the grid motion has to be discretized (Ferziger and Peric, 2002). By selecting the method for the computation of the grid velocity \mathbf{u}_g the accuracy and compliance with the SCL is prescribed.

The positions of the grid nodes $\mathbf{x}^0, \dots, \mathbf{x}^{n-1}, \mathbf{x}^n, \mathbf{x}^{n+1}$ are only known for the discrete time steps $t_0, \dots, t_{n-1}, t_n, t_{n+1}$. Therefore, the grid velocity \mathbf{u}_g in Eq. (99) has to be determined based on these values. In Farhat et al. (2001), Förster (2007) and Lesoinne and Farhat (1996) a backward-differencing scheme of first-order accuracy and a central differencing scheme of second-order accuracy are proposed. The first-order scheme is given by:

$$\mathbf{u}_g = \frac{\mathbf{x}^{n+1} - \mathbf{x}^n}{\Delta t} \quad (110)$$

and the second-order scheme is proposed as:

$$\mathbf{u}_g = \frac{3\mathbf{x}^{n+1} - 4\mathbf{x}^n + \mathbf{x}^{n-1}}{2\Delta t}. \quad (111)$$

Based on these discretization schemes the grid velocity generally does not satisfy the SCL. Thus, an alternative is required. In the discretized form the SCL is expressed by the swept volumes of the corresponding cell faces (e.g., six surfaces for a three-dimensional hexahedral control volume). While the prediction of extra grid fluxes is not necessary for the mass conservation equation in the context of moving grids, the additional grid fluxes in the momentum equation have to be consistently determined by applying the SCL in its discrete form (discrete geometric conservation laws, DGCL) (Farhat et al., 2001; Breuer et al., 2012). By computing the swept volumes split up into six tetrahedral contributions defined by the known cell face positions at each time step, these errors can be avoided (Ferziger and Peric, 2002). For the present work no information are available which discretization scheme is applied in ANSYS[®] CFX for the mesh velocity. The methodology for the mesh motion is described in Section 5.4.

5.2.4. Flow modeling near the wall

For a realistic prediction of the flow situation the boundary layers (refer to the short introduction in Section 2.4) have to be considered in the computational fluid dynamics model as well. Often the computational grid is refined towards the walls to increase the spatial resolution in the boundary layer. Based on this refinement the small-scale effects can be resolved and an appropriate prediction of the wall-bounded flow is achieved. Unfortunately, an unreasonably large amount of grid nodes in this region is necessary for a physically realistic prediction followed by excessive computational costs. Therefore, mathematical functions (denoted wall functions) are applied to approximate the velocity profile in the boundary region. Based on this approach the amount of grid nodes near the wall can be reduced leading to reduced computational costs but nevertheless acceptable approximation errors. The turbulent wall-function approach in the applied fluid solver ANSYS[®] CFX (ANSYS, 2011a) is an extension of the method of Launder and Spalding (1974). It is based on the already mentioned logarithmic law of the wall (von Kàrmàn, 1930) which describes that the average velocity of a turbulent flow at a certain point in the boundary layer is proportional to the natural logarithm of the distance from that point to the wall. Furthermore, in regions where the logarithmic law of the wall can be applied, the near-wall tangential velocity is related to the wall-shear stress τ_w by means of a logarithmic relation (ANSYS, 2011a). In the present wall-function approach the viscosity related sublayer region is approximated by empirical equations to provide the near-wall boundary conditions for the mean flow and the turbulence transport equations. These equations connect the wall conditions (for example, the wall-shear-stress) to the dependent variables at the near-wall mesh node, which is presumed to be in the fully-turbulent region of the boundary layer. The velocity distribution near the wall based on the logarithmic law of the wall is given by:

$$u^+ = \frac{U_t}{u_\tau} = \frac{1}{\kappa} \ln(y^+) + C \quad (112)$$

with the relations for y^+ :

$$y^+ = \frac{\rho_f \Delta y u_\tau}{\mu_f} \quad (113)$$

and the shear-stress velocity u_τ :

$$u_\tau = \left(\frac{\tau_w}{\rho_f} \right)^{1/2}. \quad (114)$$

In these equations u^+ denotes the near-wall velocity, u_τ describes the friction velocity, U_t is the known tangential velocity at a distance of Δy from the wall, y^+ denotes the dimensionless distance from the wall, τ_w is the wall-shear stress, κ marks the von Kàrmàn constant and C is a logarithmic-layer constant depending on the wall roughness (here the walls are assumed to be smooth which leads to $C \approx 5.1$). In the present work a special concern is put on y^+ in the mesh generation. The first cell near the wall is always in a sufficient distance that y^+ is always above 25. That means that the viscous sublayer is not intended to be resolved and no further approximations (such as provided by ANSYS[®] CFX with scalable and automatic wall functions (ANSYS, 2011a)) are necessary.

5.3. Coupling method

The numerical predictions in this thesis are carried out with the commercial multi-physics environment ANSYS[®]-CFX 14.0. The whole software is based on a partitioned approach of several modules covering the most important physical domains in engineering like structure and fluid mechanics, thermodynamics, electromagnetics and acoustics. By connecting a module with another one, a system coupling is created. Each module possesses a highly specialized solver for the specific physical domain. Based on the discretization in each module the boundary conditions of the different physical domains are defined. Depending on the system coupling (implicit, explicit or weak/strong coupling³) and the time discretization (steady or unsteady) several coupling schemes are possible (ANSYS, 2011b).

In the present case of strongly coupled vortex-induced fluid-structure interactions, an implicit unsteady strong coupling of the structural solver ANSYS[®] Mechanical 14.0 and the flow solver CFX 14.0 is applied. Within a global time step t_n of the FSI problem the interfacial boundary conditions are exchanged between the fluid (finite-volume: CFX) and the structural solver (finite-element: ANSYS[®] Mechanical) several times. Each force and displacement transfer marks the beginning of a new coupling iteration (see coupling scheme in Fig. 50). In every coupling iteration the inner CFD and CSD iterations based on the updated boundary conditions and the previously determined solution are carried out until their individual convergence criteria are reached. After that the transfer of the boundary conditions re-initiates a new coupling step.

³The coupling depends on the physical interactions between both domains. In a one-way coupled system only one physical domain is affected by the interaction. Weakly coupled systems are defined as two-way interactions as the fluid and structural domains fully interact with each other but perform only one fixed-point iteration per time step. Strongly coupled systems are also denoted two-way interactions but require inner iteration loops to fulfill a prescribed convergence criterion in each time step.

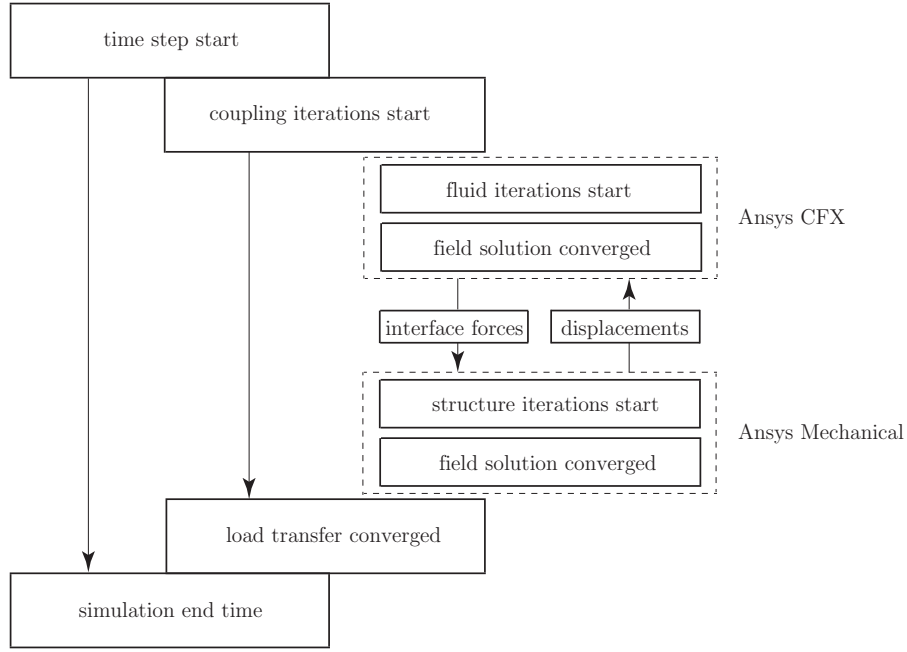


Figure 50: Coupling scheme of the FSI procedure in ANSYS®.

The variables exchanged between the two solvers are the predicted fluid forces on the FSI interface and the resulting displacements of the structure also at the interface. The implicit coupling between both solvers demands an underrelaxation of these variables to accelerate and stabilize the convergence of the coupled predictions. This is done as follows:

$$\mathbf{F}_s^{c_n} = \mathbf{F}_s^{c_{n-1}} + \alpha_F (\mathbf{F}_f^{c_n} - \mathbf{F}_s^{c_{n-1}}) \quad (115)$$

$$\mathbf{d}_f^{c_n} = \mathbf{d}_f^{c_{n-1}} + \alpha_d (\mathbf{d}_s^{c_n} - \mathbf{d}_f^{c_{n-1}}) \quad (116)$$

The transferred load $\mathbf{F}_s^{c_n}$ at the new coupling iteration c_n is determined as a combination of the old solution $\mathbf{F}_s^{c_{n-1}}$ and the newly calculated fluid solution $\mathbf{F}_f^{c_n}$ depending on the underrelaxation factor $0 < \alpha_F < 1$. Similar to this procedure the underrelaxation of the displacement $\mathbf{d}_f^{c_n}$ with $0 < \alpha_d < 1$ is processed. In the computations carried out in the present work only the force transfer is underrelaxed by $\alpha_F = 0.5$.

Often different mesh sizes and mesh types are used for the fluid and the structure discretization on the FSI interface. The ANSYS® environment handles these mismatched meshes between ANSYS® Mechanical and ANSYS® CFX by two different interpolation methods which map the transferred data from one mesh onto the other. For the displacements sent from the structural solver to the fluid solver a profile preserving interpolation (Koci and Milovanovi, 1997) is used. This method takes the profile of the variable (here, the displacements) of the structure mesh, and maps it to the fluid mesh. The force transfer from the fluid solver to the structure solver is done by a conservative interpolation scheme (Cadafalch et al., 1999) that ensures that the total force is passed across the interface. In both interpolation procedures the bucket search method (Jansen et al., 1992) is used as the mapping algorithm (ANSYS, 2011c).

5.4. Mesh movement

In order to account for the boundary deformation \mathbf{d}_{mesh} of the fluid mesh, the governing equations for the fluid are recast in an Arbitrary Lagrangian-Eulerian description (ALE, see Section 2.5) in ANSYS[®] CFX, where the fluid mesh deformation is determined based on a diffusion model. The moving mesh is faced with the requirement to conserve the grid quality after the mesh deformation on the one hand and the perpetuation of the local grid resolution (e.g., boundary layer refinement) on the other hand. Therefore, appropriate methods are necessary to avoid squeezed element angles, mesh overlaps or negative volumes. Folded or negative control volumes are fatal in any case, since they lead to an immediate termination of the solution process. ANSYS[®] CFX uses the "Displacement Diffusion Model" (similar models are proposed by Löhner and Yang (1996), Bathe et al. (1999) and Robertson and Sherwin (1999)) for the calculation of the mesh motion based on the displacements provided at the FSI interface. This method is based on the solution of three LAPLACE equations (one for each CARTESIAN components (x, y, z)) of the relative grid displacements $\Delta \mathbf{r}_{\text{mesh}} = \mathbf{r}_{\text{mesh,new}} - \mathbf{r}_{\text{mesh,old}}$ at each coupling step iteration. Here, $\mathbf{r}_{\text{mesh,new}}$ marks the previously determined mesh displacements, $\mathbf{r}_{\text{mesh,old}}$ denotes the newly calculated mesh displacements, where $\Delta \mathbf{r}_{\text{mesh}}$ corresponds to the mesh alternation between both states. The mesh motion formulation is given by:

$$\nabla \cdot (\zeta(\mathbf{x}) \nabla \Delta \mathbf{r}_{\text{mesh}}) = 0. \quad (117)$$

With Dirichlet boundary conditions (e.g., displacement of the FSI interface $\mathbf{r}_{\text{mesh}} = \mathbf{d}_s$ or stationary walls with $\Delta \mathbf{r}_{\text{mesh}} = 0$) and Neumann boundary conditions (no specified displacement in normal direction $\mathbf{n} \cdot \partial \Delta \mathbf{r}_{\text{mesh}} / \partial \mathbf{x} = 0$) the solution of Eq. (117) leads to the mesh displacement $\Delta \mathbf{r}_{\text{mesh}}$ in the inner domain. The mesh stiffness $\zeta(\mathbf{x})$ regulates the mesh deformation with the purpose of low mesh distortions. Furthermore, it is important to hold the relative node movements in certain critical areas (e.g. the refinement of the boundary layers close to the structure) as small as possible, while the necessary deformations are preferably "widely" distributed in the far-field. The formulation of $\zeta(\mathbf{x})$ as a constant, linear, parabolic or hyperbolic function depends on its position \mathbf{x} and thus distributes the mesh stiffness in different manners. For example, a constant $\zeta(\mathbf{x})$ refers to an unweighted mesh stiffness and thus mesh deformations in critical regions are possible. Contrariwise, a hyperbolic formulation can be used to increase the mesh stiffness close to the FSI interface and to transport the mesh deformation into the undisturbed flow. For the recent computations a specific hyperbolic approach is applied to control the mesh stiffness in the fluid domain depending on the wall distance $h(\mathbf{x})$:

$$\zeta(\mathbf{x}) = \left(\frac{1}{h(\mathbf{x})} \right)^c \quad (118)$$

This relationship provides an exponential increase of the mesh stiffness as the distance from the nearest boundary decreases. The stiffness model exponent c determines how strong this increase occurs and is chosen case-to-case (in the present work values from $c = 0.7$ to 0.9 delivered satisfying mesh deformations).

5.5. Validation of the coupling scheme

Several benchmarks were considered to validate the coupling of the structural solver ANSYS[®] Mechanical and the fluid solver ANSYS[®] CFX. ANSYS[®] itself published three validation studies concerning their coupling procedure in Menter et al. (2006). The first validation test case applied the flexible wall FSI benchmark by Menter et al. (2006) already mentioned in Section 1.2. The prediction shows a good agreement for three different grid resolutions in comparison to the analytical solutions of Wang (1999). The second test case consists of a rigid cylinder mounted in a spring-damper system (Fig. 51). It offers a direct comparison to similar experimental studies of Khalak and Williamson (1996). This test case was chosen to validate the mesh movement and the complex flow prediction of the coupled FSI problem. The flow around the cylinder ($Re = 10,000$) results in a vortex-induced vibration in cross-flow direction. The boundary layer on the cylinder is still laminar, although the wake is fully turbulent. To take the turbulent flow into account a RANS-based turbulence model is applied. For lower fluid velocities the results of the two-dimensional simulations were in agreement with the experiments of Khalak and Williamson (1996). With increasing inflow velocities the solution yields a slight overprediction of the peak amplitudes of the swiveling cylinder. The third validation study is compared with the "two-sided mounted tension riser towed through a water channel" test case of Chaplin et al. (2005a,b) (again refer to Section 1.2). The fully coupled three-dimensional RANS-based simulations of Menter et al. (2006) of this case show the grid dependencies of the predictions. Nevertheless, the predictions show qualitative agreement with the experiments, but especially the riser displacements in main flow directions are strongly underpredicted. Higher grid resolutions and an improved modeling of all physical effects are suggested for a more precise computation. Due to the limitations of the experiments to the structural deformation of the riser, no further validations on the fluid flow are feasible.

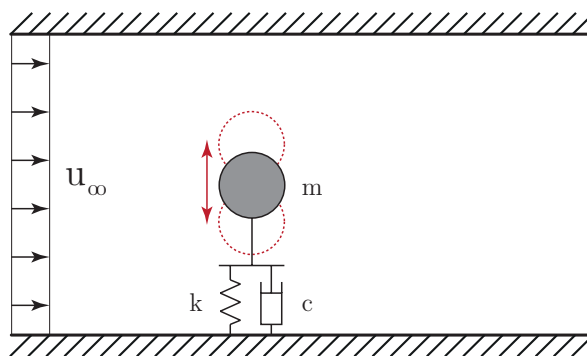


Figure 51: Elastically mounted rigid cylinder released in cross-flow direction FSI benchmark by Menter et al. (2006).

In Hübner and Seidel (2007) the mentioned benchmark of Turek and Hron (2006) is numerically investigated using ANSYS[®]-CFX. It is stated that the convergence behavior of the coupled solution strongly depends on the density ratio of the structure and the fluid, the time step size, the convergence limits and the relaxation parameters. Especially for the case of a high density ratio of the fluid in relation to the structure, the added-mass effect causes strong convergence problems. They recommended a precise determination of the applied coupling settings by try-and-error in order to obtain an efficient and converging solution method (in terms

of underrelaxation factors, mesh motion properties and coupling step iteration parameters). Similar suggestions are stated in Schildhauer (2011).

In the thesis of Schildhauer (2011) the benchmark of Turek and Hron (2006) is considered again based on the coupling of ANSYS[®] Mechanical and ANSYS[®]-CFX, but also the pure structure and fluid solver test cases are computed. With reference to the data of Turek and Hron (2006) the predictions of the test case FSI1 yield moderate deviations of the tip displacements ($\text{error}(\Delta x) = -6.8\%$, $\text{error}(\Delta y) = -0.1\%$) and almost matching lift and drag forces ($\text{error}(f_d) = 0\%$, $\text{error}(f_l) = -0.1\%$) of the entire moving structure were found. The predictions of the test case FSI3 presents a similar impression. Here, the tip displacements are again slightly under-predicted ($\text{error}(\Delta x) = -6.3\%$, $\text{error}(\Delta y) = -1.1\%$) and the lift and drag forces ($\text{error}(f_d) = 5.5\%$, $\text{error}(f_l) = -1.3\%$) are in a good agreement with the reference data. As a further proof of the prediction capabilities of the coupled ANSYS[®] solvers, Schildhauer (2011) presents FSI predictions of more complex geometries and FSI problems. An interaction of a rigid structure with an air flow is predicted on the basis of the well-known TACOMA NARROWS bridge destruction. In 1940, this bridge collapsed as the result of aeroelastic torsional flutter effects because of large cross-wind speeds. The simulation confirms the fatal swaying as a self-induced aeroelastic phenomenon and not due to the resonance with the inevitably generated VON KÀRMÀN vortex street. Another FSI example is presented by Schildhauer (2011) with the simulation of an air-damped plate vibration, which allows the validation of the coupling method in the context of a comparison with an experimentally measured decay curve. Especially the time step size is found to be important to achieve prediction results that agree with the experimental values.

In summary, the coupled solver in ANSYS[®] was already validated by a variety of different test cases. Nevertheless, a full comparison of numerical data to experimental flow and structure measurements in the turbulent regime is still missing.

6. Definition of the benchmark cases

In Section 3 several excitation mechanisms of FSI phenomena are introduced. The benchmarks of Gomes and Lienhart (2010), Gomes et al. (2010), Gomes and Lienhart (2013) and Turek and Hron (2006) mentioned in Section 1.2 as well as the test cases presented in this thesis are based on the instability-induced and movement-induced excitation mechanisms. For all test cases investigated the periodic vortex shedding at the bluff body seems to be responsible for the oscillations of the structure. Hence, the vortex shedding at circular bodies will be described in the following paragraphs before the test cases investigated in this thesis are explained and defined in detail.

6.1. Flow phenomena past bluff bodies

In fluid dynamics, vortex shedding describes an oscillating flow (liquid or gas) that appears when a fluid passes a bluff (cylindrical) body. In this flow, large rotating flow structures (vortices) are generated at the back of the body and detach periodically from either side of the body. A result of the vortex shedding is the VON KÄRMÄN vortex street which strongly depends concerning its appearance, size and dynamics on the geometry of the bluff body and the present flow conditions (laminar/turbulent regime, fluid properties). Vortex shedding at cylindrical bodies starts at about a Reynolds number of $Re \approx 40$ (refer to Fig. 53). In this case, the alternating interactions between the two separating shear layers result in the formation of vortices which grow and are fed by the circulation from their connected shear layers. Due to the counter-rotating vorticity the vortex is cut off, shed and convected downstream. At the same time the formation of a new vortex on the opposite side of the bluff body begins and leads to a periodic flow pattern in the wake. The determining factor of the wake characteristics is the place where the transition from the laminar to the turbulent regime takes place. For the common example of the flow around a circular cylinder (Breuer, 2002) a distinction is made between the transition in the wake (TrW, Fig. 52a, $Re = 180 - 400$), the transition in the free shear layer (TrSL, Fig. 52b, $Re = 400 - 100,000$), the transition in the boundary layer (TrBL, Fig. 52c and d, $Re = 100,000 - 600,000$) and the fully turbulent flow case with $Re > 600,000$ (turbulent conditions are present in the boundary layer and the wake). Typically the occurring forces on the structure induced by the flow strongly depend on these different flow states and are partly responsible for the different FSI excitations.

In general, the major forces are a function of the shape of the structure. Circular cylinders experience the major fluctuating forces normal to the main flow direction with a frequency f_0 equal to the vortex shedding frequency f_s . In main flow direction the fluctuating forces are significantly smaller but are generated with a frequency which is twice as high as f_0 , since each vortex produces a drop in the pressure during its formation while a full cycle of the lift force includes two pressure drops. The dimensionless frequency, denoted Strouhal number St , is related to the vortex shedding at bluff bodies. Figure 53 shows the Strouhal number of a circular cylinder as a function of the Reynolds number. In the laminar regime the formation of the regular periodic two-dimensional vortex shedding is marked by a strong increase of the Strouhal number. With the cross-over to the three-dimensional turbulent vortex shedding,

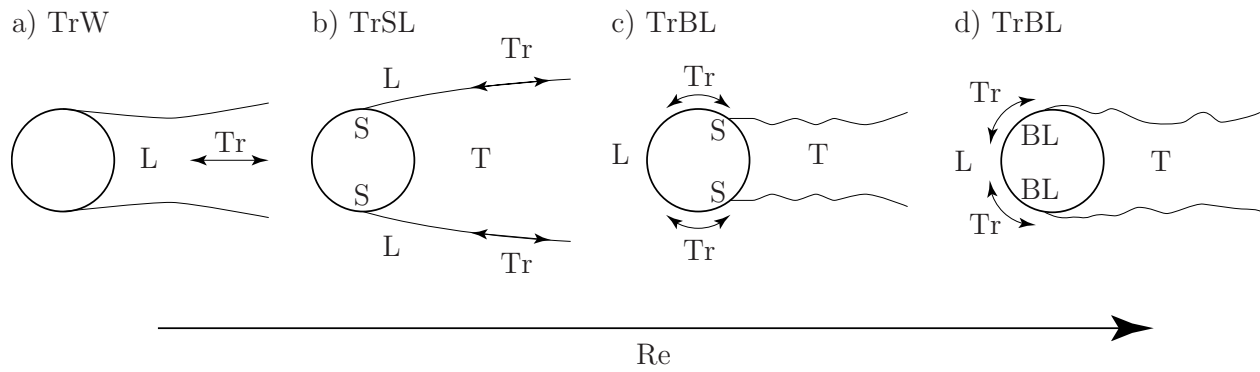


Figure 52: Flow around a cylinder: Different transition positions as a function of the Reynolds number according to Breuer (2002). L (laminar), T (turbulent), Tr (transition), S (separation), BL (boundary layer).

smaller scales of vortices are produced. The Strouhal number increases till $Re \approx 2000$ to a value of $St \approx 0.21$. For further increasing Reynolds numbers (TrSL, $Re = 400 - 100,000$) the transition takes place in the free-shear layer and affects the vortex shedding. Therefore, the Strouhal number decreases in this flow state to $St \approx 0.185$. With the transition in the boundary layers of the cylinder (TrBL, $Re = 100,000 - 600,000$) the Strouhal number increases again.

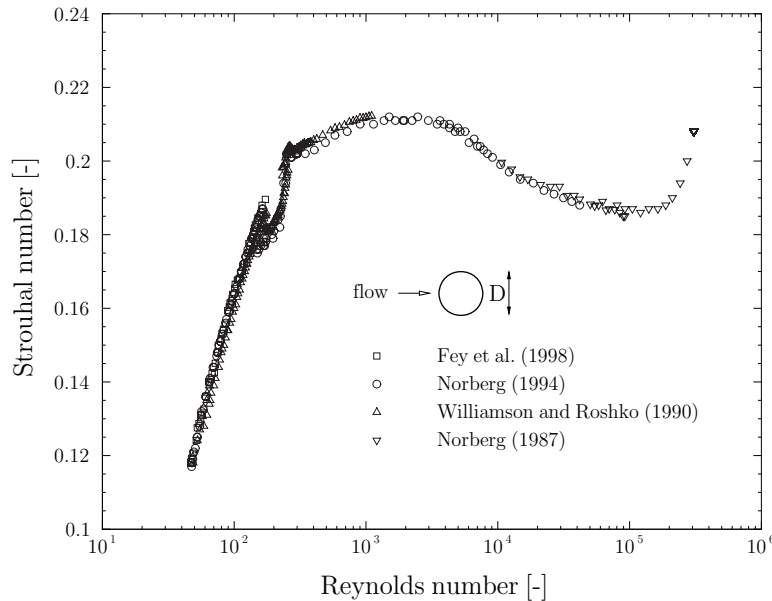


Figure 53: Strouhal number as a function of the Reynolds number for the flow around a circular cylinder (Gomes and Lienhart, 2013).

As already mentioned the vortex shedding phenomenon is related to several factors which are, e.g., the shape of the structure (aspect ratio, structure endings, flow blockage) the structure motions (deflection, swiveling mode) and the flow conditions (turbulence intensity, Reynolds number). To control aspects of the vortex formation splitter plates of different geometries in the wake of circular cylinders were investigated experimentally by Anderson and Szewczyk (1997). Based on hot-wire measurements and flow visualizations the influence of the plate length on the vortex shedding was reported. Several different regions related to the plate

length were identified for sub-critical flow conditions and compared with the reference case without an attached splitter plate ($St \approx 0.20$). For the present investigation only the last region for a length to diameter ratio above $l/D > 1.5$ is relevant. For this configuration it is reported that the splitter plate diminishes the shear layer interaction and the Strouhal number decreases progressively with l/D to values between $St \approx 0.18$ and 0.20 which is consistent with investigations of Apelt and West (1975). Furthermore, Apelt and West (1975) reported a mean drag coefficient for the front body of $\bar{c}_D = 0.8$. Despite the strong influence of the splitter plate on the shear layers at the upper and lower side the alternating vortex street is still formed (quasi-) periodically. Finally, it should be mentioned that both studies noted plate oscillations especially for larger ratios of $l/D > 1.5$. This is an indication of the extensive physical coupling of the vortex shedding to the FSI mechanisms.

6.2. Classification of the test cases

In the following paragraphs the test cases studied in this thesis are defined and explained concerning their geometry, material properties and flow conditions. In total, this thesis includes nine test cases which are investigated by experimental measurement techniques and numerical simulation methods. The test cases FSI-PfS-1*x* (1*a*, 1*b*, 1*c*) and FSI-PfS-2*x* (2*a*, 2*b*) are quasi two-dimensional test cases in the turbulent flow regime. The test cases FSI-PfS-3*x* (3*a*, 3*b*) possess a three-dimensional geometry and are also related to the turbulent regime. Finally the application-based test cases FSI-PfS-4*x* (4*a* and 4*b*) consist again of a three-dimensional geometry and are also investigated under turbulent flow conditions.

FSI-PfS-1*x* and FSI-PfS-2*x* are more or less derived from the experimental turbulent benchmark of Gomes and Lienhart (2010) and the numerical laminar benchmark of Turek and Hron (2006) which are already mentioned and described in the literature review in Section 1.2. In summary, in the test case of Gomes and Lienhart (2010) a very thin metal sheet with an additional weight at the end is attached behind a rotationally-mounted cylinder exposed to laminar and turbulent flows. Based on the different inflow velocities several periodic swiveling modes of the structural deformation are identified and proved the assumption of a strongly coupled movement-induced FSI excitation. The well-known benchmark of Turek and Hron (2006) consists of a fixed rigid cylinder with a flexible artificial rubber-like material attached to the back side. This purely numerical FSI benchmark in the laminar regime is designed for several discrete, parabolic inflow velocity profiles. The computation of this benchmark produces an almost periodic structural deflection in the second swiveling mode and displacements in the order of the cylinder diameter. Since the set-up and computation of this test case is rather simple compared to the Gomes and Lienhart (2010) benchmark and detailed integral data like the lift and drag forces are available, this test case is an often used validation case for various FSI prediction methods. However, the issue of the validation of a numerical prediction method by another numerical computation can be seen critically.

Using the set-up of Turek and Hron (2006), investigations towards the influence of the length and flexibility of the flexible splitter plate to the FSI phenomena are carried out by Lee and You (2013). Their numerical studies indicate that the drag and lift coefficients, the Strouhal number of the vortex shedding, and the magnitude of the tip displacements of the flexible splitter plate are found to be intricate functions of the plate flexibility. The obtained deflection

shapes of the flexible splitter plate are found to depend on the length of the plate, while the deflection magnitude is a function of the bending stiffness and thus the natural frequencies of the flexible plate. Furthermore, the Strouhal number of the vortex shedding and the frequency of the plate deflection was found to be difficult to estimate using the natural frequencies of the plate, which are calculated by inducing free vibration in vacuum. Lee and You (2013) explained this difference by the non-uniformly distributed fluid load over the plate in the FSI computations in contrast to the free vibration without any fluid loads in the modal analysis. The study suggests that the flexibility of the splitter plate, in general, adversely modulates the drag and lift forces acting on the cylinder surface while it promotes the oscillation of the plate.

6.3. General definitions of the test cases FSI-PfS-1x – FSI-PfS-3x

Bringing the advantages of the experimental turbulent benchmark of Gomes and Lienhart (2010, 2013) and the numerical laminar benchmark of Turek and Hron (2006) together the present test case definitions of FSI-PfS-1x, 2x and 3x are proposed to be a simpler FSI benchmark avoiding the disadvantageous features mentioned in Section 1.2. The structures of FSI-PfS-1x, 2x and 3x are installed in a water channel (see Fig. 54) and consist of a bluff body (cylinder or cone) and a flexible plate (with and without an additional steel weight) attached to it. All geometrically related variables are normalized by the cylinder diameter $D = 0.022$ m. The structures are positioned in the middle of the experimental test section with $H_c = H/2 = 0.120$ m ($H_c/D \approx 5.45$), where the test section denotes a central part of the entire water channel (see Fig. 32 in Section 4.1).

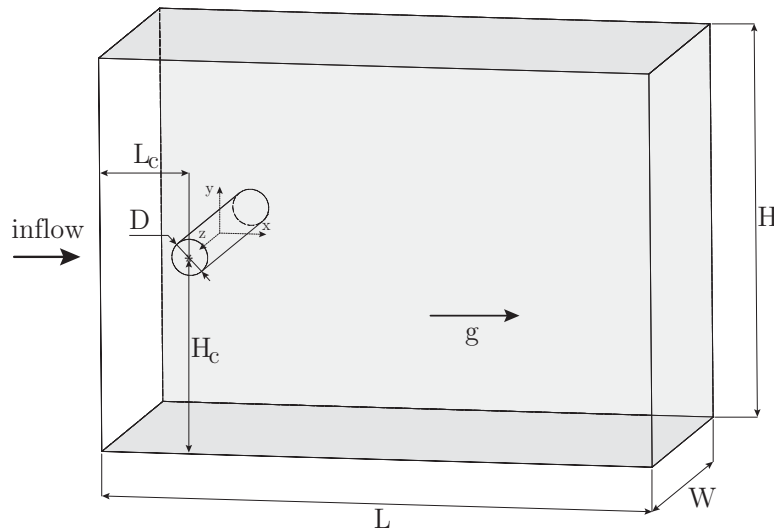


Figure 54: Sketch of the geometrical configuration of the channel (with an exemplary cylinder).

The center of the cylinder/cone is located at $L_c = 0.077$ m ($L_c/D = 3.5$) downstream of the inflow section. The flexible structures have a width of $w = 0.177$ m ($w/D = 8.05$). Therefore, in the experiments there is a small gap of about $1.5 \cdot 10^{-3}$ m between the side of the deformable structure and both lateral channel walls. The coordinate system is placed at the center of the cylinder in the middle of the cylinder/cone in spanwise direction. To avoid asymmetric effects in the flow or the structural deformation the gravitational acceleration g points in the streamwise x -direction (see Fig. 54), i.e., in the experimental set-up this section of the water channel is

Cylinder diameter	$D = 0.022$ m	
Cylinder center x -position	$L_c = 0.077$ m	$L_c/D = 3.5$
Cylinder center y -position	$H_c = H/2 = 0.120$ m	$H_c/D \approx 5.45$
Test section length	$L = 0.338$ m	$L/D \approx 15.36$
Test section height	$H = 0.240$ m	$H/D \approx 10.91$
Test section width	$W = 0.180$ m	$W/D \approx 8.18$
Width of flexible structure	$w = 0.177$ m	$w/D \approx 8.05$

Table 4: Geometrical quantities of the channel and the test case.

turned 90 degrees. FSI-PfS-1 x and FSI-PfS-2 x are developed as geometrically two-dimensional test cases, whereas FSI-PfS-3 x is a three-dimensional configuration.

6.3.1. Two-dimensional geometry without rear mass - FSI-PfS-1 x

Definition of FSI-PfS-1a

The benchmark case FSI-PfS-1a consists of a flexible rubber plate clamped behind a fixed rigid non-rotating cylinder (see Fig. 55). The cylinder has a diameter $D = 0.022$ m. The rubber plate used in the experiment has a length $l = 0.060$ m ($l/D \approx 2.72$), a width $w = 0.177$ m ($w/D \approx 8.05$) and a thickness $h = 0.0021$ m ($h/D \approx 0.10$). The inflow velocity is set to $u_{\text{inflow}} = 1.385$ m/s and relates to a Reynolds number $\text{Re} = 30,470$.

The material used for the flexible structure is an EPDM (ethylene propylene diene monomer) rubber with a density $\rho_{\text{EPDM}} = 1360$ kg m⁻³. In order to determine the material properties additional structural tests are carried out yielding a YOUNG'S modulus of $E_{\text{EPDM}} = 16$ MPa, a POISSON'S ratio of $\nu_{\text{EPDM}} = 0.48$ and the damping coefficients of the Rayleigh damping $\alpha = 0$ and $\beta = 0.0077$. The set-up, the measurement techniques and the analysis of the structural tests will be presented in Section 8.2.

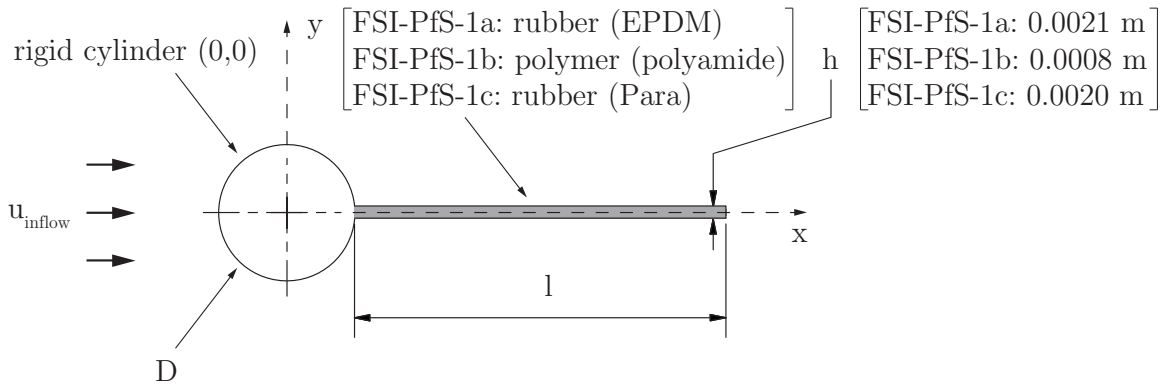


Figure 55: Sketch of the geometrical configuration of the benchmark cases FSI-PfS-1 x .

Definition of FSI-PfS-1b

The benchmark case FSI-PfS-1b consists of a thin flexible polymer plate clamped behind a fixed rigid non-rotating cylinder (see Fig. 55). Due to the increased stiffness of the polyamide material, the plate thickness is reduced to $h = 0.0008$ m to allow a structural deformation. All

other quantities (i.e., geometry, inflow velocity, Re) are identical to FSI-PfS-1a.

Concerning the polyamide material, the density is known with $\rho_{\text{polyamide}} = 1425 \text{ kg m}^{-3}$ and the structural tests result in a YOUNG's modulus of $E_{\text{polyamide}} = 580 \text{ MPa}$, a POISSON's ratio of $\nu_{\text{polyamide}} = 0.40$ and the Rayleigh damping coefficients $\alpha = 0$ and $\beta = 0.0031$. Again the set-up, results and analysis of the structural tests will be presented in Section 8.2.

Definition of FSI-PfS-1c

The benchmark case FSI-PfS-1c consists of a flexible para-rubber plate attached to a fixed rigid non-rotating cylinder (see Fig. 55). To take the increased flexibility of the material into account, the inflow velocity is reduced to $u_{\text{inflow}} = 1.18 \text{ m/s}$ leading to a Reynolds number $Re = 25,960$. All geometrical quantities except the plate thickness $h = 0.002 \text{ m}$ are identical to FSI-PfS-1a.

The flexible structure consists of a para-rubber material with the density $\rho_{\text{para}} = 1090 \text{ kg m}^{-3}$. The material properties of the para-rubber are determined by further structural tests. The outcome of these tests are a YOUNG's modulus of $E_{\text{para}} = 3.15 \text{ MPa}$, a POISSON's ratio of $\nu_{\text{para}} = 0.48$ and the Rayleigh damping coefficients $\alpha = 0$ and $\beta = 0.0065$ (refer to Section 8.2).

6.3.2. Two-dimensional geometry with rear mass - FSI-PfS-2x

Definition of FSI-PfS-2a

The benchmark case (FSI-PfS-2a) consists of a flexible para-rubber plate with an attached steel weight clamped behind a fixed rigid non-rotating cylinder (see Fig. 56). The cylinder has again the diameter $D = 0.022 \text{ m}$. The para-rubber plate used in the experiment has a length $l_1 = 0.050 \text{ m}$ ($l_1/D \approx 2.27$), a width $w = 0.177 \text{ m}$ ($w/D \approx 8.05$) and a thickness $h = 0.002 \text{ m}$ ($h/D \approx 0.09$). To achieve the same overall length of $l = 0.060 \text{ m}$ ($l/D \approx 2.72$) as in FSI-PfS-1x the steel weight has a length of $l_2 = 0.010 \text{ m}$ ($l_2/D \approx 0.45$) and the same width w and thickness h as the para-rubber plate. The inflow velocity is set to $u_{\text{inflow}} = 1.385 \text{ m/s}$ ($Re = 30,470$). The material used for the flexible structure is the same para-rubber as used in FSI-PfS-1c yielding the same material properties as evaluated in Section 8.2. The material parameters of the steel weight are given by the density $\rho_{\text{steel}} = 7850 \text{ kg m}^{-3}$, the YOUNG's modulus $E_{\text{steel}} = 200 \text{ GPa}$ and the POISSON's ratio $\nu_{\text{steel}} = 0.30$.

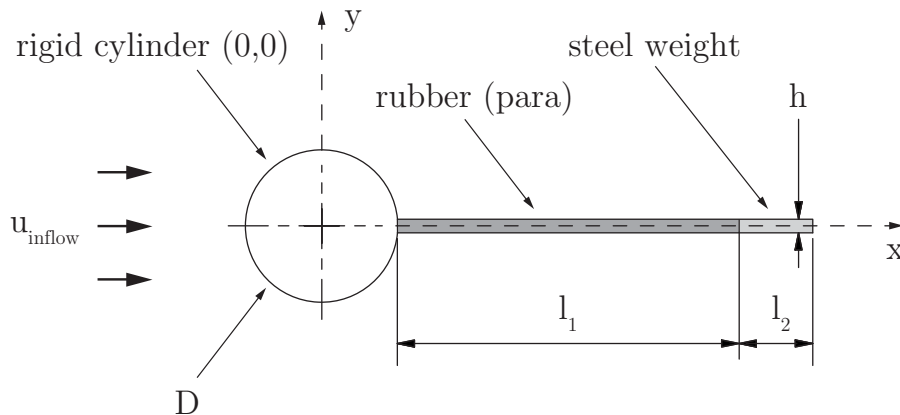


Figure 56: Sketch of the geometrical configuration of the benchmark case FSI-PfS-2a.

Definition of FSI-PfS-2b

In contrast to all other benchmarks in this thesis, the benchmark case (FSI-PfS-2b) consists of a flexible para-rubber plate with an attached steel weight clamped behind a fixed rigid but now rotationally-mounted cylinder (see Fig. 57). The cylinder still has a diameter $D = 0.022$ m. The para-rubber plate used in the experiment has a length $l_1 = 0.050$ m ($l_1/D \approx 2.27$), a width $w = 0.177$ m ($w/D \approx 8.05$) and a thickness $h = 0.002$ m ($h/D \approx 0.09$). Again the steel weight has a length of $l_2 = 0.010$ m ($l_2/D \approx 0.45$) and the same width w and thickness h as the para-rubber plate. The inflow velocity is set to $u_{\text{inflow}} = 1.385$ m/s ($\text{Re} = 30,470$). The material used for the flexible structure is the para-rubber also used in FSI-PfS-1c and 2a and thus possesses to the same material properties as presented in Section 6.3.1 and 6.3.2. The material parameters of the steel weight is again described by the density $\rho_{\text{steel}} = 7850$ kg m⁻³, the YOUNG's modulus $E_{\text{steel}} = 200$ GPa and the POISSON's ratio $\nu_{\text{steel}} = 0.30$.

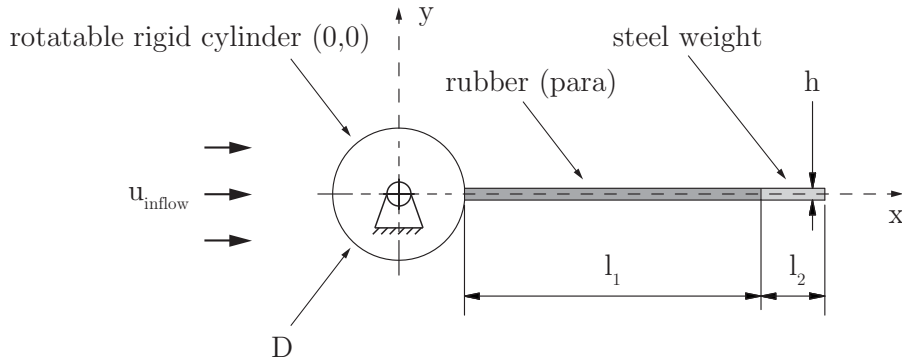


Figure 57: Sketch of the geometrical configuration of the benchmark case FSI-PfS-2b.

6.3.3. Three-dimensional geometry - FSI-PfS-3x

To enforce a fully three-dimensional flow and thus three-dimensional FSI effects the test cases FSI-PfS-3a and 3b apply tapered cylinders instead of circular cylinders. In contrast to the numerous investigations of flows around circular cylinders only a few studies are related to tapered cylinders. According to the linear increase of the diameter with the spanwise elongation of the cone the flow characteristic changes significantly in comparison to a cylinder with a constant diameter. Solely by the three-dimensional geometry the flow downstream of the cone is assumed to be three-dimensional (shed vortices are oblique) independently of the flow conditions (Palma and Silva Lopez, 2007). Several studies were carried out in the laminar regime to analyze and compare the three-dimensional flow structures in the wake of a cone (Hsiao et al., 1993; Anderson and Szewczyk, 1997; Zdravkovich, 1997; Hsiao and Chiang, 1998; Jagadeesh, 2009) to the quasi two-dimensional flow behind a cylinder. For the flow around a cylinder St is constant over the whole spanwise geometry. That means that the alternating, periodic vortex shedding is constant. For the cone, the wake is separated into discrete cells (vortex cells), where different constant local Strouhal numbers are reported (Anderson and Szewczyk, 1997). That means that over the spanwise elongation of the cone several different Strouhal numbers (or vortex shedding frequencies) are present. According to the Helmholtz theorem (Kuethe and Schetzer, 1959) vortex cores cannot suddenly end in a fluid. Therefore,

the vortices are still connected among the cells (Hsiao et al., 1993). Since the total number of vortex sheddings cannot be equal between two cells of different shedding frequencies over a sufficiently long period, a vortex dislocation appears. In Fig. 58 the vortex dislocation is illustrated by the example of a flow around a tapered cylinder. Here, two vortices at the higher frequency side are shed and connected to only one vortex core on the low-frequency side.

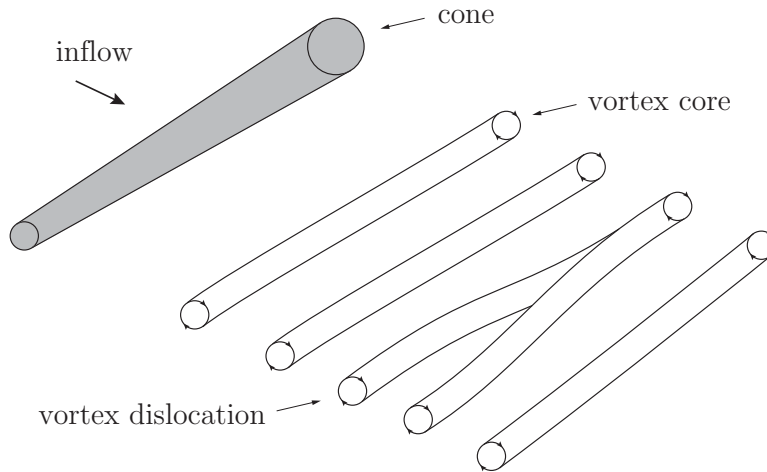


Figure 58: Vortex dislocation in the wake of a cone.

Furthermore, the discrete vortex cells are moving in spanwise direction of the cone (Jagadeesh, 2009) and are depending on the Reynolds number and the diameter ratio of the cone (Zdravkovich, 1997). Increasing Reynolds numbers are reported to increase the size of the intersection region between the vortex cells and lower the discontinuity between them. Furthermore, Anderson and Szewczyk (1997) proved that the vorticity shed from the boundary layer decreases across the spanwise direction (decreasing local diameter) leading to a spanwise variation of the strength of the primary vortices (stronger at the larger cone diameter).

The investigation on the spanwise vorticity distribution related to the local cone diameter (Anderson and Szewczyk, 1997) lead to the three-dimensional test case definitions of FSI-PfS-3x. The spanwise vorticity distribution is supposed to lead to periodic force distributions of flexible plates attached to the cone geometry, which are assumed to produce corresponding three-dimensional structural deformations. Therefore, the circular cylinder ($D = 0.022\text{ m}$) used in FSI-PfS-1x and 2x is replaced by a cone with the diameter ratio $D_2/D = 1.5$ and a taper ratio of $TR = w/(D_2 - D_1) = 16.09$ to define the test cases FSI-PfS-3x. Here the smaller diameter D_1 is equal to D . The two test cases FSI-PfS-3a and 3b only differ concerning the material of the flexible plate and the inflow velocities.

Definition of FSI-PfS-3a

The benchmark case FSI-PfS-3a is proposed as a fully three-dimensional test case and consists of a flexible rubber plate clamped behind a fixed rigid non-rotating cone (see Fig. 59). The small diameter of the cone has a size of $D_1 = 0.022\text{ m}$ and the large end of the cone has a diameter of $D_2 = 0.033\text{ m}$. The rubber plate has a trapezoidal form with its maximum length

$l_1 = 0.060$ m ($l_1/D \approx 2.72$) at the small cone diameter and a minimum length $l_2 = 0.0435$ m ($l_2/D \approx 1.98$). Thus overall the flexible structure has the same streamwise extension as the other test cases. The three-dimensional geometry is extended over the width $w = 0.177$ m ($w/D \approx 8.05$) and has a thickness $h = 0.0021$ m ($h/D \approx 0.10$). The inflow velocity is set to $u_{\text{inflow}} = 0.97$ m/s leading to a Reynolds number $\text{Re} = 32,000$.

The material used for the flexible structure is an EPDM rubber equal to the material used in FSI-PfS-1a and thus the same material properties as presented in Section 6.3.1.

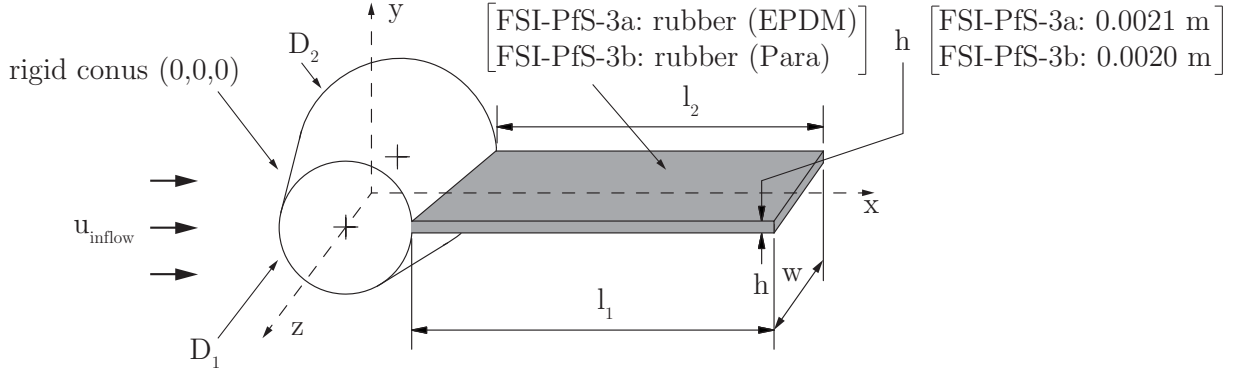


Figure 59: Sketch of the geometrical configuration of the benchmark case FSI-PfS-3x.

Definition of FSI-PfS-3b

The benchmark case FSI-PfS-3b is again proposed as a fully three-dimensional test case and consists of a flexible para-rubber plate clamped behind a fixed rigid non-rotating cone (see Fig. 59). In comparison to FSI-PfS-3a only a different material for the plate is used and the inflow velocity is changed to $u_{\text{inflow}} = 0.55$ m/s ($\text{Re} = 18,150$).

The material used for the flexible structure is a para-rubber equal to the material used in FSI-PfS-1c, 2a and 2b referring to the same material properties as presented in Section 6.3.1 and 6.3.2.

6.3.4. Application-based test cases - FSI-PfS-4x

General definitions of the test case FSI-PfS-4x

The test cases FSI-PfS-4a and 4b are developed in terms of an application-oriented FSI benchmark. Several different studies investigated the effect of vortex-induced vibrations (VIV) on circular cylinders by experimental and numerical methods (Williamson and Govardhan, 2004; Chang et al., 2011; Zhao et al., 2013). Often VIV investigations apply rigid cylinders which are mounted on an elastic spring-damper system (to allow the inhibition of a single DOF) and reduce the system to an almost two-dimensional FSI phenomenon. Related to the free DOFs of the system and the flow conditions different FSI phenomena and oscillation modes are reported (Williamson and Govardhan, 2004; Zhao et al., 2013). In contrast, the present two test cases FSI-PfS-4x use a long elastic cylinder which is fixed on one channel wall and free on the other ending (see Fig. 60). While FSI-PfS-4a consists of a single flexible cylinder, the flexible cylinder in FSI-PfS-4b is surrounded by rigid cylinders in a 3×3 array. This configuration is

often used in technical application like tube bundles, where structural failures caused by excessive vibrations are very expensive to repair (Weaver and Fitzpatrick, 1988; Païdoussis and Li, 1992; Goyder, 2002; Païdoussis, 2006). Another application related to VIV in cylinder arrays are those effects of fuel rods in nuclear power plants (Païdoussis, 2006). Here, any structural damage caused by the FSI phenomena would lead to fatal consequences to the power plant and its environment.

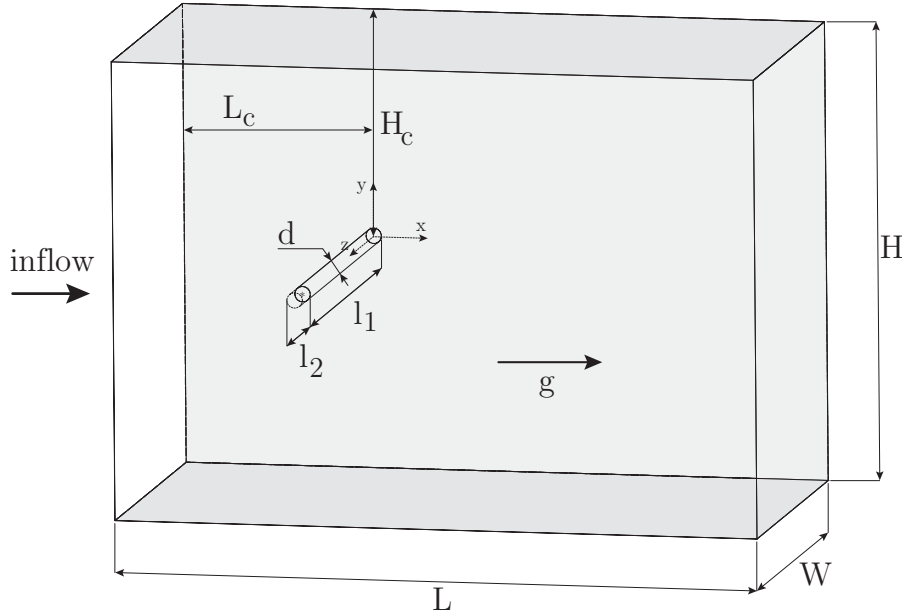


Figure 60: Sketch of the geometrical configuration of the channel (FSI-PfS-4a).

Here, all geometrically related variables are now normalized by the cylinder diameter $d = 0.008$ m. The structures are positioned in the middle of the experimental test section with $H_c = H/2 = 0.120$ m ($H_c/d = 15$). The center of the elastic cylinder is located at $L_c = 0.140$ m ($L_c/d = 17.5$) downstream of the inflow section. The flow channel has a width of $w = 0.180$ m ($w/d = 22.5$). The coordinate system is placed in the center of the elastic cylinder at its fixation on the channel wall. Similar to the other test cases the gravitational acceleration g points in the streamwise x -direction (see Fig. 60) to avoid asymmetric effects in the flow or the structural deformation.

Definition of FSI-PfS-4a

The benchmark case (FSI-PfS-4a) is proposed as a fully three-dimensional test case and consists of a single flexible polyethylene cylinder fixed at the backplate of the flow channel (see Fig. 61). The cylinder has a diameter of $d = 0.008$ m and a length $l_1 = 0.170$ m ($l_1/d \approx 21.25$). Consequently there is a gap between the free end of the cylinder and the transparent channel wall of $l_2 = 0.01$ m ($l_2/d \approx 1.25$). The inflow velocity is set to $u_{\text{inflow}} = 1.69$ m/s ($\text{Re} = 13,520$). The material used for the flexible cylinder is polyethylene referring to its well-known material properties with a density $\rho_{\text{polyethylene}} = 930$ kg m⁻³, a YOUNG's modulus $E_{\text{polyethylene}} = 800$ MPa and a POISSON's ratio $\nu_{\text{polyethylene}} = 0.42$. Despite the wide-spread application of

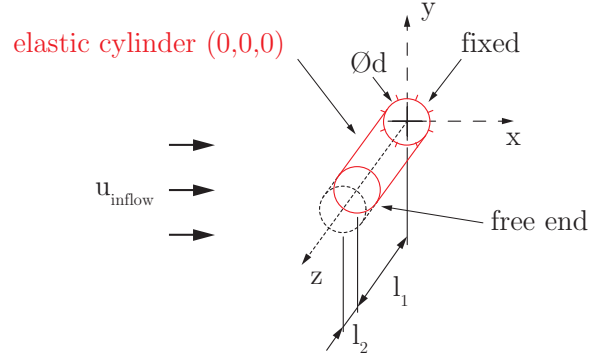


Figure 61: Sketch of the geometrical configuration of the benchmark case FSI-PfS-4a.

this material and the safe handling in structural mechanics, additional structural tests are performed to provide measurement data for the validation of the numerical predictions (see Section 8.2).

Definition of FSI-PfS-4b

The benchmark case (FSI-PfS-4b) consists of an array of one flexible and eight rigid cylinders. The elastic polyethylene cylinder is surrounded by eight rigid glass cylinders as illustrated in Fig. 61. Similar to FSI-PfS-4a all cylinders are fixed at the backplate of the flow channel and have a diameter of $d = 0.008$ m. The rigid cylinders are expanded over the entire width of the channel with a length $w = 0.180$ m ($w/d = 22.50$) and thus fixed on both channel walls.

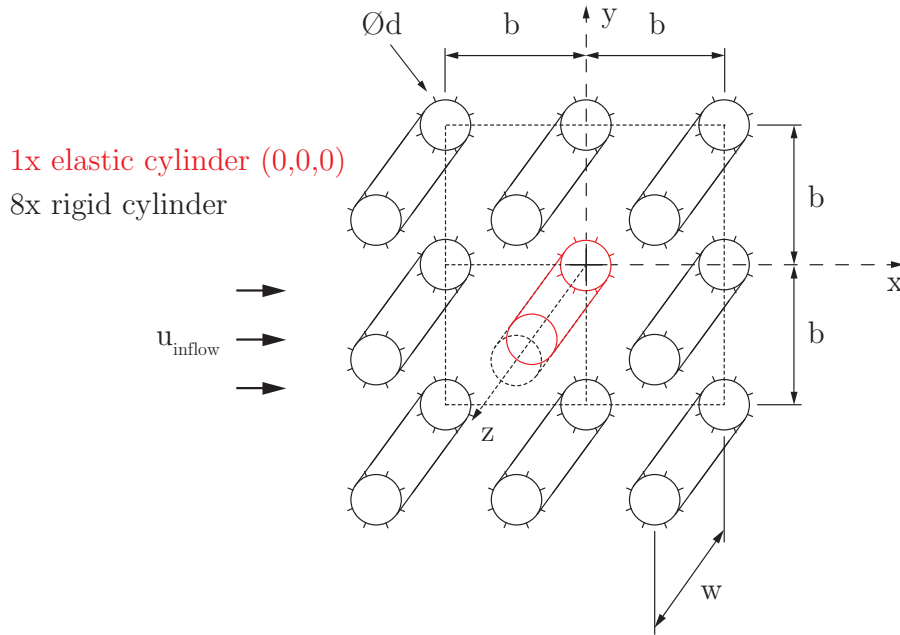


Figure 62: Sketch of the geometrical configuration of the benchmark case FSI-PfS-4b.

Analog to the geometry of the single elastic cylinder in FSI-PfS-4a here again the elastic cylinder has a length of $l_1 = 0.170$ m ($l_1/d = 21.25$) and the gap between the free end of the cylinder and the transparent channel wall has a length of $l_2 = 0.01$ m ($l_2/d \approx 1.25$). The distance between the centers of the cylinders in x - and y -direction is given by $b = 0.036$ m ($b/d = 4.5$).

The inflow velocity is set to $u_{\text{inflow}} = 1.69$ m/s ($\text{Re} = 13,520$). The material used for the flexible cylinder is again polyethylene (similar to FSI-PfS-4a).

The materials applied in this thesis are summarized in Table 5. Finally, all test cases and their individual characteristics are summarized in Table 6.

material	density [kg m^{-3}]	YOUNG's modulus [MPa]	POISSON's ratio
EPDM rubber	1360	16	0.48
para-rubber	1090	3.25	0.48
Polyamide	1425	580	0.40
Polyethylene	930	800	0.42
Steel	7850	$2 \cdot 10^5$	0.30

Table 5: Material properties of the benchmark cases.

test case	behavior	bluff body	mount	plate material	thickness [mm]	u_{inlet} [m/s]	Re
FSI-PfS-1a	2D	cylinder	fixed	EPDM rubber	2.1	1.385	30,470
FSI-PfS-1b	2D	cylinder	fixed	polymer	0.8	1.385	30,470
FSI-PfS-1c	2D	cylinder	fixed	para-rubber	2.0	1.179	25,960
FSI-PfS-2a	2D	cylinder	fixed	para-rubber + steel weight	2.0	1.385	30,470
FSI-PfS-2b	2D	cylinder	rotatable	para-rubber + steel weight	2.0	1.385	30,470
FSI-PfS-3a	3D	cone	fixed	EPDM rubber	2.1	0.969	32,000
FSI-PfS-3b	3D	cone	fixed	para-rubber	2.0	0.549	18,150
FSI-PfS-4a	3D	single cylinder	fixed	polyethylene	8	1.69	13,520
FSI-PfS-4b	3D	cylinder array	fixed	polyethylene	8	1.69	13,520

Table 6: parameters of the benchmark cases.

7. Experimental set-up

This section addresses the experimental set-up, the flow conditions in the channel and the post-processing procedures consisting of the phase-averaging method and the proper orthogonal decomposition (POD).

In Section 7.1 the alignment of the measuring techniques (PIV, V3V, LLT) to each other and in reference to the test section is described. The flow measurement techniques are calibrative systems. Therefore, the PIV as well as the V3V are compared with non-calibrative laser-Doppler velocimetry measurements in Section 7.1.5. Furthermore, a detailed conclusion on the measurement errors for each measurement technique is provided in Section 7.2.

Due to the validation purpose of the experimental FSI investigations a special concern is put on the boundary conditions in the channel. Therefore, the flow conditions in the test section of the channel are described in detail in Section 7.3.

To maintain the mean characteristics of each FSI test case and to enable the validation of numerical FSI computations, an averaging method is applied to the quasi-periodic but turbulent results of the experiments. The corresponding phase-averaging procedure is comprehensively explained in Section 7.4.1. Furthermore, energy-related investigations based on the flow measurements are carried out based on the proper orthogonal decomposition (POD). A brief introduction to this method is given in Section 7.4.2.

7.1. Measurement set-ups

Both flow measurement techniques (PIV and V3V, described in Section 4) applied in this thesis are aligned in a similar manner. Due to the typical set-up of a mono-PIV system the camera is aligned normal to the light sheet (see Fig. 63). For the mono-PIV measurements of FSI-PfS-1x and 2x a plane in the middle of the test section ($z/D = 0$) is illuminated and the Cartesian velocity components u and v in the main flow direction x and in the cross-flow direction y are measured. To investigate the three-dimensional behavior of the test cases FSI-PfS-3x, three planes at $z/D = -2.72$, $z/D = 0$ and $z/D = 2.72$ are illuminated and both velocity components u and v are measured. Finally, the investigations of the test cases FSI-PfS-4x use one plane near the extremity of the flexible cylinder at $z/d = 20.63^4$.

In general, the applied optical flow investigation techniques (PIV, V3V) have to deal with the blockage of the light sheet by the structure. Here, large areas behind the structure are shadowed and no flow measurements are possible. In the present mono-PIV measurements a special method to illuminate the backward area of the test section is applied. For this purpose, a beam splitter divides the beam emitted by the PIV laser into two beams. The beam splitter distributes the energy of the incoming laser beam approximately by 50/50% to the outgoing beams. Furthermore, the 45° justification of the beam splitter to the incoming laser beam results in a right-angled redirection of one beam while the other passes the beam splitter without any angular change. This beam is expanded to a light sheet with the help of a light sheet optic and directly illuminates the test section on a plane at $z/D = 0$. The second beam is directed around the test section by several plane laser mirrors in a 45° justification to

⁴Due to the smaller diameter d of the cylinder in FSI-PfS-4x all quantities referring to FSI-PfS-4x are related to $d = 0.008$ m.

the beam. Another light sheet optic expands this beam to illuminate the remaining shadowed parts of the measurement plane as illustrated in Fig. 63.

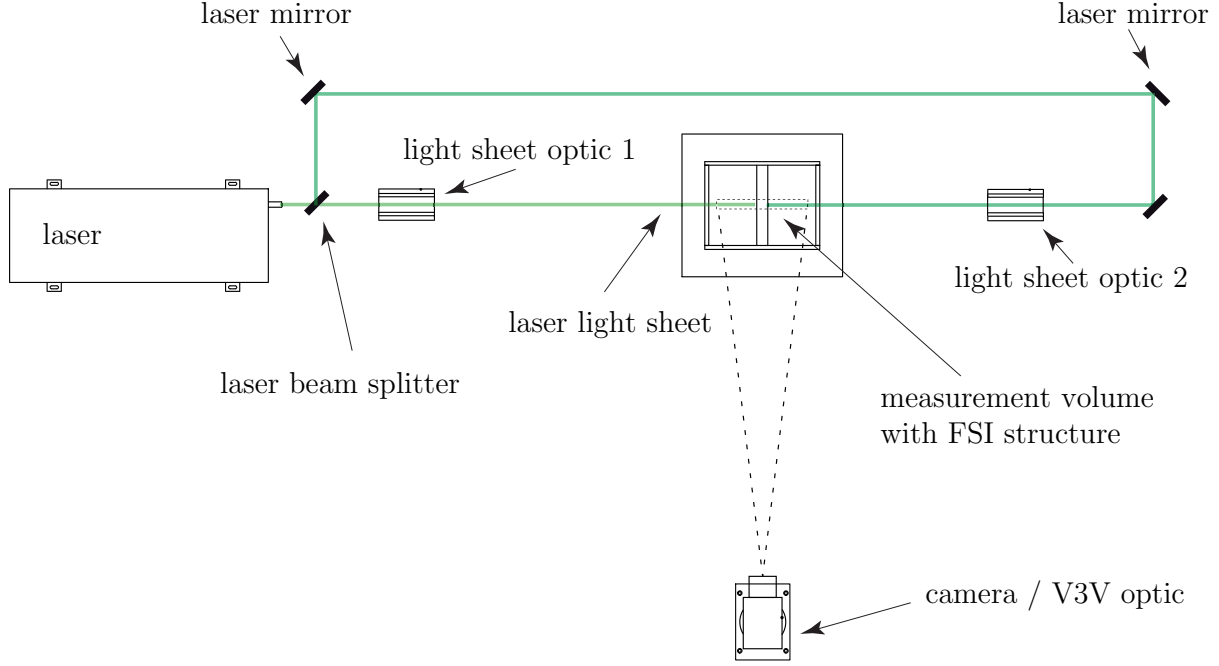


Figure 63: Sketch of the alignment of the measurement set-up (in the case of a mono-PIV set-up).

7.1.1. Mono PIV measurement set-up

In the mono-PIV set-up the reflection images are obtained by a 4 Mega-pixel camera (TSI Powerview 4MP, charge-coupled device (CCD) chip, 2048 pixel \times 2048 pixel (px)) equipped with an appropriate objective (Nikon AF Nikkor, $f = 50$ mm, aperture 1:1.8) and a pulsed dual-head Neodym:YAG laser (Litron NanoPIV 200) with an energy of 200 mJ per laser pulse. The high energy of the laser allows to use silver-coated hollow glass spheres (SHGS) with an average diameter of $d_{\text{avg,SHGS}} = 10 \mu\text{m}$ and a density of $\rho_{\text{SHGS}} = 1400 \text{ kg m}^{-3}$ as tracer particles. To prove the following behavior of these particles, the Stokes number Sk and the particle sedimentation velocity u_{SHGS} is calculated as follows:

$$\begin{aligned}
 Sk_{\text{SHGS}} &= \frac{\tau_{\text{p,SHGS}}}{\tau_{\text{f,SHGS}}} = \frac{\rho_{\text{SHGS}} d_{\text{avg,SHGS}}^2}{18 \mu_f} \frac{u_{\text{inflow}}}{d_{\text{avg,SHGS}}} = 1.08 \\
 u_{\text{SHGS}} &= \frac{d_{\text{avg,SHGS}}^2 g (\rho_{\text{SHGS}} - \rho_f)}{18 \mu_f} = 2.18 \cdot 10^{-5} \text{ m/s}
 \end{aligned} \tag{119}$$

With this Stokes number and particle sedimentation velocity which is much lower than the expected velocities in the experiments, an eminent following behavior is approved (refer to Section 4.2.1 for further considerations about the following behavior of the particles). The camera takes 12 bit pictures with a frequency of about 6.0 Hz and a maximum resolution of 2048 \times 2048 px. With respect to the rectangular size of the test section only the area within a rectangle of 1695 px \times 1211 px is employed to neglect channel walls and unessential areas. For one phase-resolved position (described in Section 7.4.1) 40 to 70 measurements are taken. This

number of measurements assures a sufficient input for the subsequent phase-averaging method by reasonable measurement time, processing costs and data storage. The final PIV grid has a size of 150×138 cells and is calibrated with an average magnification factor of $\gamma = 126 \mu\text{m}/\text{px}$ covering the planar flow field of $x/D \approx -2.36$ to 7.26 and $y/D \approx -3.47$ to 3.47 in the middle of the test section at $z/D \approx 0$ for FSI-PfS-1x and 2x and at $z/D = -2.72$, $z/D = 0$ and $z/D = 2.72$ for FSI-PfS-3x. With respect to the smaller cylinder diameter used in FSI-PfS-4x, here the flow field is obtained in the area $x/d \approx -5.40$ to 21.95 and $y/d \approx -11.87$ to 12.39 at $z/d = 20.63$.

The calibration applies a calibration target plate (physical: $l_w = 220 \text{ mm} \times l_h = 180 \text{ mm}$, projection on the camera: $L_w = 1746 \text{ px} \times L_h = 1428 \text{ px}$) with a dot pattern which enables a field-based calibration in the whole measurement area. The magnification factor is based on:

$$\gamma = \frac{l_w \cos \theta}{L_w} \quad \text{or} \quad \gamma = \frac{l_h \cos \theta}{L_h} \quad (120)$$

and is calculated to $126 \mu\text{m}/\text{px}$. The angle θ denotes a small angular dislocation of the calibration target to the camera image and is assumed to be approximately zero (more details on the measurement/alignment errors are given in Section 7.2).

The time interval between the frame-straddled laser pulses is set to $\Delta t = 200$ to $600 \mu\text{s}$ according to the inflow velocity of each test case (longer time intervals Δt correspond to lower inflow velocities u_{inflow} while increased inflow velocities require shorter time intervals Δt). Laser and camera are controlled by a TSI synchronizer (TSI 610035) with a 1 ns temporal resolution. The data processing of the phase-resolved fluid velocity fields involving the structural deflections is described in Section 7.4.1. A summary of the measurement set-up of the mono-PIV configuration is given in Table 7.

7.1.2. V3V measurement set-up

The set-up of the V3V system applies three CCD-cameras (TSI Powerview 4MP, charge-coupled device (CCD) chip, $2048 \text{ px} \times 2048 \text{ px}$) and three equal objectives (Nikon AF Nikkor, $f = 50 \text{ mm}$, aperture 1:1.8) to obtain the particle reflection fields. The alignment of the V3V system is similar to the mono-PIV set-up. The light sheet optics are replaced by two cylindrical lenses which are rotated by 90 degrees to each other to expand the light sheet into a light volume on each side of the FSI structure (see Fig. 64).

The illuminated measurement volume has a size of $x = 156 \text{ mm} \times y = 156 \text{ mm} \times z = 128 \text{ mm}$ and is placed in the wake of the structure ($x/D \approx 3.00$ to 10.90 , $y/D \approx -3.54$ to 3.54 and $z/D \approx -2.91$ to 2.91) for FSI-PfS-1x, 2x and 3x while for FSI-PfS-4x the flow field is placed at $x/d \approx 1.03$ to 17.72 , $y/d \approx -9.09$ to 9.09 and $z/d \approx 3.41$ to 19.53 . These positions are chosen to prevent larger measurement errors due to the moving structure in the V3V images. The tracer particles used for these measurements are polyamide spheres with an average diameter of $d_{\text{avg,PA}} = 50 \mu\text{m}$ and a density of $\rho_{\text{PA}} = 1140 \text{ kg m}^{-3}$. In comparison to the SHGS tracers of the mono-PIV set-up these polyamide particles are five times larger. That is necessary since the laser energy density in the light volume is several orders of magnitude smaller than in the light sheet. Furthermore, the V3V velocity processing applies a particle tracking method instead

Flow properties	
fluid	water
measurement section	240 mm × 338 mm
acquisition area	258 mm × 258 mm
inflow velocity	0.55 – 1.69 m/s
Calibration	
calibration area ($l_w \times l_h$)	220 mm × 180 mm
calibration dot distance	$l_d = 10$ mm
calibration area projection ($L_w \times L_h$)	1746 px × 1428 px
calibration factor γ	126 $\mu\text{m}/\text{px}$
Flow visualization	
tracer particle	silver-coated hollow glass spheres
tracer diameter	10 μm
standard deviation of tracer diameter	1 μm
$\rho_{\text{SHGS}}/\rho_f$	1.41
light source	double pulsed Nd:YAG laser
laser power	200 mJ
laser beam diameter $d_{\text{laser beam}}$	6.35 mm
laser sheet thickness $h_{\text{light sheet}}$	1.00 mm
Δt	200 μs - 600 μs
Image detection	
camera	CCD
maximum spatial resolution	2048 px × 2048 px
applied spatial resolution	1695 px × 1211 px
sampling frequency	6 Hz
gray scale resolution	12 bit (4096 gray scales)
pixel size on CCD chip	7.4 μm × 7.4 μm
distance from the light sheet l_l	1200 mm
camera objective	$f = 50$ mm, aperture 1:1.8
PIV processing	
sub-pixel analysis	three-point Gaussian fitting
displacement analysis	cross-correlation method
initial correlation area	36 px × 36 px
final correlation area	12 px × 12 px

Table 7: PIV measurement properties.

of the probability-based search method in the mono-PIV processing. For a clear identification of each particle the particle tracking method requires lower tracer densities. To compensate these issues, larger tracers need to be used to provide enough light on the reflection images. To prove the following behavior of these larger particles, the Stokes number Sk and the particle sedimentation velocity u_{PA} is calculated as follows:

$$\begin{aligned}
 Sk_{\text{PA}} &= \frac{\tau_{\text{p,PA}}}{\tau_{\text{f,PA}}} = \frac{\rho_{\text{PA}} d_{\text{avg,PA}}^2}{18 \mu_f} \frac{u_{\text{inflow}}}{d_{\text{avg,PA}}} = 4.39 \\
 u_{\text{PA}} &= \frac{d_{\text{avg,PA}}^2 g (\rho_{\text{PA}} - \rho_f)}{18 \mu_f} = 1.91 \cdot 10^{-4} \text{ m/s}
 \end{aligned} \tag{121}$$

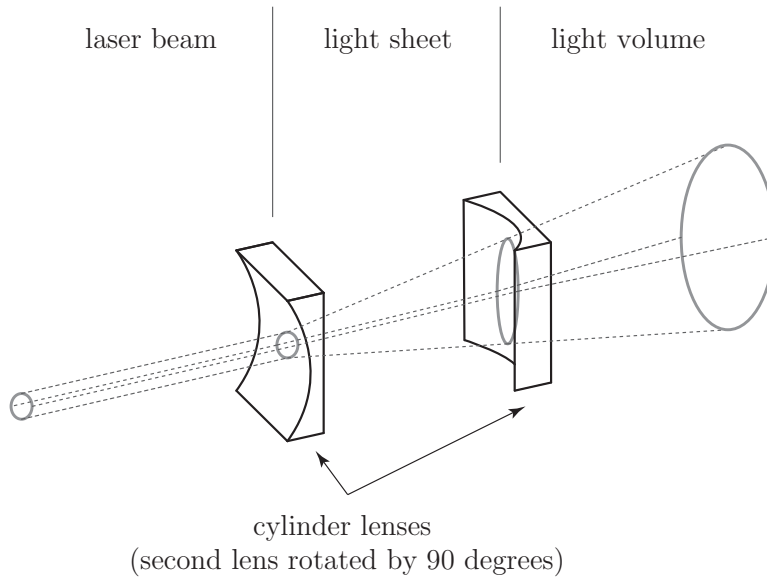


Figure 64: Sketch of the laser beam expansion from a light sheet to a light volume.

Based on this Stokes number and a particle sedimentation velocity which is much lower than the expected velocities in the experiments, again a sufficient following behavior of the particles is approved. The three cameras take 12 bit frame-straddled pictures sets with a frequency of about 6.0 Hz within a short time interval ($\Delta t = 200$ to $600 \mu\text{s}$). The post-processing computes an equidistant grid with a step size of 4 mm and a cell overlap of 50%. The image pairs are recorded with a resolution of $1940 \text{ px} \times 1940 \text{ px}$, while the resulting grid has a size of $40 \times 40 \times 33$ cells and is calibrated with an average factor of $79 \mu\text{m}/\text{px}$.

The calibration of the V3V system is performed by traversing the calibration target through the test section. On the target (Fig. 65) a dot pattern is laser-engraved. Based on the known distances between the dots the spatial calibration on each calibration plane is done (as already described in Section 4.3). To recognize the origin of the target, three dots in its center are missing. Furthermore, the arrangement of these points also define the orientation of the target. The resulting calibration of the V3V system is shown in Fig. 66. On the left side of the figure the dewarping error, the pinhole adjustment and the pinhole magnification at each calibration plane are presented. The dewarping error shows the standard deviation of the grid dot position error after the image dewarping (perspective correction of the left and right camera images), where the error is defined as the distance between the detected dot position and its perfect (physical) position. A typical error is less than 0.25 pixels (TSI, 2007) and decreases with the distance of the target from the V3V optic. The pinhole magnification graph compares the magnification of the dot pattern (in pixel) of the actual camera with a theoretical pinhole camera at each calibration plane. The deviation of the theoretical model to the present calibration is shown in the pinhole adjustment graph. A typical pinhole adjustment is given by values between 0.95 and 1.05 (TSI, 2007). Furthermore, this calibration result is used to correct the magnification during the triplet search by adjusting the pixel size in each of the three views. In the present calibration the dewarping error is less than 0.28 pixel and the linear pinhole adjustment for all cameras ranges between 1.00 and 1.05. Based on these results the calibration is reasonably accurate but slightly larger than the reference values given by the manufacturer.

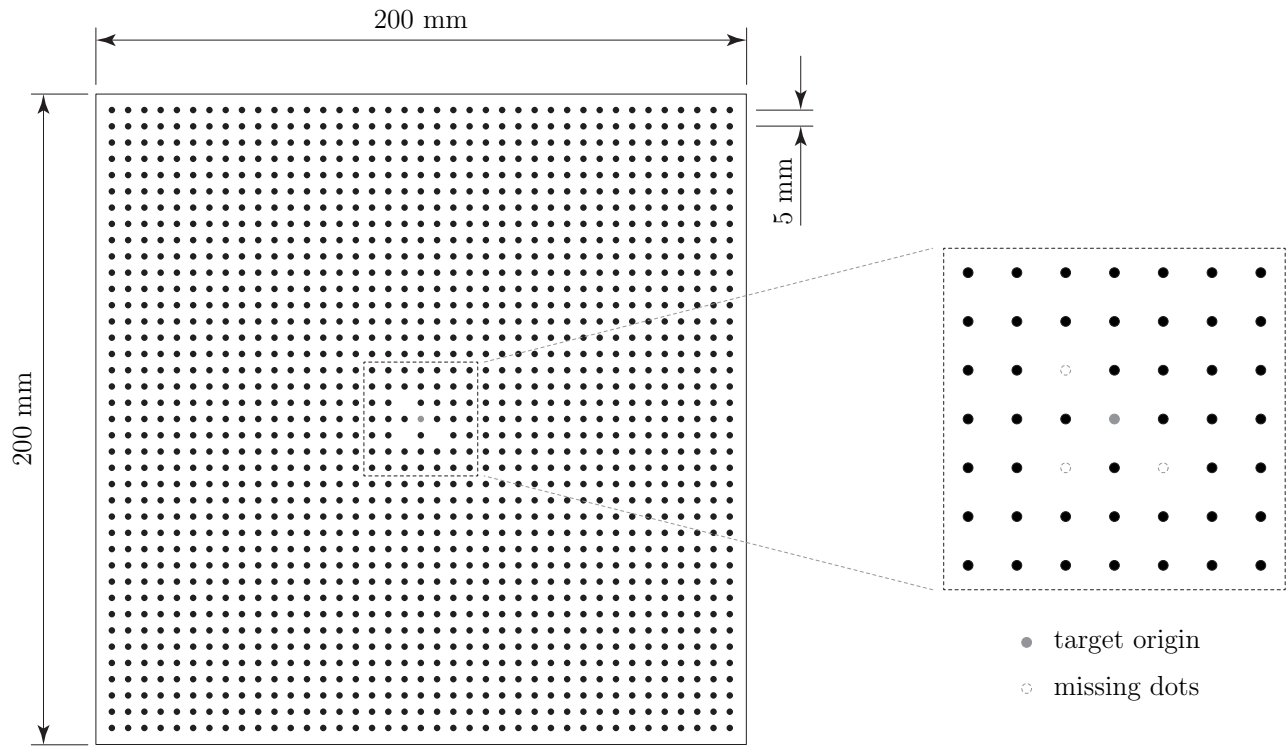


Figure 65: Calibration target of the V3V system.

The reason is the manual traversing of the calibration target. This manual traversing of the calibration target is necessary due to the restricted access in the test section. The camera signature graph (Fig. 66, right) shows the target origin in all three images at each calibration plane (each blue, green, and red circle represents one target origin location in its associated image). The linear characteristic of the origin displacements over the measurement volume indicates a successful and precise calibration of the V3V system. The processing of the phase-resolved fluid velocity fields involving the structural deflections is described in Section 7.4.1.

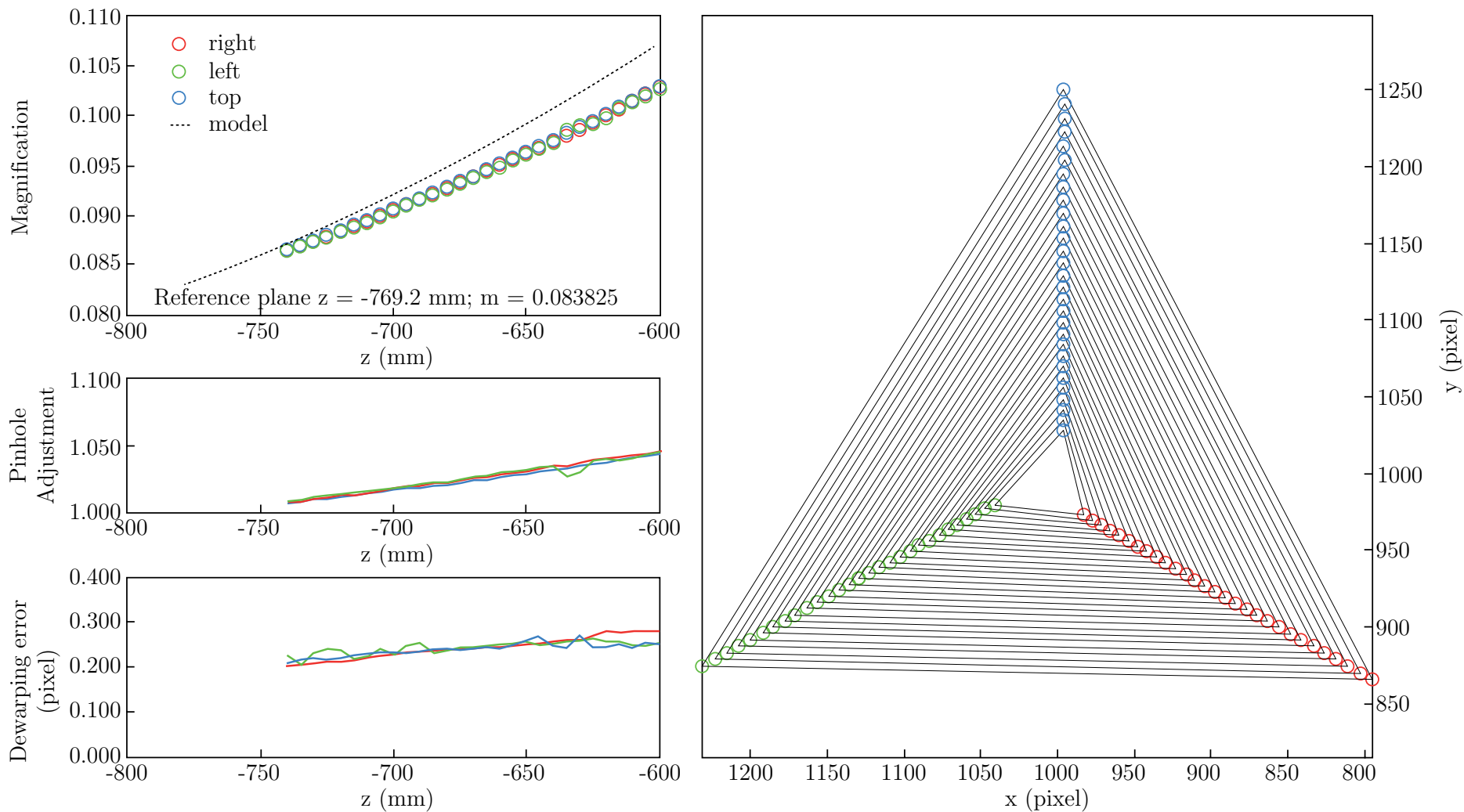


Figure 66: Calibration results of the V3V system (left: pinhole and dewarping parameters, right: camera signature).

7.1.3. LLT measurement set-up

The laser line triangulation (LLT) sensor applied (Micro-Epsilon, scanCONTROL 2750-100) uses a 10 mW solid-state laser which emits a 658 nm laser beam. The receiving unit of the sensor is a complementary metal oxide semiconductor (CMOS) high-speed line-camera. The laser line sensor is used in two different orientations for FSI-PfS-1x, 2x and 3x. One is positioned along the spanwise direction z/D near the trailing edge of the structure following the motion of the structure in the yz -plane as illustrated in Fig. 67a. Due to the limited measurement range of 140 mm in spanwise direction not the entire structure with a width of $w = 177$ mm is measurable. The other orientation covers the outline of the structure and its corresponding deformation in the xy -plane (Fig. 67b). For FSI-PfS-4x only the circular outline of the cylinder at $z/d = 20.63$ is measured.

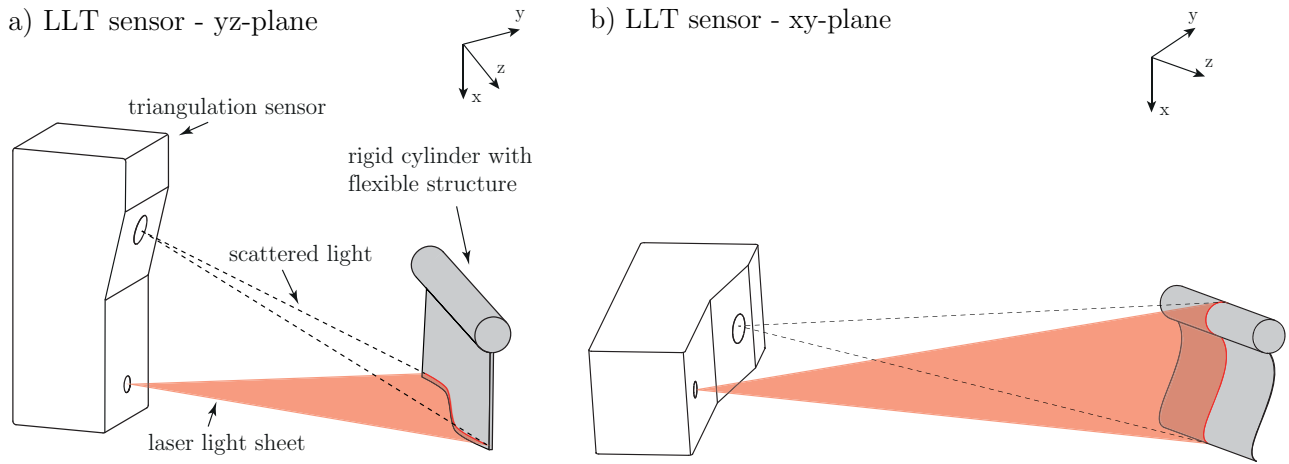


Figure 67: Set-up and alignment of the LLT sensor on the flexible structure in both orientations.

The projected laser line on the structures surface consists of maximal 640 points. Special care is taken that the fine resolution of the sensor with a precision of 15 to 40 μm is orientated in the direction of the largest deformation of the structure (y -direction). In addition to the internal calibration of the sensor referring to the position of the scattered light on the CCD array, the influence of the different refraction indices of the air, the glass of the test section and the flow medium water is taken into account by an additional linear calibration. This calibration is performed for each test case to take the individual characteristics of the structure (size, elongation extrema) into account. For this purpose the corresponding submerged structure in the channel is applied to identify the spatial calibration function of the measurement setup. Due to the known geometry of the structure (e.g., the cylinder $D = 0.022$ m with the attached rubber plate $l = 0.060$ m) and the unadjusted measurement values of the sensor the individual magnification factors are calculated. For all test cases a temporal resolution of 800 Hz is used for the structural measurements.

7.1.4. Illustration of the entire measurement set-up

The whole experimental set-up is illustrated in Fig. 68 including the data connections between the single measurement components.

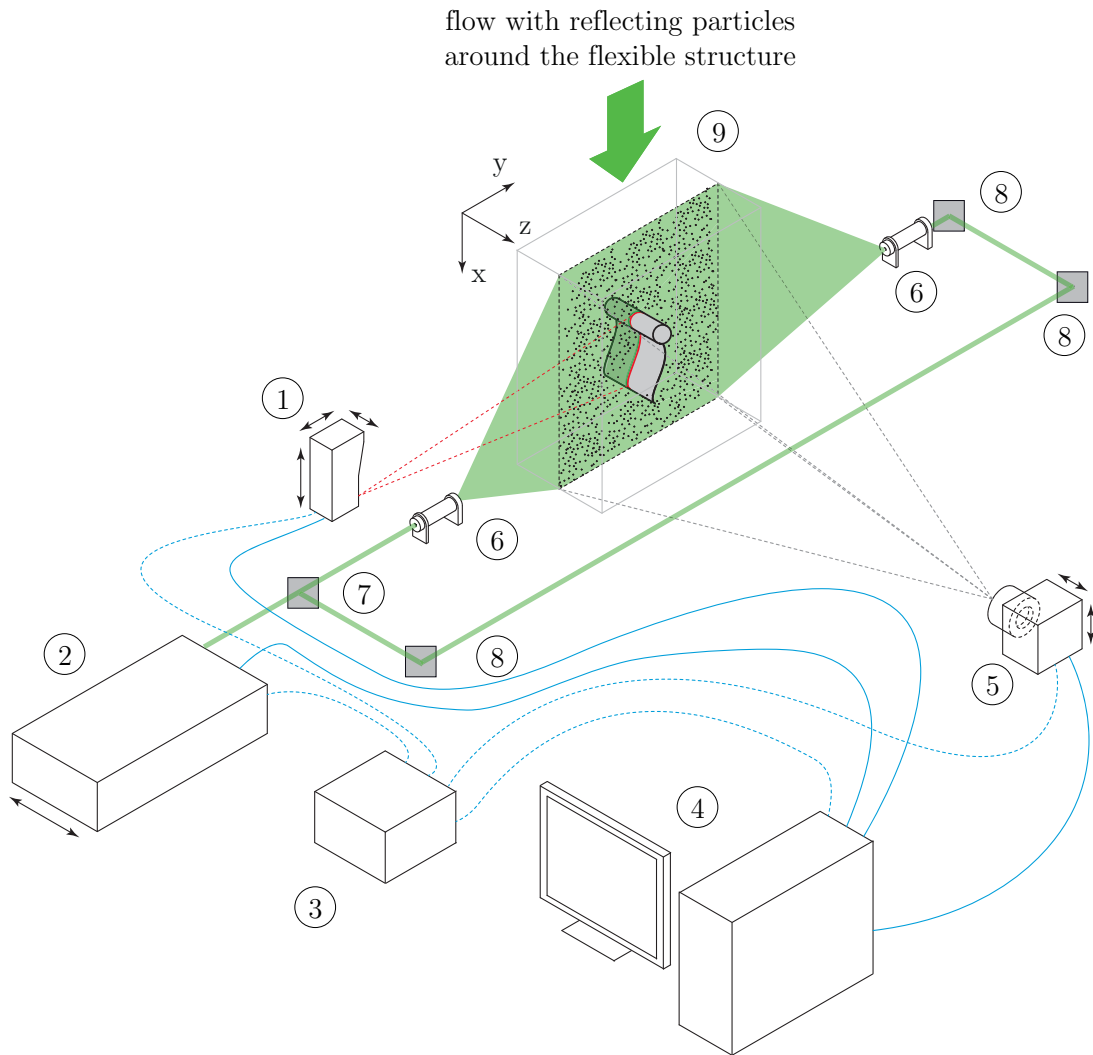


Figure 68: Entire measurement set-up (mono-PIV set-up) ① LLT-sensor, ② PIV-laser, ③ PIV synchronizer, ④ PC (including data acquisition, processing and post-processing), ⑤ PIV-camera/V3V optic, ⑥ light sheet/volume optic, ⑦ laser beam splitter, ⑧ laser mirror, ⑨ test section; blue lines illustrate the data connections between the single measurement components; arrows illustrate the possible movement directions of the components.

7.1.5. Comparison of the applied flow measurement techniques

To validate the calibrative flow measurement techniques (PIV, V3V) complementary non-calibrative laser-Doppler velocimetry (LDV) measurements are performed. The LDV technique is another standard method in fluid mechanics and is based on the Doppler shift observed in the scattered light of a moving tracer particle while passing a laser beam in a flowing medium (Tropea et al., 2007). Due to the direct proportionality of the velocity to the Doppler frequency, no additional velocity calibration is necessary and therefore the LDV technique is often used to validate other flow measurement techniques. The LDV, PIV and V3V measurements are performed in the water channel without an installed structure and at inflow velocities ranging from $u_{\text{inflow}} = 0.396$ m/s to 4.190 m/s. The comparison of the results between the different techniques for the time-averaged velocity \bar{u} and its fluctuations $\overline{u'}$ (given as the root mean square $\overline{u'} = \sqrt{\frac{1}{n}(u_1'^2 + u_2'^2 + \dots + u_n'^2)}$) in main flow direction is shown in Table 8 and partly in Fig. 69.

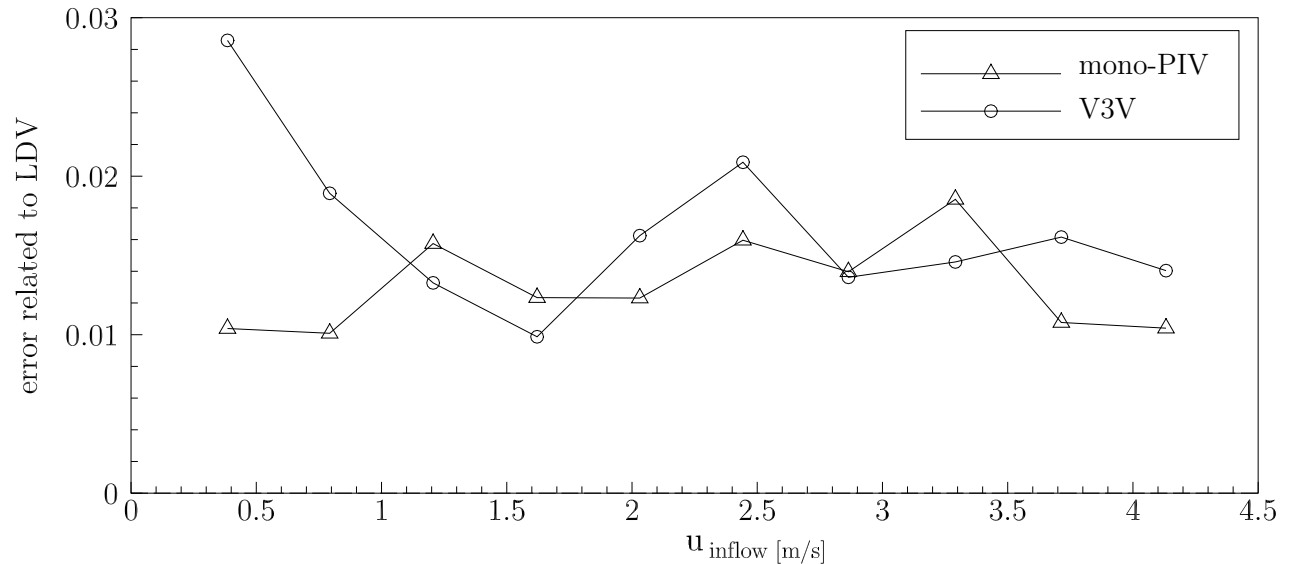


Figure 69: Relative velocity error of mono-PIV and V3V data with reference to LDV measurements.

With relative errors less than 3% for the time-averaged main flow velocity in relation to the LDV measurements, the V3V system achieved reasonable results similar to the 2D-PIV data (see Table 8). Only for the velocity fluctuations $\overline{u'}$ at higher mean velocities above $\bar{u}_{\text{inflow}} = 3.7$ m/s both field-resolving methods (PIV, V3V) are not sufficiently accurate in relation to the LDV results. As the inflow velocity of the current test cases is below 1.7 m/s, these deviations are not relevant for the present measurements in this thesis.

A qualitative comparison of the phase-averaged flow fields measured by V3V and mono-PIV in the midplane of the test section is presented in Figs. 70 and 71 for an arbitrarily chosen phase-angle exemplary shown for the test case FSI-PfS-2a. Due to the limited measurement ranges of both techniques only a small area is directly comparable as depicted in Fig. 70. In this area the position and the extension of the dominating vortical structures are found by both measuring methods (Fig. 71). The PIV results appear to be slightly rougher than the V3V results. This can be explained by the higher spatial resolution of the PIV system ($\Delta x_{PIV}/D = 0.068$ to $\Delta x_{V3V}/D = 0.182$) and the specific post-processing of the V3V data, where the overlap in the

f_{pump} [Hz]	\bar{u}_{V3V} [m/s]	\bar{u}_{PIV} [m/s]	\bar{u}_{LDV} [m/s]	$\overline{u'_{\text{V3V}}}$ [%] (RMS)	$\overline{u'_{\text{PIV}}}$ [%] (RMS)	$\overline{u'_{\text{LDV}}}$ [%] (RMS)
5	0.396	0.389	0.385	2	2	1
10	0.808	0.801	0.793	3	2	2
15	1.222	1.225	1.206	5	4	3
20	1.637	1.641	1.621	3	5	3
25	2.064	2.056	2.031	8	6	5
30	2.494	2.482	2.443	8	7	5
35	2.903	2.904	2.864	8	7	6
40	3.339	3.352	3.291	8	8	8
45	3.774	3.754	3.714	12	13	9
50	4.190	4.175	4.132	23	17	9

Table 8: Time-averaged velocity \bar{u} and velocity fluctuations $\overline{u'}$, given as the root mean square (RMS), in the main flow direction measured by V3V, 2D-PIV and LDV for an increasing pump frequency f_{pump} .

grid interpolation leads to an additional averaging step of the volumetric flow field as already mentioned in Section 4.3.

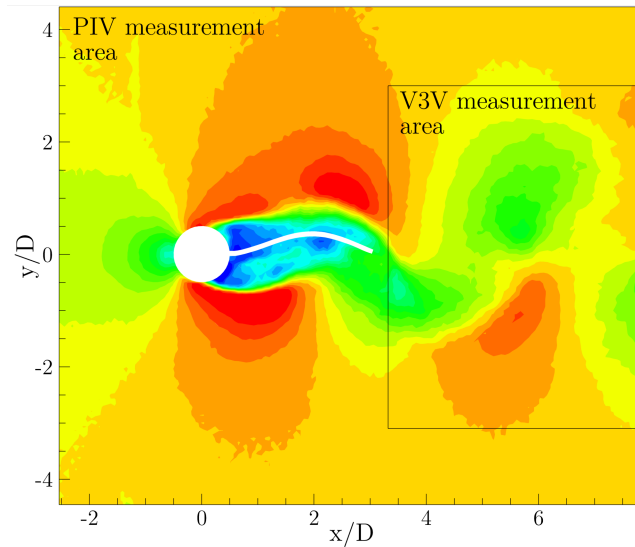


Figure 70: Measurement areas for the PIV and the V3V technique showing the distribution of the velocity magnitude for an arbitrarily chosen phase-angle of the test case FSI-PfS-2a.

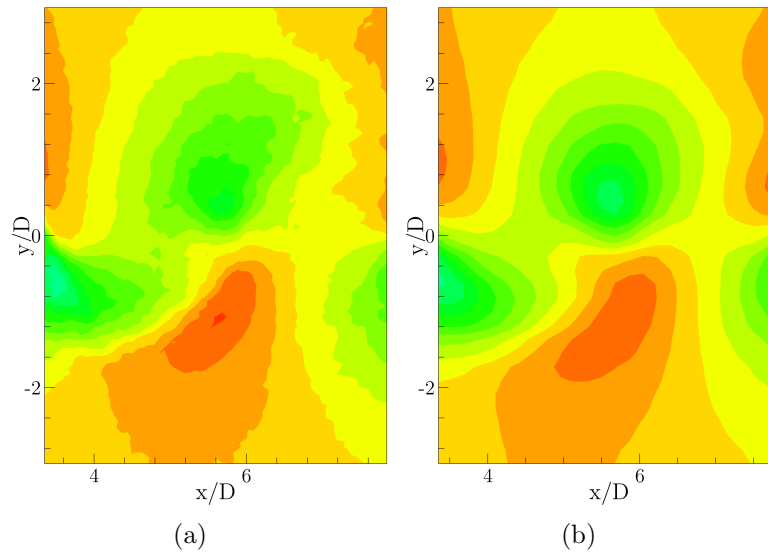


Figure 71: PIV (left) and V3V (right) phase-averaged flow results in the midplane at $z/D = 0$.

7.2. Measurement errors

Experimental investigations always contain measurement errors. In the following section the measurement faults for the applied measurement techniques (PIV, V3V, LLT) in their specific test configurations are considered. Since the particle-image velocimetry is the central part of the present investigations, it should be especially addressed here concerning the propagation of errors (Tropea et al., 2007).

In general, a measured quantity y is influenced by several individual measurement quantities χ_i :

$$y = f(\chi_1, \chi_2, \chi_3, \dots, \chi_n). \quad (122)$$

Based on the Gaussian law of error propagation (Gauss, 1821, 1823, 1826), the resulting error from the error sources χ_i to the derived quantity y is found by using a first-order Taylor series expansion (aborted after the first term under the requirement of small errors $\delta\chi_i$) and is summarized in the total differential of y as follows:

$$\delta y = \frac{\partial f}{\partial \chi_1} \delta \chi_1 + \frac{\partial f}{\partial \chi_2} \delta \chi_2 + \frac{\partial f}{\partial \chi_3} \delta \chi_3 + \dots + \frac{\partial f}{\partial \chi_n} \delta \chi_n, \quad (123)$$

where the first part of each term is denoted the sensitivity factor $c(\chi_i) = \partial f / \partial \chi_i$, $\delta\chi_i$ the individual error value and δy the overall error. Due to different signs of the errors the absolute values are applied to determine the overall absolute maximum error:

$$\delta y = \left| \frac{\partial f}{\partial \chi_1} \delta \chi_1 \right| + \left| \frac{\partial f}{\partial \chi_2} \delta \chi_2 \right| + \left| \frac{\partial f}{\partial \chi_3} \delta \chi_3 \right| + \dots + \left| \frac{\partial f}{\partial \chi_n} \delta \chi_n \right|. \quad (124)$$

In the following paragraphs this method is applied to the PIV measurements to derive the overall error of the flow velocity \mathbf{u} (based on the reference set-up of FSI-PfS-1a, including the inflow velocity u_{inflow} and the PIV time interval Δt).

7.2.1. PIV measurement errors

The PIV method is a field measurement technique for flow velocities \mathbf{u} on a two-dimensional plane inside a flowing medium. In other words, it detects the displacement of particle images $\Delta \mathbf{X}$ within the time interval Δt and thus the flow velocity can be described by:

$$\mathbf{u} = \gamma \left(\frac{\Delta \mathbf{X}}{\Delta t} \right) + \delta \mathbf{u}. \quad (125)$$

The physical magnitude of the flow velocity is based on the magnification factor γ which is identified by a spatial calibration of the specific field of view of the camera in the measurement plane. Since the PIV measurements are based on visualized flow images, these information differ from the physical flow field due to the lag velocity between the tracers and the fluid flow and furthermore due to the spatial calibration. All uncertainties are summarized to the parameter $\delta \mathbf{u}$. In the following paragraphs the main error sources in terms of a PIV measurement are explained and quantified for the present measurement set-up based on Eq. (120) and Table 7.

Calibration γ : The calibration of the present PIV set-up applies a calibration target with the size of the measurement plane (220 mm \times 180 mm) and is inserted at the same positions as the light sheet in the test section of the water tunnel at the different measurement planes. On the target several hundred dots are located according to an equidistant dot-pattern in x - and y -direction. To perform the spatial calibration, an image of the dot-pattern is captured and analyzed. Based on the known distance between the dots, the spatial calibration on the whole measurement plane is performed. Despite the high resolution of the CCD camera, uncertainties in the spatial detection of the grid dots on the calibration target are present. This uncertainty is estimated in the sub-pixel region to $\delta\gamma_a = 0.5$ px. A sensitivity factor for the magnification factor γ is derived from Eq. (120) and is given by its partial derivative with respect to the image projection L_w :

$$c(\gamma_a) = \frac{\partial\gamma}{\partial L_w} = \frac{-l_w \cos\theta}{L_w^2} = \frac{-220 \text{ mm} \cdot \cos(2^\circ)}{(1746 \text{ px})^2} = -7.21 \cdot 10^{-5} \text{ mm/px}^2. \quad (126)$$

The dot-pattern on the calibration target itself is laser-engraved with a precision of $\delta\gamma_b = 20 \mu\text{m}$. The sensitivity factor for this uncertainty is given by:

$$c(\gamma_b) = \frac{\partial\gamma}{\partial l_w} = \frac{\cos\theta}{L_w} = \frac{\cos(2^\circ)}{1746 \text{ px}} = 5.72 \cdot 10^{-4} \text{ 1/px}. \quad (127)$$

Based on this field-based calibration using the calibration target additional errors related to the image distortion by the lens or the camera chip and the influence of the light refraction on the channel glasses can be avoided. On the other hand, further errors are generated by the positioning of the target in the channel. The non-parallel alignment of the calibration target to the laser light sheet is assumed to be less than $\delta\gamma_c = \theta = 2$ deg. Here, the sensitivity factor is estimated to:

$$c(\gamma_c) = \frac{\partial\gamma}{\partial\theta} = \frac{-l_w \sin\theta}{L_w} = \frac{-220 \text{ mm} \cdot \sin(2^\circ)}{1746 \text{ px}} = -4.28 \cdot 10^{-3} \text{ mm/px}. \quad (128)$$

The position error of the whole target with respect to the light plane is assumed to be less than $\delta\gamma_d = 0.5$ mm based on the firm construction of the target mount. Here, γ can be also expressed by $\gamma = l_w/L_w = l_l/f$ under the neglect of the small angular dislocation of the target. In this equation l_l denotes the distance of the camera to the target and f is the focus length of the aperture. The sensitivity factor for the magnification factor related to the position error of the target is given by:

$$c(\gamma_d) = \frac{\partial\gamma}{\partial l_l} = \frac{1}{f} = \frac{l_w}{L_w l_l} = \frac{220 \text{ mm}}{1746 \text{ px} \cdot 1200 \text{ mm}} = 1.05 \cdot 10^{-4} \text{ 1/px}. \quad (129)$$

Particle displacement $\Delta\mathbf{X}$: During the PIV measurements several uncertainties related to the detection of the particle position are present. Laser power fluctuations may affect the particle image projection on the camera chip. Uncertainties in the size of the tracer $\delta\Delta X_a = d_{\text{avg,SHGS}} = 10 \mu\text{m}$ are conceivable. The sensitivity factor is derived from the transformation $\Delta X = \Delta x/\gamma$ from image coordinates (in pixel) to real coordinates (in mm) and is calculated

to:

$$c(\Delta X_a) = \frac{\partial \Delta X}{\partial \Delta x} = \frac{1}{\gamma} = \frac{1}{126 \mu\text{m}/\text{px}} = 7.94 \text{ px}/\text{mm}. \quad (130)$$

In the data processing the position of the tracers is determined by a sub-pixel analysis of the particle image. Several factors like the particle diameter, the particle concentration, potential particle overlaps or the noise level of the image influence this procedure. Based on the analysis of a standard PIV image (Okamoto et al., 2000) the uncertainties of the sub-pixel analysis is determined to $\delta \Delta X_b = 0.02 \text{ px}$.

Since the PIV method is based on statistics, the mismatch of particle pairs is possible. While large mismatches are easily detectable by comparing the resulting velocity vector with the surrounding vectors, smaller errors in the cross-correlation cannot be identified. Again the processing of artificial PIV images (Okamoto et al., 2000) enables a statistical estimation of this uncertainty to a value of about $\delta \Delta X_c = 0.05 \text{ px}$.

Laser pulse generation Δt : The time interval between the two PIV images is controlled by a synchronizer. The manufacturer specifies the uncertainty of the pulse generation to $\delta \Delta t_a = 1 \text{ ns}$. The laser itself has an uncertainty in the laser pulse emission of $\delta \Delta t_b = 5 \text{ ns}$.

Velocity \mathbf{u} : In Section 4.2.1 the following behavior of tracer particles to the flow field is discussed. Especially in liquid flows the following behavior of solid tracer particles is unproblematic (Raffel et al., 1998) according to the small density difference (here $\rho_{\text{SHGS}}/\rho_f = 1.4$). Based on the small particle diameter of $10 \mu\text{m}$ the error related to the velocity lag is estimated to be less than 0.01% ($\delta \mathbf{u}_a = 0.0001 \cdot u_{\text{inflow}} = 0.14 \text{ mm/s}$, for FSI-PfS-1a) (Tropea et al., 2007). Another uncertainty is related to the non-parallel alignment of the light-sheet to the camera chip. As a consequence the angular displacement leads to an artificial out-of-plane velocity component which affects the in-plane measured values. The resulting measured velocity \mathbf{u}_{res} is described as follows:

$$\mathbf{u}_{\text{res}} = \mathbf{u} + w \cdot \tan \Gamma, \quad (131)$$

where w denotes the out-of-plane velocity component. The angular displacement Γ can be assumed to be less than 2 degrees and the out-of-plane velocity component w as approximately 1% of the velocity \mathbf{u} ($\delta \mathbf{u}_b = 0.01 \cdot u_{\text{inflow}} \cdot \tan \Gamma = 0.48 \text{ mm/s}$, for FSI-PfS-1a).

Thus, the main error sources and their corresponding components of the flow velocity measurements are identified. To quantify their specific error level, Eq. (124) is applied to combine the unit-based errors $\delta \chi_i$ with the sensitivity factors $c(\chi_i) = \partial f / \partial \chi_i$ in order to achieve the absolute maximum uncertainty of each error source. Furthermore, all components can now be summarized as the unit conformity is retained. Each main error source is now given in its individual unit related to its maximum failure impact on the flow measurements. All uncertainties related to the PIV measurements are listed in Table 9. In the sixth column the resulting values of each measurement error are given, while in the last column the summarized value of each main error source is calculated.

In the previous paragraphs the errors related to their main error sources are calculated. Since the maximum error of the measured flow velocity of the PIV system should be evaluated, a second error calculation based on the previously obtained values of each error source is performed. To quantify the influence of these main error sources on the velocity \mathbf{u} , its measurement uncertainty $\delta\mathbf{u}_{\text{error}}$ is calculated and reported in Table 10 (again exemplarily presented for the set-up of FSI-PfS-1a). Analog to the calculation of the main errors (γ , $\Delta\mathbf{X}$, Δt and \mathbf{u}) out of their individual components, now the summarized main errors are used to calculate the overall failure $\delta\mathbf{u}_{\text{error}}$. Thus, the sensitivity factor of the calibration error $c(\gamma)$ based on Eq. (125) is given by:

$$c(u_a) = \frac{\partial \mathbf{u}}{\partial \gamma} = \frac{\Delta \mathbf{X}}{\Delta t} = \frac{\Delta \mathbf{x}}{\Delta t} \frac{\Delta \mathbf{X}}{\Delta \mathbf{x}} = \frac{u_{\text{inflow}}}{\gamma} = \frac{1.385 \text{ m/s}}{126 \text{ } \mu\text{m/px}} = 10,992 \text{ px/s}. \quad (132)$$

Similarly, the sensitivity factor of the image displacement $c(\Delta\mathbf{X})$ is given by:

$$c(u_b) = \frac{\partial \mathbf{u}}{\partial \Delta \mathbf{X}} = \frac{\gamma}{\Delta t} = \frac{126 \text{ } \mu\text{m/px}}{200 \text{ } \mu\text{s}} = 630 \text{ mm/(px s)}. \quad (133)$$

The sensitivity factor of the laser pulse generation $c(\Delta t)$ is based on the general definition of the flow velocity $\Delta\mathbf{x}/\Delta t$ and is obtained by:

$$c(u_c) = \frac{\partial \mathbf{u}}{\partial \Delta t} = -\frac{\Delta \mathbf{x}}{\Delta t^2} = -\frac{\mathbf{u}}{\Delta t} = \frac{1.385 \text{ m/s}}{200 \text{ } \mu\text{s}} = -3.46 \cdot 10^6 \text{ mm/s}^2. \quad (134)$$

The uncertainty related to the calibration is calculated to $u_\chi(\gamma) = 2.75 \text{ mm/s}$, the image displacement including the acquisition and the analysis of the particle motion is determined to $u_\chi(\Delta\mathbf{X}) = 81.90 \text{ mm/s}$ and the velocity failures are summarized to $u_\chi(\mathbf{u}) = 0.62 \text{ mm/s}$. In contrast, the laser pulse generation error is negligible with $u_\chi(\Delta t) = 0.02 \text{ mm/s}$ according to the high temporal resolution of the synchronizer. The sum of these errors is calculated to $\delta\mathbf{u}_{\text{error}} = 85.29 \text{ mm/s}$ (6.16% of u_{inflow} for FSI-PfS-1a). Obviously, the image displacement causes the largest measurement uncertainty. This circumstance shows the significant impact of the chosen time interval Δt on the measurement results. With decreasing particle displacements between both images, the measurement error increases. To lower this error source, Δt is adapted to the specific inflow velocity during preliminary experiments to find the best fitting compromise between the time interval and the particle displacement correlation possibility in the PIV processing. However, it must be assumed that PIV measurements with small particle displacements are affected by higher errors (for example in the wake of a solid body). The relative error of the velocity measurements related to maximum and minimum inflow velocity are calculated to be 5.05% for $u_{\text{inflow},4x} = 1.69 \text{ m/s}$ and 5.59% for $u_{\text{inflow},3b} = 0.55 \text{ m/s}$ depending on the inflow velocity and the chosen time interval (low inflow velocity \rightarrow long Δt , high inflow velocity \rightarrow short Δt). Since a broad distribution of flow velocities are assumed to be present in the whole measurement area and the above mentioned error values are only calculated using the specific inflow velocity of the test cases, a general conclusion on the measurement errors is not reasonable. As already mentioned, the measurement of lower flow velocities is affected by higher errors. To illustrate this issue Fig. 72 shows the summarized relative flow velocity error $\delta\mathbf{u}_{\text{error}}$ over the most-likely present flow velocity \mathbf{u} for the three applied PIV time intervals

$\Delta t = 200, 400$ and $600 \mu\text{s}$. This figure is based on the previously presented propagation of errors by applying the different time intervals Δt to the sensitivity factor of the image displacement $c(\Delta \mathbf{X})$. It shows that lower flow velocities process an increased uncertainty especially for a short Δt . In contrast, higher velocities are well measured due to the increased particle displacement. The high errors for low velocities should be considered for the comparison for instance with numerical data, e.g. in the wake behind a structure. To enhance the final flow fields, a phase-averaging method (which will be described later in Section 7.4.1) is applied in the present thesis.

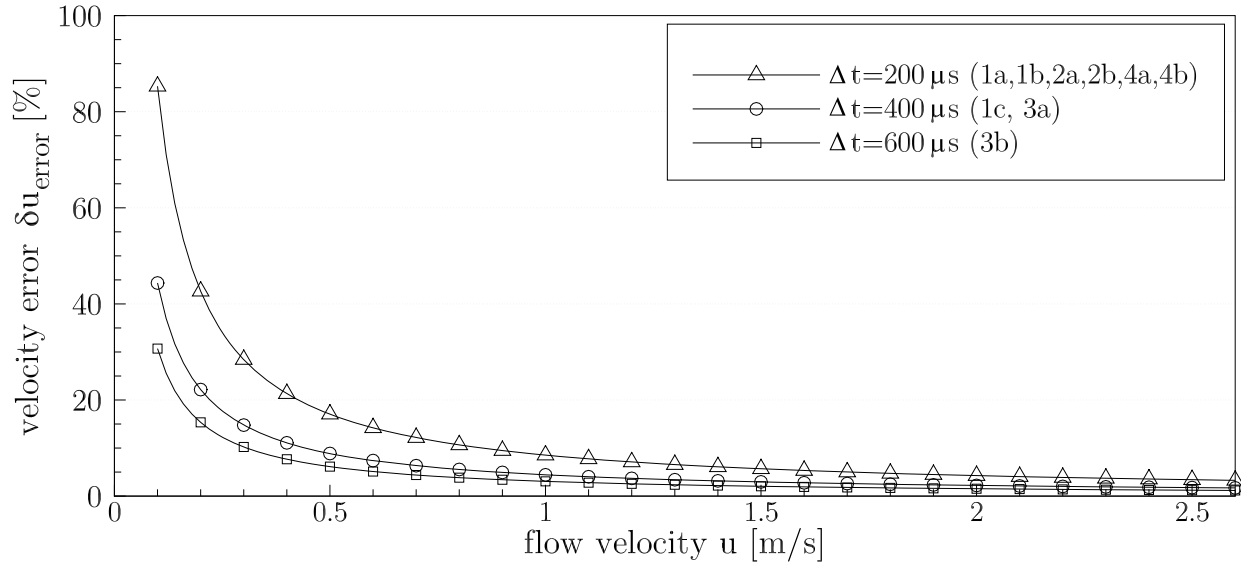


Figure 72: Summarized velocity error $\delta \mathbf{u}_{\text{error}}$ of the mono-PIV measurements over the local flow velocity \mathbf{u} .

parameter χ_i	Category	Error source i	$\delta\chi_i$	$c_{\chi_i} = \partial f / \partial \chi_i$	$u_{\chi}(c_{\chi_i}) = c_{\chi_i} \cdot \delta\chi_i $	Error $\sum u_{\chi_i}$
γ (mm/px)	Calibration	a) reference image b) physical distance c) target alignment d) target position	0.50 px 0.02 mm 0.035 rad 0.5 mm	$-7.21 \cdot 10^{-5}$ mm/px ² $5.72 \cdot 10^{-4}$ 1/px $-4.28 \cdot 10^{-3}$ mm/px $1.05 \cdot 10^{-4}$ 1/px	$3.60 \cdot 10^{-5}$ mm/px $1.15 \cdot 10^{-5}$ mm/px $1.50 \cdot 10^{-4}$ mm/px $5.25 \cdot 10^{-5}$ mm/px	$2.50 \cdot 10^{-4}$ mm/px
$\Delta \mathbf{X}$ (px)	Acquisition Analysis	a) laser fluctuations b) sub-pixel analysis c) mismatching error	$1.00 \cdot 10^{-3}$ mm 0.02 px 0.1 px	7.94 px/mm 1.00 1.00	$7.94 \cdot 10^{-3}$ px 0.02 px 0.1 px	0.13 px
Δt (s)	Acquisition	a) pulse generator b) pulse time	$1.00 \cdot 10^{-9}$ s $5.00 \cdot 10^{-9}$ s	1 1	$1.00 \cdot 10^{-9}$ s $5.00 \cdot 10^{-9}$ s	$6.00 \cdot 10^{-9}$ s
\mathbf{u} (m/s)	Velocity	a) lag velocity b) out-of-plane-velocity	0.14 mm/s 0.48 mm/s	1 1	0.14 mm/s 0.48 mm/s	0.62 mm/s

Table 9: Calculation of uncertainties for the main error sources related to the present PIV measurements (here, exemplarily for FSI-PfS-1a).

parameter χ	Error source i	$\delta\chi_i$	$c_{\chi_i} = \partial f / \partial \chi_i$	$u_{\chi}(c_{\chi_i}) = c_{\chi_i} \cdot \delta\chi_i $
γ	a) Calibration error	$2.50 \cdot 10^{-4}$ mm/px	10,992 px/s	2.75 mm/s
$\Delta \mathbf{X}$	b) Image displacement	0.13 px	630 mm/(px s)	81.90 mm/s
Δt	c) Laser pulse generation	$6.00 \cdot 10^{-9}$ s	$-3.46 \cdot 10^6$ mm/s ²	$2.08 \cdot 10^{-2}$ mm/s
\mathbf{u}	d) Velocity	0.62 mm/s	1.00	0.62 mm/s
			Sum $\delta \mathbf{u}_{\text{error}}$	85.29 mm/s (6.16 %)

Table 10: Calculation of uncertainties for the velocity \mathbf{u} for the present PIV set-up (here, exemplarily for FSI-PfS-1a).

7.2.2. V3V measurement errors

Most of the considerations for the PIV error analysis can be transferred to the V3V method. Similar uncertainties in both methods are the general findings concerning the calibration process, the time acquisition and the particle following behavior (despite the use of the much larger polyamide particles for the V3V measurements, their following behavior in water in the applied velocity range is again approved (Tropea et al., 2007)).

An obvious difference of the V3V method to a standard PIV set-up is the extension of the laser light sheet to a volume. Therefore, all related errors (i.e., the alignment of the camera optic to the light sheet) are non-relevant. Nevertheless, the errors due to the calibration remain and are slightly increased due to the manual positioning of the calibration target in the different measurement planes. On the other hand, only a successful and sufficiently precise V3V calibration (see Fig. 66) enables the three-dimensional reconstruction of the particle positions and their velocity vectors.

Related to the image analysis the manufacturer (TSI[®]) specifies an uncertainty in the identification of the particle positions of 20 μm in the x - and y -directions and 80 μm in the z -direction. Since a particle tracking algorithm is used for the velocity processing the critical mismatching of particles (by far the largest error in PIV) should be reduced. However, it has to be considered that many three-dimensionally distributed particles are projected on two-dimensional images and the overlap of particles in these images is inevitable. As a consequence the mismatch of particles is assumed to be again the most critical error source. This is also supported by the low ratio of matched particle triplets in both frames (t_0 and $t_1 = t_0 + \Delta t$). Here, the relevant value is found to be 60% of the identified particles (for turbulent flows). That means that about 40% of the particles in each camera image cannot be applied to construct a triplet. This may result in a false triplet construction of another particle as they appear as a possible candidate for the next triplet construction. All together, similar uncertainties found for the PIV method are expected to be also present in the V3V technique. Moreover, due to the three-dimensional measurement volume and the reduced spatial resolution an increased uncertainty for the velocity processing is assumed in comparison to the PIV set-up. Since only qualitative measurements of three-dimensional structures are intended, the limitations of the V3V system are acceptable.

7.2.3. LLT measurement errors

The manufacturer (micro-Epsilon[®]) of the applied LLT sensor (scanControl 2750-100) specifies the average absolute error of the position measurement to ± 15 to 40 μm (micro Epsilon, 2013) in-line to the sensor (y -direction) and depending on the chosen measurement range (small measurement range \rightarrow low error, larger measurement area \rightarrow increased error). Related to the applied maximum measurement range of about 33 mm ($\Delta y/D = \pm 1.5$ in FSI-PfS-2b) in y -direction, the relative error is calculated to 0.10%. The error in the other direction is based on the chosen resolution and the applied measurement range of the sensor. In the present measurements the maximum resolution of 640 measurement points is chosen. Based on the maximum measurement range of 140 mm, the resolution of this direction is calculated to 0.22 mm.

Similar to the PIV measurements the refraction on the glass of the test section alters the

structural position measurement. Therefore, a corresponding linear calibration of the sensor is applied. Uncertainties are assumed by the calibration process. Based on an error analysis of the similar PIV calibration, a minor influence of the calibration lower than 0.5% on the structural measurement data is assumed. Since the LLT is a more direct and less complex measurement method compared to PIV, the entire uncertainties are expected to be lower than 1%.

7.3. Flow conditions

Several preliminary tests are performed to find the best working conditions for each test case in terms of appropriate structural displacements, good reproducibility and measurable and moderate swiveling frequencies within the turbulent flow regime. Regarding the flow around the structure, in all benchmark cases the flow is in the sub-critical regime. That means the boundary layers are still laminar, but transition to turbulence takes place in the free shear layers evolving from the separated boundary layers behind the apex of the structure. Except the boundary layers at the section walls the inflow is found to be nearly uniform (see Fig. 73).

Furthermore, a low inflow turbulence level of $Tu_{\text{inflow}} = 1/u_{\text{inflow}} \cdot \sqrt{1/2 \cdot (\overline{u'^2} + \overline{v'^2})} = 0.02$ is measured by laser-Doppler velocimetry (LDV). All experiments are performed with water under standard conditions at $T = 20^\circ \text{ C}$ ($\rho_f = 998.20 \text{ kg m}^{-3}$, $\mu_f = 1.0 \cdot 10^{-3} \text{ Pa s}$).

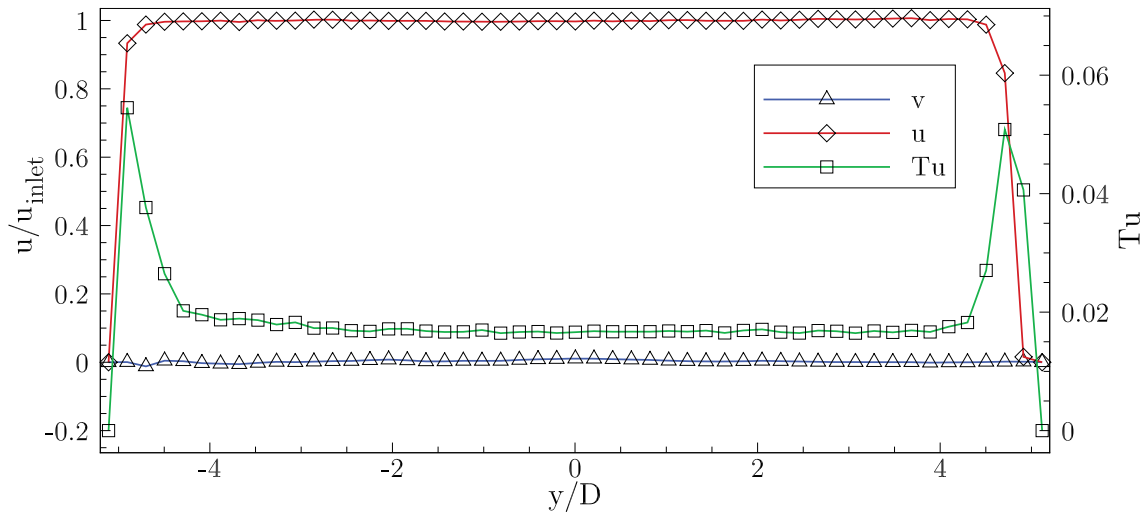


Figure 73: Inlet velocity conditions in y-direction (measured by LDV).

7.4. Post-processing procedures

7.4.1. Generation of phase-resolved data

Similar to the considerations on turbulent flows in Section 2.3 each flow characteristics of a FSI problem can be written as a function $f = \bar{f} + \tilde{f} + f'$, where \bar{f} describes the global mean part, \tilde{f} the quasi-periodic part and f' a random turbulence-related part (Reynolds and Hussain, 1972; Cantwell and Coles, 1983). This splitting can also be expressed in the form $f = \langle f \rangle + f'$, where $\langle f \rangle$ is the phase-averaged part, i.e., the mean at a constant phase. In order to be able to compare numerical results and experimental measurements, the irregular turbulent part f' has to be averaged out. This measure is indispensable due to the nature of turbulence, which is

fully irregular and chaotic. Thus, minor changes for example in the initial conditions may lead to a completely different time history of the flow field, in both cases, the measurements and the predictions. Therefore, reasonable comparisons are only possible based on statistical data. The lowest level of these statistical data would be the time-averaged mean data. However, for a quasi-periodic phenomenon as in the present FSI test cases the phase-averaged data are much more reasonable since they contain more information than the global mean. Therefore, the present data are phase-averaged to obtain only the phase-resolved contribution $\langle f \rangle$ of the problem. In this section the procedure to generate phase-resolved results for the experiments will be explained. For the numerical URANS predictions presented in Section 10.2 no phase-averaging is required since turbulence-related small-scale fluctuations of the flow field are not appearing in this approach as explained in Section 2.3.

In experimental investigations of quasi-periodic fluid-structure interactions often the deflection or deformation of the structure is used for the phase detection. A direct and a reconstruction method can be applied. The direct method uses one or more sensors to detect a pre-specified phase moment of the structure deflection. By reaching this moment, the sensor indicates a trigger impulse which controls the flow measurements, e.g., the PIV or V3V system. The advantage of this method is the small post-processing effort and the direct control of the measured structure position (Breuer and Kalmbach, 2011).

The second method reconstructs the averaged period of the structural motion out of a sequence of measurements carried out for the more or less randomly chosen, non-predefined moments in time. Gomes and Lienhart (2006) use this method with a FPGA (Field Programmable Gate Array) monitoring an angular position sensor for the front cylinder, the PIV system and an internal clock. In the post-processing step the measured periods are detected and the time-phase angle⁵ within the structure cycle is computed. Afterwards, the data are sorted into a reference structural motion period and a predefined number of corresponding phase-averaged fluid velocity fields. To apply this method, a directly measurable quantity containing the phase information of the structure deflection is necessary. In the case of Gomes and Lienhart (2006) the angular displacement of the front cylinder is directly measured by a magnetic field sensor. In the present set-up an appropriate directly measurable quantity is not available, since the (front) cylinder/cone is fixed on the back-plate of the test section (except for FSI-PfS-2b). Therefore, a similar but less complex reconstruction method (Kalmbach and Breuer, 2013b; De Nayer et al., 2014) is applied in the present work. This method consists of the laser line triangulation sensor (described in Section 4.4) and the synchronizer of the PIV/V3V system (see Fig. 68). Each measurement pulse of the PIV/V3V system (measurement frequency: 6 Hz) is detected in the data acquisition of the LLT sensor, which measures the structural deflection with a measurement frequency of 800 Hz simultaneously with the PIV or V3V system. In comparison to the method of Gomes and Lienhart (2006) the measurement frequency of the present trigger signal (LLT sensor) has a reduced temporal resolution, but still provide enough information to precisely quantify the structural deflection in time and phase.

⁵The time-phase angle declares in which phase of a period but also at which time, for example in measurement series, a quantity is located.

Out of the structural data the last measurable point S near the edge of the structure (see Fig. 74) is monitored. With the resulting displacements as a function of the time, the reference period of the structures movement is calculated.

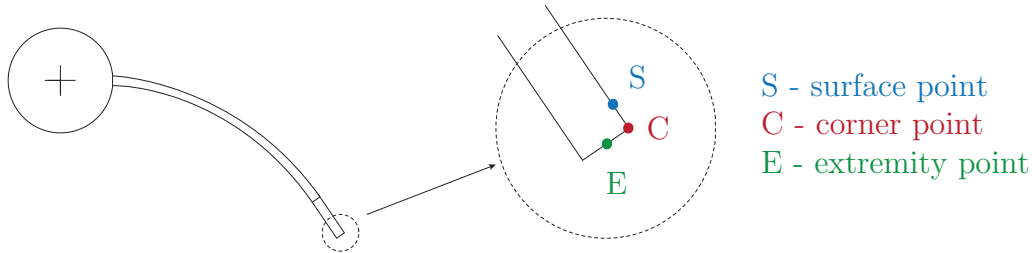


Figure 74: Sketch of the measurement points exemplarily shown for FSI-PfS-2a.

Due to the phase-to-phase fluctuations of the structure motion, its period length also deviates. For the determination of the period length, the zero-crossings from negative to positive values of the y -displacements are used. Applied to the whole time series of y -displacements, this method provides the beginning and the end of all periods independent of their period length as displayed in Fig. 75a. Afterwards, the average period duration is calculated by arithmetically averaging all period lengths found in the previous step leading to the reference period duration.

As a first step of the averaging procedure the average y -displacements covering all available measuring data from the LLT sensor in time and space are calculated. For this purpose, each period of the swiveling motion with varying period length is divided into n equidistant segments. n is calculated based on the measurement rate of the LLT sensor of 800 Hz in relation to the swiveling frequency f of the structure leading to $n = 800 \text{ Hz}/f$. In the present thesis f ranges in most case around $\mathcal{O}(10)$ leading to typical values for n of about 80. For each individual segment an average value of the y -displacements is calculated resulting in a reference period consisting of n data points. With this fine decomposition allowing a detailed representation of the structure deformation, each segment only contains a small number of flow measurements ($\approx 5 - 15$). Therefore, the phase-angle interval per segment has to be enlarged by a second averaging step for the structure and fluid data. The reference period and all recorded periods are now split into m segments covering larger equidistant phase-angle intervals (Fig. 75b) than before. In all present benchmark cases m is set to 23, since it is a good compromise regarding a reasonable resolution of the phase-averaged motion and the number of measurements building each specific moment of the phase-averaged representation. Finally, the fluid and structure measurements are assigned to the specific time-phase angle of the reference period, enabling the phase averaging of the PIV, V3V and structure measurements.

For the PIV experiments 1100 single measurements and for V3V 550 single measurements are taken enabling a phase-averaging out of about 48 PIV measurements and about 24 V3V measurements per phase angle. This is a compromise between the result quality and the measurement issues (the amount of data to be stored, the resulting post-processing costs, especially for V3V, and the limitations of the recording time of the LLT sensor). Preliminary studies carried out yield that the averaging of approximately 45 PIV flow measurements is sufficiently accurate to produce a characteristic mean flow field at its particular phase angle.

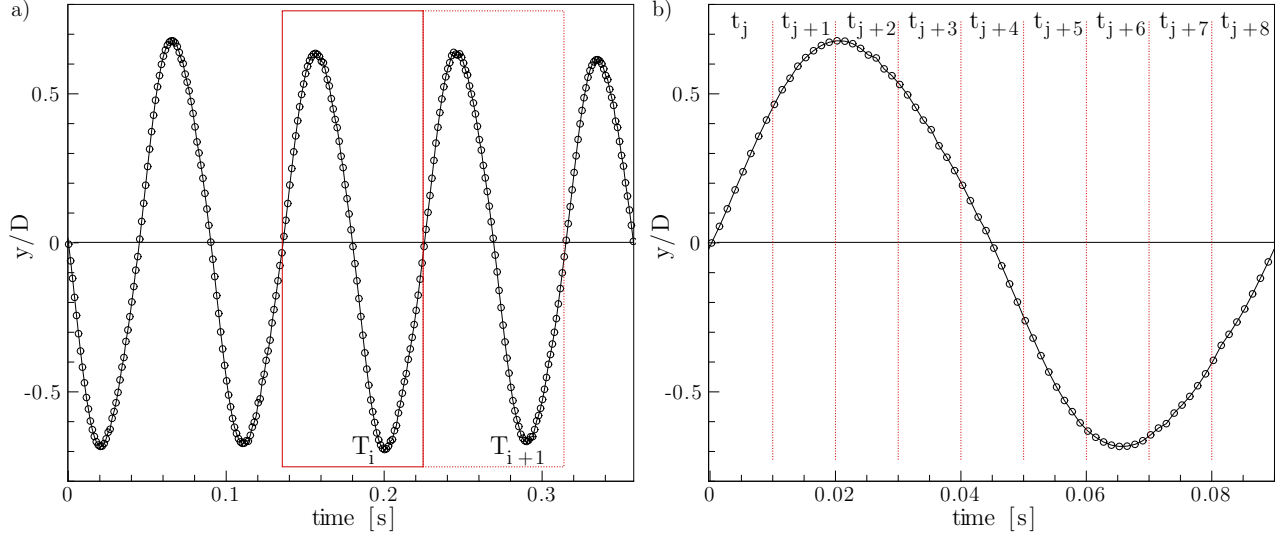


Figure 75: Phase-averaging procedure: a) Period detection in y -displacements at the point S near the trailing edge of the structure, b) Period splitting into m parts (here for visibility only 9 parts) for the phase-averaging method.

Despite this evaluation, the obtained flow fields (e.g., Fig. 70) are not fully smooth. To achieve a smoother flow field much more measurements per phase angle would be necessary. It is found that about 300 measurements produce noticeably smoother results, but increase the data acquisition time, the data storage and the processing time disproportionately. For the V3V measurements a lower number of measurements are found to be necessary to produce a sufficiently accurate flow result. Here, the averaging mechanisms in the velocity vector processing and the coarse grid resolution are responsible for the faster convergence requiring fewer measurements. Furthermore, the V3V measurements are intended to be only of qualitative kind.

The test cases FSI-PfS-1*x*, 2*x* and 4*x* are processed as explained in the previous paragraphs. In FSI-PfS-4*x* only the reference point is changed to the center of the cylinder at the measurement plane $z/d = 20.63$. In FSI-PfS-3*x* three planes are measured. Since the phase period can only be defined once, it is linked to the structure deflection at the large cone diameter ($z/D = -2.72$). All structure and flow results at the middle ($z/D = 0$) and small cone diameter ($z/D = 2.72$) are related to this period definition.

7.4.2. Proper orthogonal decomposition

The study of the eddy structures is a common way in fluid mechanics to identify and compare different classes of turbulent flows. The knowledge of the turbulent structures can lead to modifications, optimizations or new designs of engineering solutions including flow phenomena like drag reduction, heat transfer, combustion, noise suppression or fluid-structure interactions. In the present thesis the proper orthogonal decomposition (POD) is chosen to identify the major vortical flow structures and to estimate their energy content. The POD was first described in Lumley (1981) as a method to obtain information concerning the large-eddy structures in a flow. The flow structures are identified by the most energy-laden eigenfunctions in the decomposition under the condition that the size of the eddies increases roughly with their energy

content.

In this thesis the "snapshot POD" method by Sirovich (1987) is applied. Here, each instantaneous PIV measurement is seen as a snapshot of the flow. Especially in highly unsteady flows like assumed for the present FSI test cases, a large amount of PIV measurements at one plane is required for the POD analysis.

In Section 7.4.1 the flow is described by the decomposition $f = \bar{f} + \tilde{f} + f'$, where \bar{f} describes the global mean part, \tilde{f} the quasi-periodic part and f' a random turbulence-related part. In Section 2.3 the more general consideration of Reynolds and Hussain (1972) summarizes all unsteady flow fluctuations (e.g., the quasi-periodic part \tilde{f} and the random turbulence-related part f') to the global unsteady part $\hat{f} = \tilde{f} + f'$ of the flow.

As a first step in the two-dimensional POD method, the mean field $\bar{f}(\mathbf{x})$ of the chosen flow quantity $f(\mathbf{x})$ (i.e., the flow velocity $\mathbf{u}(\mathbf{x})$ or the vorticity $\boldsymbol{\omega}(\mathbf{x})$) is computed. To analyze only the unsteady part

$$\hat{f}^m(\mathbf{x}) = f^m(\mathbf{x}) - \bar{f}^m(\mathbf{x}) \quad (135)$$

of the flow the mean field $\bar{f}(\mathbf{x})$ is subtracted from all instantaneous flow fields (here, the single PIV measurements) marked by the upper index $m = 1$ to M in the two-dimensional flow field (Sirovich, 1987). Applied to the velocity field $\hat{\mathbf{u}}(\mathbf{x}) = (\hat{u}(\mathbf{x}), \hat{v}(\mathbf{x}))$ the matrix of the fluctuating velocity field is given by

$$\hat{\mathbf{u}}(\mathbf{x}) = [\hat{\mathbf{u}}(\mathbf{x})^1 + \hat{\mathbf{u}}(\mathbf{x})^2 + \dots + \hat{\mathbf{u}}(\mathbf{x})^M]. \quad (136)$$

To correlate all instantaneous PIV measurements to each other, the autocovariance matrix \mathbf{C} is predicted as:

$$\mathbf{C} = \hat{\mathbf{u}}(\mathbf{x})^T \hat{\mathbf{u}}(\mathbf{x}) \quad (137)$$

and the related eigenvalue problem

$$\mathbf{C} \mathbf{A}^i = \lambda_i \mathbf{A}^i \quad (138)$$

is solved. The eigenvectors of the correlation matrix are the temporal coefficients $\mathbf{A}^i = (A_1^i, A_2^i, \dots, A_M^i)$. The solutions are ordered according to the size of the eigenvalues:

$$\lambda^1 > \lambda^2 > \dots > \lambda^I = 0 \quad (139)$$

and are denoted as POD modes from $i = 1$ to I . The POD-based flow velocity \mathbf{u} in the modes λ_i are computed as follows:

$$\mathbf{u}_i = \frac{1}{M \lambda_i} \sum_{m=1}^M A_m^i \hat{\mathbf{u}}^m \quad (140)$$

Since the eigenvalues are a measure of the kinetic energy in each mode, the energy content E_i is given by:

$$E_i = \frac{\sum_{i=1}^m \lambda_i}{\sum_{i=1}^I \lambda_i}. \quad (141)$$

In Fukunaga (1990) it is shown that the amount of the total kinetic energy from the velocity fluctuations in an unsteady flow field associated with a given POD mode is proportional to the

corresponding eigenvalue. As a consequence, the ordering of the eigenvalues and eigenvectors in Eq. (139) ensures that the most important modes in terms of the energy content are the first modes. Usually, this means that the first modes will be associated with major large-scale flow structures which dominate the flow. By using the vorticity ω as the input quantity f for the POD analysis, the enstrophy of the flow results. Similar to the total kinetic energy the enstrophy is directly related to the kinetic energy of the flow.

As a consequence of the correlation of the flow fields and the following summation of the kinetic energy in each node, the size of the grid has a direct influence on the total kinetic energy calculated for each POD mode. Therefore, only equal grids or grid-related energy quantities are comparable to each other. In the present thesis a Matlab-based post-processing procedure is applied to obtain the single POD modes and their corresponding energy levels.

8. Preliminary studies

In this section several preliminary studies concerning the applied material properties and the flow around the rigid structure of each test case are carried out.

To improve the understanding how the fluid-structure interaction alters the flow physics, the experiments concerning the flow around the rigid structures are developed and both cases are compared to each other (see Section 8.1). To determine the properties of the applied materials (EPDM rubber, para-rubber, polyamide and polyethylene) used in this thesis, additional structural tests are developed and performed. These measurement results also provide an additional data source for the comparison with structural mechanics computations. The set-up and the results of these tests are presented in Section 8.2.

8.1. Flow measurements around rigid structures

In the following paragraphs the flow around the rigid bluff bodies for each test case is examined. Contrary to the FSI investigations presented in Section 10, the structures are fixed and non-deformable. The PIV measurements are carried out in the middle of the test section ($z/D = 0$) and use the same measurement set-up as explained in Section 7.1. Unfortunately, only averaged results are available due to the lack of an appropriate phase-averaging method for the vortex shedding. While in the FSI investigations the phase-averaging of the flow field is based on the quasi-periodic deflection of the flexible structure, here this approach is not applicable. A reliable method would directly measure the flow velocity at a fixed measurement point in the fluid. Invasive, time-resolved techniques like constant temperature anemometry (CTA) or pressure-based velocity measurements could not be employed in the experimental set-up due to several circumstances (mounting of the probe, positioning of the probe in the flow, effect of the probe on the flow). For the present experimental set-up these restrictions do not apply to non-invasive techniques like LDV. However, tentative LDV measurements exhibit that the temporal resolution of this technique is not sufficient for an assured phase-averaging signal. Especially, the high concentration of the tracer particles necessary for the LDV measurements prohibit the PIV measurements due to the overexposure of the particles images.

As a consequence, only time-averaged results for the flow fields are presented in the following paragraphs.

8.1.1. FSI-PfS-1x/2x

The test cases FSI-PfS-1x and 2x are based on an almost equal geometry⁶. Therefore, these cases are summarized to one experiment for the rigid structures. Furthermore, all test cases related to FSI-PfS-1x and 2x refer to the inflow velocity of $u_{\text{inflow}} = 1.385$ m/s (except FSI-PfS-1c). Therefore, the experiment on the fully rigid structure is also run with this inflow condition. Since a 2 mm metal plate substitutes the rubber or polymer plate, their deformation is almost inhibited. The experiments showed that minor structural deflections are still present despite the great stiffness of the metal. Reasons are supposed to be the clamping of the metal plate

⁶The geometric difference of FSI-PfS-1b in relation to the other cases is the plate thickness which is neglected.

in the cylinder. Here, the manufacturing tolerances of the cylinder nut allow a small angular displacement which results in the displacements on the plate tip in the order of one millimeter, i.e., $y/D \approx 0.045$.

The time-averaged result for the velocity magnitude ($\sqrt{(u^2 + v^2)}/u_{\text{inflow}}$) over 1000 single PIV measurements is depicted in Fig. 76a.

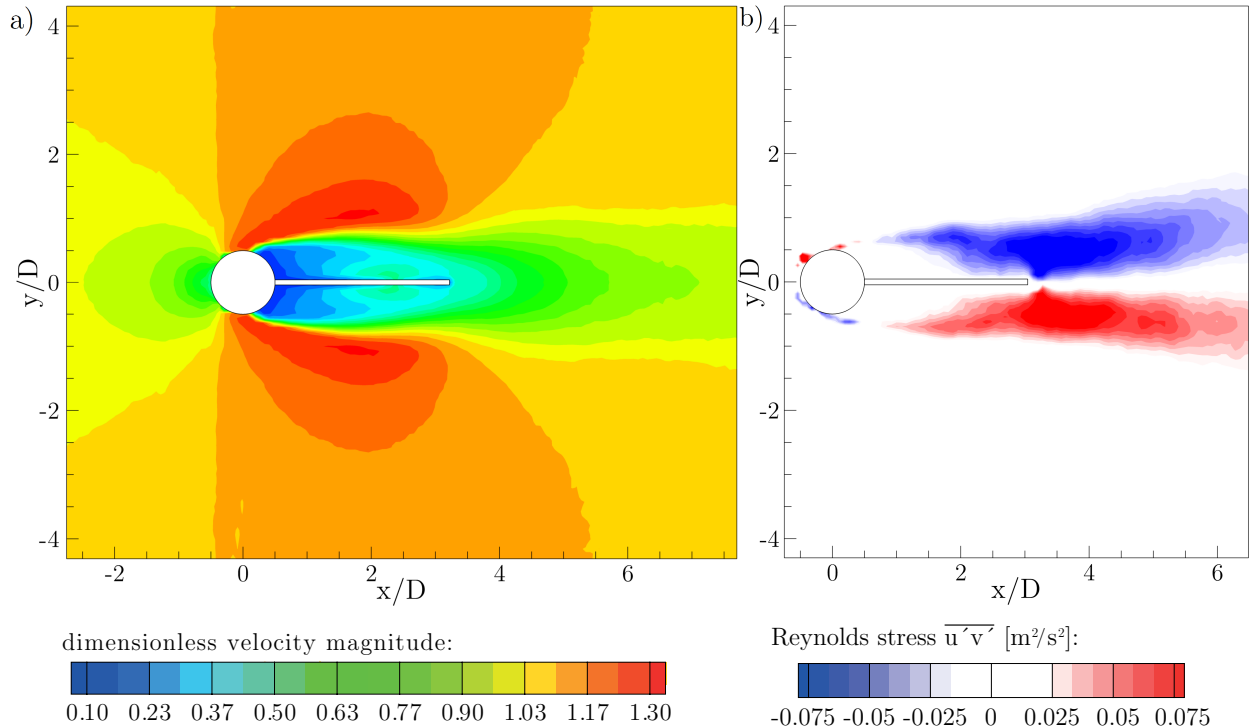


Figure 76: Time-averaged PIV results of the flow around the fixed structure related to the test configuration of FSI-PfS-1x and 2x at $z/D = 0$ for a) dimensionless velocity magnitude and b) Reynolds shear stress $\overline{u'v'}$.

The flow field is similar to time-averaged flow around a long circular cylinder under the same flow conditions (Breuer, 2002). In front of the rigid structure the stagnation point is present, while above and below the cylinder the acceleration areas are visible. Behind the cylinder a long wake is formed including low flow velocities. Single PIV measurements indicate that vortex shedding is present for this flow state despite the splitter plate attached to the cylinder. Due to the lack of a proper phase-averaging method, the characteristic alternating vortex pattern are not visible in the result. Close to the end of the splitter plate the wake area is slightly broaden, which is assumed to be an effect of the already mentioned small vibrations of the plate tip.

The time-averaged results of the Reynolds shear stress $\overline{u'v'}$ are given in Fig. 76b. Again no indication of vortex shedding is apparent, here. The maximum Reynolds stresses are present in the vicinity of the rigid structure. Furthermore, the stresses are almost anti-symmetric according to the reversed trend of the velocity fluctuations in the cross-flow direction.

To analyze the energy content of the flow, the POD⁷ (see Section 7.4.2) is applied to the PIV measurements. The results for the flow velocity components u and v and for the vorticity component ω_z are presented in Fig. 77. Here, only the first ($k_{\text{abs},1\text{st}} = 200.93 \text{ m}^2/\text{s}^2$, $k_{\text{rel},1\text{st}} = 24\%$ of the total turbulent kinetic energy of the flow) and the second mode ($k_{\text{abs},2\text{nd}} = 188.33 \text{ m}^2/\text{s}^2$, $k_{\text{rel},2\text{nd}} = 23\%$ of the total turbulent kinetic energy of the flow) of the POD analysis are included as these two modes contain almost 47% of the total turbulent kinetic energy ($k_{\text{abs},\text{all}} = 824.83 \text{ m}^2/\text{s}^2$, $k_{\text{rel},\text{all}} = 100\%$) present in this flow. The occurrence of the POD-modes and their large energy content is common for flows in which alternating vortices detach (Siegel et al., 2007). Figure 77a and b correspond to the kinetic energy of the streamwise velocity u . Characteristic for this component is the antisymmetric pattern of the energy due to the formation and transportation of the clockwise-rotating (red) and counterclockwise-rotating (blue) vortices behind the rigid structure (along the trajectories of the detached vortices). The energy of the cross-flow velocity component v is also related to the alternating vortex shedding on the cylinder. The first two modes are presented in Fig. 77c and d and rise in the area, where the vortices detach from the shear layers.

To identify the regions where most of the energy related to the velocity fluctuations are present, the POD-based vorticity component ω_z is shown in Fig. 77e and f. Here, the momentum transfer in the shear layers on the upper and lower side of the cylinder is visible in the first and second mode. This energy distribution of the main vorticity component is typical for flows with alternating vortex shedding (Cierpka, 2007). The small regions of kinetic energy close to the plate can be explained by the weak vibrations of the plate during the experiments.

8.1.2. FSI-PfS-3x

The rigid configuration of FSI-PfS-3x applies the inflow velocity of FSI-PfS-3a $u_{\text{inflow}} = 0.969 \text{ m/s}$ ⁸. Again a time-averaging and the POD are performed on 1000 single PIV measurements to analyze the flow situation.

Figure 78a shows the time-averaged velocity magnitude field around the structure at the plane $z/D = 0$ (midplane of the cone). The present flow field is comparable to the flow around the rigid configuration of FSI-PfS-1x and 2x. Again the stagnation point, the upper and lower acceleration areas, the wake and the symmetry of the flow field to the neutral axis ($y/D = 0$) are visible.

The results of the time-averaged Reynolds shear stress is depicted in Fig. 78b and provides a similar stress distribution as obtained for the rigid configuration FSI-PfS-1x and 2x. Again, the maximum stresses are found in the wake of the structure.

The POD analysis of the rigid configuration of FSI-PfS-3x in Fig. 79 also depicts similar results as achieved for the rigid configuration of FSI-PfS-1x and 2x. Therefore, the large regions of high kinetic energy are again related to the vortex shedding for the streamwise and cross-flow

⁷Note that the energy related values are directly dependent on the grid size of the input data. Therefore, the results do not represent the physically stored kinetic energy of the flow. Furthermore, the presented absolute values refer only to the fluctuating velocity since the mean velocity field is subtracted during the POD processing. The present results are only qualitatively evaluated and compared to each-other under the compliance of equal grid sizes.

⁸The presented results are almost equal to the results achieved with the lower inflow velocity of FSI-PfS-3b.

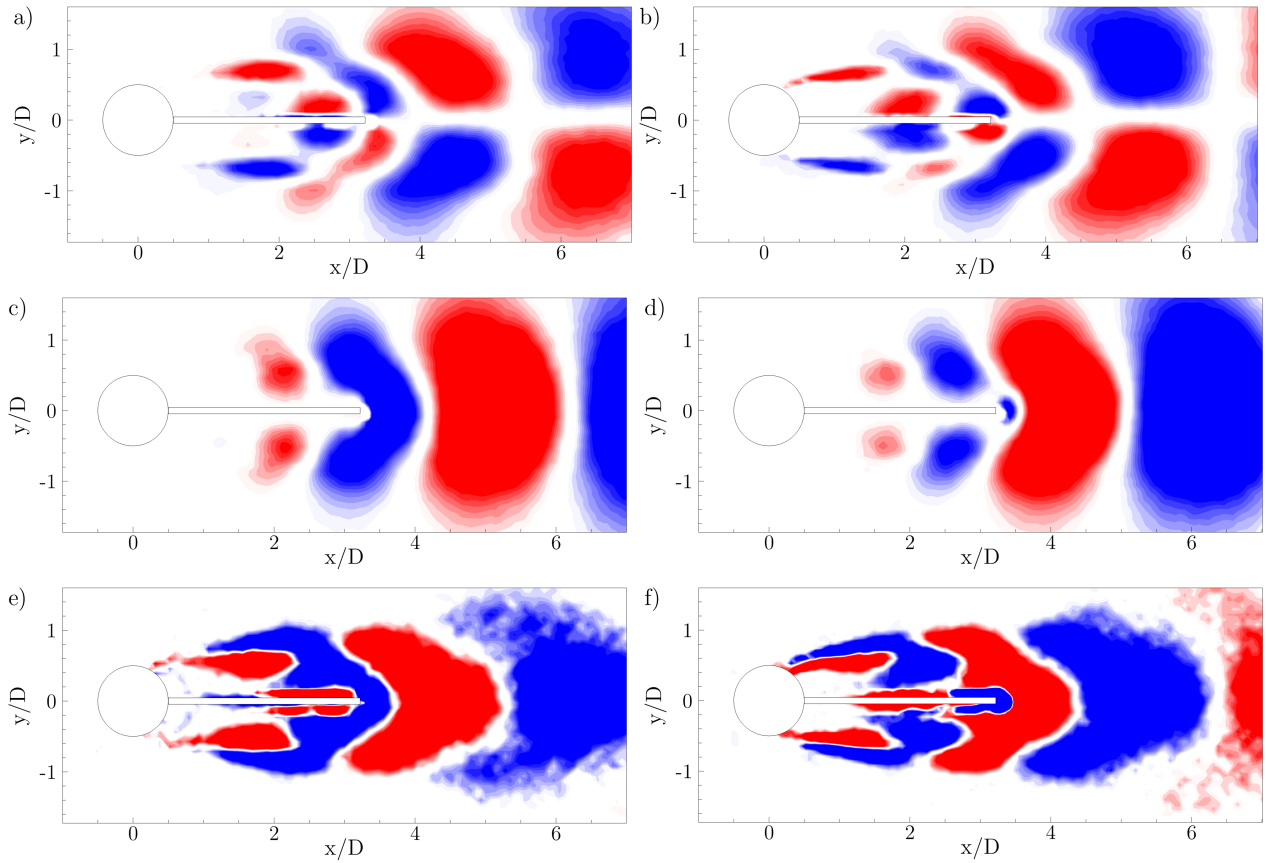


Figure 77: POD analysis of the two-dimensional flow field in the midplane ($z/D = 0$) of the rigid configuration of FSI-PfS-1x and 2x a) velocity component u first mode; b) velocity component u second mode; c) velocity component v first mode; d) velocity component v second mode; e) vorticity component ω_z first mode; f) vorticity component ω_z second mode.

velocity components. The POD-based vorticity field again reveals the shear layers and the broad regions where unsteady flow effects in the vicinity of the rigid structure are present.

The POD analysis calculates the turbulent kinetic energy of the first POD mode to $k_{\text{abs},1\text{st}} = 92.79 \text{ m}^2/\text{s}^2$ which represents $k_{\text{rel},1\text{st}} = 20\%$ of the total turbulent kinetic energy of the flow. For the second POD mode the turbulent kinetic energy is computed to $k_{\text{abs},2\text{nd}} = 80.63 \text{ m}^2/\text{s}^2$, $k_{\text{rel},2\text{nd}} = 18\%$ of the total turbulent kinetic energy of the flow. Both modes together contain almost 38% of the total turbulent kinetic energy ($k_{\text{abs,all}} = 457.46 \text{ m}^2/\text{s}^2$, $k_{\text{rel,all}} = 100\%$) for this flow state in the midplane of the test section.

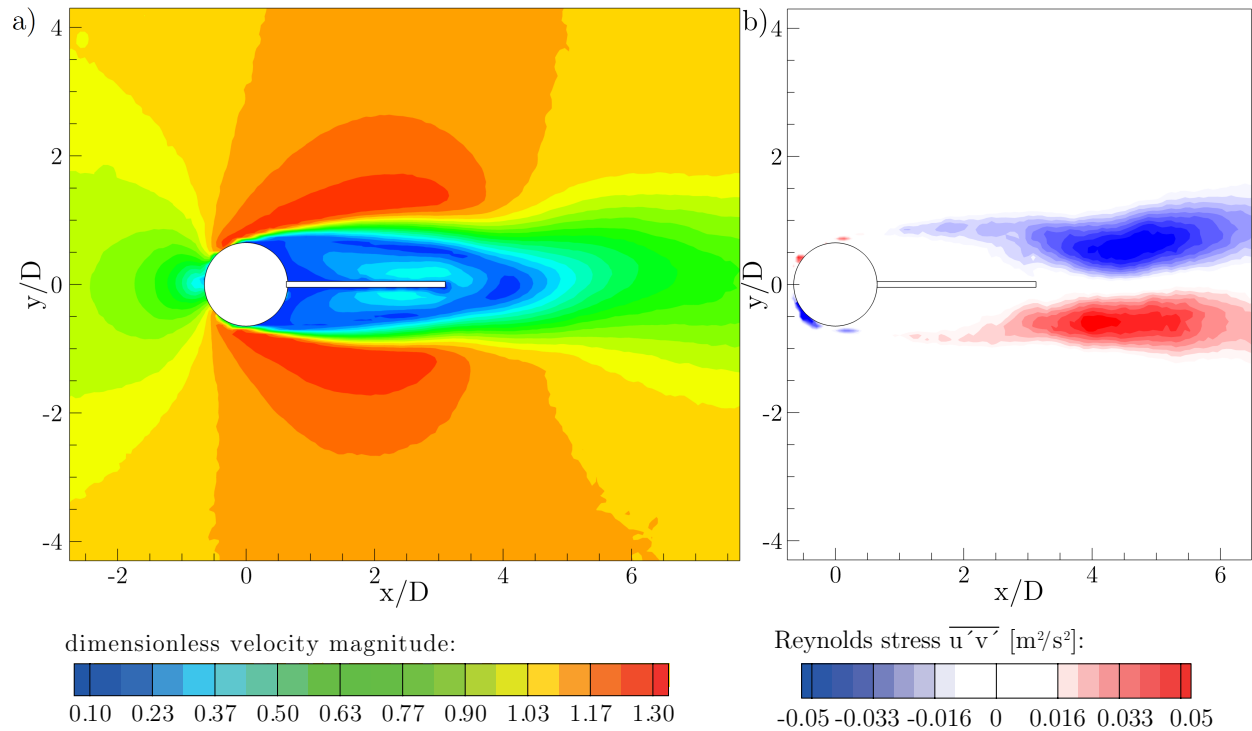


Figure 78: Time-averaged PIV results of the flow around the fixed structure related to the test configuration of FSI-PfS-3x at $z/D = 0$ for a) dimensionless velocity magnitude and b) Reynolds shear stress $\overline{u'v'}$.

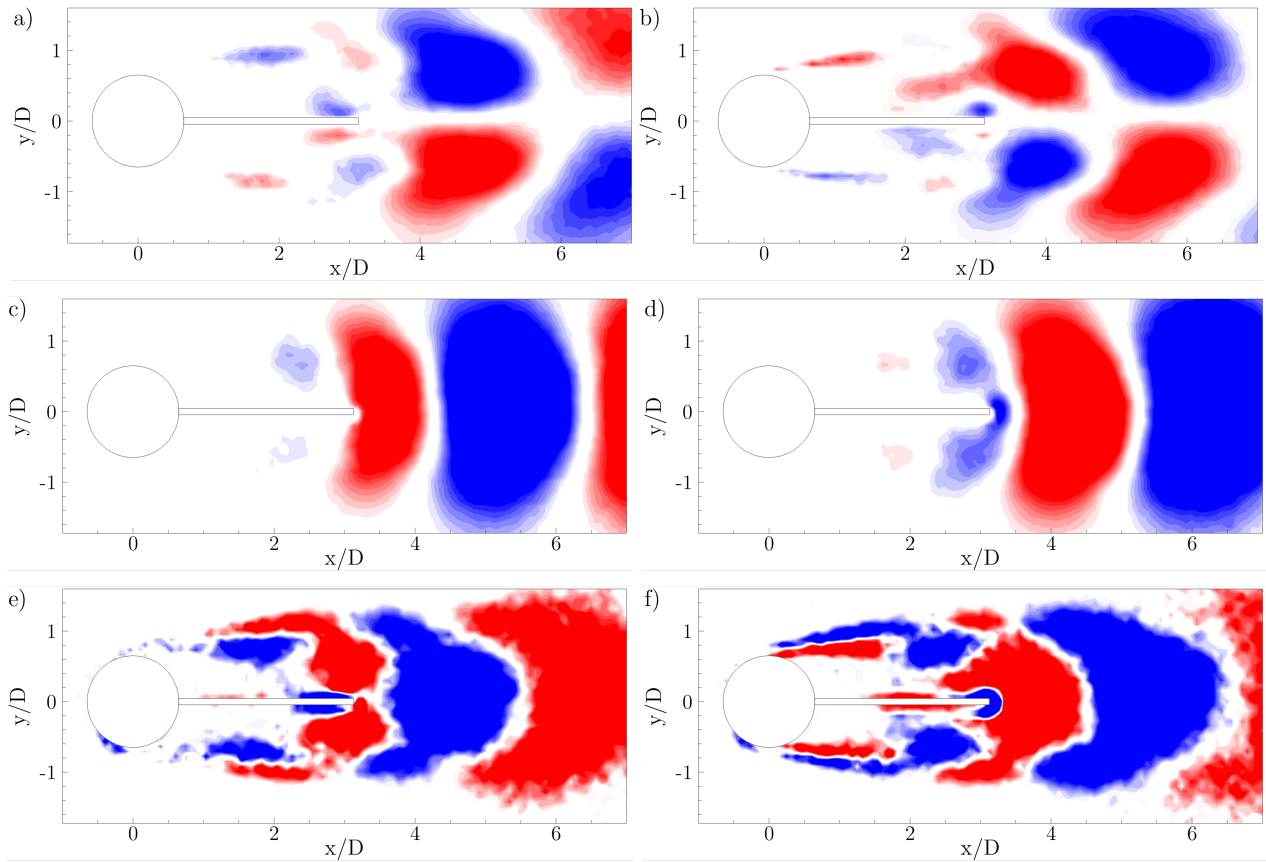


Figure 79: Two-dimensional POD analysis of the flow field in the x - y midplane of the rigid configuration of FSI-PfS-3a a) velocity component u first mode; b) velocity component u second mode; c) velocity component v first mode; d) velocity component v second mode; e) vorticity component ω_z first mode; f) vorticity component ω_z second mode.

8.1.3. FSI-PfS-4x

Based on the FSI configuration FSI-PfS-4a the corresponding rigid configuration uses a single rigid cylinder which extends over the entire test section and is placed at the same position as described in Section 6.3.4. Furthermore, the same inflow velocity as used for FSI-PfS-4a ($u_{\text{inflow}} = 1.69 \text{ m/s}$) is applied for the rigid configuration. Again, time-averaged results are generated and a POD analysis is carried out at the measurement plane $z/d = 20.63$ (near to the glass pane of the test section).

The time-averaged results based on 1000 single PIV measurements are presented in Fig. 80a. The almost symmetric flow field around the rigid cylinder reveals the stagnation point in front of the structure, the acceleration areas on the upper and lower side of the cylinder and the characteristics of the wake behind it. Again, the single PIV measurements indicate a vortex shedding on the cylinder surface.

Figure 80b illustrates the Reynolds shear stress $\overline{u'v'}$ of the time-averaged PIV measurements. The maximum positive and negative stresses are found in the vicinity of the rigid cylinder, where a vortex shedding is assumed to be present. According to the vortex dissipation also the Reynolds stresses decrease further downstream.

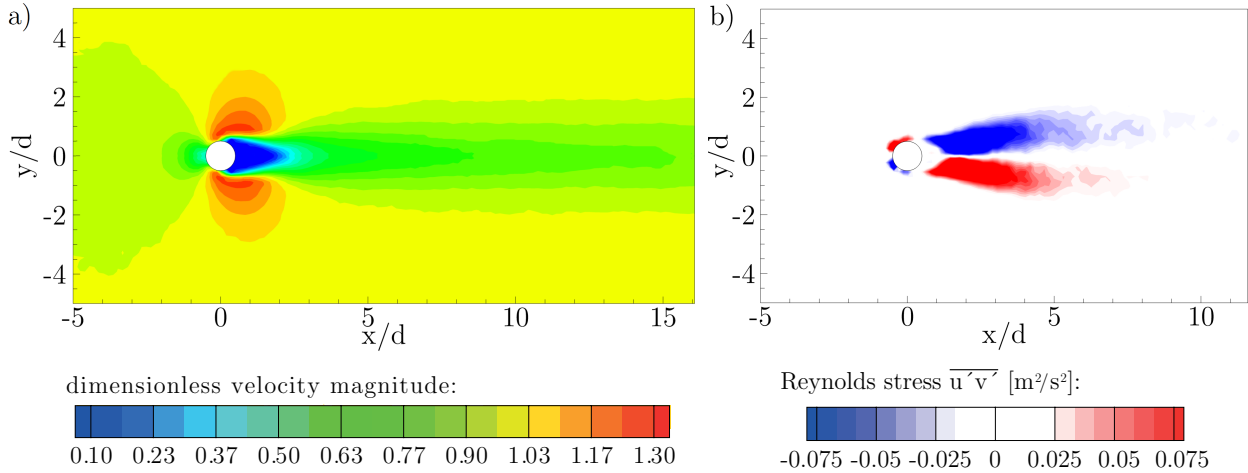


Figure 80: Time-averaged PIV results of the flow around the fixed structure related to the test configuration of FSI-PfS-4a at $z/d = 20.63$ for a) dimensionless velocity magnitude and b) Reynolds shear stress $\overline{u'v'}$.

The POD analysis of the rigid configuration of FSI-PfS-4a is shown in Fig. 81. The first ($k_{\text{abs},1\text{st}} = 107.33 \text{ m}^2/\text{s}^2$, $k_{\text{rel},1\text{st}} = 16\%$ of the turbulent kinetic energy) and the second POD mode ($k_{\text{abs},2\text{nd}} = 103.17 \text{ m}^2/\text{s}^2$, $k_{\text{rel},2\text{nd}} = 16\%$ of the turbulent kinetic energy) contain almost 32% of the total turbulent kinetic energy ($k_{\text{abs},\text{all}} = 652.74 \text{ m}^2/\text{s}^2$, $k_{\text{rel},\text{all}} = 100\%$) for this flow state. An indication that vortex shedding is present is the alternating pattern of the kinetic energy distribution in Fig. 81a and b for the streamwise velocity component along the trajectories of the detached vortices. For the cross-flow velocity component large vortical areas behind the structure are visible in Fig. 81c for the first and in Fig. 81d for the second POD mode. The vorticity-based POD energy distributions are shown in Fig. 81e and f. Both modes reveals large energy-laden areas in the vicinity of the cylinder. Further downstream the clearly defined areas diminish due to the vortex dissipation and the influence of the outer bulk flow.

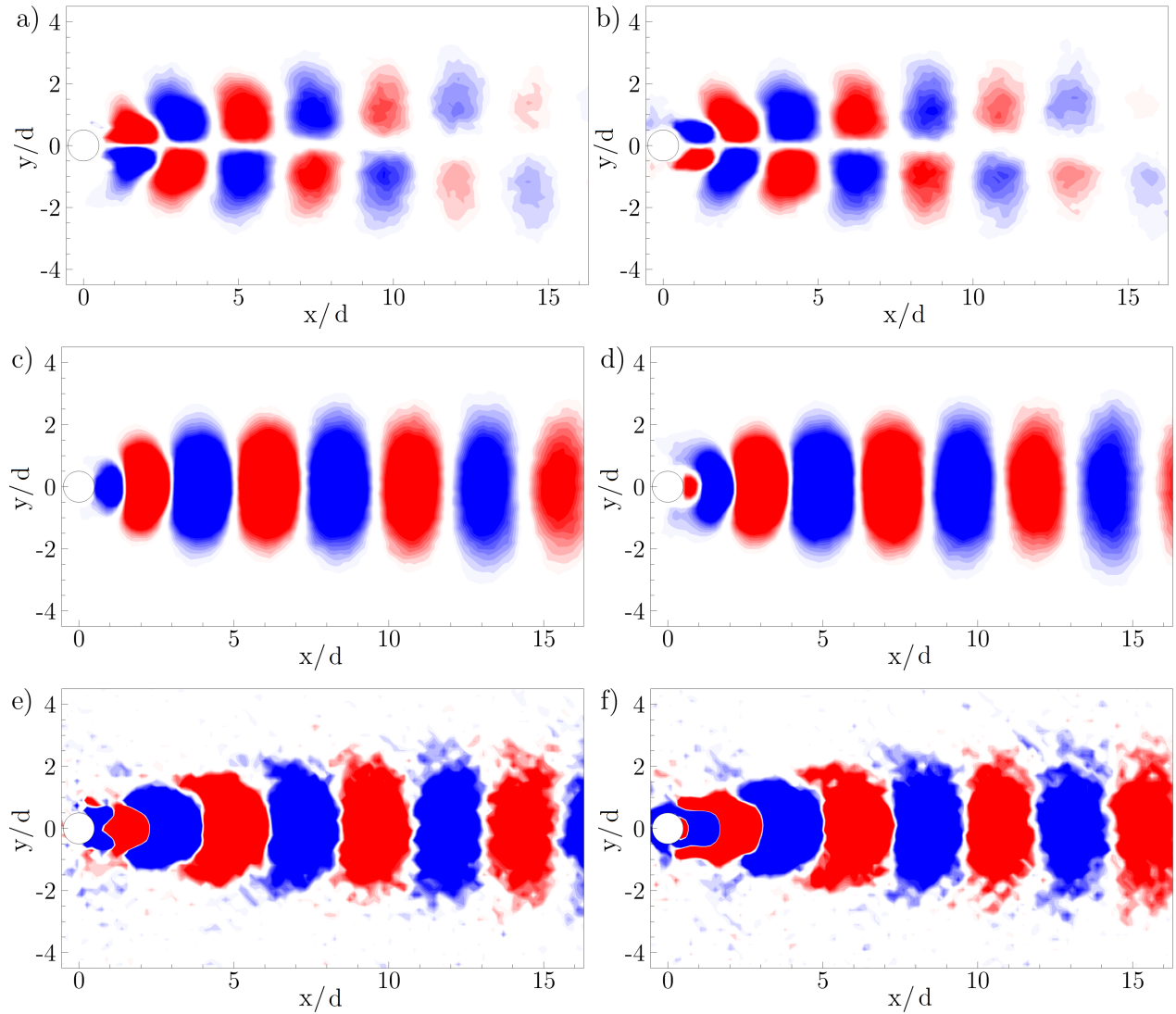


Figure 81: POD analysis of the two-dimensional flow field at $z/d = 20.63$ of the rigid configuration of FSI-PfS-4a a) velocity component u first mode; b) velocity component u second mode; c) velocity component v first mode; d) velocity component v second mode; e) vorticity component ω_z first mode; f) vorticity component ω_z second mode.

Similar to the single cylinder the 3×3 configuration of FSI-PfS-4b is fully rigid in this preliminary study. All cylinders extend over the entire test section and are placed at the same position as described in Section 6.3.4. Furthermore, the same inflow velocity as used for FSI-PfS-4a ($u_{\text{inflow}} = 1.69$ m/s) is applied for the rigid configuration. Again, time-averaged results and a POD analysis are performed at the measurement plane at $z/d = 20.63$.

The time-averaged result based on 1000 single PIV measurements is presented in Fig. 82a. Here, the velocity magnitude of the flow around the rigid cylinders is shown. Due to the coarse resolution of the measurement set-up and the small diameter of the cylinders, the stagnation points of the first cylinder row are hardly visible. However, the acceleration and wake areas are well captured. The wake behind the first cylinder row dominates the flow situation in the second and third cylinder row. Here, no specific acceleration areas on the upper and lower surface of the cylinders are visible. Only between the cylinders in the last row the flow is stronger accelerated. Downstream of the bundle the characteristic wake is formed. In contrast to the previous test cases, single PIV measurements do not clearly indicate a vortex shedding on the cylinders. In the flow fields of the single PIV measurements strong turbulent effects are visible, but no clear periodic vortex shedding is recognizable.

The distribution of the time-averaged Reynolds shear stress $\overline{u'v'}$ is shown in Fig. 82b. Here, on the upper and lower side of each rigid cylinder the influence of the shear layers and the wake behind these structures on the Reynolds stresses is clearly visible. In the vicinity of the first cylinder row the magnitude of the Reynolds stresses increase in comparison to the second and third row. This result indicates that the fluctuations in the flow decrease to lower energy levels further downstream.

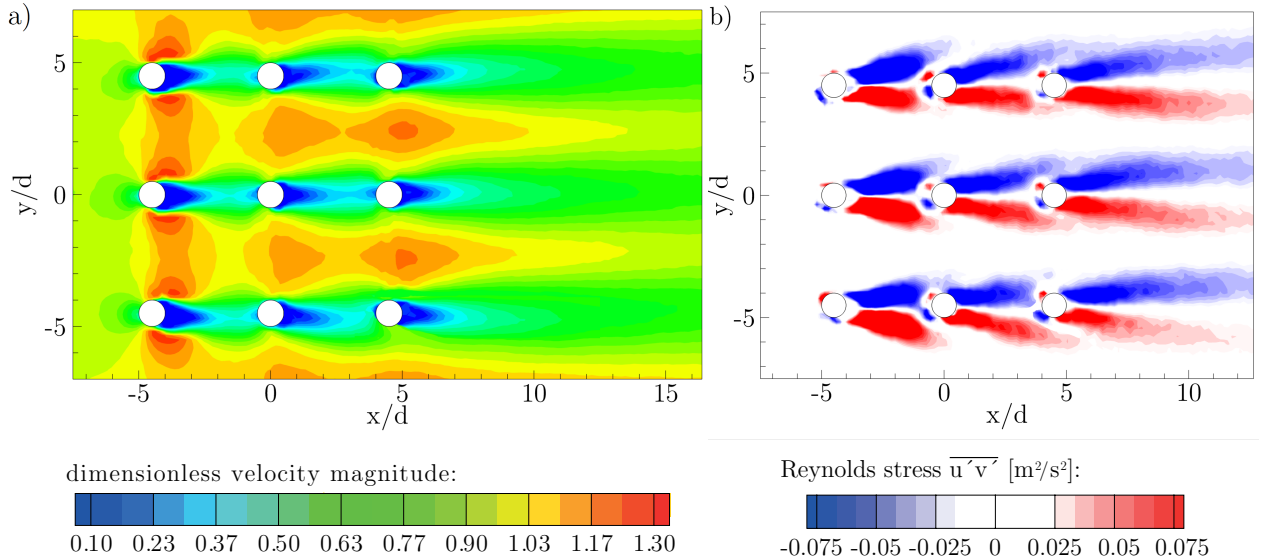


Figure 82: Time-averaged PIV results of the flow around the fixed structure related to the test configuration of FSI-PfS-4b at $z/d = 20.63$ for a) dimensionless velocity magnitude and b) Reynolds shear stress $\overline{u'v'}$.

The fact that a vortex shedding is present in this configuration is indicated by the POD analysis of the 1000 PIV measurements. Figure 83a and b show the first and second POD mode of the streamwise velocity. Here, again the antisymmetric pattern of the energy due to

the formation and transportation of vortices behind the first cylinder row is visible. In the second row only small acceleration areas and the wake region indicate a periodic flow there. Further downstream no significant energy-laden flow effects are present in these first two POD modes. Vortex shedding is still present also on the cylinders in the second row indicated by the POD analysis of the cross-flow velocity component in Fig. 83a (first mode) and b (second mode). By taking the vertical fluctuations into account which seems to be more energetic than in the streamwise direction, a clear vortex pattern is obtained. After the third cylinder row this pattern finally disappears. Thus, it can be assumed that the vortex shedding there is strongly disturbed or completely suppressed. A similar conclusion can be drawn from the POD-based vorticity field. In both modes large energy-laden areas downstream the first and second cylinder row are present. Behind the third row these clearly identifiable areas disappear. It can be assumed that no periodic effect containing a significant amount of energy is present there. The quantitative analysis of the energy calculated for each POD modes reveals that the first ($k_{\text{abs},1\text{st}} = 105.29 \text{ m}^2/\text{s}^2$, $k_{\text{rel},1\text{st}} = 5\%$ of the turbulent kinetic energy) and the second POD mode ($k_{\text{abs},2\text{nd}} = 90.38 \text{ m}^2/\text{s}^2$, $k_{\text{rel},2\text{nd}} = 4\%$ of the turbulent kinetic energy) only contain 9% of the overall turbulent kinetic energy ($k_{\text{abs,all}} = 2385.08 \text{ m}^2/\text{s}^2$, $k_{\text{rel,all}} = 100\%$) for this flow state. In comparison to the rigid configuration of FSI-PfS-4a this is an increase in the kinetic energy of about 365%. As a consequence it can be assumed that the turbulent effects are so dominant that the relative energy level of the vortex shedding is more or less negligible.

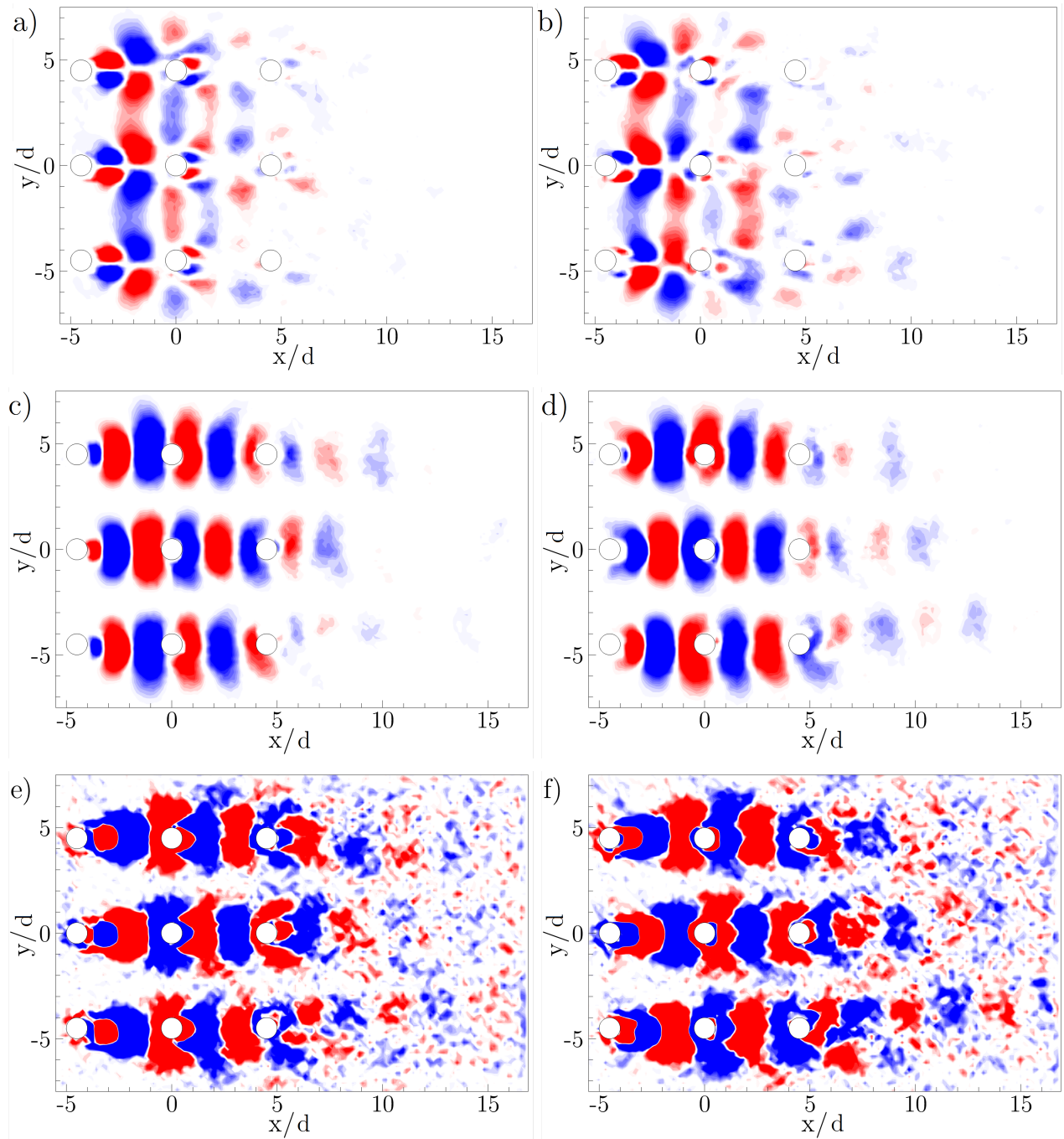


Figure 83: POD analysis of the two-dimensional flow field at $z/d = 20.63$ of the rigid configuration of FSI-PfS-4a a) velocity component u first mode; b) velocity component u second mode; c) velocity component v first mode; d) velocity component v second mode; e) vorticity component ω_z first mode; f) vorticity component ω_z second mode.

8.2. Structural tests

To provide reliable properties of the materials used in the experiments, detailed experimental and numerical structural tests are developed. With the density, the YOUNG's modulus, the POISSON's ratio and the structural damping coefficients all relevant parameters for the description of the structural dynamics are identified. In the following considerations the experimental and numerical set-ups of the structural tests, their results and the final derivation of the structural properties are presented for the materials applied in the present thesis (EPDM rubber, para-rubber, polyamide and polyethylene). The different test scenarios are also developed due to the lack of an appropriate tensile testing apparatus, which provides information about the material characteristics under similar load excitations as present in the FSI experiments.

Rubber materials as well as plastics are widely used in many different applications. In the case of rubber materials, it is not surprising that in the last decades many different material models (i.e., St. Venant-Kirchhoff, Neo Hooke, Mooney-Rivlin etc.) for the description of the elastic behavior of these hyper-elastics were defined. For understanding the behavior of the rubber and plastic materials used for the present structural models and to determine the characteristic material parameters, a static, a decay and a dynamic structural test (without surrounding water) are performed. The static test refers to the stress-strain behavior of the material under a constant load allowing an estimation of the YOUNG's modulus E and the POISSON's ratio ν . The decay test points on the structural damping coefficients of the materials. Finally, the dynamic test is focused on the unsteady behavior of the materials under time-dependent excitations. The achieved experimental results are compared with complementary numerical studies to find the most appropriate material properties.

8.2.1. Structural tests for FSI-PfS-1x, 2x and 3x

The structural tests use a similar geometry as employed in the FSI test cases (described in Section 6). For the structural tests of the EPDM rubber and the polyamide plastic, slight modifications in the geometry are necessary to provide an adequate non-linear deformation of the structure. Due to the high stiffness of the 2.1 mm thick EPDM rubber plate, a polyoxymethylene (POM) cylinder with a diameter $D = 0.022$ m and a density of $\rho_{\text{POM}} = 1420$ kg/m³ is attached at the end of the rubber plate (Fig. 84a). On the stiffer polyamide plate an aluminum cylinder with the same diameter $D = 0.022$ m and a density of $\rho_{\text{Al}} = 2770$ kg/m³ is added at the extremity of the structure (Fig. 84b). The configuration related to the para-rubber is similar to the test cases FSI-PfS-2x, which consists of the para-rubber plate and an attached steel weight at the end (Fig. 84c).

8.2.1.1. Static tests

In the static cases the front cylinder (C1) is fixed, but the elastic plate and the additional weight (C2) are free. The entire configuration is arranged in a horizontal alignment. Due to the gravitational force (pointing in negative y -direction) acting on the elastic plate and the weight, a static deformation of the elastic plate results (after a certain time). Complementary numerical predictions using the same configuration regarding the geometry and alignment are performed with ANSYS[®] Mechanical 14.0 (ANSYS, 2011c) to estimate the YOUNG's modulus E and the POISSON's ratio ν in comparison to the experimental results.

In these CSD predictions the elastic structure is discretized by $70 \text{ cells} \times 4 \text{ cells} \times 1 \text{ cell}$ building a quasi two-dimensional structured mesh of 280 second-order accurate SOLID186 elements (refer to Section 5.1.1). Based on preliminary studies this grid is found to be excessively accurate and fine for the computation of the expected structural deformations. The weights (C2) are assumed to be rigid, therefore they are modeled as rigid bodies with only two degrees of freedom in x - and y -direction. To provide the two-dimensional characteristics of the structural tests, also the elastic structure is only allowed to deflect in x - and y -direction. The convergence criterion of the steady numerical solution is set to 10^{-4} .

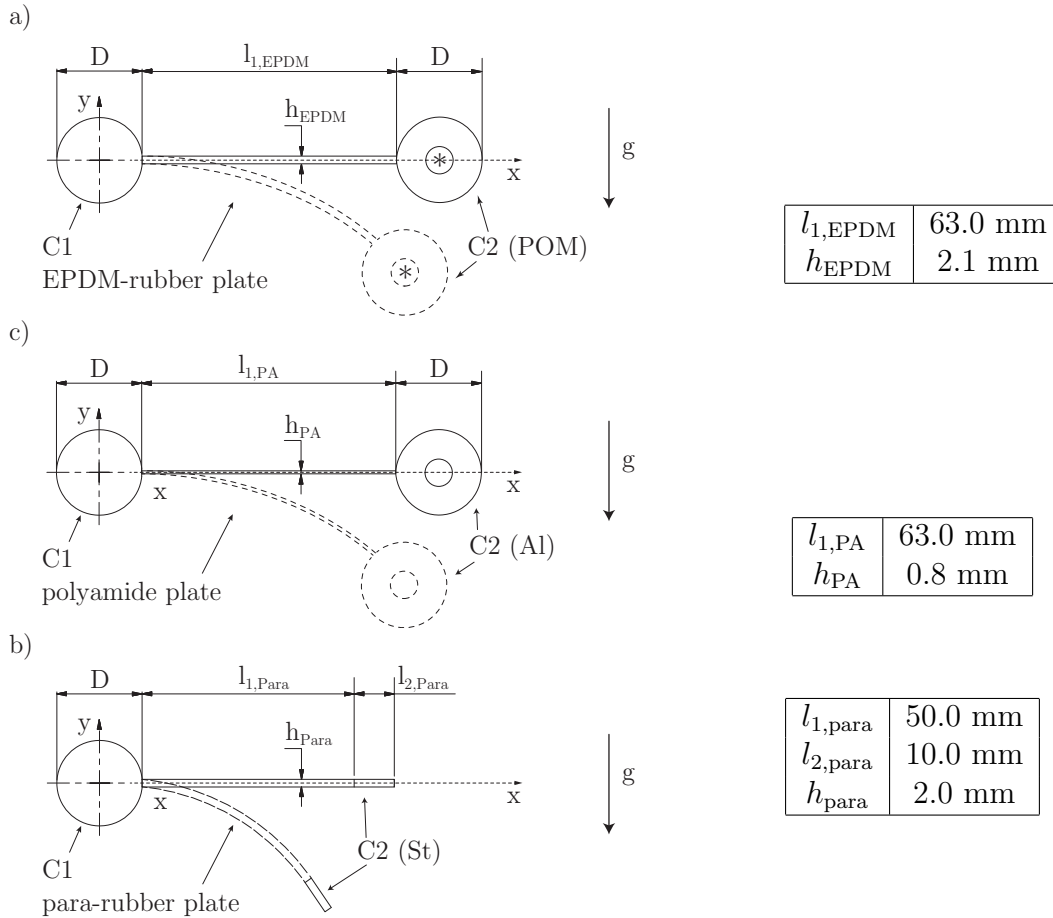


Figure 84: Set-up of the static structural tests.

Figure 85 compares the experimental data measured by the LLT technique with the corresponding numerical predictions according to the static test configurations depicted in Fig. 84. Using the same test conditions as provided in the experiments and the isotropic hyperelastic material model of St. Venant-Kirchhoff (refer to Section 2.1.3), different values of the YOUNG'S modulus are applied to the numerical set-up to prove and enhance the manufacturer's reference (material data-sheets). For a correct physical modeling of the EPDM and the para-rubber material a POISSON'S ratio of $\nu_{ideal} = 0.4999$ is theoretically necessary. In this case the numerical computation does not converge with acceptable effort. As a compromise between the correct physical properties and the convergence issues, the POISSON'S ratio is set to $\nu_{rubber} = 0.48$ for both rubber materials. For the polyamide material it is common to use a POISSON'S ratio of $\nu_{PA} = 0.40$.

Comparisons are performed concerning the predicted results and the experimental measurements of the deformation of the elastic structure and the position of the weight C2 at the tail of the structure (center). For the numerical predictions a wide parameter space of different YOUNG'S modulus are applied to find the best matching fit (ranging from $E = 10$ MPa to 20 MPa for the EPDM rubber, $E = 500$ MPa to 700 MPa for the polyamide and $E = 2$ MPa to 5 MPa for the para-rubber). Here, the comparison of the coordinates of the weight C2 and an error criterion postulating an error of less than 1% for the predictions are applied. Based on these comparisons between the experimental measurements and the simulations, the YOUNG'S moduli of the different materials ($E_{\text{EPDM}} = 16$ MPa, $E_{\text{PA}} = 580$ MPa and $E_{\text{para}} = 3.15$ MPa) are determined.

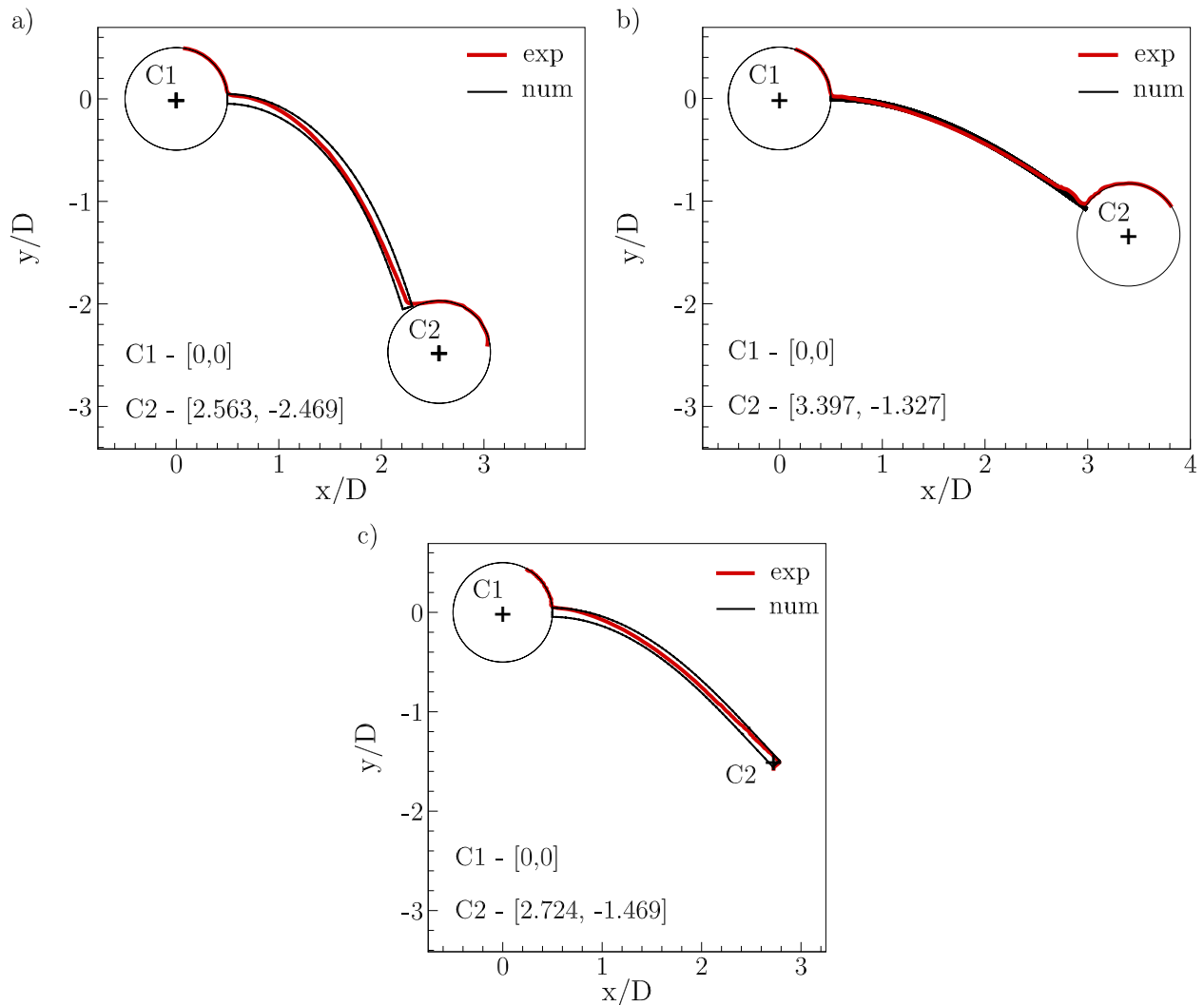


Figure 85: Comparison of experimental and numerical results of the static structural test on a) the EPDM rubber, b) the polyamide plastic and c) the para-rubber; coordinates refer to the experimentally measured position of the front cylinder C1 and the tail weight C2 (+).

Comparing the static test results of the EPDM rubber, a slight deviation in the bending curve between the measured data and the numerical prediction is visible. An explanation of this failure is the clamping of the rubber in the front cylinder C1. Due to the elasticity of

the rubber material, no perfect horizontal clamping could be provided in the experiments. A sufficiently accurate match of the position of the tail cylinder C2 with the corresponding measured midpoint coordinates ($(x/D)_{\text{exp}} = 2.56$, $(y/D)_{\text{exp}} = -2.47$) is provided by using a YOUNG's modulus of $E_{\text{EPDM}} = 16$ MPa in the numerical predictions ($(x/D)_{\text{num}} = 2.54$, $(y/D)_{\text{num}} = -2.48$). The much stiffer polyamide material reaches the best accordance to the experimental data with $E_{\text{PA}} = 580$ MPa. In this case, the bending curve fits excellently to the measured curvature and the midpoint coordinates of the tail cylinder position $(x/D)_{\text{exp}} = 3.40$ and $(y/D)_{\text{exp}} = -1.33$ closely agrees with the predictions yielding $(x/D)_{\text{num}} = 3.40$, $(y/D)_{\text{num}} = -1.32$. Similar to the restriction by the applied clamping in the static test of the EPDM rubber, the test set-up of the para-rubber reveals the same problem regarding the horizontal clamping and causes a slightly different bending curve compared to the predicted one for the best fitting YOUNG's modulus of $E_{\text{para}} = 3.15$ MPa for this material ($(x/D)_{\text{exp}} = 2.72$, $(y/D)_{\text{exp}} = -1.47$ and $(x/D)_{\text{num}} = 2.74$, $(y/D)_{\text{num}} = -1.42$). In conclusion, this static test only offers a qualitative view on the material properties, but is a reasonable approach due to the lack of an appropriate tensile testing apparatus.

8.2.1.2. Dynamic tests

To prove the estimations of the material properties based on the static tests, further decay and dynamic tests scenario are developed. Using the same geometry as in the static tests, the dynamic and decay tests are using a vertical alignment as depicted in Fig. 86. Similar to the static tests the cylinder in the decay experiment is fixed and a single initial displacement of the tail weight produces a damped oscillation of the system till it reaches its neutral position. To increase the inertia of the configuration for the EPDM rubber, the polymer cylinder (C2) is replaced by an aluminum cylinder for the decay and the dynamic structural tests. For the dynamic test cases the fixation of the cylinder (C1) is replaced by a rotatable bearing to release its rotational DOF along the cylinder axis. A crank drive stimulates the cylinder by a periodic excitation given by:

$$\phi(t) = \phi_{\text{peak}} \cdot \sin(\omega \cdot t) + \phi_{\text{offset}}. \quad (142)$$

Here, ω denotes the angular frequency and ϕ_{peak} the amplitude of the angular deflection. Depending on the parameters of the angular frequency and the amplitude of the angular deflection, different excitations of the structure are reached. The inertia of the tail weight increases the displacements and alters the deflection behavior of the flexible structure to non-linear deformations. The offset in Eq. (142) is necessary due to the experimental set-up of the crank drive that creates a slightly asymmetric angular excitation of the rigid cylinder (for all tests the offset is determined to $\phi_{\text{offset}} = 0.5^\circ$). The offset is not taken into account in the numerical predictions of the structural tests since its effect on the results can be neglected.

The parameters and the experimental and numerical results of the dynamic tests are listed in Table 11. The parameters of the present deflection states are determined by experimental observations of the dynamic behavior of the flexible structure in a wide parameter space by varying ω and ϕ_{peak} . The chosen values produce moderately non-linear and well measurable structural displacements in the first bending mode. This mode is chosen due to the large mea-

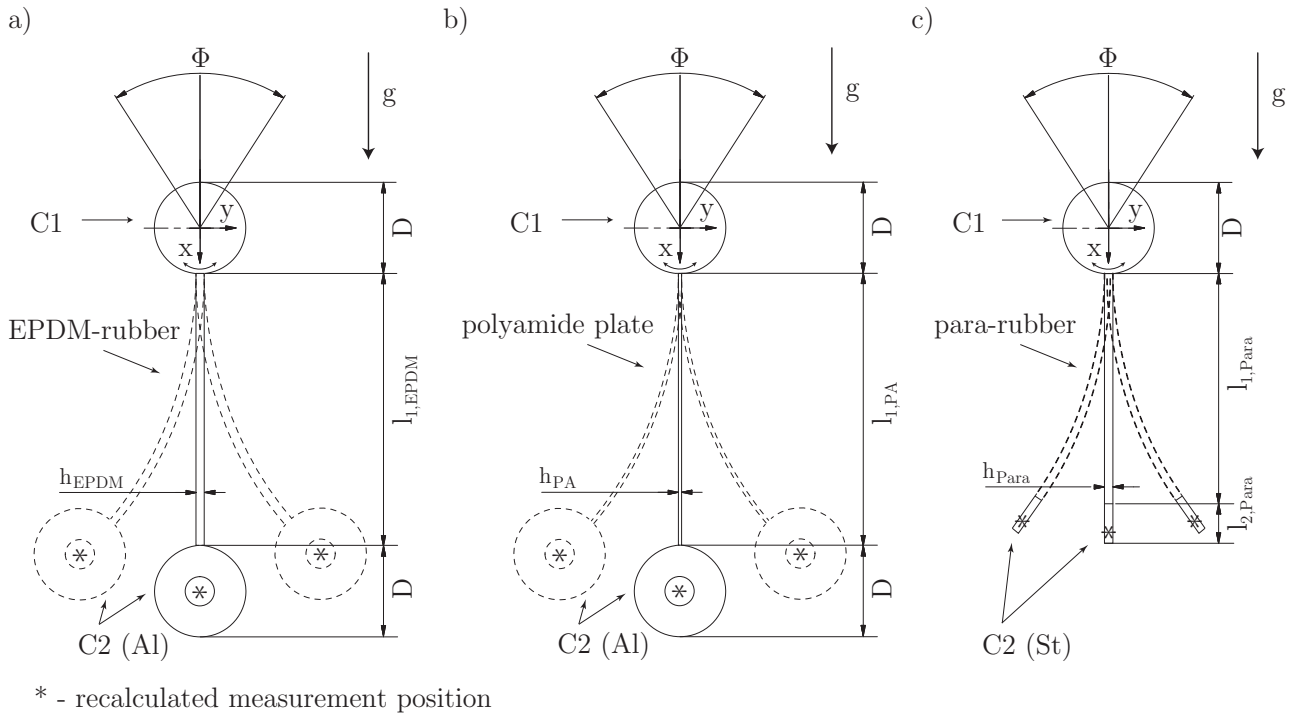


Figure 86: Set-up of the dynamic structural tests.

surable deflections and the moderate excitation frequencies. The deflections of the structure is measured in all dynamic and decay tests by the laser line triangulation technique described in Section 4.4 with a high spatial accuracy and a measuring frequency of 800 Hz.

Unsteady numerical predictions using ANSYS[®] Mechanical 14.0 are carried out for a comparison with the measured data under equal numerical conditions (grid and element type) as applied for the static computations. In the unsteady simulations the front cylinder is additionally modeled and excited with the specified angular deflection. For the comparison, again different points of the structure are used. For the EPDM rubber and the polyamide plastic the midpoint of the tail cylinder (C2) is compared. In this case parts of the circular outline of the rear weight is measured. Based on the known cylinder diameter D and several points on the circle, its center is calculated. For the para-rubber a point near the extremity of the steel weight at $x/D \approx 3.13$ is applied for the comparisons.

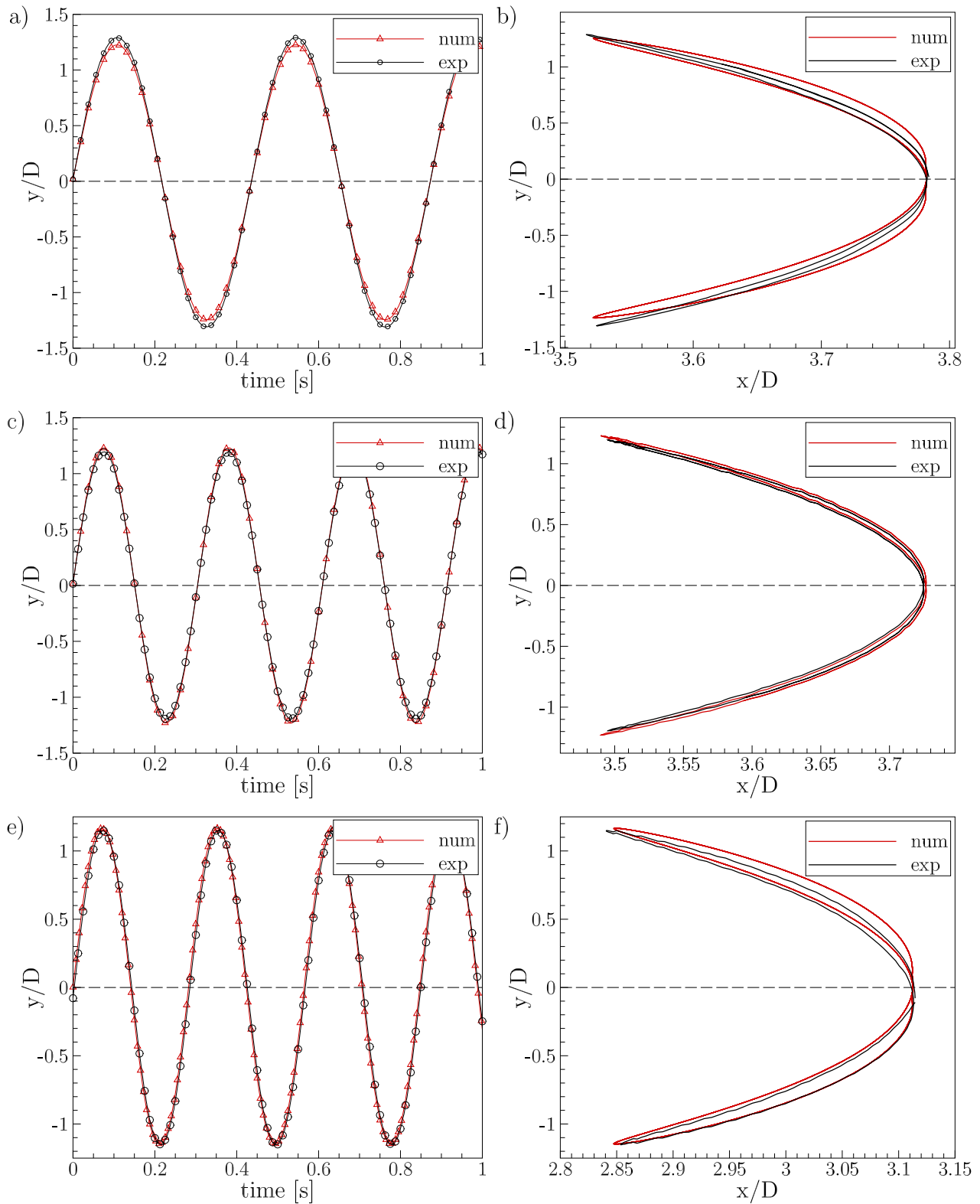


Figure 87: Complementary experimental and numerical results of the dynamic structural tests for a, b) the EPDM rubber, c, d) the polyamide plastic and e, f) the para-rubber.

The EPDM rubber plate with the attached aluminum cylinder is excited by a sinusoidal angular displacement of $\phi_{\text{peak}} = 7.09^\circ$ and a frequency of $f = 2.29$ Hz. This results in a periodic and almost symmetric deflection of the rear-end of the structure with y -displacements between $(y/D)_{\text{max,exp}} = 1.28$ and $(y/D)_{\text{min,exp}} = -1.31$ as presented in Fig. 87a as a time series and in Fig. 87b as a xy -plot. Similar results are obtained for the structural tests of the polyamide material. Here, the excitation ($\phi_{\text{peak}} = 6.98^\circ$, $f = 3.28$ Hz) produces a rear-end displacement with $(y/D)_{\text{max,exp}} = 1.20$ and $(y/D)_{\text{min,exp}} = -1.19$ (Fig. 87c and d).

For the para-rubber a point near the tailing edge ($x/D = 3.11$) is applied as the reference point. Based on the excitation of $\phi_{\text{peak}} = 6.51^\circ$ and $f = 3.54$ Hz, the measured structural response in the first bending mode is ranging from $(y/D)_{\text{max,exp}} = 1.15$ to $(y/D)_{\text{min,exp}} = -1.15$ as presented in Fig. 87e and f.

material	EPDM rubber	polyamide	para-rubber
$\phi_{\text{peak}} [^\circ]$	7.09	6.98	6.51
$\phi_{\text{offset}} [^\circ]$	0.50	0.50	0.50
$f [s^{-1}]$	2.29	3.28	3.54
$\omega [s^{-1}]$	14.39	20.61	22.24
$(y/D)_{\text{max,exp}}$	1.28	1.20	1.15
$(y/D)_{\text{min,exp}}$	-1.31	-1.19	-1.15
$(x/D)_{\text{max,exp}}$	3.78	3.73	3.11
$(x/D)_{\text{min,exp}}$	3.52	3.50	2.84
$(y/D)_{\text{max,num}}$	1.24	1.22	1.17
$(y/D)_{\text{min,num}}$	-1.23	-1.23	-1.15
$(x/D)_{\text{max,num}}$	3.78	3.73	3.11
$(x/D)_{\text{min,num}}$	3.52	3.49	2.85

Table 11: Excitation parameters and complementary experimental/numerical results of the dynamic structural tests.

The experimental results of the dynamic tests are well reproduced (errors under 3%) by the unsteady ANSYS[®] Mechanical computations applying a Rayleigh damping (Rayleigh, 1877). Only the experimental results of the dynamic structural test of the para-rubber are slightly asymmetric. Here, the applied offset due to the experimental set-up may have a small influence on the deflections of the structure. The Rayleigh damping is introduced because the numerical predictions of the dynamic test cases without damping show non-periodic displacements of the structure with increasing amplitudes in contrast to the experiments, where a sinusoidal signal with a constant amplitude is observed. With the damping ($\alpha = 0$, $\beta_{\text{EPDM}} = 0.0077$, $\beta_{\text{PA}} = 0.0031$, $\beta_{\text{para}} = 0.0065$), these problems are solved and the numerical predictions show a good agreement with the experimental results as presented in Fig. 87. The method how the Rayleigh damping coefficients of each material are extracted out of the experimental decay experiments is described in the following paragraphs.

8.2.1.3. Decay tests

The Rayleigh damping approach (Rayleigh, 1877) models the damping matrix \mathbf{b} in Eq. (57) which is proportional to the linear combination of the mass m and the stiffness k . The damping

matrix \mathbf{b} is given by

$$\mathbf{b} = \alpha \mathbf{m} + \beta \mathbf{k} \quad (143)$$

where α and β are constants of proportionality of the mass and stiffness matrices, respectively. The contribution proportional to the mass is related to an outer damping resulting from the surrounding medium and is responsible for the damping effect due to rigid body motions. The stiffness related part corresponds to the inner structural damping and is only connected to strains and not to rigid body motions. The damping coefficients can be determined by the eigenfrequency and the modal damping values (LEHR's damping ratio) D of the structure (Nasdala, 2010). These quantities are related as follows:

$$2 D = \frac{\alpha}{\omega} + \beta \omega. \quad (144)$$

It is common practice to use only the stiffness proportional term for single elastic structures. Therefore, the mass coefficient α is set to zero. The reason for this decision is that the stiffness proportional damping is considered to be more realistic (see, e.g., Krätzig et al., 1996) in this case, since the mass-proportional damping factor results in decaying damping effects on higher modes. Reasons are that the physical counterpart of the mass-proportional term is a viscous damper connecting a structural degree of freedom to the displacements in the structure. Then, the mass-proportional term can lead to unrealistically high damping forces (Hall, 2006). Consequently, here only the stiffness-proportional component is considered.

LEHR's damping ratio D can be extracted out of the decay tests. Generally, decreasing oscillations like in the present decay tests can be described as weakly damped. According to Fig. 88 the peak amplitudes $y(t)$ decay according to an exponential function of the time t with the decay constant δ , which is a measure for the decrease of the amplitude $y(t)$.

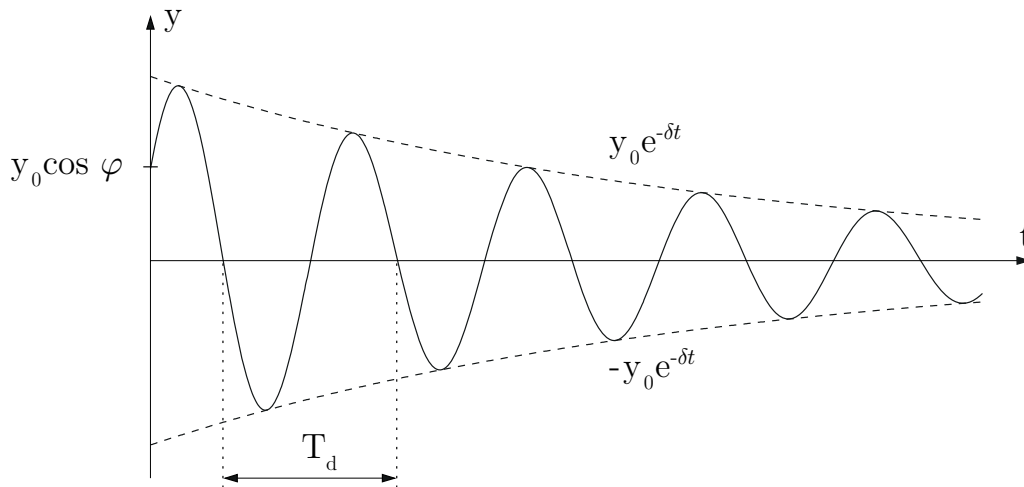


Figure 88: Weakly damped oscillations.

Alternatively to the decay constant δ , the logarithmic decrement Λ (Eq. (145)) as the relation of two peaks in the distance of one period $T_d = 1/f_d = 2\pi/\omega_d$ can be employed:

$$\Lambda = \ln \left| \frac{y_i}{y_{i+1}} \right| = \ln \left| \frac{y_0 e^{-\delta t} \cos(\omega_d t - \phi)}{y_0 e^{-\delta(t+T_d)} \cos(\omega_d (t + T_d) - \phi)} \right| = \ln e^{\delta T_d} = \delta T_d = \frac{2\pi}{\omega_d} \delta = \frac{1}{f_d} \delta. \quad (145)$$

In contrast to the determination of δ out of the exponential envelope function, Λ is directly measurable and can be set in relation to δ and D using the natural angular frequency of the undamped oscillation ω_0 by :

$$D = \frac{\delta}{\omega_0} = \frac{\Lambda}{\sqrt{\Lambda^2 + (2\pi)^2}} \quad (146)$$

according to Nasdala (2010).

The results of the decay tests are presented in Fig. 89 with a half-logarithmic scaling. Due to the different geometries, the structures are released at different initial deflections. The EPDM rubber is released at $y/D = 1.06$, the para-rubber at $y/D = 0.94$ and the polyamide plate at $y/D = 1.14$. According to the initial deflection, the mass of the weight and the inner structural damping, different decay oscillations are measured. Therefore, a direct comparison of the decay characteristics of the three materials is not applicable due to these dependencies. The EPDM rubber shows a rapid decay within 3.5 s to its neutral position caused by its high stiffness and damping. In the experiments using the para-rubber and the polyamide material the decay to the neutral position takes about 6.0 s. The oscillation frequencies are $f_{\text{decay,EPDM}} = 2.66$ Hz for the EPDM rubber, $f_{\text{decay,PA}} = 3.82$ Hz for the polyamide and $f_{\text{decay,para}} = 3.78$ Hz for the para-rubber, respectively.

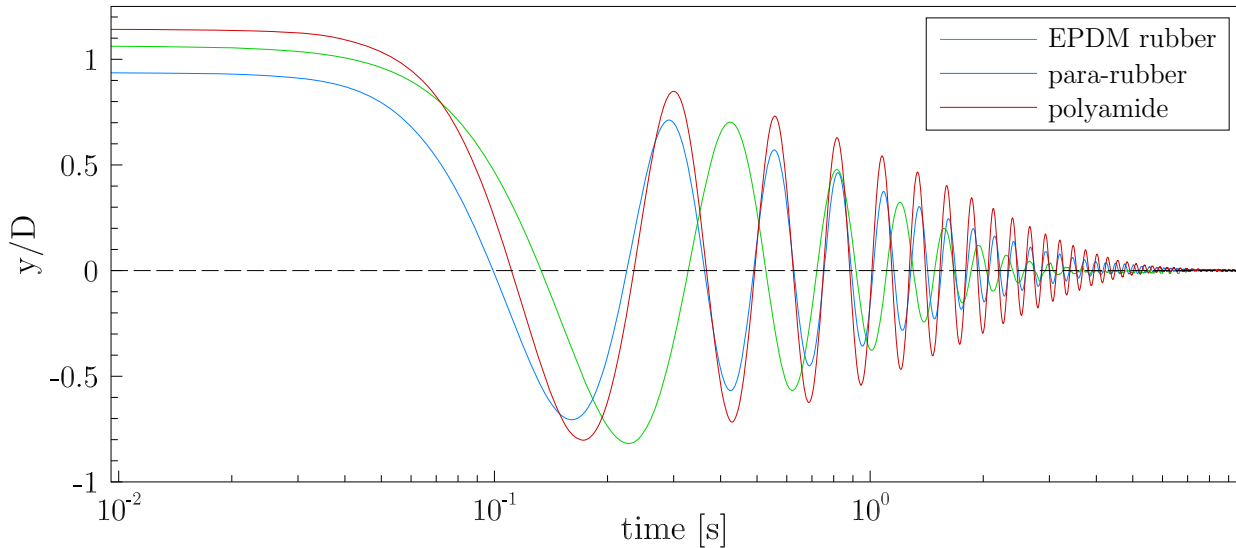


Figure 89: Results of the decay test for the EPDM rubber, the polyamide and the para-rubber.

In Table 12 the damping parameters are listed according to Eq. (144) to (146) and Fig. 89. The numerical predictions of the dynamic tests show a large deviation from the experimentally determined values of the damping coefficient β . Here, several reasons are possible. The most probable reason is the usage of the St.Venant-Kirchhoff material model which excludes velocity-related elasticity effects like strain hardening (especially for the para-rubber).

material	f_{decay} [Hz]	Λ	δ	D	α	β_{exp}	β_{num}
EPDM rubber	2.66	0.45	1.21	0.072	0	0.0086	0.0077
polyamide	3.82	0.15	0.58	0.024	0	0.0020	0.0031
para-rubber	3.78	0.21	0.78	0.034	0	0.0029	0.0065

Table 12: Mean damping parameters of the different materials.

In conclusion, the material parameters are adequately estimated with the help of the static, dynamic and decay structural test in combination with the complementary numerical investigations. Due to the special behavior of hyper-elastic materials like the EPDM rubber or the para-rubber, a certain tolerance especially for rapid and large deformations has to be accepted. In order to avoid these velocity-related deformation behavior, the focus in the FSI benchmarks is set to moderate deflections as well as low swiveling frequencies. In the numerical FSI predictions of the FSI test cases it is found that the influence of the damping coefficients are negligible (see Section 10.2). Therefore, the Rayleigh damping is only applied to the predictions of the dynamic structural tests but not in the FSI simulations.

8.2.2. Structural tests for FSI-PfS-4x

Despite the well-known material properties of polyethylene, a static structural test is realized to validate the numerical prediction capabilities of ANSYS[®] Mechanical 14.0 for this material. The applied configuration is similar to the test case definition of FSI-PfS-4a, but performed in air. The polyethylene cylinder is aligned in a horizontal position and fixed on the back-plate. At the free end of the cylinder three additional weights are attached ($m_1 = 0.06180$ kg, $m_2 = 0.08133$ kg, $m_3 = 0.10042$ kg). Due to the gravitational force the cylinder and the weights are displaced in positive x -direction (aligned with the gravitational acceleration). The measurements are carried out with the LLT sensor. As a consequence of the sensor limitation concerning the measurement range, not the whole bending line of the cylinder could be determined ($3.00 > z/d < 21.25$).

The numerical predictions are performed with the static analysis module of ANSYS[®] Mechanical 14.0 using a fixed constraint at the clamping of the cylinder and three different forces in x -direction according to the applied weights (m_1, m_2, m_3). According to the properties of the polyethylene material a YOUNG's modulus of $E = 800$ MPa and a POISSON's ratio of $\nu = 0.42$ are applied. The unstructured mesh of the cylinder consists of 4600 tetrahedrons of the SOLID187 element, which is a second-order accurate 10-node tetrahedron element (ANSYS, 2011c).

In Fig. 90 the comparison of the measured data with the numerically predicted results in relation to its initial position are presented. The predicted structural deformation for the three different weights are in good agreement (errors below 5%, see Table 13) with the measured bending line on the surface of the cylinder. According to the higher load with increasing weights, the displacement in x -direction rises. The simulations validated by the measured data proves the manufacturer's data of the polyethylene material (YOUNG's modulus $E = 800$ MPa, POISSON's ratio $\nu = 0.42$).

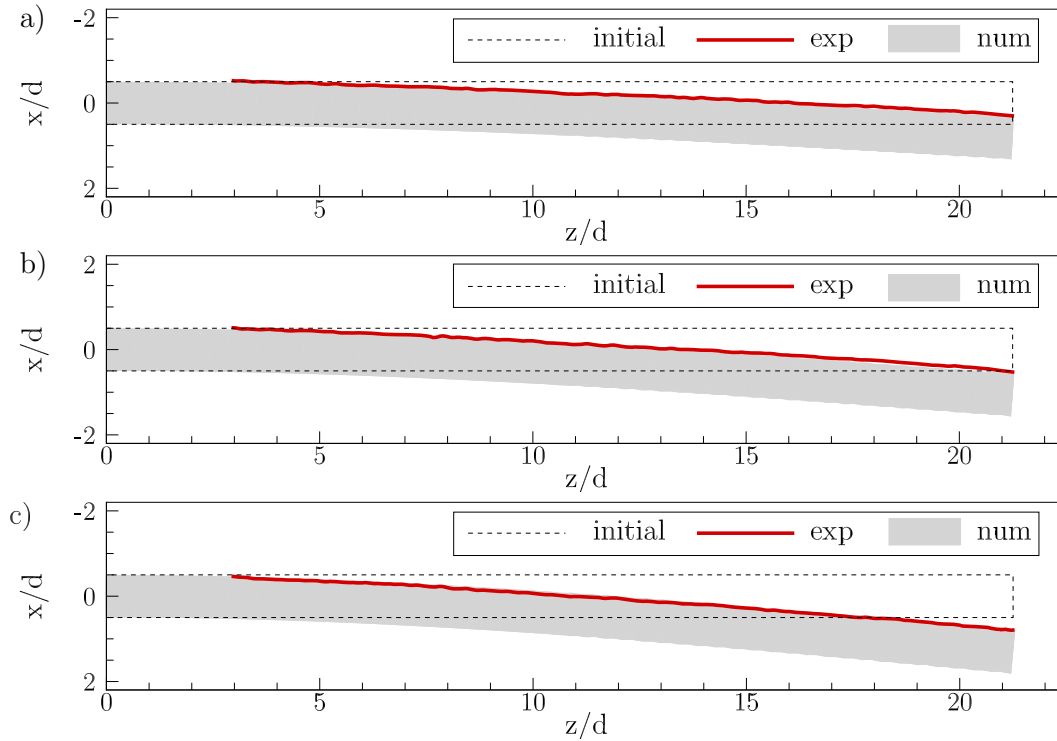


Figure 90: Comparison of the measured with the numerically predicted results of the static structural test for the polyethylene cylinder with a) $m_1 = 0.06180$ kg, b) $m_2 = 0.08133$ kg and c) $m_3 = 0.10042$ kg.

weight	$m_1 = 0.06180$ kg	$m_2 = 0.08133$ kg	$m_3 = 0.10042$ kg
$(y/d)_{\text{exp}}$	0.3032	0.5267	0.7940
$(y/d)_{\text{num}}$	0.3161	0.5552	0.7988
error(y/d)	+4.25 %	+5.41 %	+0.5 %

Table 13: Comparison of the experimental/numerical results for the static structural test for the polyethylene cylinder (for a point on the cylinder surface at $z/d = 21.24$).

8.3. Modal analysis

To determine the vibration characteristics (natural mode shapes and eigenfrequencies) of the different test case structures during a free vibration, a modal analysis using ANSYS® Mechanical 14.0 is performed. For the computation of the elastic structure a grid consisting of $28 \text{ cells} \times 4 \text{ cells} \times 40 \text{ cells}$ is applied to build a three-dimensional structured mesh of 4480 elements for the test cases FSI-PfS-1*x*, 2*x* and 3*x*. The rigid bodies given by the weight in FSI-PfS-2*x* and the front cylinder in FSI-PfS-2*b* are again modeled as rigid bodies without a numerical discretization. For FSI-PfS-4*x* the grid used for the static structural tests consisting of 4600 tetrahedrons of the SOLID187 elements is applied.

Due to the nature of the modal analysis, any non-linearities in the material behavior are ignored. Therefore, only the physical properties such as the density, the YOUNG's modulus and the POISSON's ratio of the elastic materials are taken into account for the modal analysis. The purpose of these investigations is the subsequent comparison of the bending modes and frequencies of the structures observed in the FSI experiments. To enable a direct comparison the same geometry for the moving parts of the structure as defined for the FSI experiments

is applied for the modal analysis (see test case definitions in Section 6). However, this means that the rigid fixed front cylinder or cone is not considered (except for FSI-PfS-2*b*). In Table 14 the first eight eigenfrequencies of each test case structure are listed. According to the different material properties and geometries large differences between the predicted natural frequencies and mode shapes are obtained. Therefore, only the dominant and FSI-related bending modes⁹ are discussed. Generally, all structures of FSI-PfS-1*x*, 2*a* and 3*x* reach the first bending mode (in Fig. 91a marked by \square) with the first eigenfrequency. This mode is characterized by moderate non-linear deformations with a bending node at the fixation of the structure. The first twisting mode (\diamond) exemplarily shown in Fig. 91b for the structure of FSI-PfS-2*a* is defined by a twisting of the opposite corners of the three-dimensional elastic structure. The FSI experiments (refer to Section 10) will show that in the test cases FSI-PfS-1*x* and 2*x* this twisting mode will not be reached in a quasi-periodic deflection state. The second bending mode (\triangle) is characterized by an additional bending node positioned near the end of the structure. Within this mode the deformations become large and strongly non-linear. This bending mode is only reached in low frequency ranges with less material stiffness and/or an added weight as applied in FSI-PfS-1*c* or FSI-PfS-2*x*.

Eigenfrequency	1st	2nd	3rd	4th	5th	6th	7th	8th
FSI-PfS-1 <i>a</i>	11.57 \square	13.83 \diamond	20.82	33.40	52.68	71.86	71.90 \triangle	88.48
FSI-PfS-1 <i>b</i>	25.24 \square	31.06 \diamond	47.72	76.60	120.47	158.19 \triangle	161.93	185.78
FSI-PfS-1 <i>c</i>	5.43 \square	7.41 \diamond	29.68	33.85 \triangle	37.19	38.22	48.13	60.86
FSI-PfS-2 <i>a</i>	2.64 \square	6.01 \diamond	27.88 \triangle	52.25	52.31	57.65	65.27	67.31
FSI-PfS-2 <i>b</i>	0.03 \square	5.15 \triangle	5.98 \diamond	28.18	51.96	52.02	57.36	64.99
FSI-PfS-3 <i>a</i>	19.00 \square	22.28 \diamond	29.04	41.58	60.61	86.54	110.51	121.51
FSI-PfS-3 <i>b</i>	9.42 \square	11.04 \diamond	14.39	20.60	30.04	42.89	54.77	60.22
FSI-PfS-4 <i>x</i>	35.66 \square	35.67 \square	221.77	221.82	613.45	613.59	801.08	1181.8

Table 14: First eight structural eigenfrequencies calculated by the modal analysis, \square - first bending mode, \diamond - first twisting mode and \triangle - second bending mode (all values in Hz).

The strong influence of the material properties on the first eigenfrequency for the structures of FSI-PfS-1*a*, *b* and *c* is obvious. According to the soft para-rubber the eigenfrequency $f_{1c,1} = 5.43$ Hz of FSI-PfS-1*c* is relatively low. The stiffer material of the two other cases causes higher first eigenfrequencies with $f_{1a,1} = 11.57$ Hz and $f_{1b,1} = 25.24$ Hz, respectively. This influence is also visible for the first and second eigenfrequencies of FSI-PfS-3*a* and 3*b*. The asymmetric three-dimensional geometry impedes slightly the structural deformation. This results in a higher first ($f_{3a,1} = 19.00$ Hz, $f_{3b,1} = 9.42$ Hz) and second eigenfrequency ($f_{3a,2} = 22.28$ Hz, $f_{3b,2} = 11.04$ Hz) in comparison to the two-dimensional cases. Again only the choice of the material from the soft para-rubber to the stiffer EPDM rubber increases the first and second eigenfrequencies of the geometrically identical structures.

Another influence is given by the additional degree of freedom in FSI-PfS-2*b* which changes the whole modal behavior of the system in contrast to FSI-PfS-2*a*. Note that both cases

⁹The different mode shapes and eigenfrequencies are visually identified and assigned to each other, higher eigenfrequencies are often characterized by complex mode shapes, which will not appear in the FSI experiments.

are identical concerning the geometry and material; only the rotational DOF in z -direction is released. The first natural mode with the low frequency of $f_{2b,1} = 0.03$ Hz refers to a rigid body rotation which is not observed in the FSI-PfS-2a experiments, where the first mode appears at $f_{2a,1} = 2.64$ Hz. The first twisting mode is almost equal in both cases with an eigenfrequency of $f_{2a,2} = 6.01$ Hz and $f_{2b,2} = 5.98$ Hz, respectively. This mode is mostly unaffected by the additional DOF and only corresponds to the three-dimensional elongation of the structure in z -direction. The second bending mode is rather different in both cases with frequencies of $f_{2a,3} = 27.88$ Hz and $f_{2b,3} = 5.15$ Hz, respectively. In the case of FSI-PfS-2b this mode even has a smaller frequency than the previously defined second bending mode. This leads to the assumption that the free z -rotation of the front cylinder supports the formation of this bending mode. The comparison of FSI-PfS-1c and FSI-PfS-2a, which share the same material and differ concerning the added weight of FSI-PfS-2a, reveals the influence of this additional inertia. Especially the first eigenfrequencies vary between $f_{1c,1} = 5.43$ Hz and $f_{2a,1} = 2.64$ Hz. The modal analysis of FSI-PfS-4x results in high first and second eigenfrequencies $f_{4x,1} = 35.66$ Hz and $f_{4x,2} = 35.67$ Hz, respectively. Basically, both eigenfrequencies describe the same bending mode only in different directions. Therefore, both eigenfrequencies are associated with the first bending mode (one bending node at the clamping of the cylinder). All other bending modes reveal eigenfrequencies over 200 Hz and are related to bending modes which will not appear in the FSI experiments, because the vortex shedding in the defined velocity ranges will not reach excitation frequencies over 20 Hz.

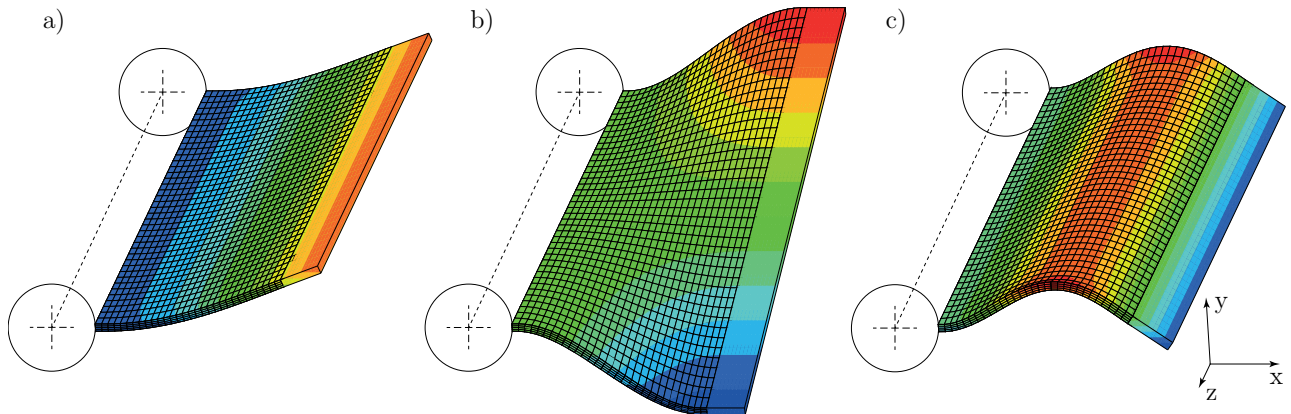


Figure 91: Results of the modal analysis: a) first bending mode \square , b) first twisting mode \diamond and c) second bending mode \triangle related to FSI-PfS-2a (color levels refers to the y -displacements).

9. Numerical setup

To prove the predictability of the developed test cases, numerical simulations are carried out with the commercial multi-physics code ANSYS[®]-CFX 14.0 (as already described in detail in Section 5). The solution of the structural mechanics is carried out by the FEM approach coupled by an implicit FSI coupling scheme to the flow predictions. These unsteady flow predictions are based on the Reynolds-averaged Navier-Stokes equations and the statistical SST turbulence model applying two- and three-dimensional grids. In comparison to large-eddy simulations (LES) as carried out by De Nayer et al. (2014) and De Nayer and Breuer (2014) the present approach possesses the advantage that a coarser grid resolution and a larger time-step size leads to drastically reduced simulation times. Additionally, since turbulence-induced cycle-to-cycle oscillations are averaged out by the statistical URANS approach, a phase-averaging as described in Section 7.4.1 for the experimental measurements is not required for the simulation data. Consequently, the coupled URANS predictions can be carried out within a short time and thus represent a reasonable step for the demonstration of the predictability of the newly-developed benchmarks. The simulations of the different test cases are performed using the benchmark definitions in Section 6 and the material parameters determined in Section 8.2. In the following paragraphs the applied computational meshes, the boundary conditions of the flow and structure solver and the FSI coupling parameters between both solvers are explained.

9.1. Grids and boundary conditions of FSI-PfS-1x and 2x

9.1.1. CFD

The focus of the present work is the development of FSI benchmarks which are simple concerning geometry and boundary conditions. An advantage for the numerical discretization is the equal geometry of the flow region of FSI-PfS-1x and FSI-PfS-2x. Here, the same numerical grid is applied for all test cases except FSI-PfS-1b. FSI-PfS-1b uses a slightly modified grid to take the thinner structure of $h = 0.8$ mm instead of $h = 2.0$ mm into account. In all these cases the flow prediction uses a block-structured grid of the xy -cross-section at $z/D = 0$ in the midplane of the test section (see Section 4.1 and Section 6). Due to the two-dimensional behavior of the flow expected for the statistical turbulence modeling approach, it is modeled as a quasi two-dimensional grid with one cell in the spanwise direction z . In the context of a URANS turbulence model a reasonable mesh with 285,000 cells is used as shown in Fig. 92. The stretching factors of the grid point distributions using geometrical series are kept below 1.1 with the first cell center located at a distance of $\Delta y/D = 1.59 \cdot 10^{-3}$ from the structure (see Figs. 92b and 92c). Based on the wall shear stresses on the structure, the average y^+ value is predicted to be below 25, i.e., the first cell center is in the buffer layer. The applied turbulence model (k - ω shear stress transport model, SST, Menter (1994)) uses a logarithmic wall function to calculate the shear stresses at the wall (for more details refer to Section 5.2). Since the boundary layers at the upper and lower channel walls (no-slip condition applied) are not intended to be adequately resolved and the walls are sufficiently far away from the structure, no grid refinement is required here.

On the CFD side no-slip boundary conditions incorporating the logarithmic wall functions are applied at the upper and lower channel walls, at the rigid front cylinder and the attached struc-

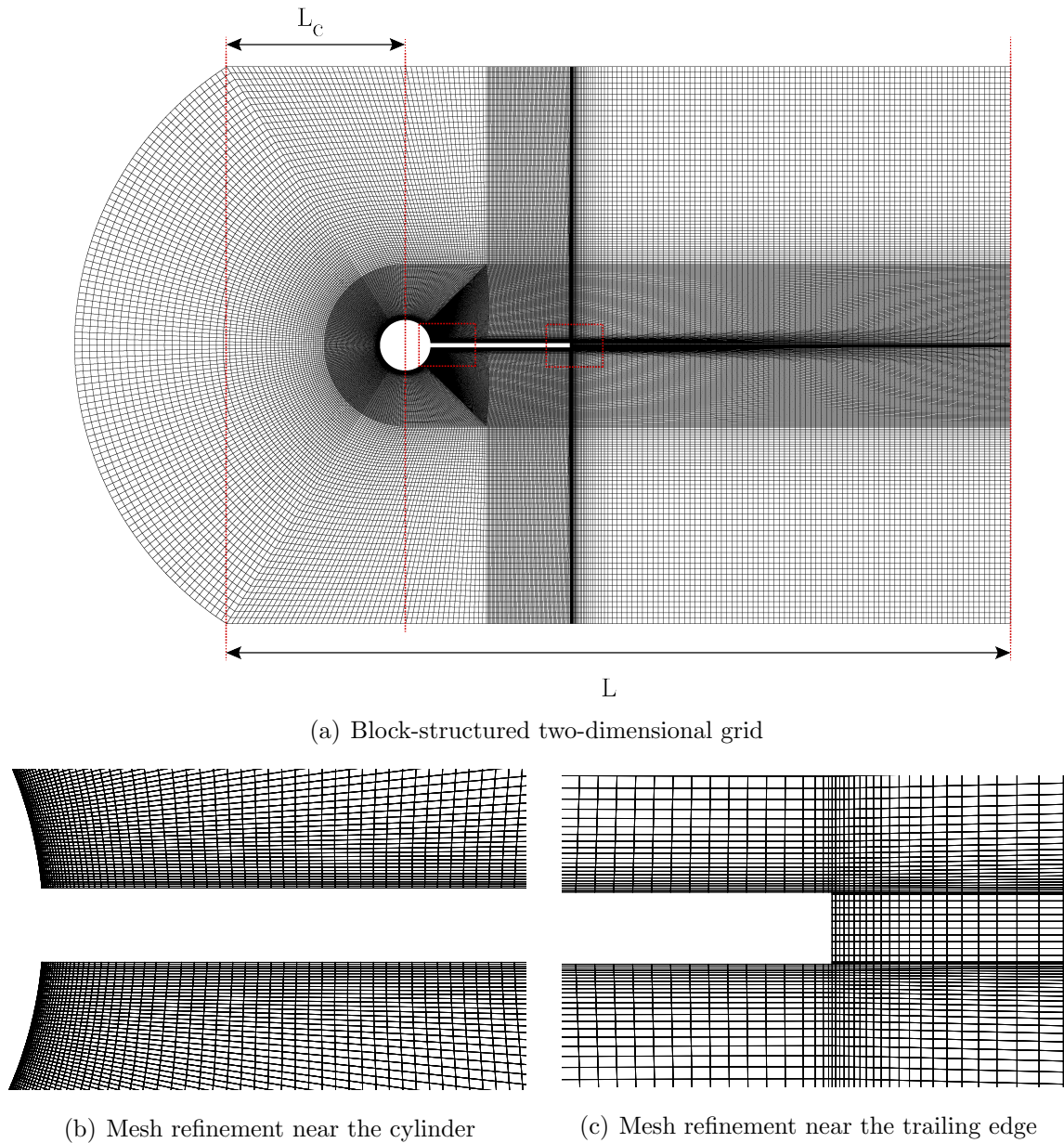


Figure 92: Two-dimensional grid used for the test cases FSI-PfS-1x and 2x.

ture. At the inlet a constant velocity according to the applied test case in x -direction is set as inflow condition with a random turbulence intensity of 2% according to the LDV measurements in the channel (see Section 7.3) and a turbulence length scale which is automatically estimated by ANSYS[®] CFX based on the mentioned turbulence intensity, the inflow velocity, the fluid density and the k - ϵ turbulence model constant C_μ (ANSYS, 2011c). Since the flow is in the subcritical regime, transition to turbulence is also a relevant issue. However, here no additional transition condition is applied so that the flow is predicted in a fully turbulent mode. At the outlet an opening boundary condition with entrainment (relative pressure set to 0 Pa) is applied.

In z -direction the symmetry condition is chosen to mimic a quasi two-dimensional domain. Due to the fact that the lateral walls are two planes and the structure is perpendicular to

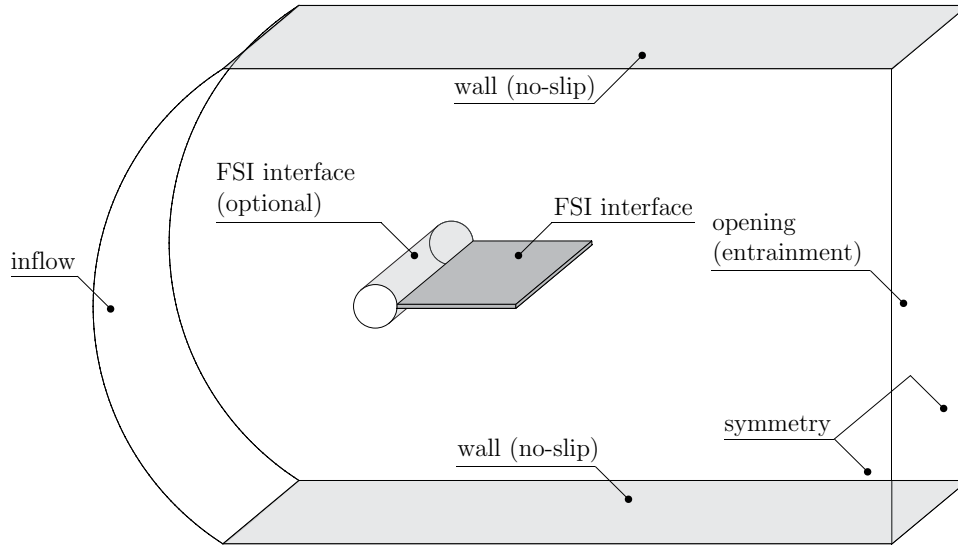


Figure 93: Flow boundary conditions for FSI-PfS-1x and 2x.

them, the symmetry condition is equivalent to the slip condition. A no-slip condition would create an additional unphysical resistance to the structure since the flexible plate is free and not fixed on the channel walls (where the real physical no-slip condition of the flow is present) and is therefore not applied here. As a consequence the small gap between the structure and the lateral channel walls is not modeled to maintain the two-dimensional modeling of the fluid domain and the fact that a disproportional increase of cells would be required for the grid refinement of the additional boundary layers there. The FSI interface is set to the boundaries of the elastic structures. In the cases of FSI-PfS-2x the additional steel weight is also defined as a FSI interface. For FSI-PfS-2b the cylinder surface is a further FSI interface due to its free rotational degree of freedom around the z -axis. The set-up including the boundary conditions of the flow is depicted in Fig. 93.

To rule out any prediction uncertainties related to the applied grid, a grid study based on the present medium mesh (285,000 cells) and a finer mesh (635,000 cells) refined in x - and y -direction) is performed. This study uses a transient uncoupled CFD simulation with the same boundary conditions as employed for the coupled case. Figure 94 represents an arbitrarily chosen snapshot of the predicted turbulent kinetic energy normalized by u_{inflow}^2 for both meshes. In this case no apparent deviation is recognizable. For the quantitative analysis the average lift $\overline{c_L}$ and the average drag coefficient $\overline{c_D}$ on the entire structure covering 15 cycles of the quasi-periodic vortex shedding are compared in Table 15 resulting in a relative error of 0.1668% for the drag coefficient. The average lift coefficient theoretically tends to zero. Thus, no relative error is calculated. The analysis shows that the medium grid ensures a high prediction quality of all relevant physical characteristics of the phase-averaged flow.

9.1.2. CSD

In the CSD prediction the elastic structure is discretized by 70×4 cells building a structured mesh of 280 SOLID186 elements (Zienkiewicz, 1977) for all FSI-PfS-1x (as illustrated in Fig 95) and FSI-PfS-2x cases (Figs. 96 and 97). This element is a second-order accurate

mesh	F_D (N)	F_L (N)	\bar{c}_D	\bar{c}_L	Error \bar{c}_D (%)
medium (285,000 cells)	1.478E-02	1.202E-04	0.707	5.727E-03	0.167
fine (635,000 cells)	1.476E-02	6.035E-05	0.705	2.884E-03	

Table 15: Comparison of the lift and drag forces on the entire structure (cylinder and flexible plate) for the uncoupled unsteady flow predictions on the medium and the fine mesh.

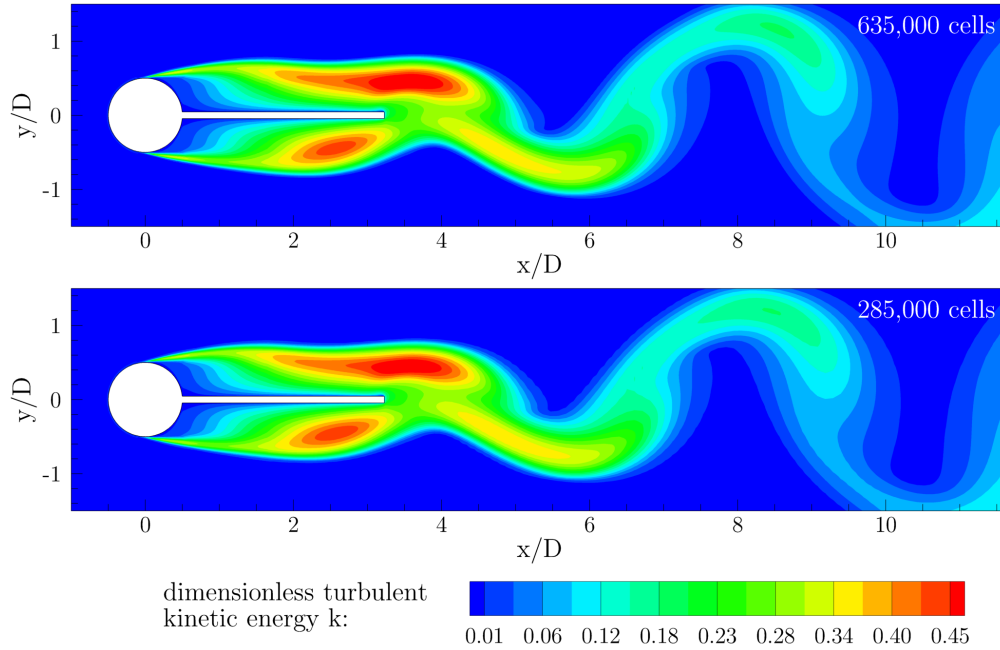


Figure 94: CFD predictions on the fine (top, 635,000 cells) and the medium mesh (bottom, 285,000 cells).

three-dimensional 20-node solid element that exhibits quadratic displacement behavior and supports hyper-elasticity, large deflections and large strain capabilities. In the test cases FSI-PfS-2x 10×4 elements for the steel weight attached to the shorter para-rubber plate (compare definition of FSI-PfS-1x in Section 6.3.1) are added.

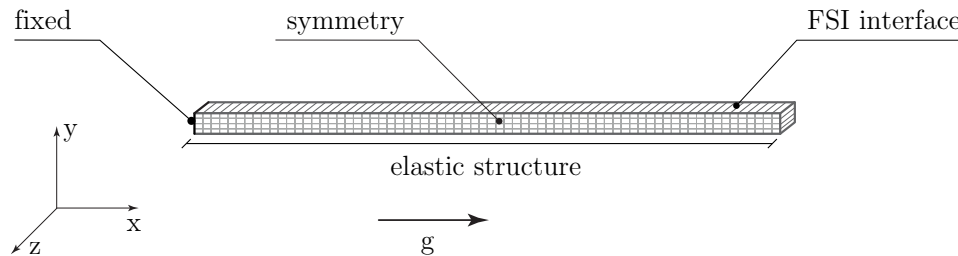


Figure 95: Grid used for the structure with boundary conditions for FSI-PfS-1x.

Regarding the boundary conditions of FSI-PfS-1x (Fig. 95) and 2a (Fig. 96) on the CSD side, the flexible structure is clamped to the rigid cylinder. Thus, the nodes at this boundary have zero degree of freedom (except FSI-PfS-2b). All other nodes are free for x - and y -translation and for z -rotation. The lateral sides are bounded by a frictionless support (slip condition) and all other faces are defined as a FSI interface for transmitting displacements to the fluid solver and receiving forces F_i from the fluid solver. Again, FSI-PfS-2b needs an additional condition

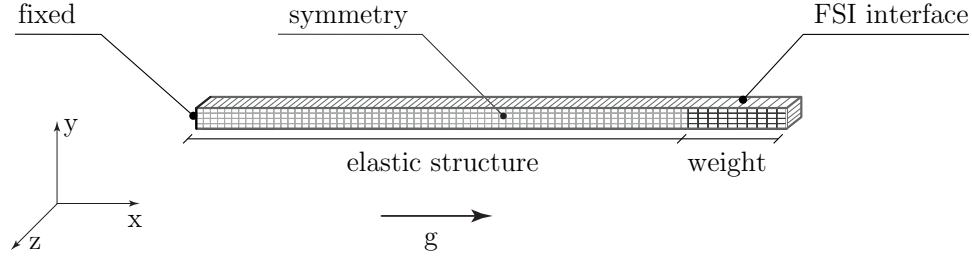


Figure 96: Grid used for the structure with boundary conditions for FSI-PfS-2a.

to take the FSI interface on the cylinder and its free rotational degree of freedom around the z -axis into account (Fig. 97).

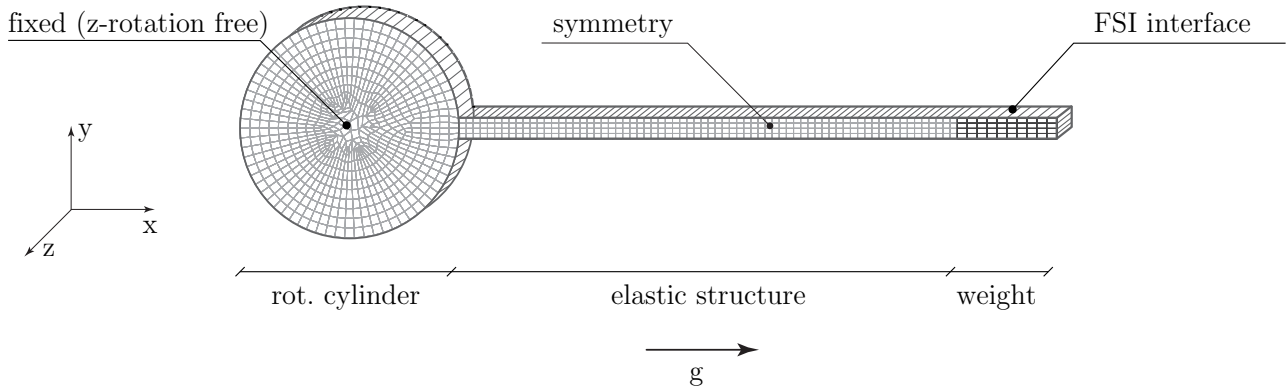


Figure 97: Grid used for the structure with boundary conditions for FSI-PfS-2b.

9.1.3. Coupling conditions

For both, the flow and structural solver, a time-step size of $\Delta t_f = 2 \cdot 10^{-3}$ s ($\Delta t_f^* = 1.26 \cdot 10^{-1}$ in dimensionless form using u_{inflow} and D as reference quantities) is chosen. To prove the independence of the predicted CFD results according to the time-step size, a corresponding study is presented in Table 16. Similar to the grid study again the lift and drag coefficients on the whole structure are compared for the case of the pure CFD prediction. Despite the larger time-step size the solution is in a good agreement to the results of the prediction applying a four times smaller time-step size.

time step [s]	F_D (N)	F_L (N)	\bar{c}_D	\bar{c}_L	Error \bar{c}_D (%)
$\Delta t_f = 2 \cdot 10^{-3}$	1.478E-02	1.202E-04	0.707	5.727E-03	0.702
$\Delta t_f = 5 \cdot 10^{-4}$	1.489E-02	8.551E-05	0.712	4.074E-03	

Table 16: Comparison of the lift and drag forces on the entire structure for the uncoupled unsteady flow prediction for two time-step sizes.

Due to the large time-step size the constant underrelaxation factor for the force is set to $\omega_f = 0.5$ to obtain the force convergence within a maximum of 30 coupling steps. To guarantee an adequate grid quality also for larger deformations of the structure, the mesh motion solver required for the Arbitrary Lagrangian-Eulerian (ALE) method applied in the fluid solver is forced to compute the mesh motion at least 5 times but maximally 23 times at each coupling

iteration.

The mesh motion method "Displacement Diffusion Model" is applied by CFX to compute the new mesh as described in Section 5.4. Here, the formulation of $\zeta(\mathbf{x})$ uses a hyperbolic approach dependent on the wall distance \mathbf{x} and the corresponding distance to the structure walls $h(\mathbf{x})$ to regulate the mesh stiffness in the different areas of the computational grid. Following Eq. (118), the applied equation is given by:

$$\zeta(\mathbf{x}) = \left(\frac{1 [m^{2.9}/s]}{(h(\mathbf{x}) + 0.0000001[m])^{0.9}} \right). \quad (147)$$

Using this formulation, it is possible to increase the mesh stiffness near to the FSI interface and to transport the mesh deformation into the bulk flow near the channel walls. Furthermore, this approach controls the grid deformation in such a way that grid features like the refinements close to the walls are kept in good order.

All solver settings listed in Table 17 are preliminarily tested and evaluated for receiving a good compromise between computational costs and reasonable results.

fluid solver (CFX)	advection scheme time-marching scheme convergence control convergence criterion time step	high resolution 2nd-order Backward Euler 5-18 loops RMS (u_i) = 10^{-4} $\Delta t_f = 2 \cdot 10^{-3}s$
fluid mesh motion (CFX)	coefficient loops mesh motion convergence criterion	5-23 RMS (Δx_i) = 10^{-5}
structure solver (ANSYS®)	time step large deformation	$\Delta t_s = 2 \cdot 10^{-3}s$ on
coupling (MFX)	coupling steps force underrelaxation factor force convergence criterion	20-30 0.5 RMS (F_i) = 10^{-2}

Table 17: Summary of solver and coupling method.

9.2. Grids and boundary conditions of FSI-PfS-3x

9.2.1. CFD

The further development of the two-dimensional benchmarks FSI-PfS-1x and 2x leads to the three-dimensional test cases FSI-PfS-3x. Based on the substitution of the cylinder by a cone, the whole flow field behaves completely three-dimensional. Therefore, three-dimensional grids and boundary conditions for the CFD and CSM predictions are necessary.

Due to ANSYS® solver license restrictions only a maximum number of 500,000 cells was possible for these three-dimensional test cases. Due to this reason the numerical grid of FSI-PfS-3x is rather coarse and will only provide qualitative conclusions about the predictability of these two test cases. To reduce the number of cells, the flow domain is separated into two parts (see Fig. 98). The first grid part includes the inlet and the refined boundary layers at the structure. Behind the structure the second part of the domain is attached with a coarser

grid resolution representing the wake flow area. Both grids are block-structured and contain 410,000 cells for the first and 88,000 cells for the second mesh part. In spanwise direction both parts are divided into 20 cells. To connect both grids, an interpolation interface is applied. This interface is similar to the FSI interpolation method used between the fluid and the structural grids. In case of a grid interface, the flow information on the unequally distributed nodes is interpolated from the finer first mesh to the coarse second mesh and vice versa. Despite the cell restrictions the first cell center has a distance of $\Delta y/D = 2.27 \cdot 10^{-3}$ from the structure and the y^+ value is predicted to be below 25.

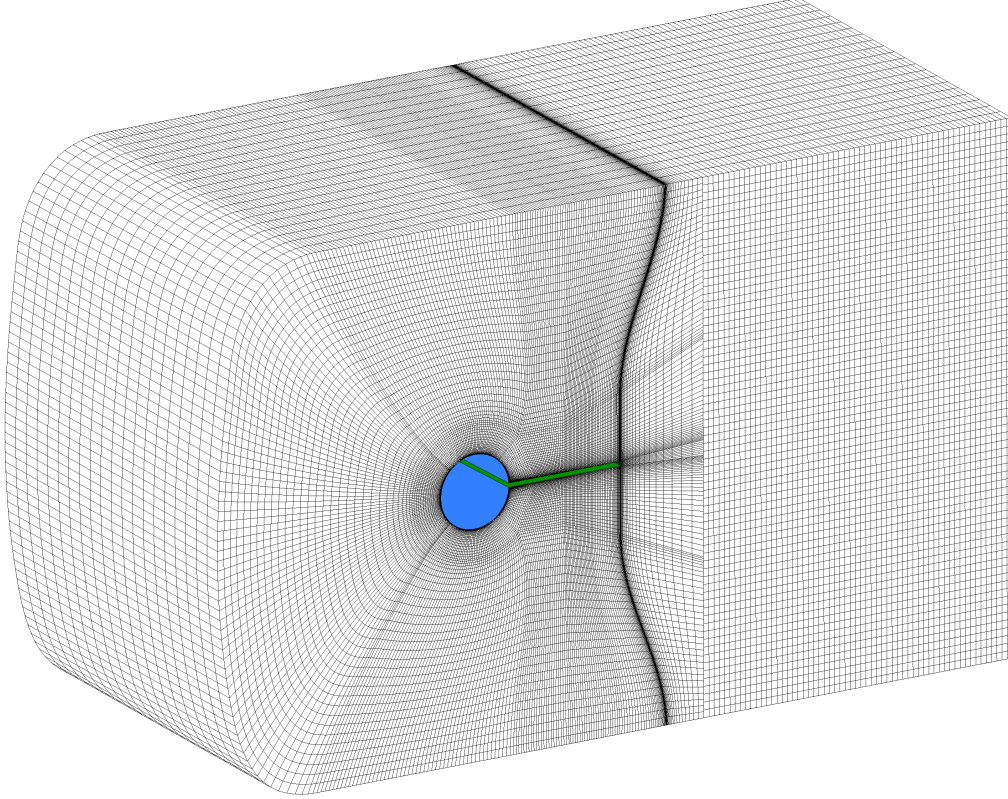


Figure 98: Three-dimensional grid used for the test cases FSI-PfS-3x.

On the CFD side no-slip boundary conditions incorporating the logarithmic wall functions are applied at the upper and lower channel walls, at the rigid cone and the attached structure. At the inlet a constant velocity of $u_{\text{inflow}} = 0.969$ m/s for FSI-PfS-3a and $u_{\text{inflow}} = 0.549$ m/s or FSI-PfS-3b is set in x -direction. The applied turbulence intensity, the turbulence length scale and the transition conditions are equal to the two-dimensional set-ups of FSI-PfS-1x and 2x. Again, at the outlet an opening boundary condition with entrainment (relative pressure set to 0 Pa) is applied. According to the three-dimensional character of FSI-PfS-3x special concern has to be put on the boundary conditions of the lateral sides of the flow region. Slip conditions are applied to the lateral sides of the three-dimensional flow region. In the present case the slip condition in addition to the three-dimensional flow grid is necessary since a symmetry for the phase-averaged flow and structure motion in spanwise direction can no longer be assumed. The small gaps between the structure and the lateral channel walls are again not modeled referring to the same considerations like in the two-dimensional test cases

mentioned in Section 9.1.1. The FSI interface is set to the boundaries of the elastic structure. The definition of the boundary conditions for the flow is illustrated in Fig. 99.

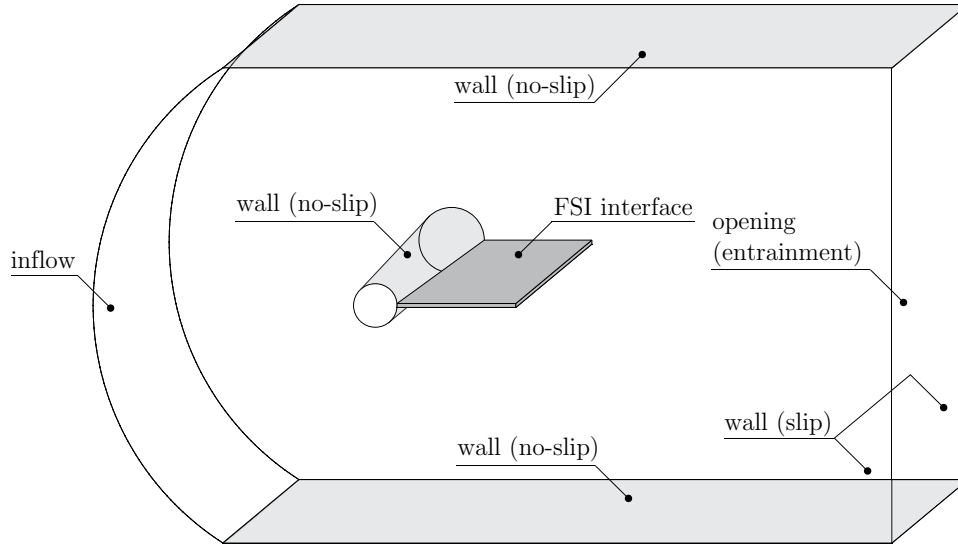


Figure 99: Boundary conditions of the flow for FSI-PfS-3x.

9.2.2. CSD

In the CSD prediction the elastic structure consists of $30 \times 40 \times 4$ cells building a structured mesh of 4800 SOLID186 elements (Zienkiewicz, 1977). Regarding the boundary conditions of FSI-PfS-3x (Fig. 100) on the CSD side, the flexible structure is fixed at the rigid cone. The lateral sides of the elastic structure are bounded by a frictionless support allowing x - and y -translation and z -rotations. All other degrees of freedom are disabled to prevent negative volumes due to out of plane deformations¹⁰. All other faces in the flow domain are set to the FSI interface for transmitting displacements to the fluid solver and receiving forces F_i from the fluid solver.

9.2.3. Coupling conditions

The coupling conditions for FSI-PfS-3x are mostly similar to the parameters of FSI-PfS-1x and 2x as listed in Table 17. Furthermore, the time-step size for FSI-PfS-3a is set to $\Delta t_f = 2 \cdot 10^{-3}$ s. Owing to the smaller inflow velocity of FSI-PfS-3b with $u_{\text{inflow}} = 0.549$ m/s the time-step size is increased to $\Delta t_f = 3 \cdot 10^{-3}$ s. The formulation of $\zeta(x_i)$ concerning the grid motion is unchanged and refers to Eq. (147).

9.3. Grids and boundary conditions of FSI-PfS-4x

9.3.1. CFD

The previously described test cases have no direct practical background. In contrast, the test cases FSI-PfS-4x are related to several VIV investigations by Naudascher and Rockwell (1994).

¹⁰In the results of these numerical investigations (see Section 10.2.3) this condition will have a fatal influence on the predicted structural deflection. In the result chapter different approaches to this issue are explained and discussed.

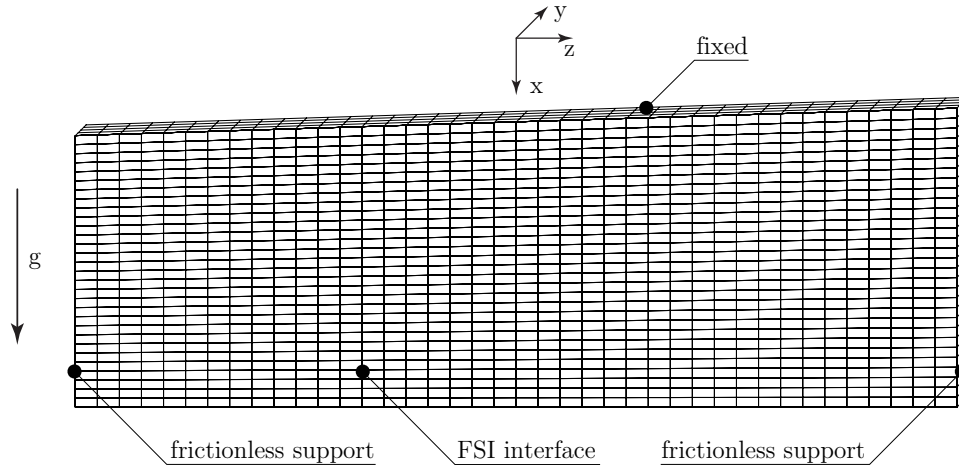


Figure 100: Grid used for the structure with boundary conditions for FSI-PfS-3x.

In the first case FSI-PfS-4a a single elastic cylinder is excited by the surrounding turbulent flow. The cylinder is fixed at one channel wall and free on the opposite side. In Fig. 101 the corresponding block-structured mesh of the numerical investigation is shown. Again, this computation is restricted to 500,000 cells. Therefore, only a part of the whole flow channel with the measures of $144 \text{ mm} \times 144 \text{ mm} \times 180 \text{ mm}$ is discretized. The cylinder with a diameter of $d = 8 \text{ mm}$ is the center of the mesh and constitutes the origin of the coordinate system.

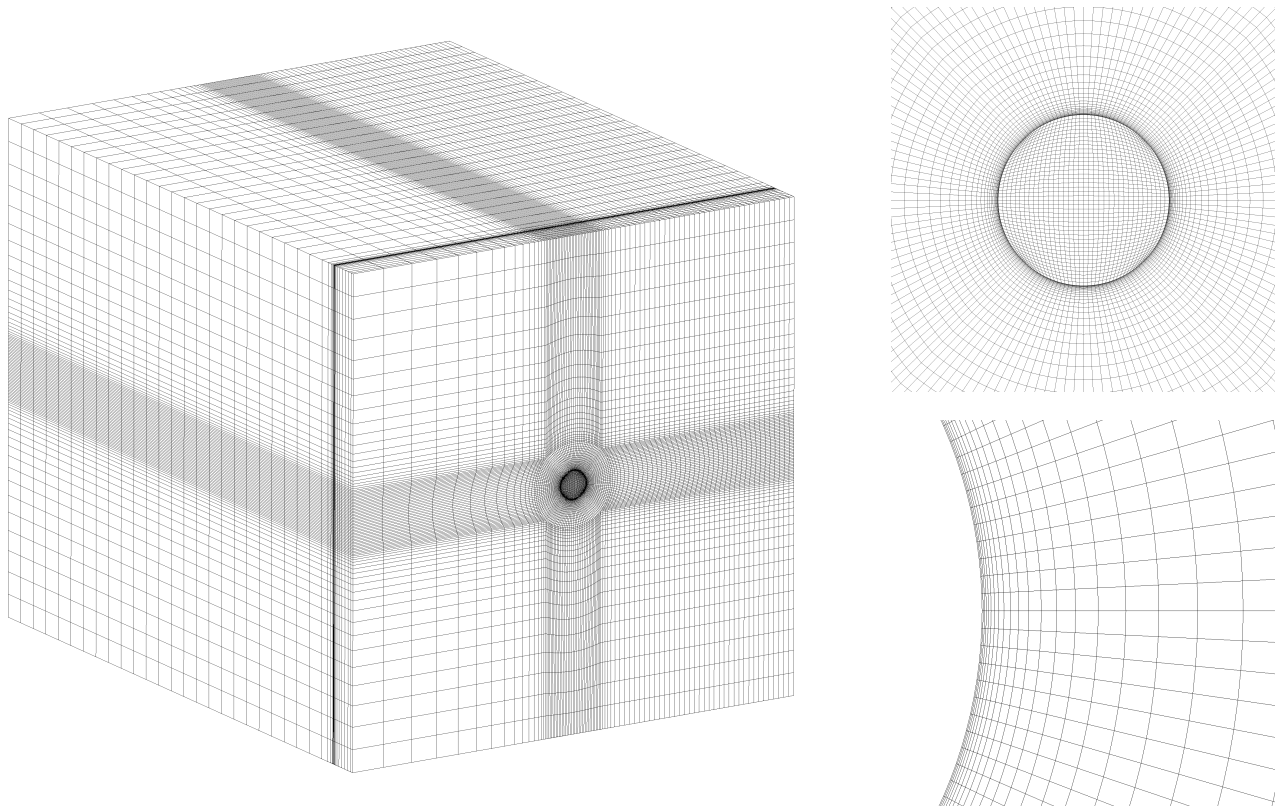


Figure 101: Three-dimensional grid used for the test case FSI-PfS-4a (left), refinement near the cylinder (right).

To take the free end of the cylinder and boundary layers on its surface into account, this part is

refined in all coordinate directions and the y^+ value is predicted to be below 22. In FSI-PfS-4b eight rigid circular cylinders are added to the configuration of FSI-PfS-4a. The nine cylinders are aligned as an 3×3 array surrounding the elastic cylinder in the middle of the array. Concerning this set-up the computational mesh is based on the former mesh of FSI-PfS-4a adding the eight fixed cylinders and their boundary refinements (see Fig. 102). To comply the maximal number of cells, the grid refinement close to the free cylinder surface has to be reduced so that only a y^+ value below 30 is maintained.

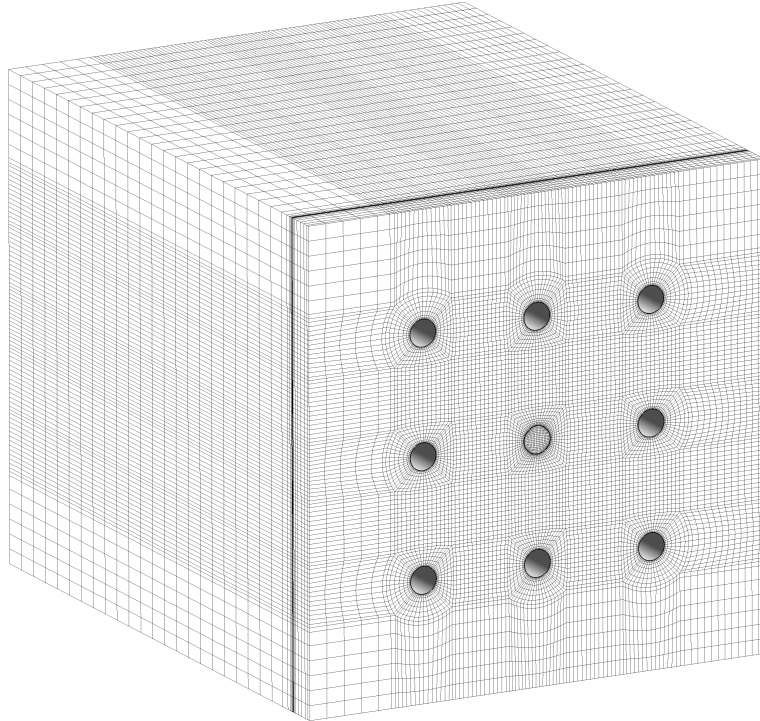


Figure 102: Three-dimensional grid used for the test case FSI-PfS-4b .

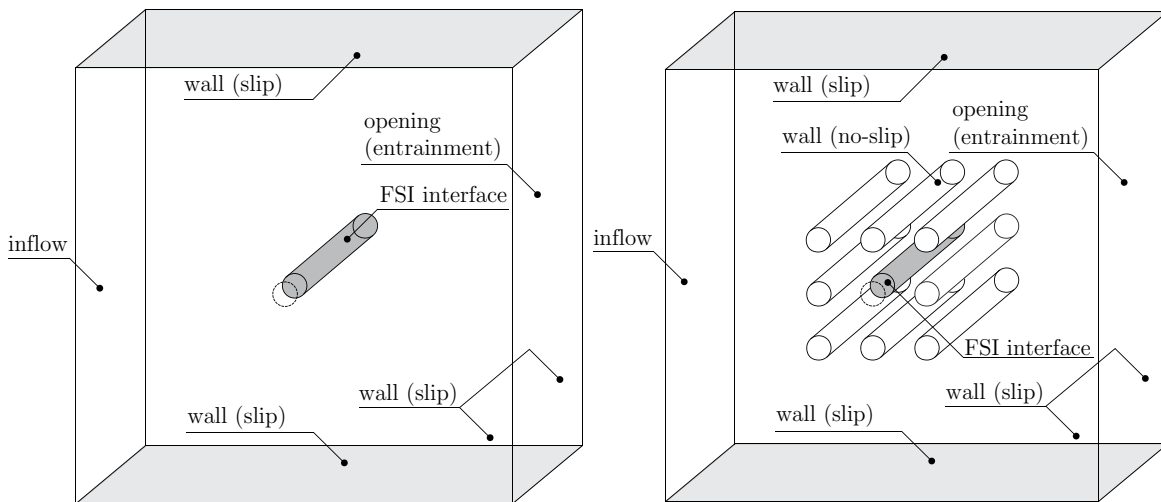


Figure 103: Boundary conditions of the flow for FSI-PfS-4a (left) and FSI-PfS-4b (right).

In Fig. 103 (left) the applied boundary conditions for the numerical simulation are presented. There are slip conditions set on the spanwise and lateral boundaries of the numerical domain.

The inlet condition is defined by a constant normal inflow velocity of $u_{\text{inflow}} = 1.69$ m/s. The outlet is modeled as an opening with entrainment (relative pressure set to 0 Pa). Finally, the whole cylinder surface is mapped as an FSI interface. Migrating the boundary conditions of FSI-PfS-4a, in the more complex test case FSI-PfS-4b no-slip conditions are added on the surfaces of the eight rigid cylinders (Fig. 103 right).

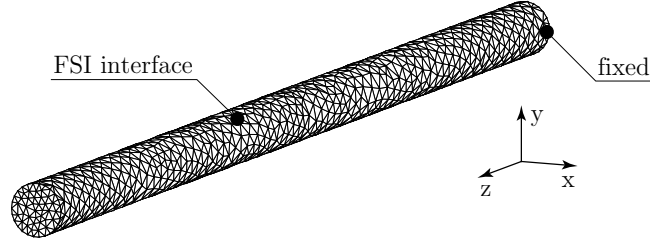


Figure 104: Grid used for the structure with boundary conditions for FSI-PfS-4x.

9.3.2. CSD

The unstructured mesh on the CSD side of both test cases FSI-PfS-4x consists of 4600 tetrahedra as shown in Fig. 104. The elastic structure is fixed on one end at the channel walls and free on the opposite side. All remaining faces belong to the FSI interface. The material parameters of the cylinder are set to the properties of polyethylene according to Section 8.2.2.

9.3.3. Coupling conditions

Again, the coupling conditions for FSI-PfS-4x are similar to the parameters of FSI-PfS-1x and 2x as listed in Table 17. For both cases the time-step size is set to $\Delta t_f = 5 \cdot 10^{-4}$ s taking the fast motion of the free cylinder into account. The formulation of $\zeta(x_i)$ concerning the grid motion again refers to Eq. (147).

10. Results and Discussion

In this section the experimental and numerical investigations of each test case are presented and discussed. The experimental data consist of measurements of the structural deflection and the flow field. Regarding the structural results the response of the structure within a reasonable range of inflow velocities is investigated. The results are shown in terms of amplitudes, swiveling frequencies, swiveling modes and the Strouhal number of the structural motion. The data provided here are the mean of 10 measurement series. This time-averaging step is necessary due to the cycle-to-cycle variations of the structural deflections which are also present during the slow increase of the inflow velocities. The presented plots are based on the displacement of a point near the vicinity of the structure at $x/D = 3.13$ and $z/D = 0$ ¹¹. Furthermore, detailed information of the time-dependent structure deflections and their phased-averaged mean are presented for each test case and the finally chosen inflow velocity. Generally, the flow measurements are focused on the two-dimensional PIV measurements and the specific inflow velocity of the test cases according to Table 6. Time-averaged and phase-averaged data are provided. According to the huge amount of data of the three-dimensional V3V flow results these data will not be shown for every test case. V3V results are only depicted for the nominally two-dimensional test cases of FSI-PfS-1a and FSI-PfS-2a, for the three-dimensional case of FSI-PfS-3a and the application-based test cases FSI-PfS-4a and 4b.

For all experimental test cases a POD analysis is performed to identify the large, energy-carrying flow structures past the flexible structure. The flow data used for this purpose are the time-dependent non-averaged two-dimensional flow fields (u, v) obtained by the PIV-system. Due to the large computational effort necessary for the coupled FSI predictions, the numerical investigations are only carried out for the finally chosen inflow velocity of each test case. Again flow and structure information concerning the time-dependent structural deflections and the corresponding phase-averaged flow fields will be displayed in the second part of this chapter. Parts of this chapter are already published in reviewed journals or conference proceedings e.g., in Breuer and Kalmbach (2011), De Nayer et al. (2012, 2014), Kalmbach and Breuer (2012, 2013a,b) and Kalmbach et al. (2013).

¹¹In the journal (De Nayer et al., 2014) and QNET publication of FSI-PfS-1a a different measurement point at $x/D = 2.82$ is applied. In the present thesis further optimization in the measurement set-up and post-processing allow the use of a measurement point closer to the extremity of the flexible plate. As a consequence both measurement points at $x/D = 2.82$ and $x/D = 3.13$ are presented for the structural results of FSI-PfS-1a.

10.1. Experimental results and analysis

10.1.1. FSI-PfS-1x (Two-dimensional geometry without rear mass)

The first set of test cases (FSI-PfS-1x) consists of an elastic plate clamped behind a fixed rigid non-rotating cylinder (see test case definitions in Section 6.3.1). Three different materials are used to investigate the FSI coupling with a stiff EPDM rubber, a very stiff but elastic polyamide plastic and a softer para-rubber material.

FSI-PfS-1a - Structural results

The stiff EPDM rubber plate attached to the cylinder limits the structure response to moderate deformations in the range of the cylinder diameter. Furthermore, the configuration of this test case allows only the first bending mode to be present. In the following paragraphs the structure and flow measurements and their analysis are presented to provide a complete insight into the coupled system. At first, the behavior of the elastic structure over a wide range of inflow velocities is described, before the specific test case according the finally chosen inflow velocity of $u_{\text{inflow}} = 1.385$ m/s is examined more closely.

Figures 105 and 106 refer to the structural response during a continuous increase of the inflow velocity up to $u_{\text{inflow}} = 2.2$ m/s. In Fig. 105 the maxima and minima of the averaged structure deformation are displayed while Fig. 106 presents the corresponding swiveling frequencies of the flexible plate. An arbitrarily-chosen characteristic snap-shot of the structure deflection at different inflow velocities is presented in Fig. 107. Unfortunately, these high-speed camera snap-shots do not display strong deformations of the rubber plate since the deflections found in the specific inflow velocity range are rather small.

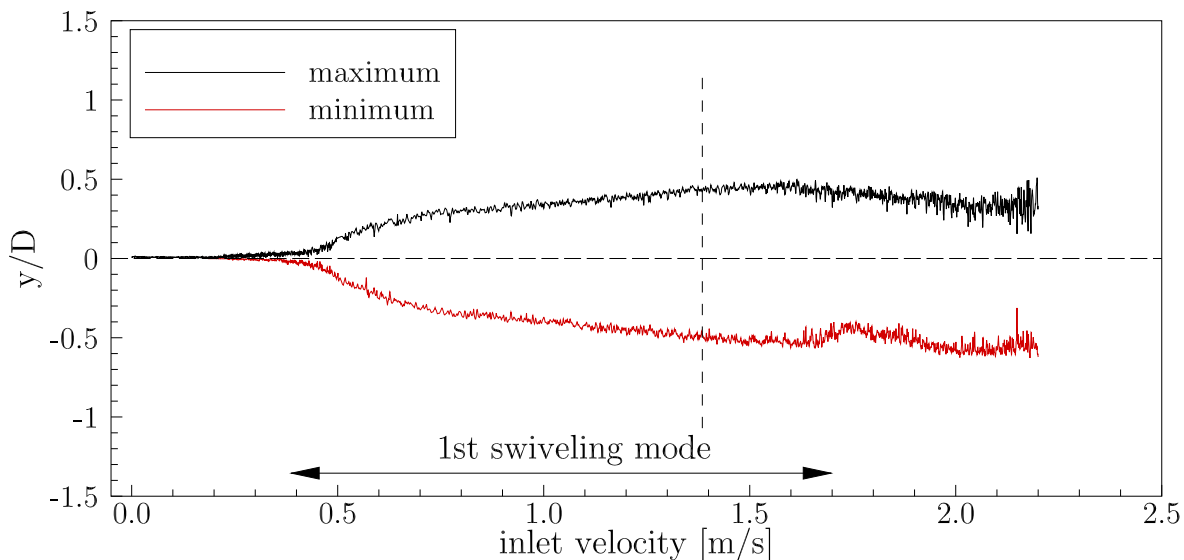


Figure 105: FSI-PfS-1a: Averaged maximal/minimal structural deflections as a function of the inflow velocity.

For this case the FSI coupling starts with an inflow velocity of $u_{\text{inflow}} = 0.2$ m/s with tiny and aperiodic deformations until the inflow velocity reaches a magnitude of 0.4 m/s. Starting with this critical inflow velocity the amplitudes of the structure deformation rises with increasing

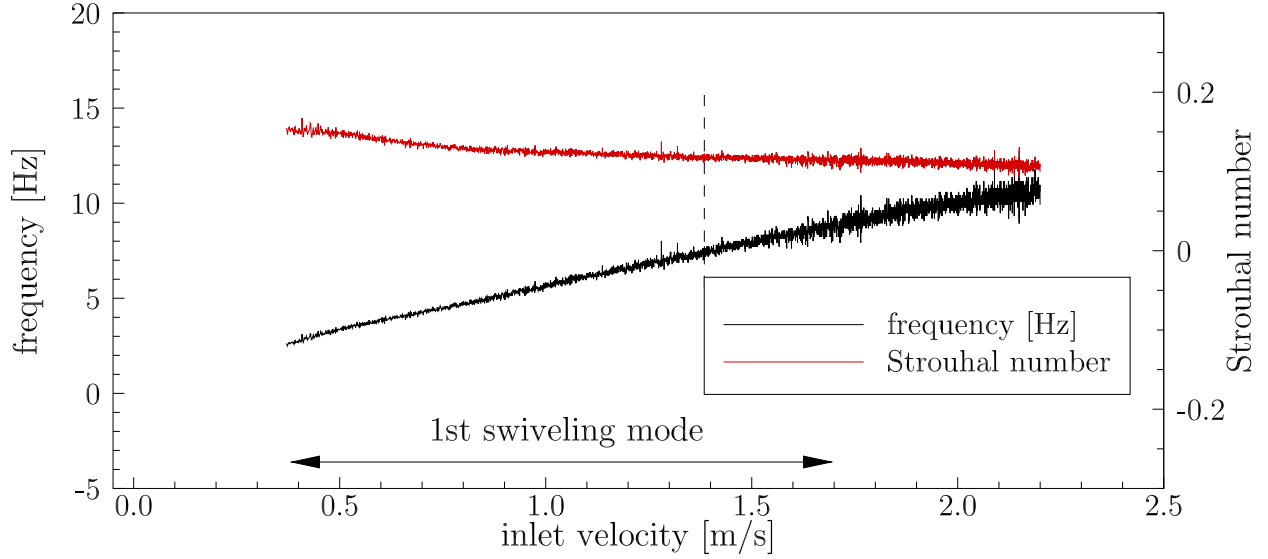


Figure 106: FSI-PfS-1a: Averaged frequency and Strouhal number as a function of the inflow velocity.

inflow velocities. Over the wide range of inflow velocities from $u_{\text{inflow}} = 0.4$ m/s to 1.6 m/s this continuous increase of the displacements is observable. Within this velocity range the structure swivels in the first bending mode. This mode is found to be dominant for the test case. It is characterized by quasi-periodic nearly two-dimensional deflections in the xy -plane. Higher inflow velocities beyond $u_{\text{inflow}} = 1.6$ m/s result in an almost three-dimensional, aperiodic motion with smaller peak amplitudes but much larger cycle-to-cycle variations for the deflection and oscillation frequency.

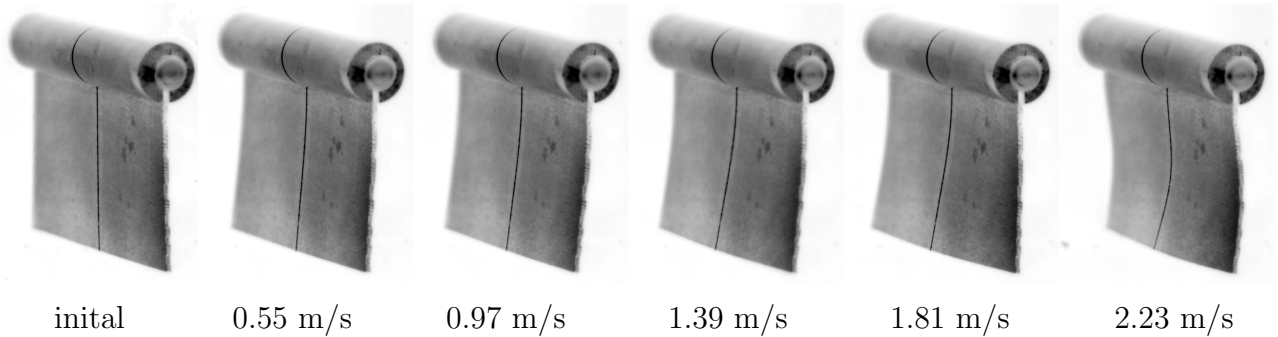


Figure 107: FSI-PfS-1a: Characteristic moments of the structural deformation at several inflow velocities for FSI-PfS-1a.

The swiveling frequencies f and its dimensionless equivalent denoted Strouhal number St show the same dependencies on the inflow velocities. After the non-periodic settling phase a cyclic motion starts at an inflow velocity of $u_{\text{inflow}} = 0.4$ m/s with a swiveling frequency of $f = 2.75$ Hz. Based on this frequency, the corresponding inflow velocity and the cylinder diameter, the Strouhal number is

$$St = \frac{f \cdot D}{u_{\text{inflow}}} = 0.15. \quad (148)$$

The further increase of the inflow velocity results in a linear rise of the swiveling frequency with a gradient $\delta f/\delta u = 4.50 \text{ Hz}/(\text{m s}^{-1})$. At the transition from the periodic to the irregular oscillation at a velocity of about 1.6 m/s the EPDM rubber plate swivels with a frequency of $f = 8.16 \text{ Hz}$. In the same interval the Strouhal number decreases to $\text{St} = 0.11$. This transition frequency $f = 8.16 \text{ Hz}$ is almost equal to the first eigenfrequency of $f_{1a,1} = 8.18 \text{ Hz}$ of the structure obtained by the modal analysis in Section 8.3. Possibly, the response of the structure in conjunction with the further existing external excitation leads to the change into the irregular mode. Another possibility is that the unsteady effects in the turbulent flow around the structure increase and thus the three-dimensional effects provoke the irregular deformations of the rubber plate.

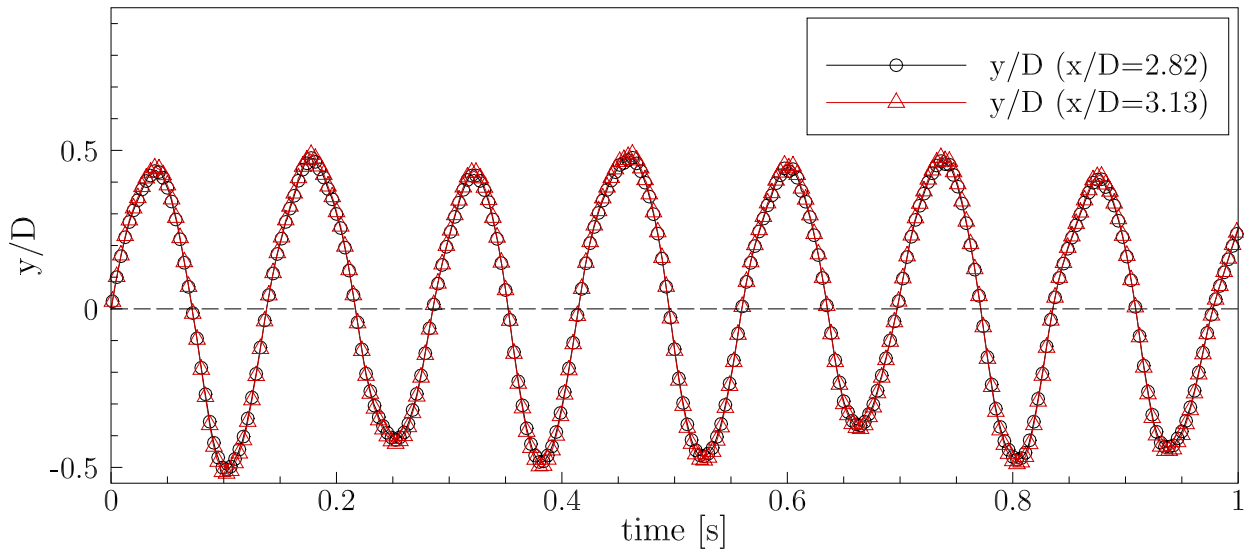


Figure 108: FSI-PfS-1a: Experimental structural results: Time history of the structural deflections (extract) for measurement points at $x/D = 2.82$ and $x/D = 3.13$ at $z/D = 0$.

Based on the previous investigations the final test case velocity $u_{\text{inflow}} = 1.385 \text{ m/s}$ is chosen in the middle of the periodic interval. The time history of the structural deflection is shown in Fig. 108 at the measurement points $x/D = 2.82$ and $x/D = 3.13$ near the extremity of the EPDM rubber plate. Both time-dependent signals are quasi-periodic but exhibit larger amplitude variations over several cycles. The deflections at $x/D = 3.13$ are slightly larger than at $x/D = 2.82$ since $x/D = 3.13$ is closer to the rear end of the structure. With an average maximum peak $y/D_{\text{max}} = 0.420$ and an average minimum peak $y/D_{\text{min}} = -0.418$ for the measurement point at $x/D = 2.82$ (Fig. 109) and $y/D_{\text{max}} = 0.439$ and $y/D_{\text{min}} = -0.440$ at $x/D = 3.13$ (Fig. 110), the standard deviation σ of all positive and negative peaks is calculated to be $\sigma_{\text{max}} = 0.054$ (12.59%) and $\sigma_{\text{min}} = 0.049$ (11.34%) over all 1500 recorded periods. Both signals are in-phase to each-other but slightly asymmetric due to the imperfect clamping of the rubber material in the front cylinder and a supposed initial pre-stress in the rubber material. The mean swiveling frequency at this inflow velocity is found to be $f_{\text{avg}} = 7.10 \text{ Hz}$ ($\text{St} = 0.113$) and its standard deviation is calculated to $f_{\text{std}} = 0.22 \text{ Hz}$ (3.09%).

To quantify the three-dimensional deformation of the plate, the phase-averaged measurement data in the yz -orientation of the LLT sensor at $x/D \approx 3.13$ are analyzed. In addition to the

already known measurement point at $x/D = 3.13$ at the midplane ($z/D = 0$) of the channel, two further measurement points at $z/D = -2.72$ and $z/D = 2.72$ are introduced. The analysis reveals slightly smaller mean deflections of about $y/D_{\max} = 0.402$ and $y/D_{\min} = -0.399$ at $z/D = -2.72$ and similar values at $z/D = 2.72$ with $y/D_{\max} = 0.400$ and $y/D_{\min} = -0.396$. Despite these differences in the structural displacements, the motion of the entire plate is almost in-phase with the midplane. Only minor aberrations of about $+7$ deg are observed on both sides. Another outcome of this study is that the maximum and minimum displacements of the rubber plate are present in the midplane of the channel. Unfortunately, not the entire rubber plate with its expansion in z -direction is measured due to the limited measurement range of the LLT sensor. Therefore, no data for the lateral sides of the rubber plate are available.

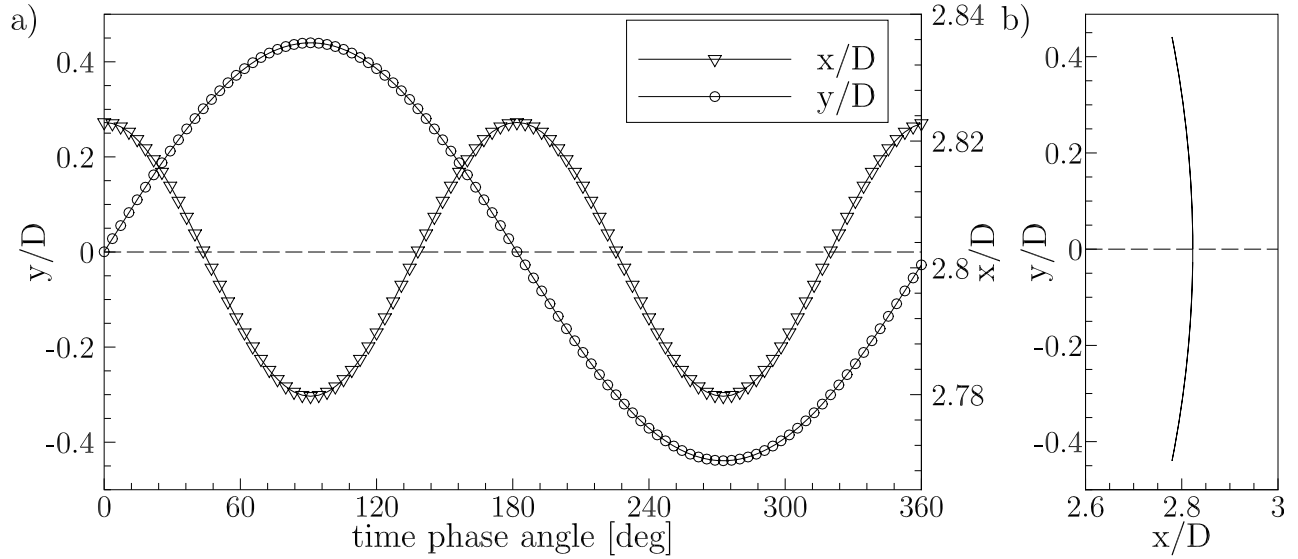


Figure 109: FSI-PfS-1a: Experimental structural results: a) phase-averaged reference period and b) phase-averaged phase-plane, both for the structural deflections at the measurement point at $x/D = 2.82$ in the midplane of the channel at $z/D = 0$.

The phase-averaged structural results are presented in Fig. 110 and 111. The nearly sinusoidal oscillation consists of 113 phase-averaged data points calculated out of the 1500 recorded periods. Covering the whole structure within the mean time-phase interval, Fig. 111 illustrates the moderate deflection of the rubber plate in the first bending mode. Due to the stiff rubber material only the rear end of the elastic structure undergoes large deformations forming a flat ”)”) xy -plot as visible in Fig. 110b.

FSI-PfS-1a - Flow results

By time-averaging over all PIV measurements without applying a phase-reconstruction method the flow is found to be almost symmetric. This result is depicted in Fig. 112a. On the upper and lower side of the cylinder the acceleration areas are visible. In front of the cylinder the stagnation point is present. Past the cylinder, the wake region with its characteristic lower fluid velocity is observed. Between the outer bulk flow and the inner wake area the shear layers on both sides of the structure mark the region where in the sub-critical flow the transition from a laminar to a fully-turbulent flow takes place. These flow features are common to sub-critical

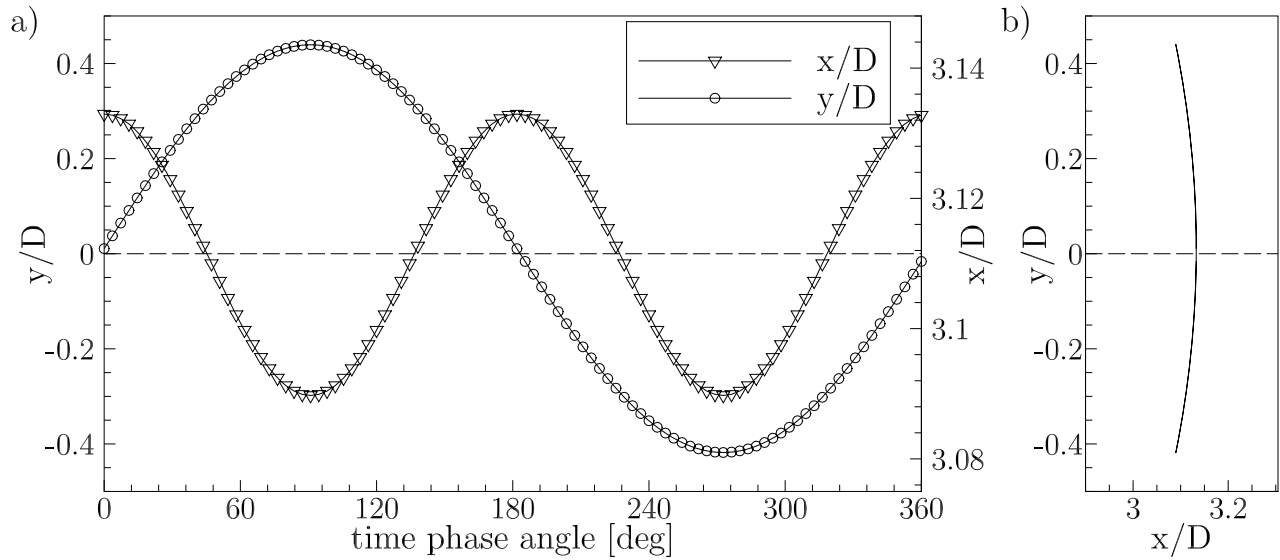


Figure 110: FSI-PfS-1a: Experimental structural results: a) phase-averaged reference period and b) phase-averaged phase-plane, both for the structural deflections at the measurement point $x/D = 3.13$ in the midplane of the channel at $z/D = 0$.

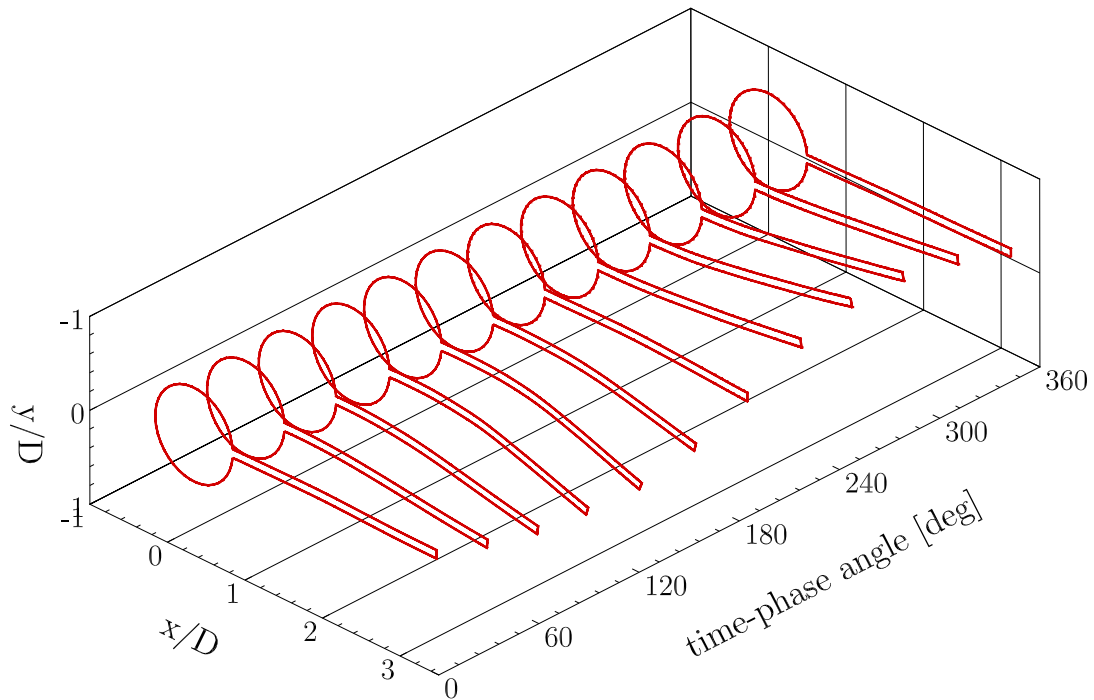


Figure 111: FSI-PfS-1a: Structural results: Structure contour for the reference period.

flows around circular cylinders (Breuer, 2002). The difference to the present FSI test case is the slight expansion of the wake starting near the extremity of the flexible structure. Due to the FSI motion of the structure containing alternating and counter-rotating eddies, the fluid receives an additional momentum in y -direction and widens the far-wake area. However, a comparison to the flow field of the corresponding rigid configuration in Fig. 76a only reveals a small influence of the FSI on the mean flow field.

In contrast the distribution of time-averaged Reynolds stresses $\overline{u'v'}$ shows a significant increase near the motion path of the rubber plate (compare Fig. 76b of the fixed configuration with Fig. 112b of the free FSI configuration) especially in the vicinity of the entire elastic structure. Here, the increase of flow fluctuations, caused by the structural motion, are responsible for the increased Reynolds stresses.

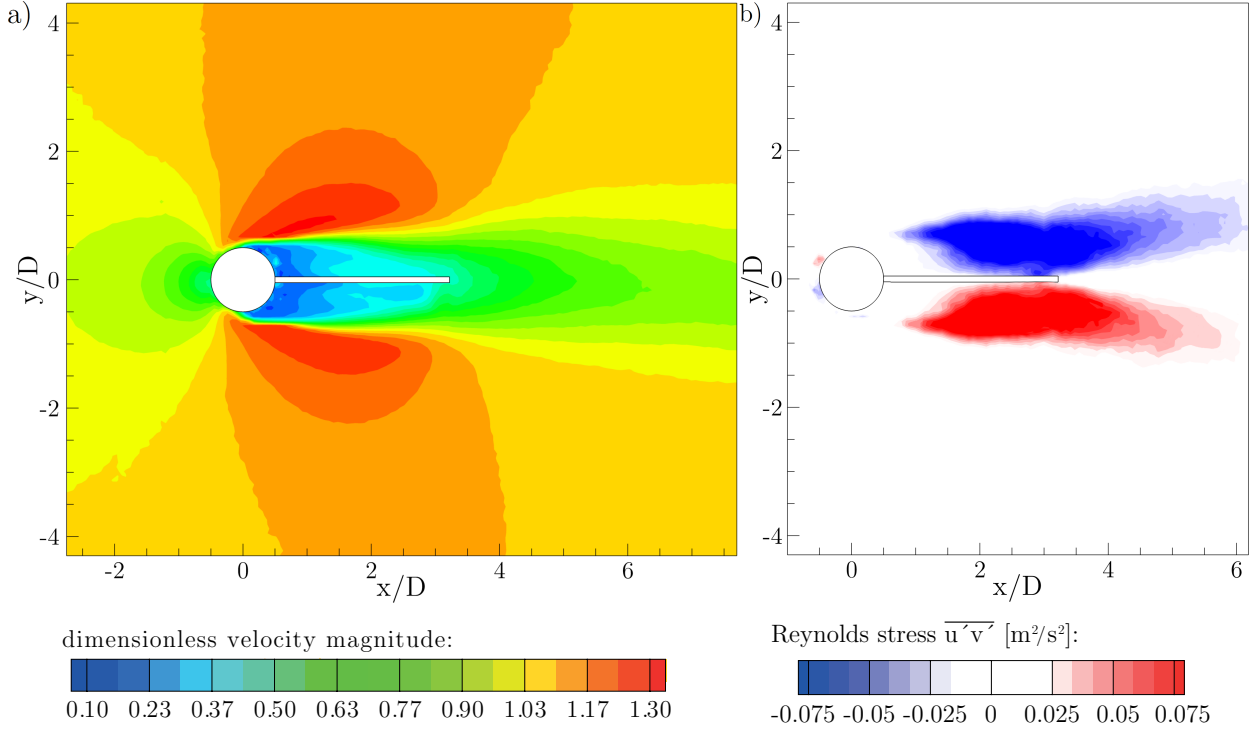


Figure 112: FSI-PfS-1a: Time-averaged flow results of FSI-PfS-1a and at $z/D = 0$ for a) dimensionless velocity magnitude and b) Reynolds shear stress $\overline{u'v'}$.

The combined phase-averaged flow and structural results are shown in Fig. 113 for six time phase angles (16, 78, 141, 204, 266 and 326 degrees). The dimensionless velocity magnitude $|u| = \sqrt{u^2 + v^2}/u_{\text{inflow}}$ is calculated based on the velocity components u and v in the xy -plane and the constant inflow velocity $u_{\text{inflow}} = 1.385$ m/s. These flow data are measured by the planar PIV system and the structural results are obtained by the LLT sensor in the xy -orientation, both at $z/D = 0$. The shown data are post-processed by the phase-averaging method including both flow and structural measurements. The combined mean phase-averaged flow and structural results consist of 23 time-phase angles representing all important information about the dynamics of this test case.

The centers of the vortices shedding alternatively from the upper and lower side of the cylinder are visible in the velocity magnitude contour plots. Looking at the temporal development of these flow structures over the entire period, the convective transport of the vortex centers in the main flow direction is noticeable. Due to the relatively coarse resolution of the PIV analysis the stagnation point in front of the cylinder is not explicitly visible. In the wake of the structure the characteristic recirculation areas are observed. However, in the direct vicinity of the flexible structure large measurement errors have to be expected for the PIV analysis (see Section 7.2). These errors can be explained by the optical reflections of the moving structure

which are captured by the PIV camera and could not easily be removed from the raw images. Furthermore, due to the fast motion of the rubber tail very large velocities are calculated by the PIV cross-correlation algorithm in contrast to the small particle displacements in the wake of the structure. With an additional post-processing step these structure-related velocities are filtered out. Despite these attempts the results near the structure are not fully satisfying, i.e., the boundary layers could not be resolved due to the coarse spatial resolution of the PIV grid and the errors of the PIV-system to determine low flow velocities (see Section 7.2.1).

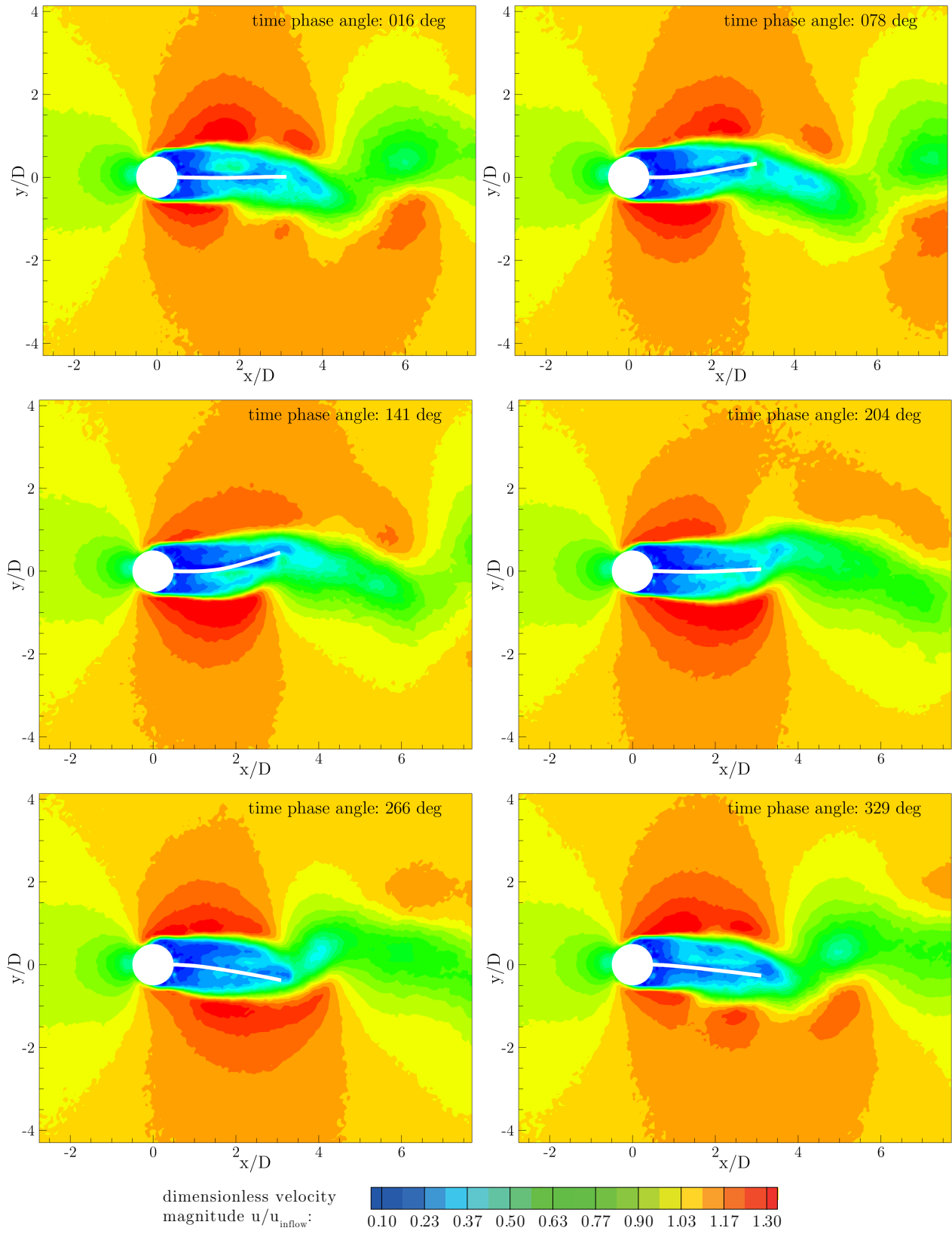


Figure 113: FSI-PfS-1a: Experimental phase-averaged flow and structural results for the reference period.

Based on the time series of the six time-phase angles shown in Fig. 113 the mean quasi-periodic FSI phenomenon of this test case is illustrated. In the first picture at a phase angle of 16 degrees (abbreviation: deg) the rubber plate is nearly in its initial position without any deformation. Nevertheless, the flow is fully developed around the structure. Due to the blockage by the bluff body the water is accelerated on its upper and lower sides. At this moment, a single vortex just detaches on the upper side while on the opposite side the acceleration area possesses its minimal extension. As a result of this alternating vortex shedding a classical vortex street is formed downstream of the structure. In this vortex street a vortex core is located at about $x/D = 6$ and $y/D = -1$.

In the next phase angle at 78 deg depicted in Fig. 113 the structure deforms non-linearly in positive y -direction as a result of the larger pressure forces on the lower side of the rubber plate than on its upper side. Simultaneously, the acceleration area on the lower side of the plate increases while all flow structures in the wake are continuously convected downstream. Between the phase angles of 78 and 141 deg the structure reaches its maximum deformation $(y/D)_{\max} = 0.439$ of the whole mean period and also the state of equal forces on the upper and lower plate side. After this maximum the plate moves back in negative y -direction as shown for the phase angle of 141 deg. Between the figures of the phase angles of 141 deg and 204 deg the structure passes its neutral position approximately at 180 deg. At this moment of the cycle the flow including the pressure force and the resulting structural deformations are reversed with respect to the first half of the period.

Due to the high deformation velocity of the plate a secondary trailing-edge vortex is generated while the structures moves through the wake area. This secondary vortex is hardly visible in the flow results due to the coarse resolution of the PIV-system and the systematic error of the phase-averaging method producing a blurred uncertainty. Since the phase-averaging method is spatially fixed and single flow elements like vortices occurring on slightly different positions and expansions due to the cycle-to-cycle variations, this blurring error is generated. Therefore, especially small structures like the mentioned trailing-edge vortex are averaged out due to their strong dependence on the structural deflection including its variations.

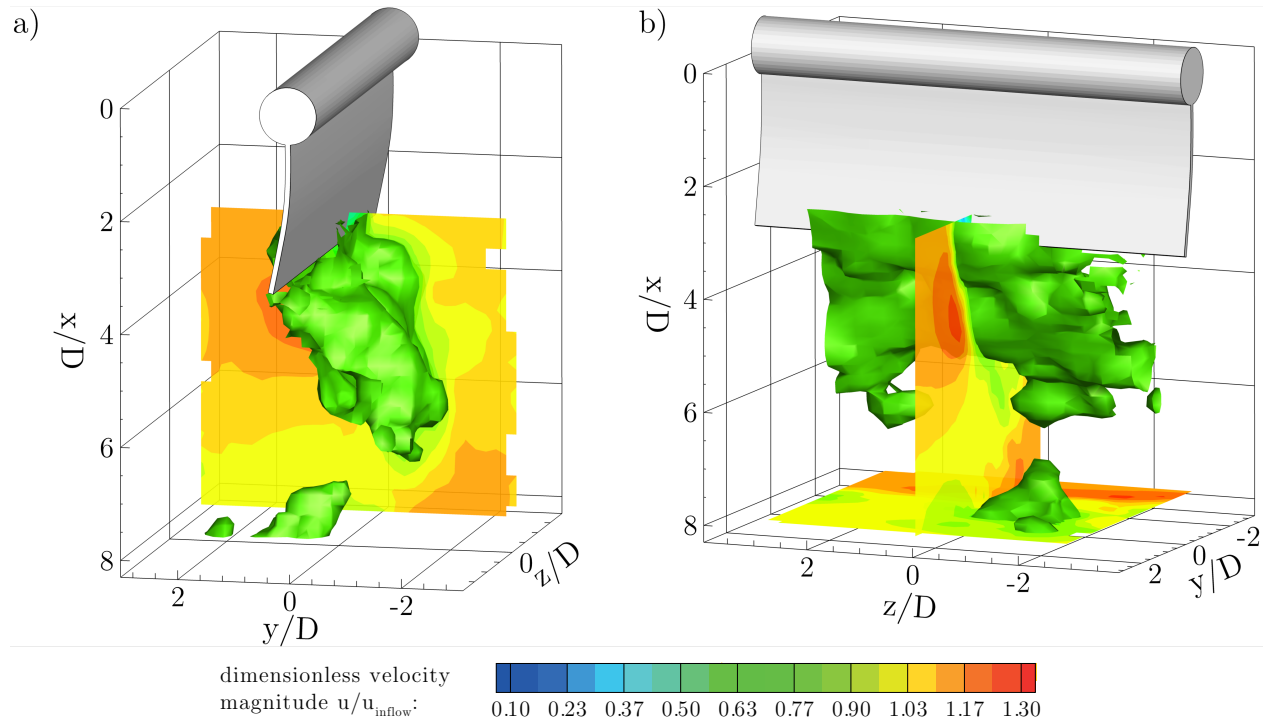


Figure 114: FSI-PfS-1a: Experimental flow results based on the V3V and the structural results, single measurement result at the phase angle of $\phi = 172$ deg for FSI-PfS-1a.

For this test case three-dimensional flow measurements are carried out. Figure 114 shows a single three-dimensional V3V flow measurement from two perspectives. The iso-surface is described by the dimensionless velocity magnitude $u/u_{\text{inflow}} = 0.79$, while the contour plots show the same quantity in the middle xy -plane ($z/D = 0$) and the yz -plane close to the end of the measurement volume of the V3V system at $x/D = 8$. This result reveals the three-dimensional characteristics of the flow present in this test case. The chosen iso-surface is strongly fragmented due to the turbulent wake past the rubber plate. The formation of a shedding vortex is visible in the contour plots at the chosen phase angle of 172 deg.

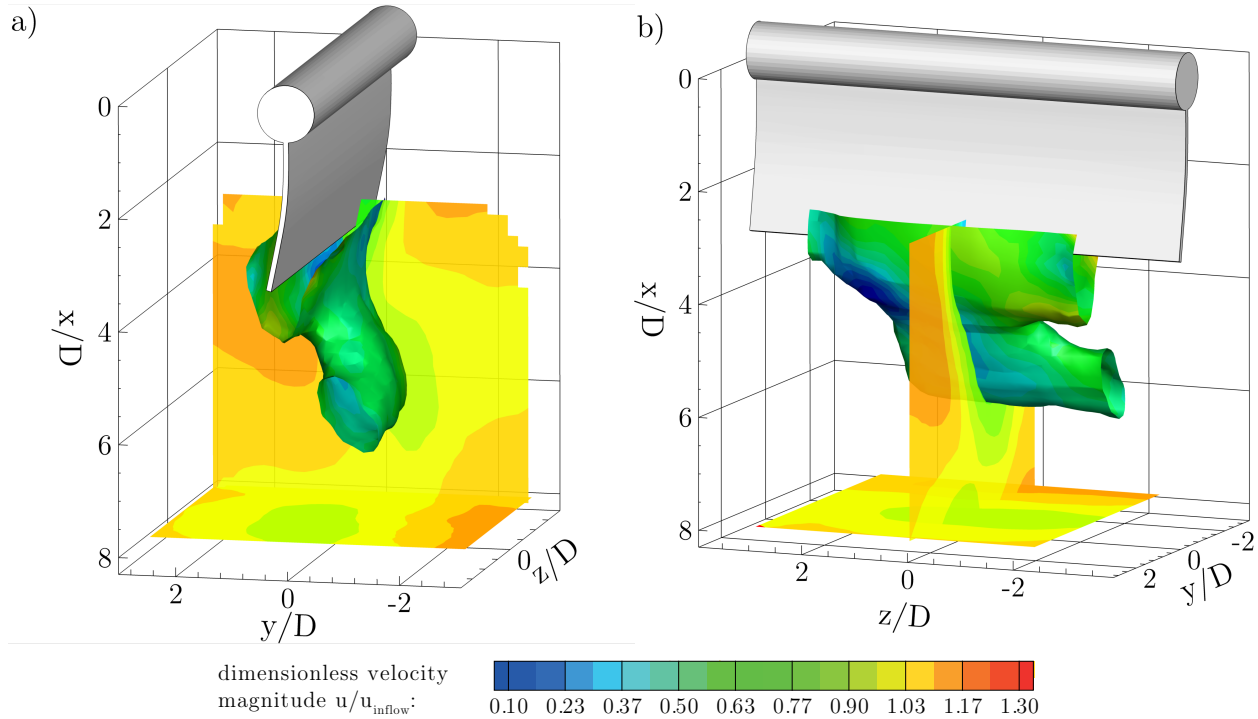


Figure 115: FSI-PfS-1a: Experimental flow results based on the V3V and the structural results, phase-averaged result at the phase angle of $\phi = 172$ deg for FSI-PfS-1a.

The corresponding phase-averaged results for the three-dimensional flow fields are presented in Fig. 115. Due to the phase-averaging the iso-surface is much smoother in contrast to the single measurement result in Fig. 114. Clearly visible are the alternatively shedding vortices in the wake of the structure. Noticeable is the appearance of these vortices which are slightly sustained in the main flow direction (oval appearance). The restriction of the structural motion in an area smaller than the cylinder diameter influences the formation of these vortices. It can be assumed that the inertia of the bulk flow and the stiff EPDM rubber hinders larger structural deformations. In addition to the structural deflection the inertia of the bulk flow also impedes the expansion of the vortices in y -direction and gives an explanation of their oval appearance.

The POD analysis of the first two modes present in FSI-PfS-1a are depicted in Fig. 116. Figure 116a and 116b correspond to the kinetic energy of the streamwise velocity u . Large areas of energy are found in the wake of the structure due to the formation and transport of the

detached vortices. The first two POD modes related to the energy of the cross-flow velocity component v are presented in Fig. 116c and 116d. The analysis shows that the energy rises in the area, where the vortices detach from the shear layers and form an antisymmetric pattern according to the alternating vortex shedding at the cylinder. The POD analysis based on the vorticity is directly related to the energy content of the unsteady effects and fluctuations in the flow and is presented in Fig. 116e and f. As assumed the largest energy content is found in the vortex formation region in the shear layers and behind the flexible structure. Positive and negative values are related to the direction of the rotation of the vortical structures. The POD analysis¹² for this test case yields that the first and second POD mode contain together about 40% of the total turbulent kinetic energy ($k_{\text{abs,all}} = 963.91 \text{ m}^2/\text{s}^2$, $k_{\text{rel,all}} = 100\%$) and exhibit the major flow structures. The most energy-carrying mode related to the flow fluctuations is calculated to $k_{\text{abs,1st}} = 204.96 \text{ m}^2/\text{s}^2$ representing $k_{\text{rel,1st}} = 21\%$ of the total turbulent kinetic energy. In this mode (Fig. 116e) negative values for the energy are obtained in the area of the moving plate and in the shear layers. Positive values are also present in the shear layers and downstream of the trailing edge of the structure. The second mode (Fig. 116f) has a total turbulent kinetic energy of $k_{\text{abs,2nd}} = 180.02 \text{ m}^2/\text{s}^2$ ($k_{\text{rel,2nd}} = 19\%$) and an almost inverse appearance of the energy distribution in relation to the first mode.

The direct comparison with the fixed configuration of the FSI-PfS-1a shows large differences in the energy distribution for all modes and all variables. However this change in the energy distribution is mostly related to the lower vortex shedding frequency for the rigid case compared to the free configuration and not to the motion of the elastic structure. Nevertheless, each energy spot is slightly enlarged for the coupled case according to the increased momentum transfer. Quantitatively, an increase of 17% of the total kinetic energy is observed for the FSI case. Since there is no significant change in the energy distribution of the first and second POD mode, it can be assumed that the FSI related effects are found in the higher POD modes, maybe interfered with other minor turbulence effects.

¹²Note that the energy magnitude is directly depending on the grid size of the input data. Therefore, the results do not represent the physically stored kinetic energy of the flow. Furthermore, the presented absolute values refer only to the fluctuating velocity since the mean velocity field is subtracted during the POD processing. The present results are only qualitatively evaluated and compared to each other under the assumption of equal grid sizes.

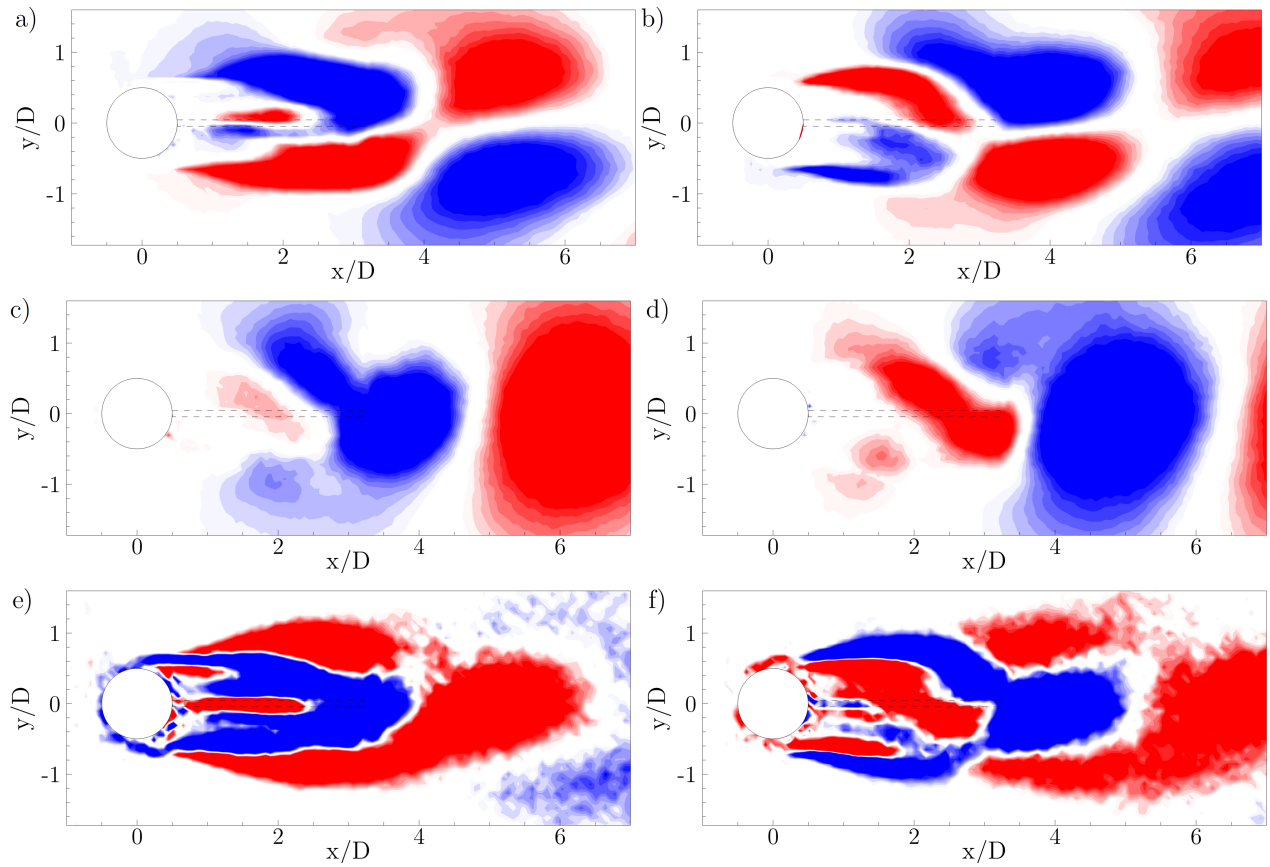


Figure 116: FSI-PfS-1a: POD analysis of the two-dimensional flow fields in the midplane ($z/D = 0$) of FSI-PfS-1a a) velocity component u , first mode; b) velocity component u , second mode; c) velocity component v , first mode; d) velocity component v , second mode; e) vorticity component ω_z , first mode; f) vorticity component ω_z , second mode.

FSI-PfS-1b - Structural results

Similar to the structural deformation in FSI-PfS-1a, here the more stiff polyamide plate attached to the cylinder limits the structure response to small deformations in the range of the cylinder diameter. Again, only the first bending mode is reached under the specific test conditions.

The structural response during a continuous increase of the inflow velocity up to $u_{\text{inflow}} = 2.3$ m/s is depicted in Figs. 117 and 118. In Fig. 117 the maxima and minima of the time-averaged structural deformations are shown while Fig. 118 displays the corresponding oscillation frequencies of the flexible plate.

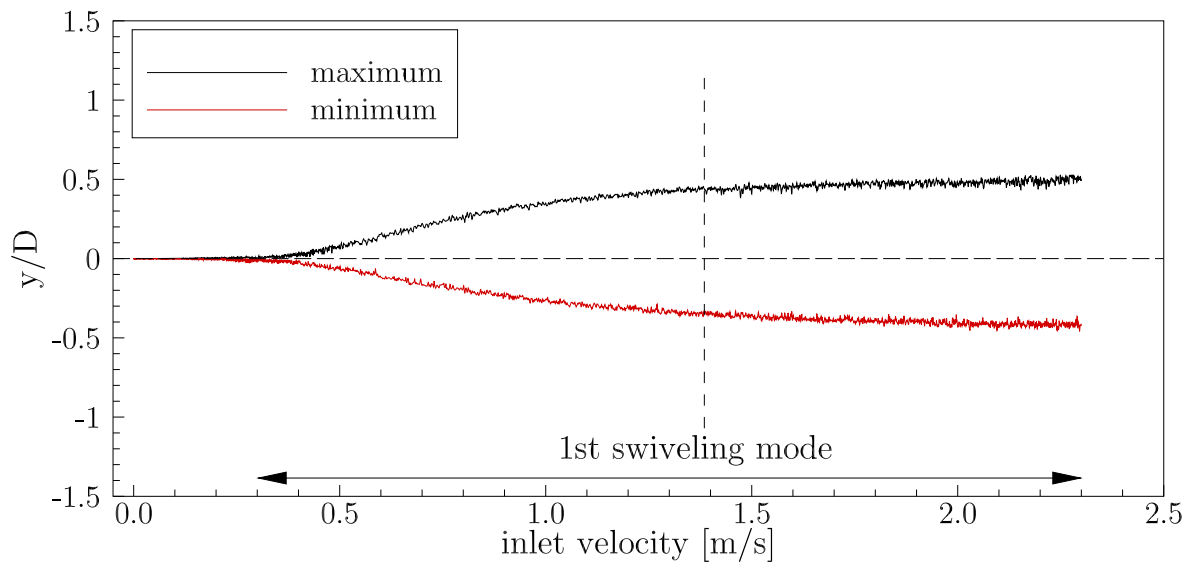


Figure 117: FSI-PfS-1b: Averaged maximal/minimal structural deflections as a function of the inflow velocity.

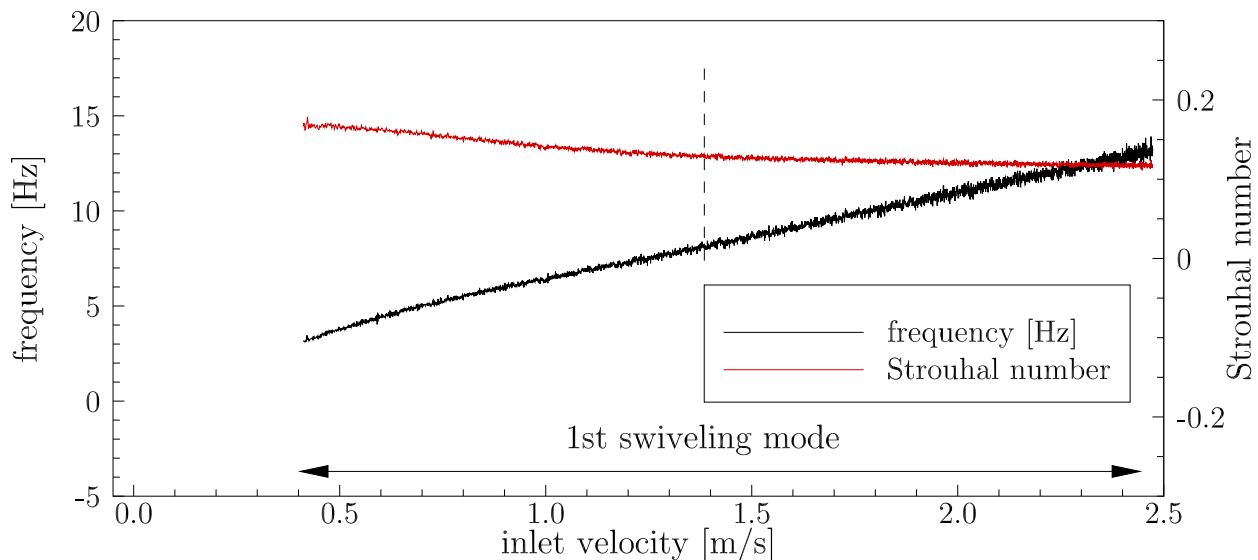


Figure 118: FSI-PfS-1b: Averaged frequency and Strouhal number as a function of the inflow velocity.

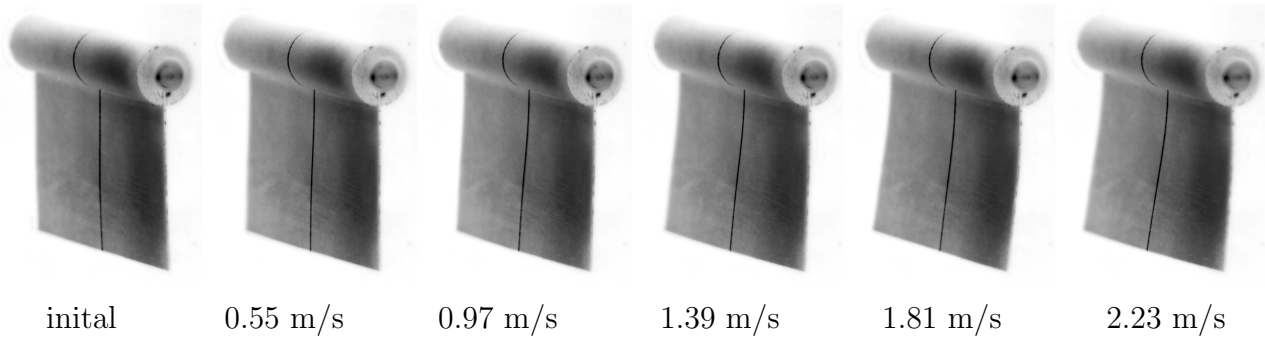


Figure 119: FSI-PfS-1b: Characteristic moments of the structural deformation at several inflow velocities for FSI-PfS-1b.

For this case the FSI-coupling begins at an inflow velocity of $u_{\text{inflow}} = 0.2$ m/s with tiny and aperiodic deformations. By reaching an inflow velocity of $u_{\text{inflow}} = 0.4$ m/s the amplitudes of the structural deformation rises with a flat slope. Over the wide range of inflow velocities from $u_{\text{inflow}} = 0.4$ m/s until the end of the measurement series at $u_{\text{inflow}} = 2.45$ m/s this increase of the deformation is more or less undisturbed. Although the displacements increase, the structure always swivels in the first bending mode. Similar to FSI-PfS-1a this mode is found to be dominant for this configuration.

The swiveling frequencies f and the Strouhal number St are proportional to the inflow velocity. After the non-periodic settling phase a cyclic movement starts at an inflow velocity of about 0.4 m/s with a swiveling frequency of $f = 2.98$ Hz ($St = 0.164$). A further increase of the inflow velocity results in an almost linear rise of the oscillation frequency with a gradient $\delta f / \delta u = 5.08$ Hz/(m s⁻¹). In contrast to FSI-PfS-1a the transition from the periodic two-dimensional to the irregular three-dimensional oscillations takes place at the much higher inflow velocity of 2.3 m/s. Furthermore, the three-dimensional deformation effect seems to be weaker in this test case, maybe as a consequence of the much stiffer polyamide material. However, the polyamide plate swivels with a frequency of $f = 12.65$ Hz. In the same interval the Strouhal decreases to $St = 0.120$. The first eigenfrequency of $f_{1b,1} = 25.24$ Hz obtained by the modal analysis in Section 8.3 is much higher than the excitation frequencies reached. Therefore, a structural resonance-induced bending mode transition, e.g., to the second bending mode, does not take place.

The final test case velocity is set to $u_{\text{inflow}} = 1.385$ m/s as in the FSI-PfS-1a case ensuring large and quasi-periodic structural deflections. The time history of the structural deflection is shown in Fig. 120 for a point near the extremity of the polyamide plate. Similar to FSI-PfS-1a the signal is quasi-periodic but exhibits large amplitude variations over several structural cycles. In the present test case the extrema are slightly lower than for FSI-PfS-1a with an average maximum peak $(y/D)_{\text{max}} = 0.380$ and an average minimum peak $(y/D)_{\text{min}} = -0.393$. The same applies to the standard deviation of all positive and negative peaks which are found to be $\sigma_{\text{max}} = 0.023$ (6.05%) and $\sigma_{\text{min}} = 0.019$ (4.83%) over all 1463 recorded periods. Again, the asymmetry in the structural deflections are assigned to the clamping of the polyamide plate in the front cylinder and possible pre-stresses in the material. Another difference is observed for the slightly increased mean swiveling frequency $f_{\text{avg}} = 8.02$ Hz ($St = 0.127$) and its standard

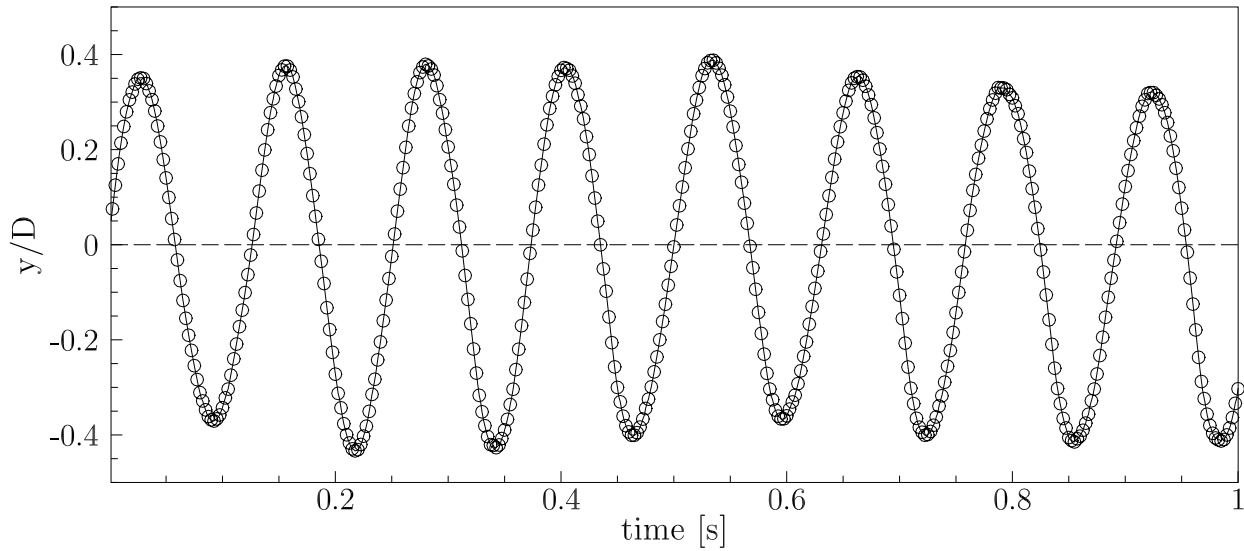


Figure 120: FSI-PfS-1b: Experimental structural results: Time history of the structural deflections (extract) for the measurement point at $x/D = 3.13$ at $z/D = 0$.

deviation $f_{\text{std}} = 0.18$ Hz (2.24%) for the chosen inflow velocity of $u_{\text{inflow}} = 1.385$ m/s.

The three-dimensional deformation of the polyamide plate is analyzed as already described for FSI-PfS-1a. Again, the yz -orientation of the structure sensor at $x/D = 3.13$ is used to determine the phase-averaged extrema at the measurement points at $z/D = -2.72$ and $z/D = 2.72$. The corresponding data are compared with the well-known measurement point at $z/D = 0$. Similar to the results of FSI-PfS-1a the structural deflections in the midplane of FSI-PfS-1b represent the extrema of the entire polyamide plate. Closer to the lateral sides values of about $y/D_{\text{max}} = 0.366$ and $y/D_{\text{min}} = -0.382$ at $z/D = -2.72$ and $y/D_{\text{max}} = 0.369$ and $y/D_{\text{min}} = -0.383$ at $z/D = 2.72$ are observed. Due to the stiff material used for the thin plate also the phase difference with about +4 deg is smaller than for FSI-PfS-1a. Therefore, the following behavior of the lateral parts of the plate is reasonable, although the plate is free to deform in z -direction.

An almost sinusoidal signal (Fig. 121 and Fig. 122) consisting of 100 phase-averaged data points is computed by applying the phase-averaging method to the 1463 recorded periods. As visible in Fig. 122 only for the rear end of the elastic structure larger deflections are observed for this first bending mode. Similar to FSI-PfS-1a the phase-averaged phase plane forms a flat ”)”) (Fig. 121b).

FSI-PfS-1b - Flow results

By applying a time-averaging to the flow fields recorded by the PIV system, an almost symmetric result of the flow is obtained (Fig. 123a). Similar to FSI-PfS-1a the characteristic flow features (i.e., the acceleration areas on the upper and lower side of the cylinder, the stagnation point in front of the cylinder, the wake area past the cylinder, the shear layers on both sides of the structure and the expansion of the wake due to the additional momentum in y -direction caused by the moving structure) are again present.

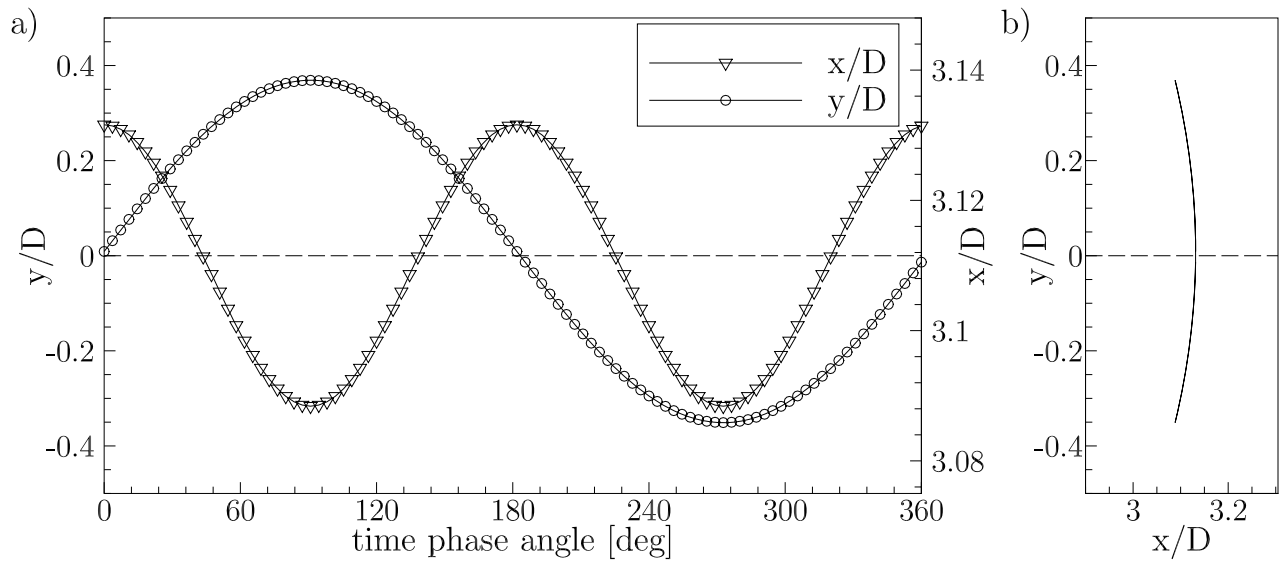


Figure 121: FSI-PfS-1b: Experimental structural results: a) phase-averaged reference period and b) phase-averaged phase-plane, both for the structural deflections at the measurement point $x/D = 3.13$ in the midplane of the channel at $z/D = 0$.

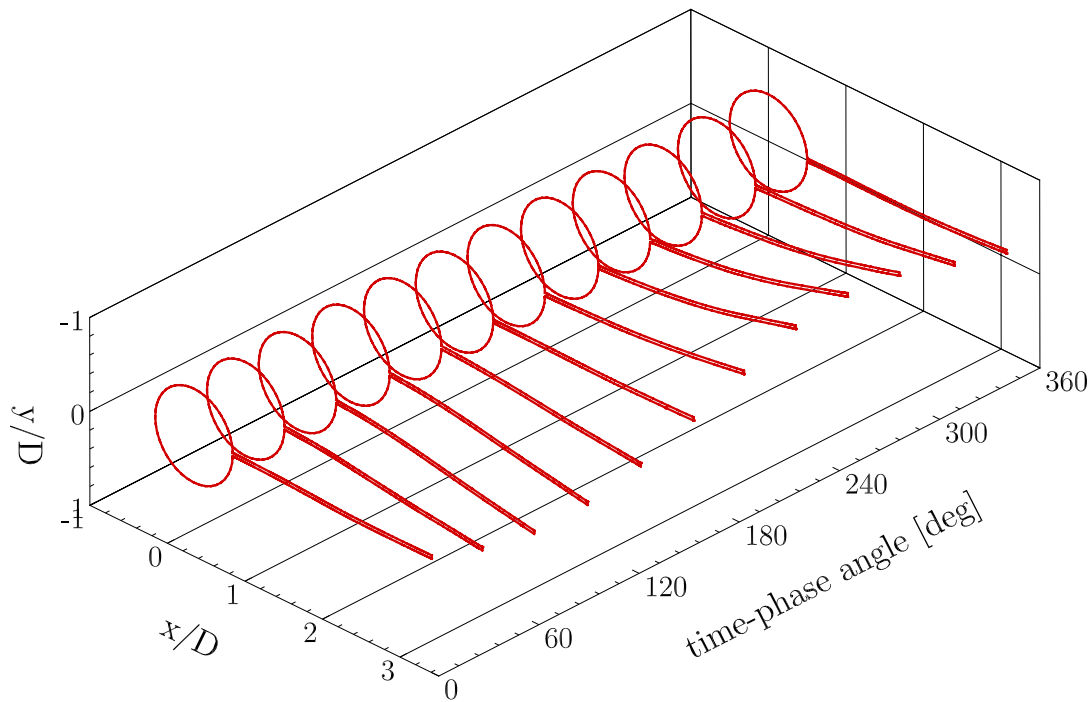


Figure 122: FSI-PfS-1b: Structural results: Structure contour for the reference period.

Again, the Reynolds stresses depicted in Fig. 123b reveal a similar but slightly increased distribution in comparison to the rigid configuration.

The combined phase-averaged flow and structural results are shown in Fig. 124 for six time phase angles (16, 78, 141, 204, 266 and 326 deg). The similarities in the flow fields to FSI-PfS-1a are large, e.g., the size and position of the detached and convected eddies in the flow are

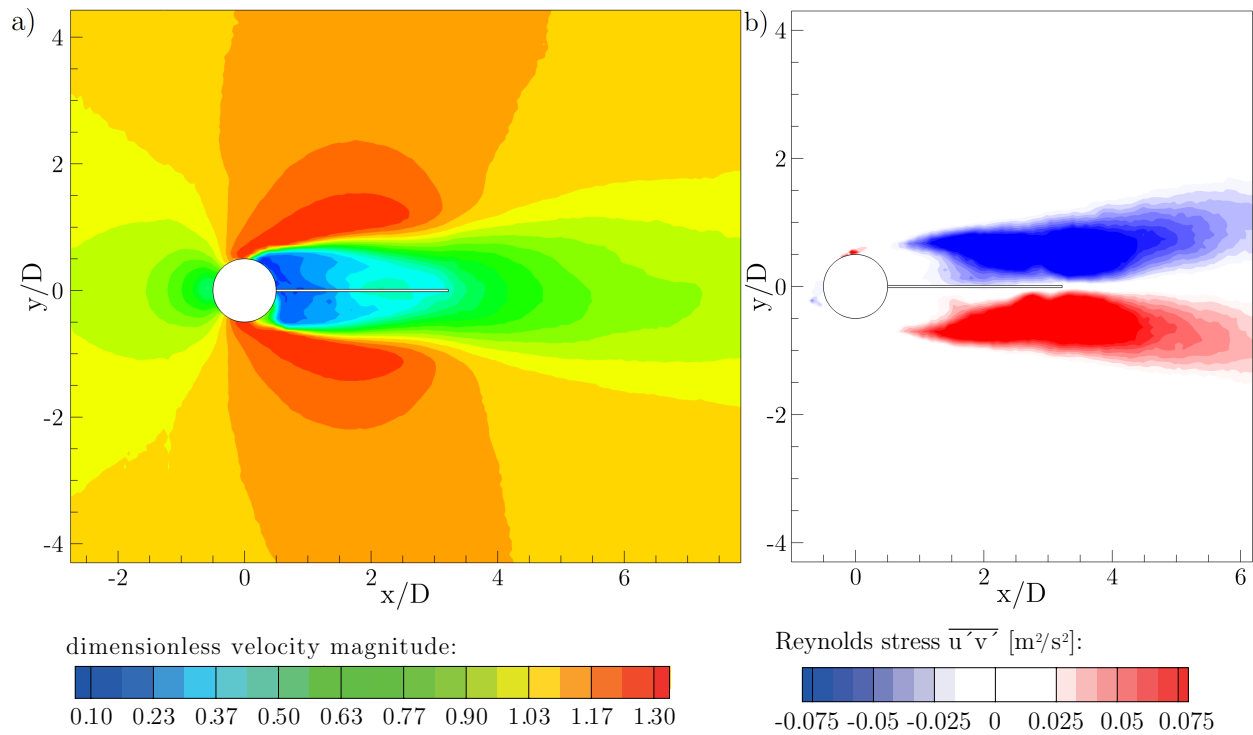


Figure 123: FSI-PfS-1b: Time-averaged PIV results of FSI-PfS-1b at $z/D = 0$ for a) dimensionless velocity magnitude and b) Reynolds shear stress $\overline{u'v'}$

almost the same in both reference periods. They only slightly differ due to the altered vortex shedding frequency in both flow states. Since the bending mode and the deflection level also almost match, a detailed description of each time-phase angle is omitted here (refer to the description of FSI-PfS-1a).

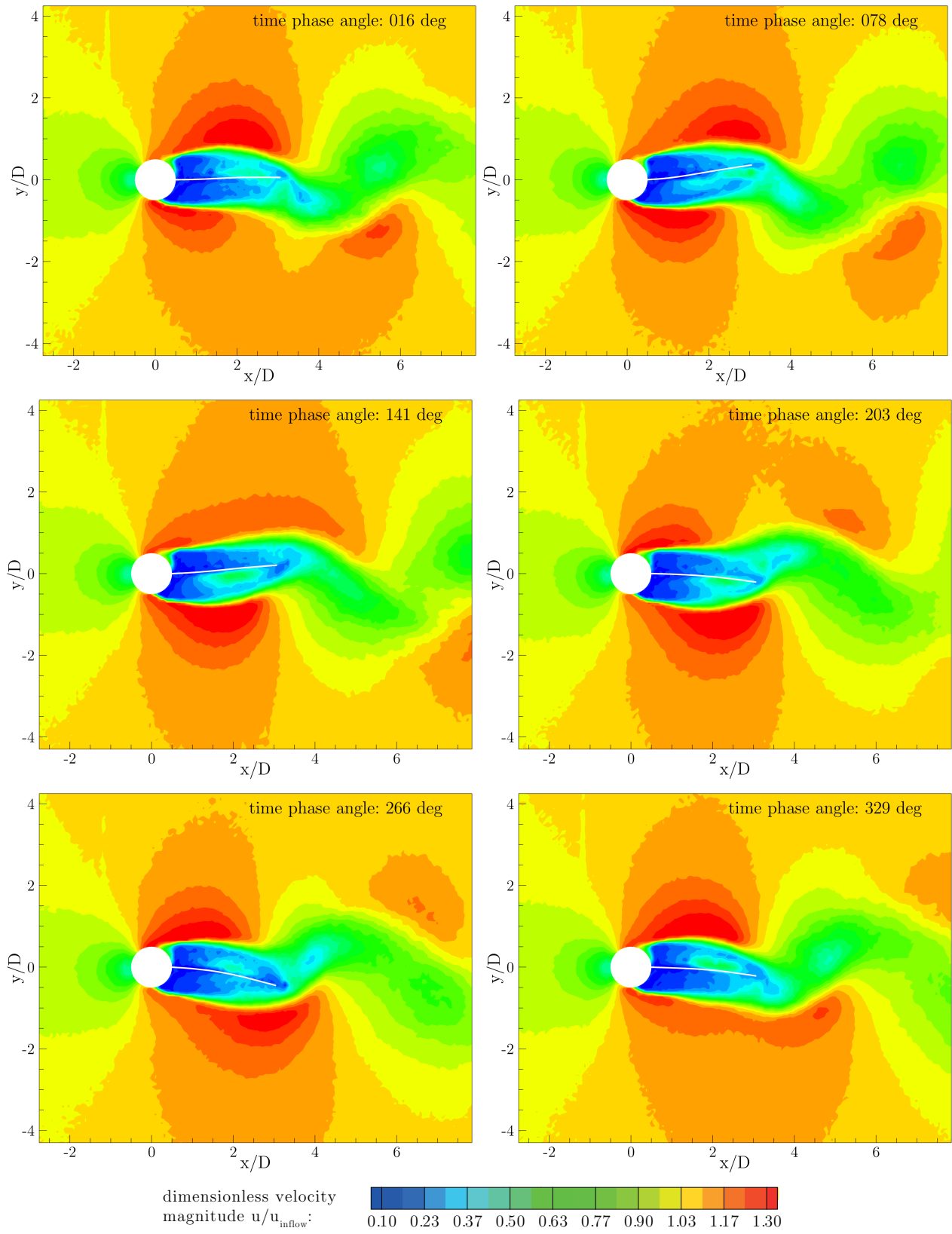


Figure 124: FSI-PfS-1b: Experimental phase-averaged flow and structural results for the reference period.

Similar to the POD analysis of FSI-PfS-1a, the first and second POD mode contain most of total turbulent kinetic energy $k_{\text{abs,all}} = 1039.72 \text{ m}^2/\text{s}^2$, $k_{\text{rel,all}} = 100\%$ (1st mode: $k_{\text{abs,1st}} = 252.13 \text{ m}^2/\text{s}^2$, $k_{\text{rel,1st}} = 24\%$, 2nd mode: $k_{\text{abs,2nd}} = 243.36 \text{ m}^2/\text{s}^2$, $k_{\text{rel,2nd}} = 23\%$) according to the unsteady effects of the flow. The energy distribution is comparable to the results of FSI-PfS-1a but more symmetrical due to the decreased cycle-to-cycle variation of the structural deflection. The first and second POD mode of the streamwise velocity component u is presented in Fig. 125a and 125b and is related to the formation of the vortices in the shear layers and their convection downstream the structure. In Fig. 125c and 125d the energy distribution of the cross-flow velocity component v is depicted. Since the first and second mode are also related to the vortex shedding, again their strong influence on the flow and energy distribution is marked by large energy-carrying regions past the flexible polyamide plate. The POD analysis of the vorticity ω_z is presented in Fig. 125e and 125f. Here, the generation and shedding of the eddies in the shear layers is obvious. Furthermore, the influence of the motion of the elastic plate is noticeable near its extremity in the range of $y/D = \pm 0.4$. This region is the only significant indication for the FSI effect in the POD analysis in comparison to the rigid configuration in Fig. 77 (except the altered vortex shedding frequency). Nevertheless, based on a quantitative comparison with the rigid configuration an increase of 26% of the total turbulent kinetic energy is observed for the free configuration. That can be assigned to the influence of the coupling effect between the flow and the structure. Again, it can be assumed that the FSI effect on the flow responds to several higher POD modes of minor energetic impact. That means that e.g., the flow motions due to the structural deformations are energetically not so relevant to appear in the first two modes.

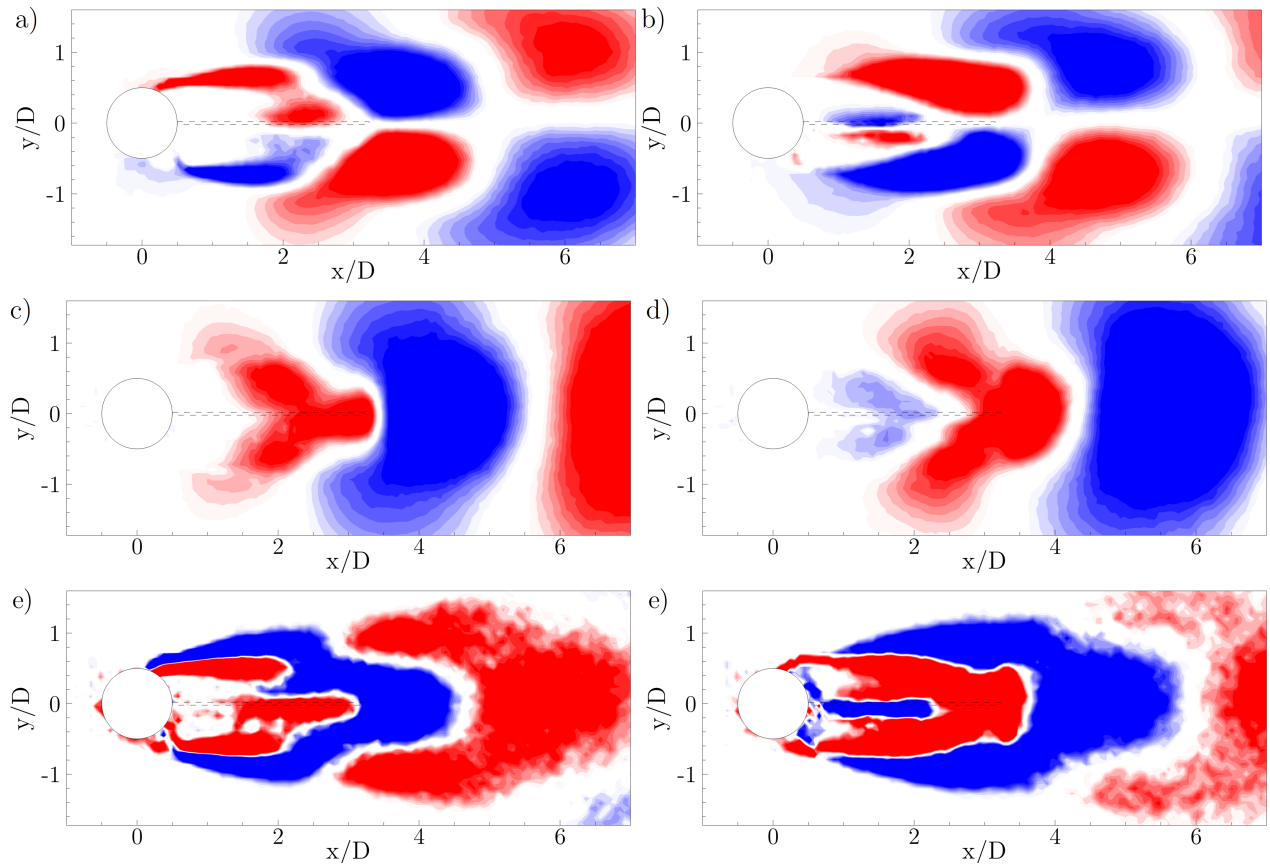


Figure 125: FSI-PfS-1b: POD analysis of the two-dimensional flow fields in the midplane ($z/D = 0$) of FSI-PfS-1b a) velocity component u , first mode; b) velocity component u , second mode; c) velocity component v , first mode; d) velocity component v , second mode; e) vorticity component ω_z , first mode; f) vorticity component ω_z , second mode.

FSI-PfS-1c - Structural results

For the configuration of FSI-PfS-1c a soft para-rubber plate is attached to the cylinder. While in FSI-PfS-1a and FSI-PfS-1b only the first bending mode is obtained, FSI-PfS-1c reaches the second bending mode. This proves the strong influence of the material properties on the physical coupling between the flow and the structure. In the following paragraphs the structural and flow results of this test case are presented.

Figures 126 and 127 refer to the structural response during a continuous increase of the inflow velocity up to $u_{\text{inflow}} = 2.0$ m/s. In Fig. 126 the maxima and minima of the averaged structural deformations are displayed. Figure 127 presents the corresponding swiveling frequencies of the flexible plate. In contrast to FSI-PfS-1a and 1b the increased structural deformation due to the second swiveling mode is visible in the high-speed camera snap-shots (Fig. 128).

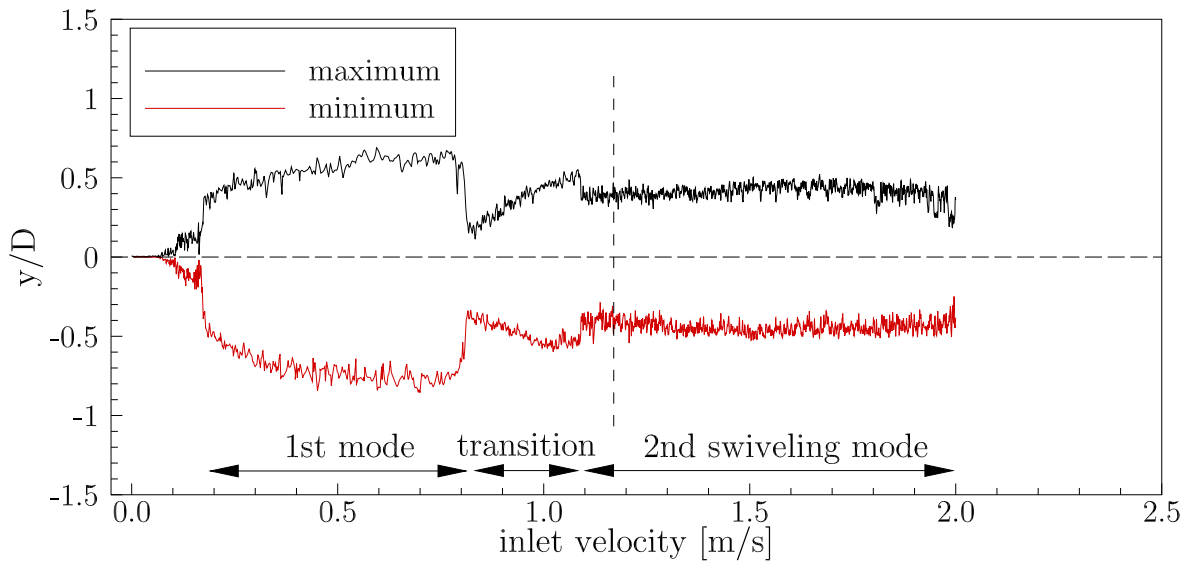


Figure 126: FSI-PfS-1c: Averaged maximal/minimal structural deflections as a function of the inflow velocity.

Due to the soft para-rubber material applied in this test case, the first effects of the FSI-coupling are noticed at the small inflow velocity of about $u_{\text{inflow}} = 0.1$ m/s with tiny and aperiodic deformations until the velocity reaches a velocity of 0.17 m/s. By reaching this critical inflow velocity the amplitudes of the structural displacements increase. At this stage the structure deforms in the first bending mode until the inflow velocity $u_{\text{inflow}} = 0.8$ m/s is reached. However, this first mode is characterized by large deformations but non-periodic and asymmetric oscillations. With peak-to-peak amplitudes of the order of $1.3 \cdot D$ this FSI excitation produces the largest deflections found for this test case in the applied velocity range. It is assumed that the FSI coupling present in this velocity interval is not stable enough to produce a quasi-periodic swiveling state. An abrupt change in the amplitudes of the deflections at $u_{\text{inflow}} = 0.8$ m/s marks the transition to the second swiveling mode. Here, the tail displacements decline to about $y/D = \pm 0.25$ and immediately start to increase again linearly with the inflow velocity. At the inflow velocity of $u_{\text{inflow}} = 1.1$ m/s the deflection becomes almost constant but no further mode transition is noticed. The second bending mode remains

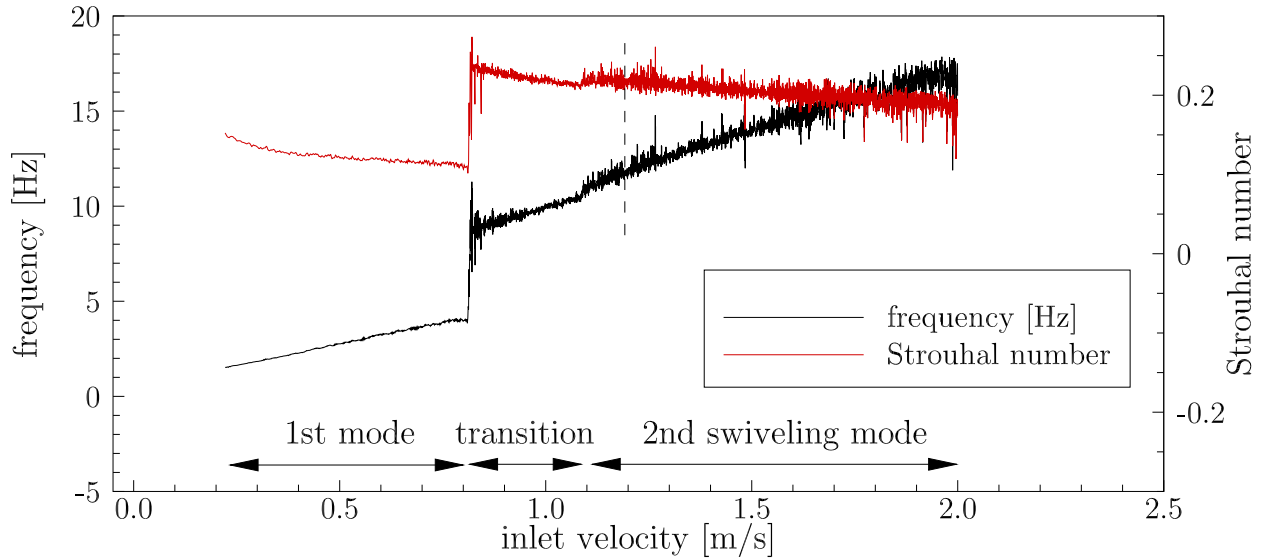


Figure 127: FSI-PfS-1c: Averaged frequency and Strouhal number as a function of the inflow velocity.

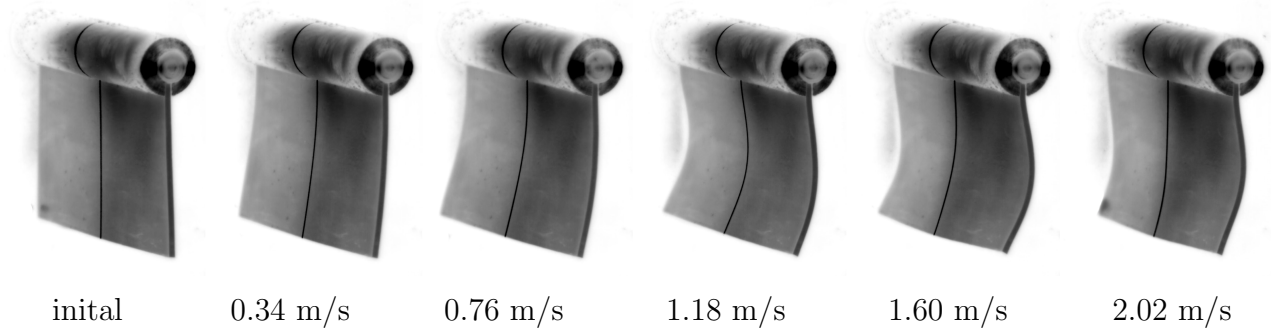


Figure 128: FSI-PfS-1c: Characteristic moments of the structural deformation at several inflow velocities for FSI-PfS-1c.

present until the end of the velocity slope investigated. Nevertheless, the increasing turbulent fluctuations in the wake of the front cylinder and the soft para-rubber material lead to large variations in the structural deformation and the swiveling frequency for inflow velocities beyond 1.4 m/s. Furthermore, stronger three-dimensional and aperiodic motions are obtained for these higher inflow velocities.

The swiveling frequency f and the Strouhal number St possess a corresponding dependence on the inflow velocity. After a small non-periodic settling phase a cyclic movement starts at an inflow velocity of about $u_{\text{inflow}} = 0.17$ m/s with a swiveling frequency of $f = 1.28$ Hz ($St = 0.163$). A further increase of the inflow velocity results in a linear rise of the swiveling frequency with a gradient of $(\delta f / \delta u_{\text{inflow}})_{1st} = 4.24$ Hz/(m s⁻¹). At the transition from the first to the second oscillation mode at the inflow velocity of 0.8 m/s the para-rubber plate swivels with a frequency of $f = 3.95$ Hz. In the same interval the Strouhal number decreases to $St = 0.107$. Due to the mode transition, a sudden doubling of the swiveling frequency from $f = 3.95$ Hz ($St = 0.107$) to $f = 8.71$ Hz ($St = 0.238$) appears. Obviously, the first ($f_{1c,1} =$

5.43 Hz) and second eigenfrequencies ($f_{1c,2} = 7.41$ Hz) of this structure (refer to Section 8.3) lie within this interval. It can be assumed that this change in the deflection behavior is a direct response of the structure according to its characteristic eigenvalues and the external flow excitation. In accordance to this phenomenon, the transition phase is characterized by large fluctuations in the deflections and the swiveling frequencies. With increasing inflow velocities the second bending mode prevails the first mode and becomes dominant. Remarkable are the low frequency fluctuations in the small interval of increasing displacements between $u_{\text{inflow}} = 0.9$ m/s and $u_{\text{inflow}} = 1.1$ m/s. Furthermore, the apparent change from a linear increase of the amplitude to constant displacements around $u_{\text{inflow}} = 1.1$ m/s comes along with stronger variations in the oscillation frequency. Reasons of this change may be found in the flow excitation, where on the one hand the maximum deflections are limited to the elongation of the wake area (due to the bulk flow) and on the other hand stronger fluctuations of the fluid forces on the structure surface appear. These considerations lead to the assumption that a lock-in of the FSI coupling is present in this swiveling state. Despite these observations the corresponding average frequencies along the velocity slope are rising in an almost linear manner with a gradient $(\delta f / \delta u_{\text{inflow}})_{\text{transition}} = 6.68$ Hz/(m s⁻¹) in the transition phase and after this settlement phase slightly change with a gradient $(\delta f / \delta u_{\text{inflow}})_{2\text{nd}} = 7.71$ Hz/(m s⁻¹).

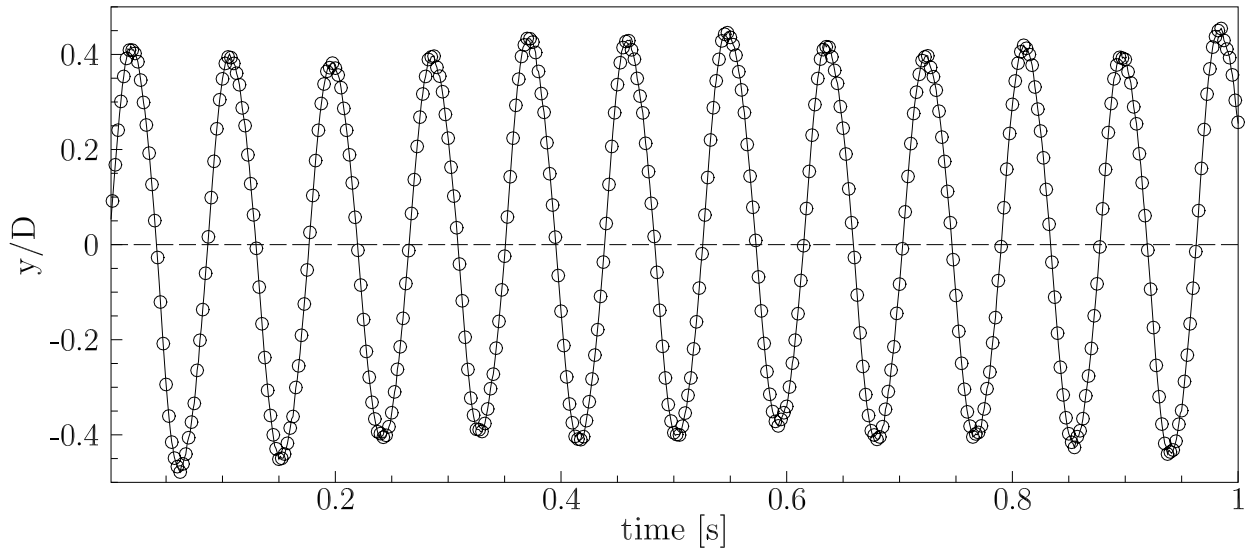


Figure 129: FSI-PfS-1c: Experimental structural results: Time history of the structural deflections (extract) for the measurement point at $x/D = 3.13$ at $z/D = 0$.

Based on these investigations the final test case velocity $u_{\text{inflow}} = 1.179$ m/s is chosen. Unfortunately, not the same inflow velocity as applied in FSI-PfS-1a and 1b could be used for this test case due to the high cycle-to-cycle variations and the increased three-dimensional deformations at the inflow velocity $u_{\text{inflow}} = 1.385$ m/s. However, the present inflow velocity is chosen in the constant deflection phase beginning at $u_{\text{inflow}} = 1.1$ m/s. Once again the time history of the structural deflection is shown in Fig. 129 for a point near the extremity of the para-rubber plate at $x/D = 3.13$ and $z/D = 0$. This time-dependent signal is quasi-periodic but exhibits large amplitude variations over several structural cycles. With an average maximum peak $(y/D)_{\text{max}} = 0.398$ and an average minimum peak $(y/D)_{\text{min}} = -0.410$ the mean

extrema are slightly asymmetric. A reason is found in the clamping of the rubber material at the front cylinder. In contrast to FSI-PfS-1a and 1b a pre-stressing effect as a cause for the asymmetry can be suspended due to the soft para-material. The standard deviation of all positive and negative peaks is calculated to $\sigma_{\max} = 0.023$ (5.78%) and $\sigma_{\min} = 0.025$ (6.10%) over all 2186 periods recorded. The mean swiveling frequency at this inflow velocity is found to be $f_{\text{avg}} = 11.39$ Hz ($\text{St} = 0.213$) and its standard deviation $\sigma_f = 0.22$ Hz (1.93%). At the lateral sides of the para-rubber plate the mean structural deflections are found to be rather small with values of about $(y/D)_{\max} = 0.392$ and $(y/D)_{\min} = -0.406$ at $z/D = -2.72$ and $(y/D)_{\max} = 0.394$ and $(y/D)_{\min} = -0.399$ at $z/D = 2.72$ for the phase-averaged period. With a phase difference smaller than 0.5 deg the deflection of the entire plate is almost in-phase.

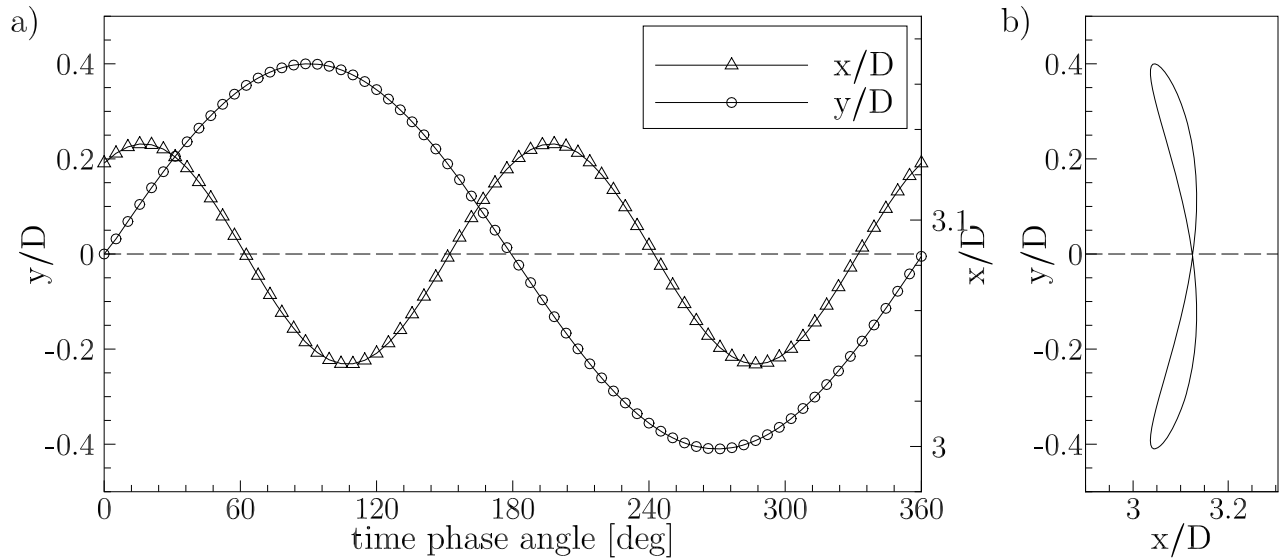


Figure 130: FSI-PfS-1c: Experimental structural results: a) phase-averaged reference period and b) phase-averaged phase-plane, both for the structural deflections at the measurement point $x/D = 3.13$ in the midplane of the channel at $z/D = 0$.

The phase-averaged structural results are presented in Figs. 130 and 131. The nearly sinusoidal oscillation consists of 70 phase-averaged data points calculated out of the 2186 periods recorded. Covering the whole structure in the mean time-phase interval, Figure 131 illustrates the moderate deflections of the rubber plate in the second swiveling mode. The second wave node at $x/D = 2.20$ is visible. The second bending mode together with the soft para-rubber material limits the deformation of the structure in the y -direction. Large deflections are found in the middle and rear part of the para-rubber plate. The xy -trajectory given by the motion of the point near the extremity of the flexible plate forms a curved and flat "8" which is a characteristic feature of the second bending mode, in general.

FSI-PfS-1c - Flow results

The mean flow field (see Fig. 132) obtained by time-averaging over all PIV measurements is almost symmetric. Again several flow phenomena (i.e., the acceleration areas on the upper and lower side of the cylinder, the stagnation point in front of the cylinder, the wake area past the cylinder, the shear layers on both sides of the structure and the expansion of the

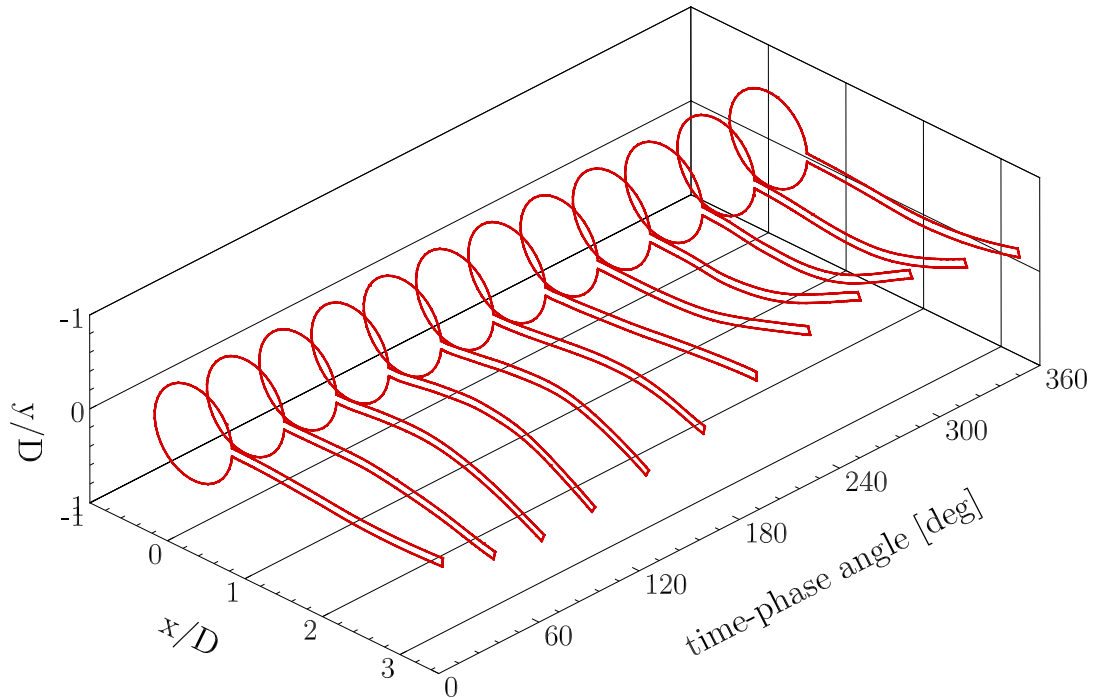


Figure 131: FSI-PfS-1c: Structural results: Structure contour for the reference period.

wake due to the additional momentum in y -direction caused by the motion of the structure) are again present in the mean field. Remarkable is the large expansion of the wake past the flexible structure which is more developed than in FSI-PfS-1a and 1b. The faster motion of the rear end of the structure in the second swiveling mode together with its increased swiveling frequency is responsible for this expansion.

The combined phase-averaged flow and structural results are shown in Fig. 133 for six time phase angles (16, 78, 141, 204, 266 and 326 deg) out of the 23 time-phase angles generated by the phase-averaging method. Similar observations as found in the flow fields of FSI-PfS-1a and 1b can be made for the single flow fields. Such flow phenomena are e.g., the vortex cores shedding alternatively from the upper and lower side of the cylinder and their convection downstream forming the characteristic vortex street, the stagnation point in front of the cylinder and the wake region past the cylinder.

Based on the time series of the six time-phase angles the mean quasi-periodic FSI problem of this test case is illustrated. In the first picture at a phase angle of 16 deg the middle and rear part of the para-rubber plate is slightly bended in positive y -direction. At this time-phase angle a single vortex just detaches on the upper side while on the opposite side the acceleration area reaches its minimum expansion. In contrast to FSI-PfS-1a and 1b in the present test case two vortex cores are visible in the flow field according to the increased shedding frequency. The vortex cores are located at about $x/D = 5.25$, $y/D = -1$ and $x/D = 7.10$, $y/D = 1$.

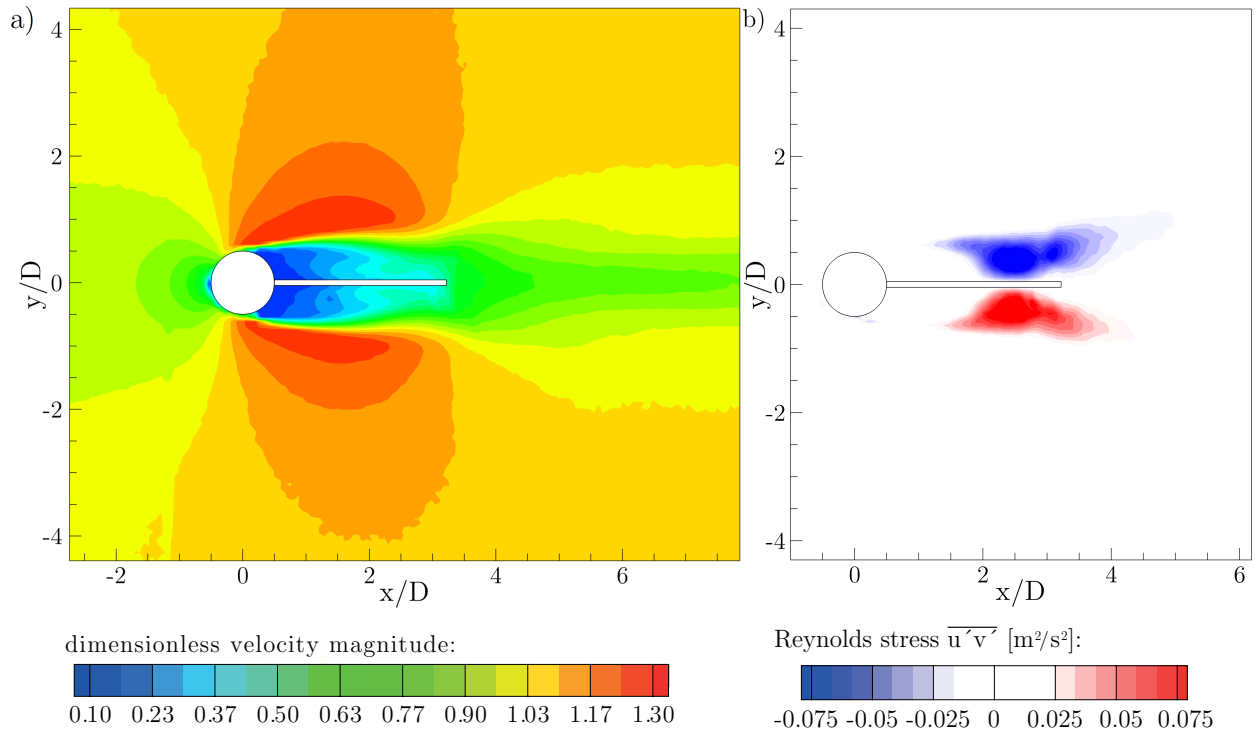


Figure 132: FSI-PfS-1c: Time-averaged PIV results of FSI-PfS-1c at $z/D = 0$ for a) dimensionless velocity magnitude and b) Reynolds shear stress $\overline{u'v'}$.

At the next phase angle of 78 deg the middle part of the para-rubber plate deforms nonlinearly in negative y -direction as a result of the larger pressure forces in this section on the upper side of the rubber plate compared to its lower side. As a consequence the rear end of the plate deflects in positive y -direction due to the contraction in x -direction of the middle part of the plate. Simultaneously, the acceleration area on the lower side of the plate increases while all flow structures in the wake are continuously convected downstream. Between the time-phase angles of 78 and 141 deg the extremity of the structure reaches its maximum deformation $(y/D)_{\max} = 0.398$ of the whole mean period while the middle part reaches its minimum deflection simultaneously. After these extrema the rear-end of the plate moves back in negative y -direction while the middle part moves in the opposite direction at the phase angle of 141 deg. During the following motion the rear end of the structure passes the neutral axis at the phase angle of approximately 180 deg. In the next figure at a phase angle of 204 deg the flow including the pressure force and the resulting structural deformations are reversed with respect to the first half of the period. A secondary trailing-edge vortex is generated while the structure moves through the wake area. Similar to the results of FSI-PfS-1a and 1b this secondary vortex is hardly visible in the flow fields according to the coarse PIV resolution and the blurring of the phase-averaging method (see explanation in the results of FSI-PfS-1a).

The POD analysis of FSI-PfS-1c yields the energy content of the first and second POD mode to be $k_{\text{abs},1\text{st}} = 164.32 \text{ m}^2/\text{s}^2$ and $k_{\text{rel},1\text{st}} = 27\%$ of the total turbulent kinetic energy for the first POD mode and $k_{\text{abs},2\text{nd}} = 160.97 \text{ m}^2/\text{s}^2$ and $k_{\text{rel},2\text{nd}} = 27\%$ of the total turbulent kinetic energy for the second POD mode. That means, that about 54% of the total turbulent kinetic energy

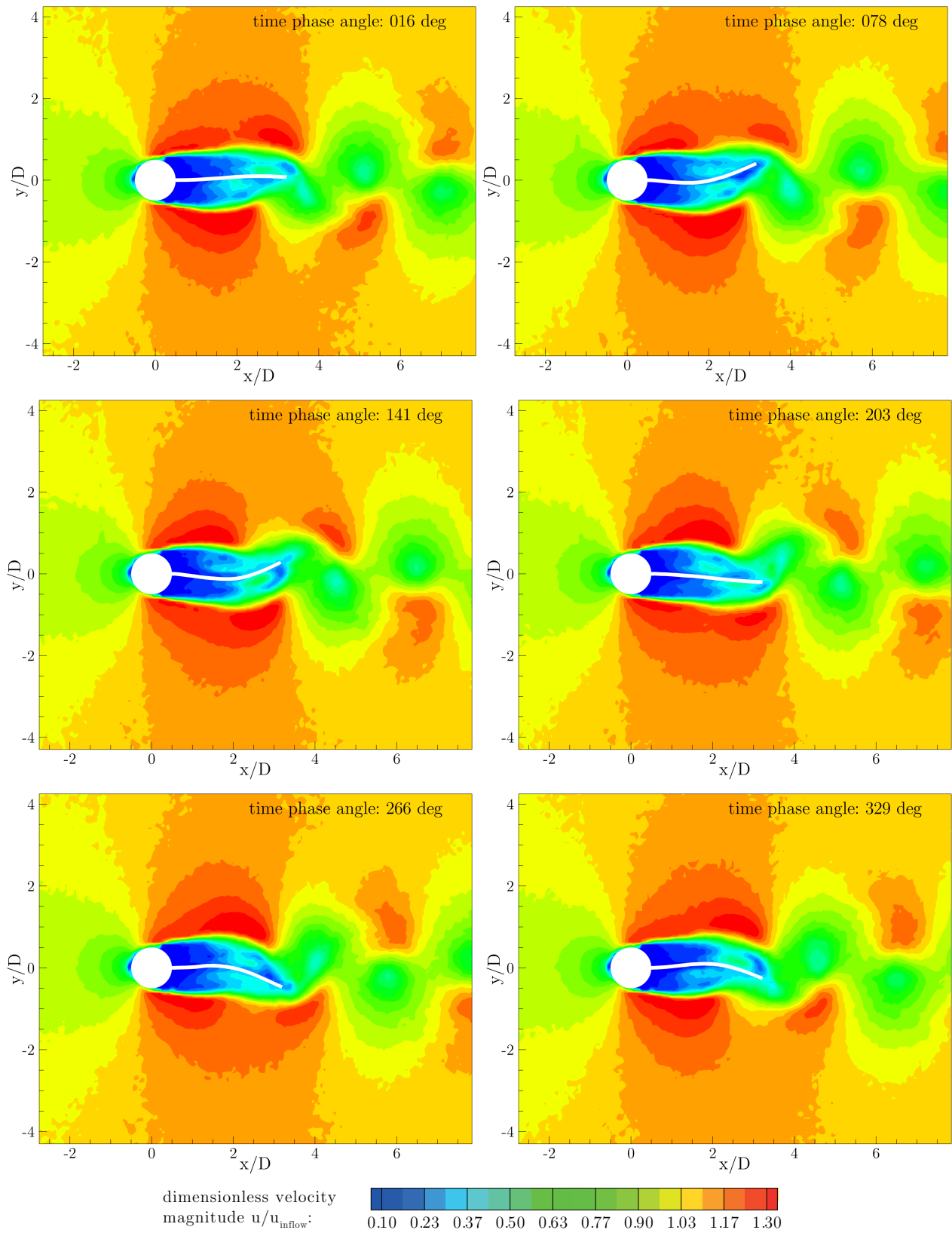


Figure 133: FSI-PfS-1c: Experimental phase-averaged flow and structural results for the reference period.

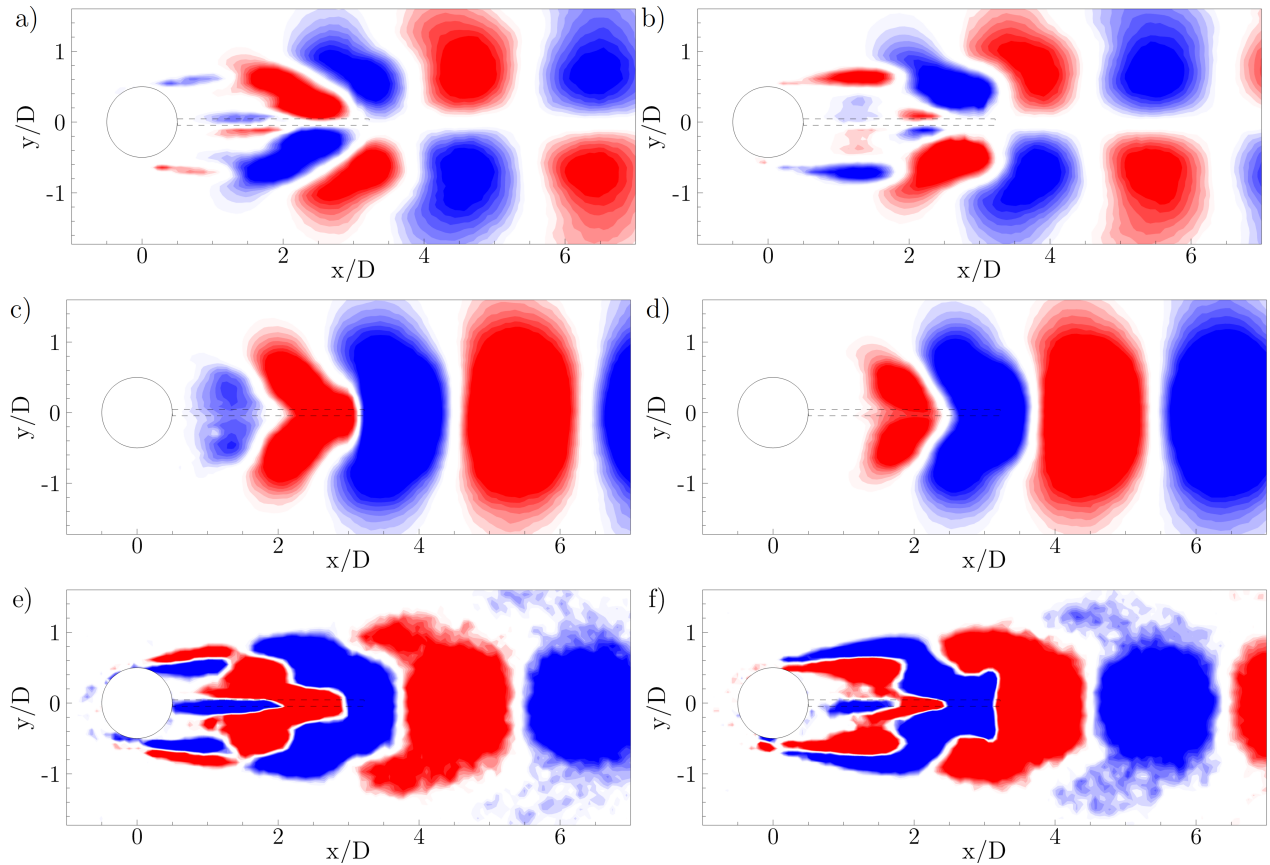


Figure 134: FSI-PfS-1c: POD analysis of the two-dimensional flow fields in the midplane ($z/D = 0$) of FSI-PfS-1c a) velocity component u , first mode; b) velocity component u , second mode; c) velocity component v , first mode; d) velocity component v , second mode; e) vorticity component ω_z , first mode; f) vorticity component ω_z , second mode.

$k_{\text{abs,all}} = 588.45 \text{ m}^2/\text{s}^2$ ($k_{\text{rel,all}} = 100\%$) is stored in these two modes¹³. It can be assumed that the strong system coupling with its high swiveling frequency and its low variations in terms of the deflections are responsible for this high energy content in these first two modes. The energy distribution of the first and second POD mode is presented in Fig. 134. In contrast to the energy distributions of FSI-PfS-1a and 1b more energy is related to the motion of the structure. While in FSI-PfS-1a and 1b most of the energy is stored in the shear layers, now the energy is stronger distributed in the direct vicinity of the moving plate. Obviously this is a consequence of the second swiveling mode of the structure which is characterized by large deformations in its middle and trailing-edge section and the doubling of the vortex shedding frequency. The energy distribution due to the alternating vortex shedding at the bluff body appears similar to the POD analysis of the rigid configuration but differs in the amount of vortices visible in the measurement section, especially in comparison with FSI-PfS-1a and 1b. That is the result of the increased swiveling frequency of FSI-PfS-1c compared to the other cases. Especially in Fig. 134f the limits of the structural deflections of the rear end are clearly visible at $x/D \approx 3$ and $y/D \approx \pm 0.4$.

¹³The energy values are lower than in the rigid configuration and in FSI-PfS-1a and 1b due to the decreased inflow velocity of the present test case.

FSI-PfS-1*x* - Conclusions

The first set of FSI test cases (FSI-PfS-1*x*) is focused on simple nominally two-dimensional geometries. Applying three different test case configurations, the influence of the material on the structural response at almost equal inflow conditions is examined. The detailed measurements concerning the chosen inflow velocities of the benchmark cases yield quasi-periodic and almost symmetric structural deflections. Due to the turbulent flow, the resulting fluctuating excitation forces and the missing steel weight at the tailing-edge of the structure, the maximum and minimum peaks of the structural deflections and the swiveling frequency are not as constant as in the benchmark cases presented by Gomes and Lienhart (2013). Despite these issues an almost two-dimensional structural deformation is achieved at the mentioned inflow conditions for the three test cases involving different materials. A summary of the integral measurement results is listed in Table 18.

Test case	FSI-PfS-1 <i>a</i>	FSI-PfS-1 <i>b</i>	FSI-PfS-1 <i>c</i>
behavior	quasi-2D	quasi-2D	quasi-2D
bending modes	1st mode	1st mode	1st mode, 2nd mode
bending shapes	flat ')',	flat ')',	flat ')', flat '8'
bending stiffness K_B	0.02986	0.05985	0.00722
u_{inflow} [m/s]	1.385 m/s	1.385 m/s	1.179 m/s
symmetry	✓	✓	✓
f [Hz]	7.11	8.02	11.39
$\sigma(f)$	$\pm 3.09\%$	$\pm 2.24\%$	$\pm 1.93\%$
St	0.113	0.127	0.213
$(y/D)_{\text{max}}$ ($x/D = 3.13$)	0.439	0.380	0.398
$(y/D)_{\text{max}}$ ($x/D = 2.82$)	0.420	–	–
$(y/D)_{\text{min}}$ ($x/D = 3.13$)	–0.440	–0.393	–0.410
$(y/D)_{\text{min}}$ ($x/D = 2.82$)	–0.418	–	–
$\sigma(y/D)_{\text{max}}$	$\pm 12.59\%$	$\pm 6.05\%$	$\pm 5.78\%$
$\sigma(y/D)_{\text{min}}$	$\pm 11.34\%$	$\pm 4.83\%$	$\pm 6.10\%$
POD energy content	963.91 m ² /s ²	1039.72 m ² /s ²	673.72 m ² /s ²

Table 18: Summary of FSI-PfS-1*x*.

In general, the structural properties, especially the YOUNG's modulus, have the largest effect on the structural deflections. The observations reveal that stiffer materials present in FSI-PfS-1*a* (EPDM) and 1*b* (polyamide) principally swivel in the first bending mode as long as the first eigenfrequency of the structure is not reached by the vortex shedding frequency. The first bending mode is characterized by one single wave node at the fixation on the cylinder and moderate non-linear deflections covering mainly the rear end of the plate. Thereby, the deflections are limited to about the size of the front cylinder.

The softer para-rubber (FSI-PfS-1*c*) allows to study the second swiveling mode which becomes dominant after a short transition phase. The transition from the first to the second mode takes place before the vortex shedding frequency reaches the first eigenfrequency. In the case of FSI-PfS-1*c* the transition causes a doubling of the vortex shedding frequency of the fluid and the

corresponding swiveling frequency of the structure. The resulting frequency after the settling phase also exceeds the second eigenfrequency. An additional wave node at about two-thirds of the plate length characterizes the second swiveling mode. In this mode the first two-thirds of the plate move in the opposite direction as its last third. Similar to the first mode, here again the maximum displacements are obtained at the end of the structure and its range is also in the order of the cylinder diameter.

The observations of the elastic behavior of the flexible structures are approved by the stiffness factor K_B given by:

$$K_B = \frac{E h^3}{12 \rho_f u_\infty^2 L^3}. \quad (149)$$

The stiffness factor defines the relation of the structural resistance to the applied fluid flow. It represents a dimensionless characteristic number that applies the material properties (YOUNG's modulus E), the geometry of the elastic structure (thickness h , length L) and the inflow velocity u_∞ of the fluid with the density ρ_f to provide an indication about the structural deformation behavior in the present flow (Lee and You, 2013). In general, small values for K_B represent more elastic structures. Obviously, the soft para-rubber plate applied in FSI-PfS-1c leads to the smallest value of $K_B = 0.00722$ in comparison to the EPDM rubber plate in FSI-PfS-1a with $K_B = 0.02986$ and the stiff polyamide plate with $K_B = 0.05985$ (FSI-PfS-1b). Regarding the mean deflections of each structure and their corresponding stiffness factors, lower deflection values could be expected. Especially the difference of almost one order of magnitude between the stiffness factors of FSI-PfS-1b and 1c a larger distinction in their deformations could be hypothesized. Since the specific load and excitation (here, the vortex shedding) is not included in this dimensionless number, it can only give a loose indication of the deformation behavior in the present fluid-structure interaction test cases.

Referring to the FSI excitation sources described in Section 3 it is assumed that the instability-induced excitation (IIE) is responsible for the physical coupling of FSI-PfS-1a and 1b. The small structural deformations in the first oscillation mode only slightly change the flow field. Therefore, a movement-induced excitation (MIE) is rather improbable. This assumption is also supported by the modal analysis which revealed eigenfrequencies larger than the obtained swiveling frequencies in the FSI experiments. It can be assumed that both configurations are closely related to the behavior of an elastic splitter plate and hinder or reduce the vortex shedding according to their stiff material response. In contrast, in FSI-PfS-1c the oscillation frequency reaches the first eigenfrequency and deflects in the second bending mode. Here, a strongly coupled system is present which is especially characterized by the increased swiveling frequency and the more complex structural deformations. All together, it can be concluded that the movement-induced excitation (MIE) is present for this test case.

The POD analysis supports this assumption by the strongly modified energy distribution in the vicinity of the structure (especially for the vorticity-based POD analysis). In FSI-PfS-1c the faster and more complex motion of the flexible structure results in an increase of the total kinetic energy. The energy distribution for each POD mode and test case is illustrated in Fig. 135a for the absolute energy content and in Fig. 135b for the relative energy in relation to the entire energy found over all POD modes. FSI-PfS-1b contains the largest value of the absolute energy. This could be the result of the low variations in the structural deflection and

the resulting correlated flow structures. Here, the lower variations may result in a more stable FSI-coupling state and abet the higher oscillation frequency (combined with more unsteady flow phenomena and a corresponding higher turbulent kinetic energy) in comparison to FSI-PfS-1a. In comparison, the energy content of FSI-PfS-1c is rather low. Here, the lower inflow velocity and the decreased kinetic energy stored in the flow is responsible for this value. In general, the turbulent kinetic energy is directly related to the magnitude of the flow fluctuations. Since a lower inflow velocity induces less flow fluctuations, the total amount of kinetic energy is decreased.

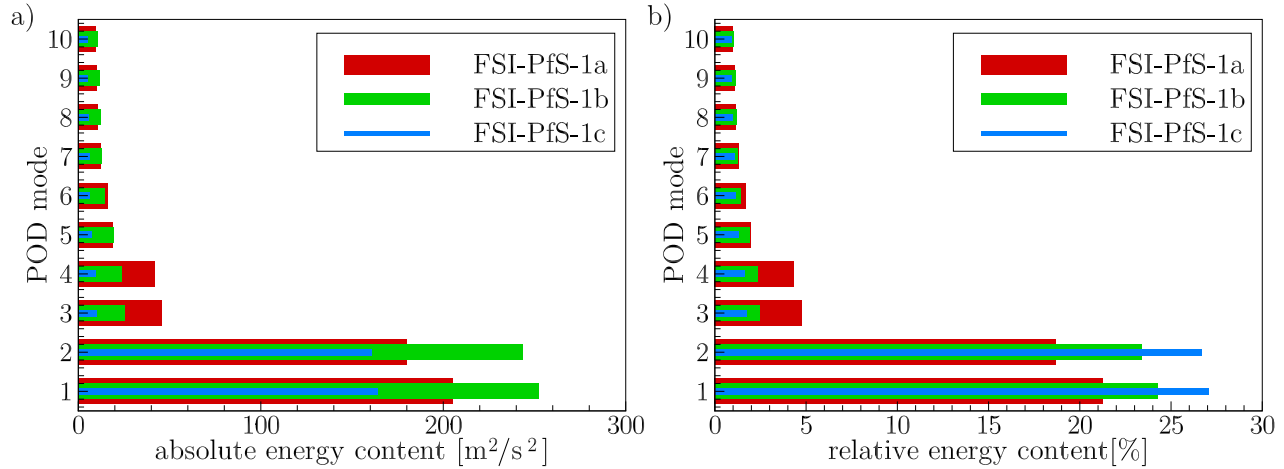


Figure 135: FSI-PfS-1x: POD results.

In relative values, FSI-PfS-1c stores about 54% of the entire unsteady flow energy in the first two POD modes while this value is 47% for FSI-PfS-1b and 40% for FSI-PfS-1a. As already mentioned, the swiveling modes and the cycle-to-cycle variations in the structural deflection are assumed to be responsible for these differences. All cases have the high concentration of energy in the first two POD modes in common (see Fig. 135). Since both modes refer to the vortex shedding, this effect is determined as the major energy-carrying flow phenomenon in these test cases.

10.1.2. FSI-PfS-2x (Two-dimensional geometry with rear mass)

The test cases FSI-PfS-1x employ a fixed cylinder and an elastic plate without a rear mass. These cases show structural deformations smaller than the cylinder diameter. In the following paragraphs the experimental results of the two test cases FSI-PfS-2a and 2b are presented. In both cases a steel weight with dimensions of $10 \times 177 \times 2$ mm is attached to the slightly shorter para-rubber plate which now measures only $50 \times 177 \times 2$ mm to maintain the overall plate length of 60 mm. For the first test case FSI-PfS-2a the front cylinder is fixed at the channel walls similar to the configuration of FSI-PfS-1x. In the second set-up FSI-PfS-2b the rotational degree of freedom around the z -direction is released. The additional DOF allows the front cylinder a rotational motion and refers to the benchmarks of Gomes and Lienhart (2013). Parts of the following measurement descriptions are already published in Kalmbach and Breuer (2012, 2013a,b).

FSI-PfS-2a - Structural results

Similar to the previous measurement descriptions first the structural response as a function of the inflow velocity is presented. Figure 136 shows the averaged displacements over 10 measurement series at a point ($x/D = 3.13$) near the extremity of the structure as a function of the increasing inflow velocity u_{inflow} .

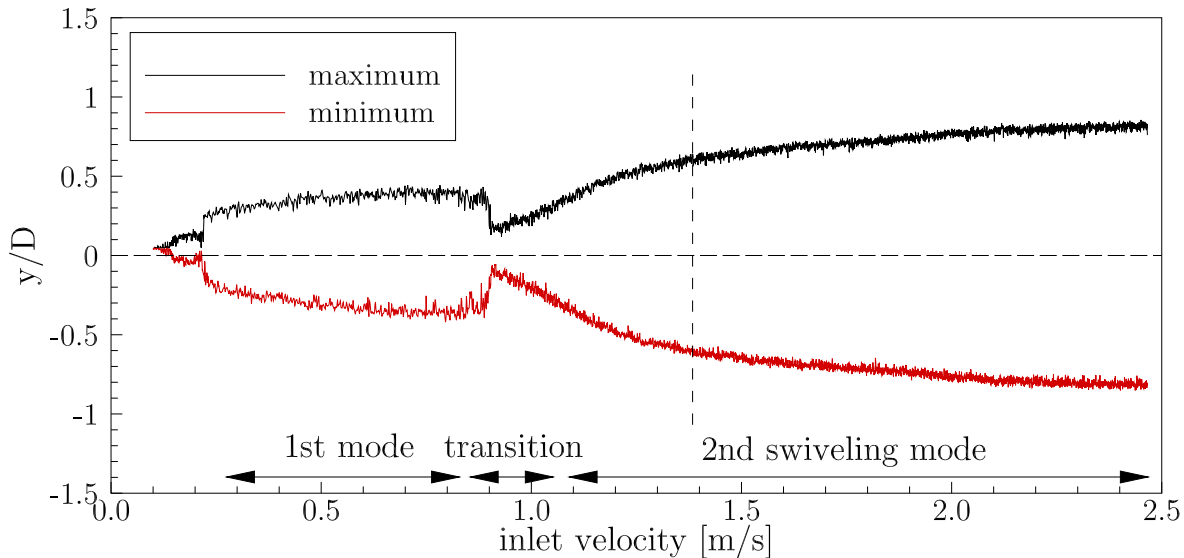


Figure 136: FSI-PfS-2a: Averaged maximal/minimal structural deflections as a function of the inflow velocity.

In this test case the motion of the elastic structure starts at about $u_{\text{inflow}} = 0.11$ m/s with small and non-periodic deformations. At $u_{\text{inflow}} = 0.22$ m/s the first swiveling mode is settled. Within the velocity interval of $u_{\text{inflow}} = 0.22$ m/s to 0.90 m/s the peak amplitudes rise from $y/D = \pm 0.25$ to ± 0.44 . The start of the mode transition is located at about $u_{\text{inflow}} = 0.90$ m/s. Similar to the transition phase in FSI-PfS-1c the peak amplitudes rapidly decrease and then linearly rise again with the increasing inflow velocity finally switching into the second swiveling mode.

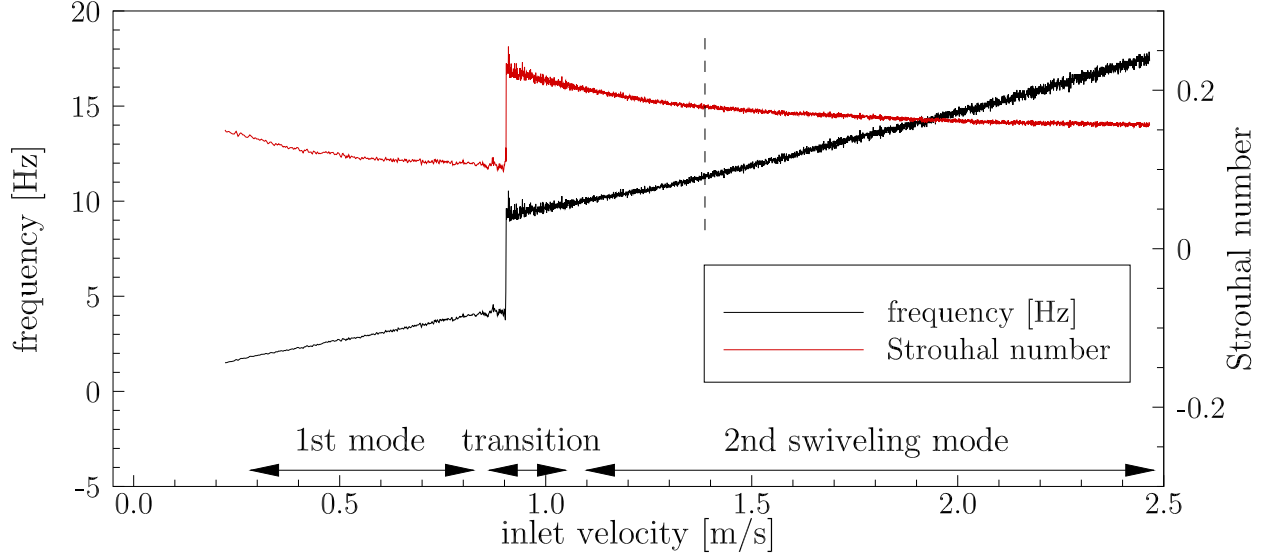


Figure 137: FSI-PfS-2a: Averaged frequency and Strouhal number as a function of the inflow velocity.

Within the subsequent velocity range the gradient of the peak amplitudes flattens more and more but the second mode is retained and the total deformations become larger than the size of the cylinder diameter. Despite the high inflow velocity $u_{\text{inflow}} = 2.45$ m/s at the end of this measurement series the structural deformations remain symmetric, quasi-periodic and only mildly fluctuating. The amplitudes of the structural deflections increase to the maximum deflection of $y/D_{\text{max},2\text{nd mode}} = -0.84$ to 0.85 in the second mode at $u_{\text{inflow}} = 2.45$ m/s. Furthermore, the second swiveling mode is found to be dominant for this test case in a large range of inflow velocities (Fig. 136). On the contrary to the first swiveling mode one wave node is located at the clamping of the flexible structure. The second wave node is found close to the bond of the para-rubber and the steel weight at $x/D = 2.6$. In Fig. 138 characteristic moments of the structure deformation at several inflow velocities are presented. The first picture relates to the initial position of the structure in the fluid at rest. The second figure shows the first bending mode of the structure at the inflow velocity $u_{\text{inflow}} = 0.55$ m/s. Here, only the rear-end of the structure undergoes large deformations. The following pictures correspond to the second swiveling mode characterized by large deformations in the middle part and rear-end of the structure. Similar to the quantitative measurement results (Fig. 136) also the qualitative high-speed camera snapshots reveal the increase of deformations with the inflow velocity.

The transition from the first to the second swiveling mode occurs at inflow velocities around $u_{\text{inflow, transition}} = 0.9$ m/s and comes along with a jump of the frequency as visible in Fig. 137. In the first mode the frequency increases nearly linearly to $f_{\text{max},1\text{st mode}} = 4.32$ Hz and the dimensionless frequency decreases to $\text{St}_{\text{min},1\text{st mode}} = 0.11$, respectively. With the transition to the second mode an abrupt increase of the frequency appears. With a minimum frequency of $f_{\text{min},2\text{nd mode}} = 9.33$ Hz in the second mode the frequency is more than doubled in comparison to the first swiveling mode. The Strouhal number shows the same abrupt change with an increase

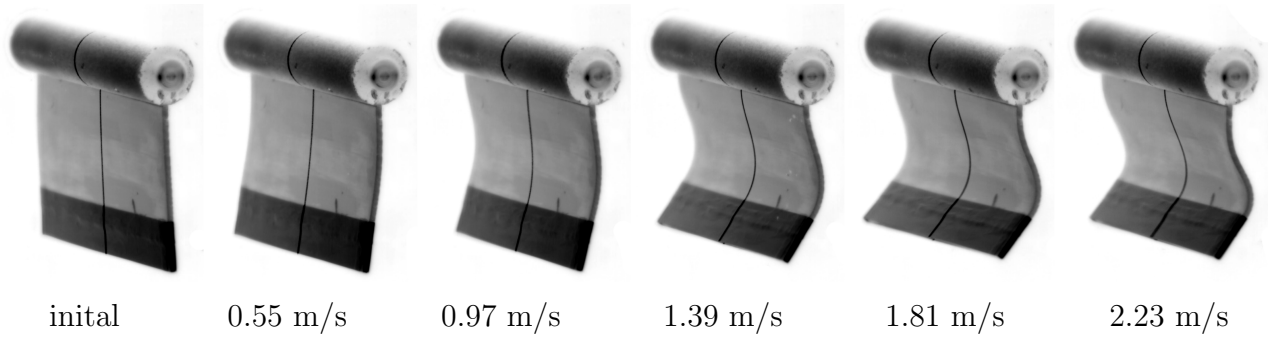


Figure 138: Characteristic moments of the structure deformation at several inflow velocities for FSI-PfS-2a.

to a maximum of $St_{\max, 2\text{nd mode}} = 0.23$ at the transition. With increasing inflow velocities St decreases again to $St_{\min, 2\text{nd mode}} = 0.16$. Furthermore, the fluctuations of the amplitudes and frequencies are significantly higher in the transition regime as for instance at the reference velocity $u_{\text{inflow}} = 1.385$ m/s. Moreover, with increasing velocities beyond $u_{\text{inflow}} = 1.385$ m/s the fluctuations rise again.

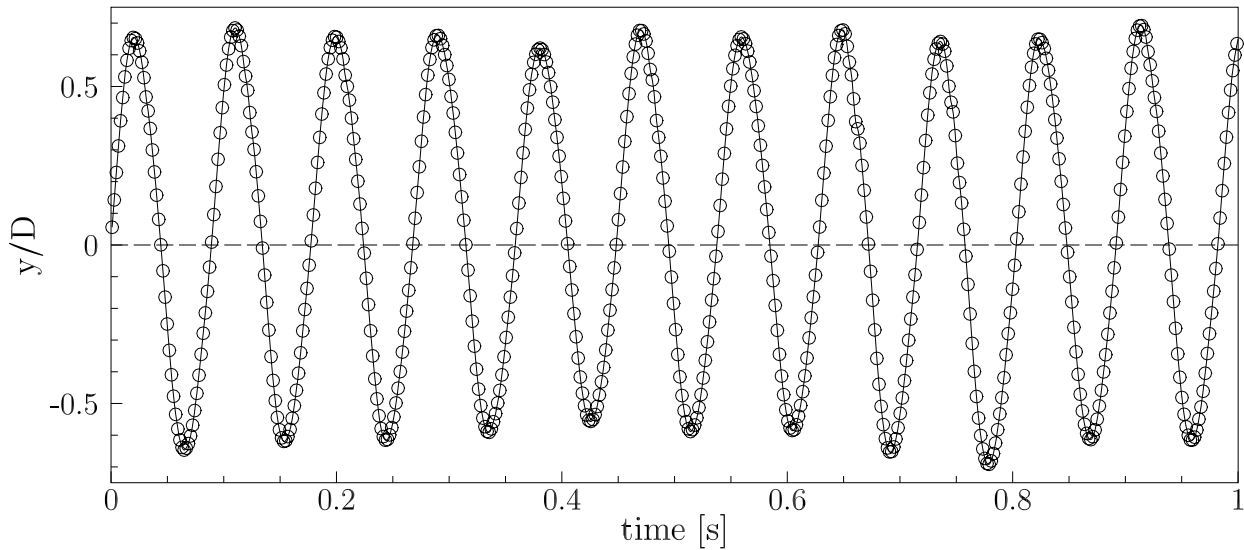


Figure 139: FSI-PfS-2a: Experimental structural results: Time history of the structural deflections (extract) for measurement point at $x/D = 3.13$ at $z/D = 0$.

Thus, the final test case velocity is set to $u_{\text{inflow}} = 1.385$ m/s in terms of large and periodic structural deflections. The time history of the structural deflections is shown in Fig. 139 for a point near the extremity of the steel weight ($x/D = 3.13$). This time-dependent signal is quasi-periodic and only small amplitude variations over several structural cycles are observed. With an average maximum peak $(y/D)_{\max} = 0.667$ and an average minimum peak $(y/D)_{\min} = -0.630$, the standard deviation of all positive and negative peaks is calculated to be $\sigma_{\max} = 0.023$ (3.45%) and $\sigma_{\min} = 0.040$ (6.35%) over all 1998 recorded periods. The mean swiveling frequency at this discrete inflow velocity is found to be $f_{\text{avg}} = 11.25$ Hz ($St = 0.179$) and its standard deviation $\sigma_f = 0.18$ Hz (1.60%).

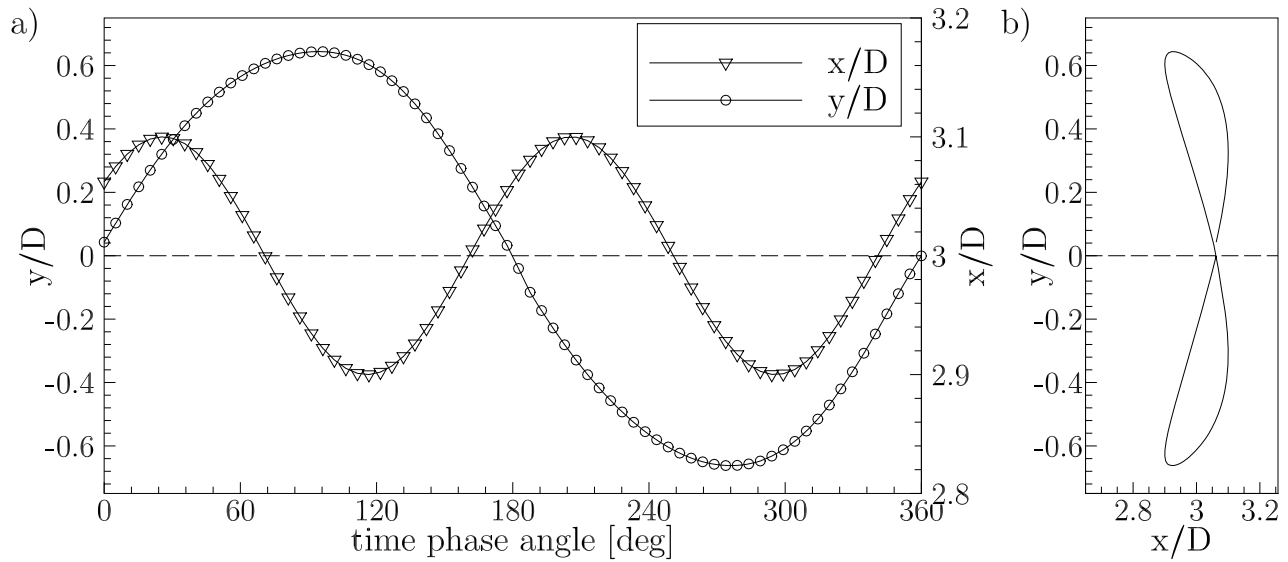


Figure 140: FSI-PfS-2a: Experimental structural results: a) phase-averaged reference period and b) phase-averaged phase-plane, both for the structural deflections at the measurement point $x/D = 3.13$ in the midplane of the channel at $z/D = 0$.

By phase-averaging all 1998 recorded structure periods (see Section 7.4.1) a nearly symmetric sinusoidal reference period is generated (see Fig. 140a). The phase-averaged xy -motion path of the plate extremity forms the characteristic "8" regarding the displacements in the second swiveling mode. Figure 141 depicts the xy -cross-sections of the whole structure plotted for 12 characteristic moments of the entire reference period at an interval of $1/12 \Delta T$. Each profile consists of approximately 180 measurement points. This figure clearly shows that the flexible structure oscillates in the second swiveling mode as mentioned above. Due to the steel weight attached to the para-rubber there are no measurable displacements in the z -direction, leading to a fully two-dimensional structure deformation behavior.

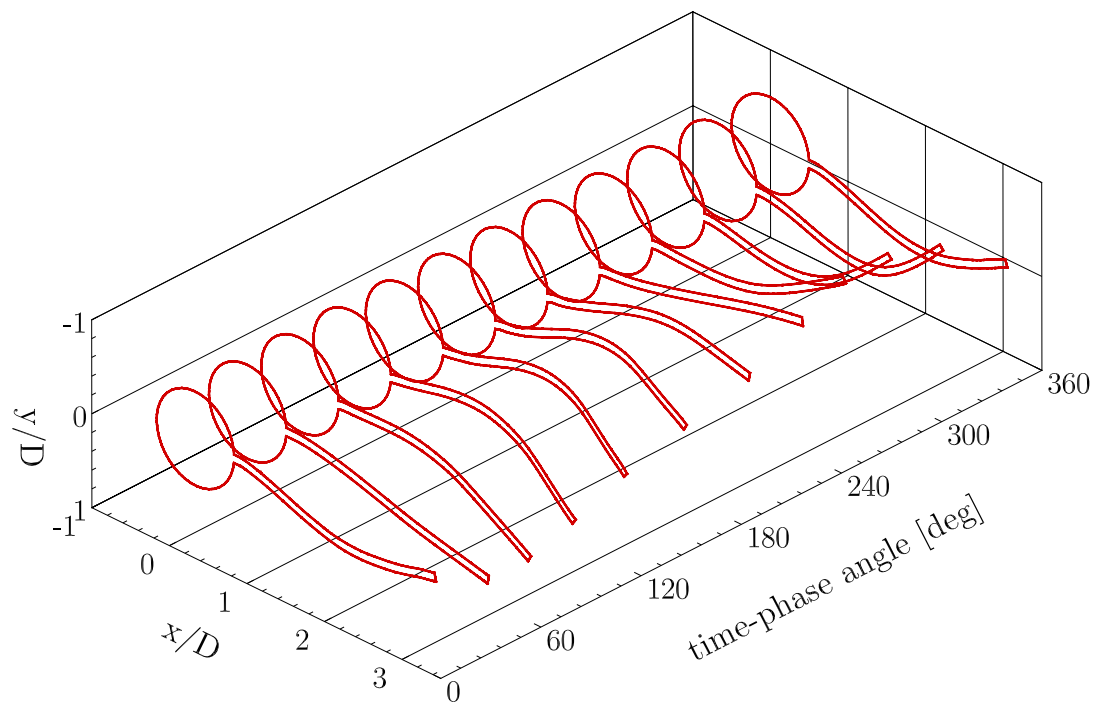


Figure 141: FSI-PfS-2a: Structural results: Structure contour for the reference period.

FSI-PfS-2a - Planar flow results

Based on the experimental set-up two-dimensional PIV measurements are carried out for this test case. The time-averaged flow results are shown in Fig. 142a. Here, the mean flow field reveals the same flow elements (i.e., the acceleration areas on the upper and lower side of the cylinder, the stagnation point in front of the cylinder, the wake area past the cylinder and the shear layers on both sides of the structure) as present in FSI-PfS-1x (see Section 10.1.1) or the corresponding fixed configuration described in Section 8.1.1. By comparing the present flexible configuration with the fixed one, the increased wake expansion in y -direction of about three cylinder diameters in the FSI case is the most obvious difference. Again, this is a direct effect of the additional flow momentum in y -direction generated by the structural deflections. The corresponding Reynolds stresses are given in Fig. 142b. Again, the largest stresses are found the shear layers and in the wake of the front cylinder, where most of the periodic and non-periodic flow fluctuations are generated (i.e., due to the vortex shedding and the resulting motion of the flexible plate).

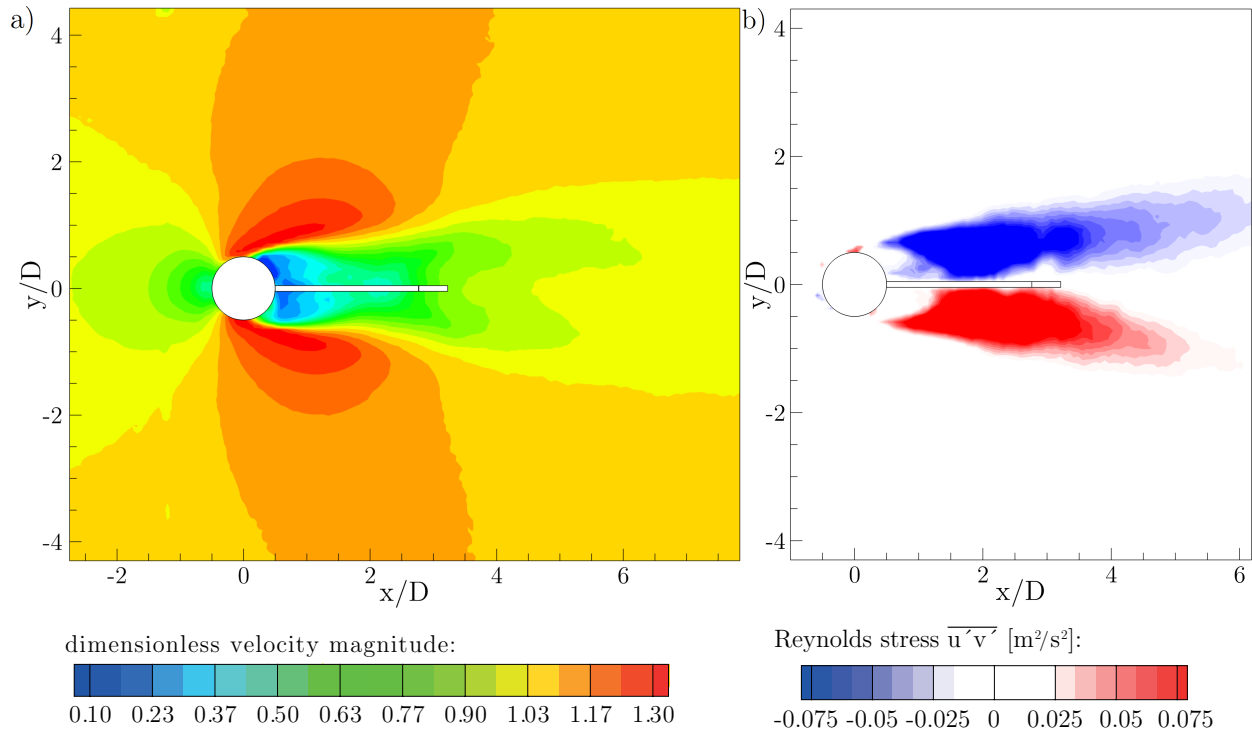


Figure 142: FSI-PfS-2a: Time-averaged PIV results of FSI-PfS-2a at $z/D = 0$ for a) dimensionless velocity magnitude and b) Reynolds shear stress $\overline{u'v'}$.

The combined flow and structural results of the phase-averaged reference period in the xy -plane at $z/D = 0$ based on the measurement data of the planar PIV system are presented in Fig. 143 for six characteristic time phase angles (16, 78, 141, 204, 266 and 326 deg). Once again the symmetric vortex centers shedding alternately from the upper and lower side of the cylinder are now visible in the velocity magnitude contour plots. Looking at the temporal development of these flow structures over the entire period, the convective transport of the vortex centers in the main flow direction is noticeable. Due to the relatively coarse resolution of the PIV analysis the stagnation point in front of the cylinder is not explicitly visible. In the wake of

the structure the characteristic recirculation areas are observed. For a detailed description of each phase-averaged flow field the quite similar flow distribution of FSI-PfS-1c is referenced (see Section 10.1.1).

FSI-PfS-2a - Volumetric flow results

For this test case again three-dimensional flow measurements based on the V3V system are available. The spatial restriction of the V3V system allows an analyzable flow volume of $x/D = 2.55$ to 9.34 , $y/D = -3.55$ to 3.55 and $z/D = -2.86$ to 2.95 . That means the flow region, in which the flexible structure oscillates, is not included.

Similar to the phase-averaged planar flow results, the quasi-periodic vortex shedding is also visible in the three-dimensional flow measurements presented in Figs. 144 and 145¹⁴. Here, the shed vortices which are visualized by iso-surfaces of the velocity magnitude with an iso-value of $u = 1.1$ m/s ($u/u_{\text{inflow}} = 0.79$) move downstream and start to interact with the flexible structure leading to an oscillating quasi-periodic motion. The extra steel weight at the end of the tail additionally supports the deflection by the higher inertia of the swiveling system. Figure 144 shows two different views of a single coupled measurement (without phase-averaging) which allows a detailed analysis of the flow behavior in the wake of the structure. In these snapshots two vortex rolls with a distance of about $\Delta x/D = 2.5$ and $\Delta y/D = 1$ to each other are visible. These vortex rolls illustrate several three-dimensional flow structures, for example the contraction in the middle of the upper vortex roll. Additionally, the contours of the instantaneous spanwise velocity component are mapped onto the iso-surfaces. As obvious from these figures the wake behind the nominally two-dimensional structure is strongly three-dimensional including vortical structures with vorticity components aligned to the main flow direction.

Figure 145 depicts the volumetric phase-averaged data (obtained by 1100 single V3V measurements) at the same time-phase angle ($\phi = 172$ deg) as shown in Fig. 144. In contrast to the single measurement only small variations in the spanwise direction of the vortex rolls are visible. By using more V3V measurements for the phase averaging, the phase-averaged flow field should converge towards a two-dimensional problem. For the same reason also the spanwise velocity component diminishes for a longer averaging period and finally vanishes completely.

Figure 146 presents the results of the first and second mode of the POD analysis of this test case. Similar to the POD analysis of the test cases FSI-PfS-1x these two modes (first mode: $k_{\text{abs},1\text{st}} = 380.92$ m²/s², $k_{\text{rel},1\text{st}} = 26.24\%$ and second mode: $k_{\text{abs},2\text{nd}} = 365.24$ m²/s², $k_{\text{rel},2\text{nd}} = 25.16\%$) contain most of the total kinetic energy present in the flow field $k_{\text{abs},\text{all}} = 1451.67$ m²/s² ($k_{\text{rel},\text{all}} = 100\%$).

Figures 146a and 146b correspond to the kinetic energy of the streamwise velocity u . The first two POD modes related to the energy of the cross-flow velocity component v are presented in Figs. 146c and 146d. In comparison to the test cases FSI-PfS-1x the energy distribution in FSI-PfS-2a is increased in size and amount for both velocity components. Here, the enlarged motion area of the flexible plate is responsible for this increase. Similar to the already mentioned

¹⁴Please note that in Kalmbach and Breuer (2013b) slightly different figures are presented due the use of a left-hand coordinate system.

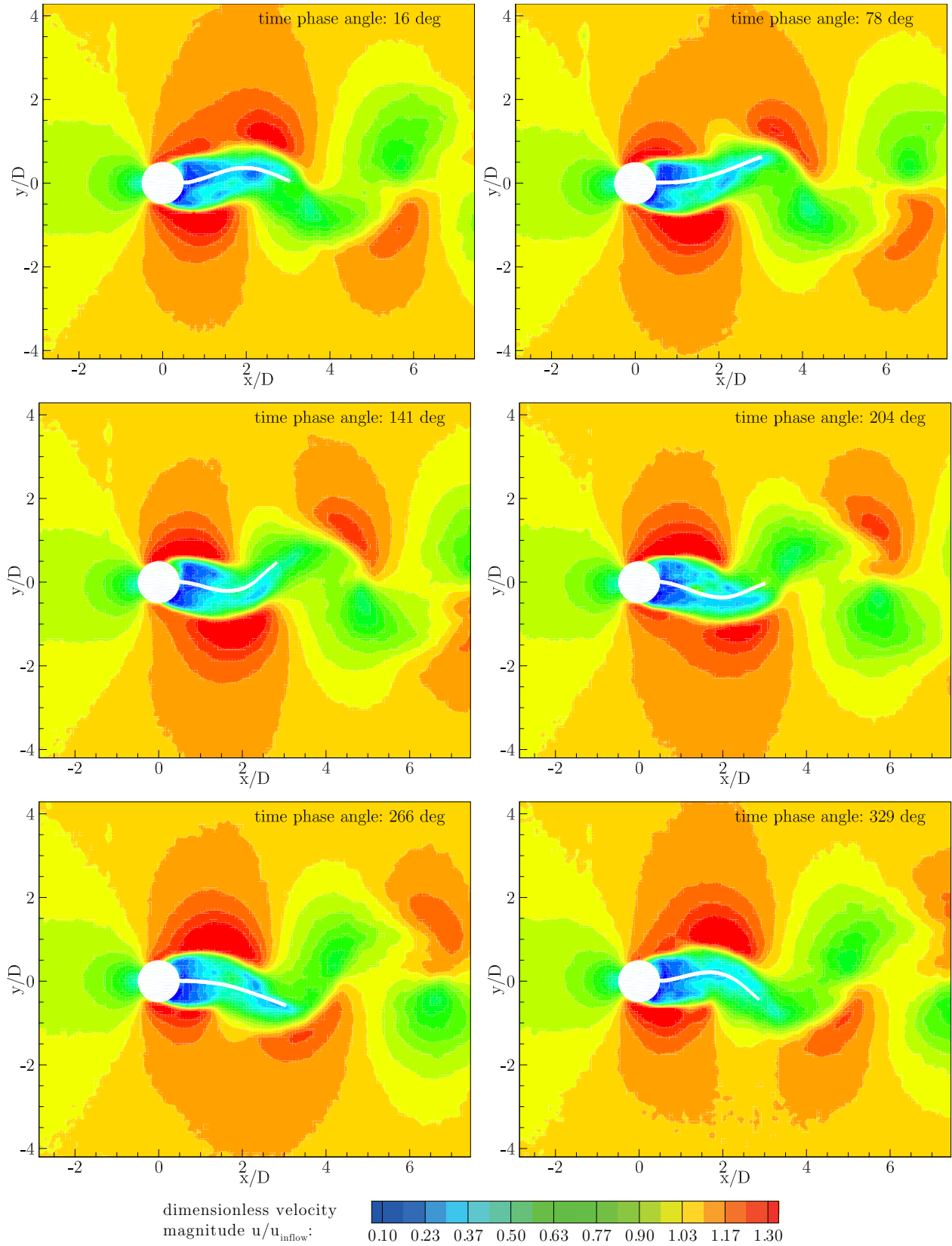


Figure 143: FSI-PfS-2a: Experimental phase-averaged flow and structural results for the reference period.

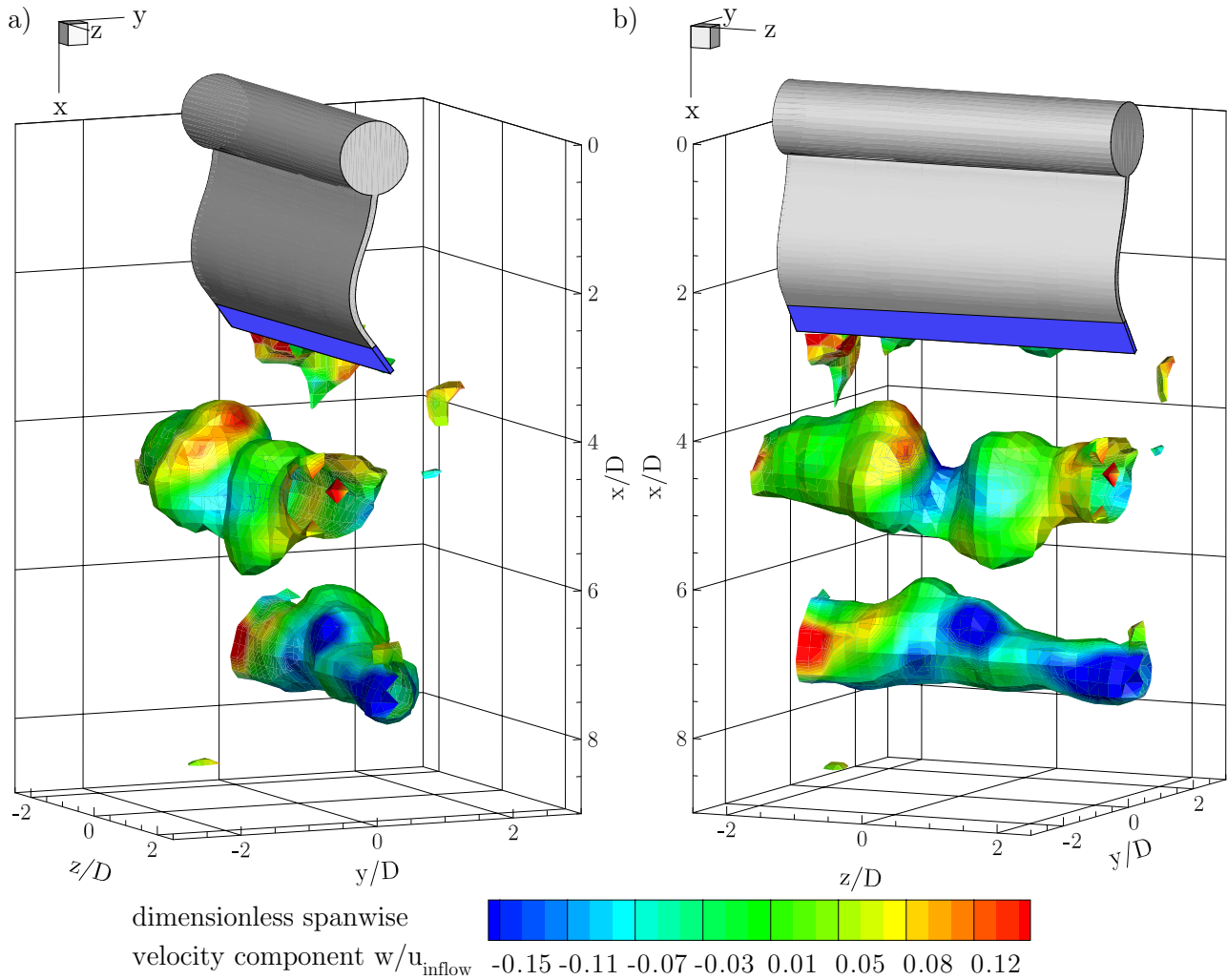


Figure 144: FSI-PfS-2a: Experimental flow results based on the V3V-system and the structural results, single measurement result at the phase angle of $\phi = 172$ deg.

test cases the energy rises in the area, where the vortices detach from the shear layers and form an antisymmetric (u -component) and a symmetric pattern (v -component) according to the alternating vortex shedding at the cylinder. The POD analysis based on the vorticity component ω_z is presented in Figs. 146e and 146f. Most of the kinetic energy of the flow is found in the vicinity of the flexible plate. In both POD modes the motion path of the structure is roughly visible, showing the influence of the second swiveling mode on the energy distribution.

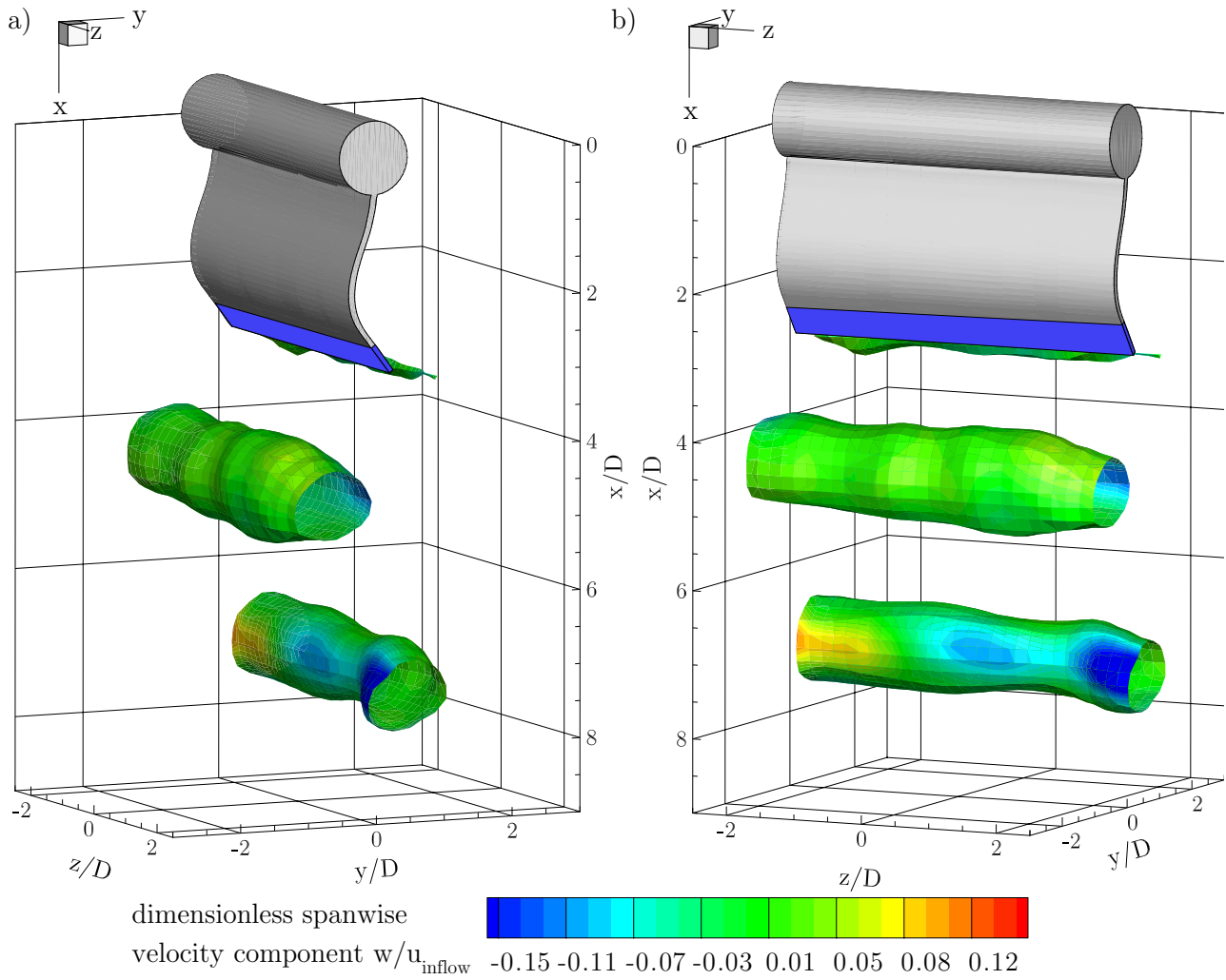


Figure 145: FSI-PfS-2a: Experimental flow results based on the V3V-system and the structural results, phase-averaged result at the phase angle of $\phi = 172$ deg.

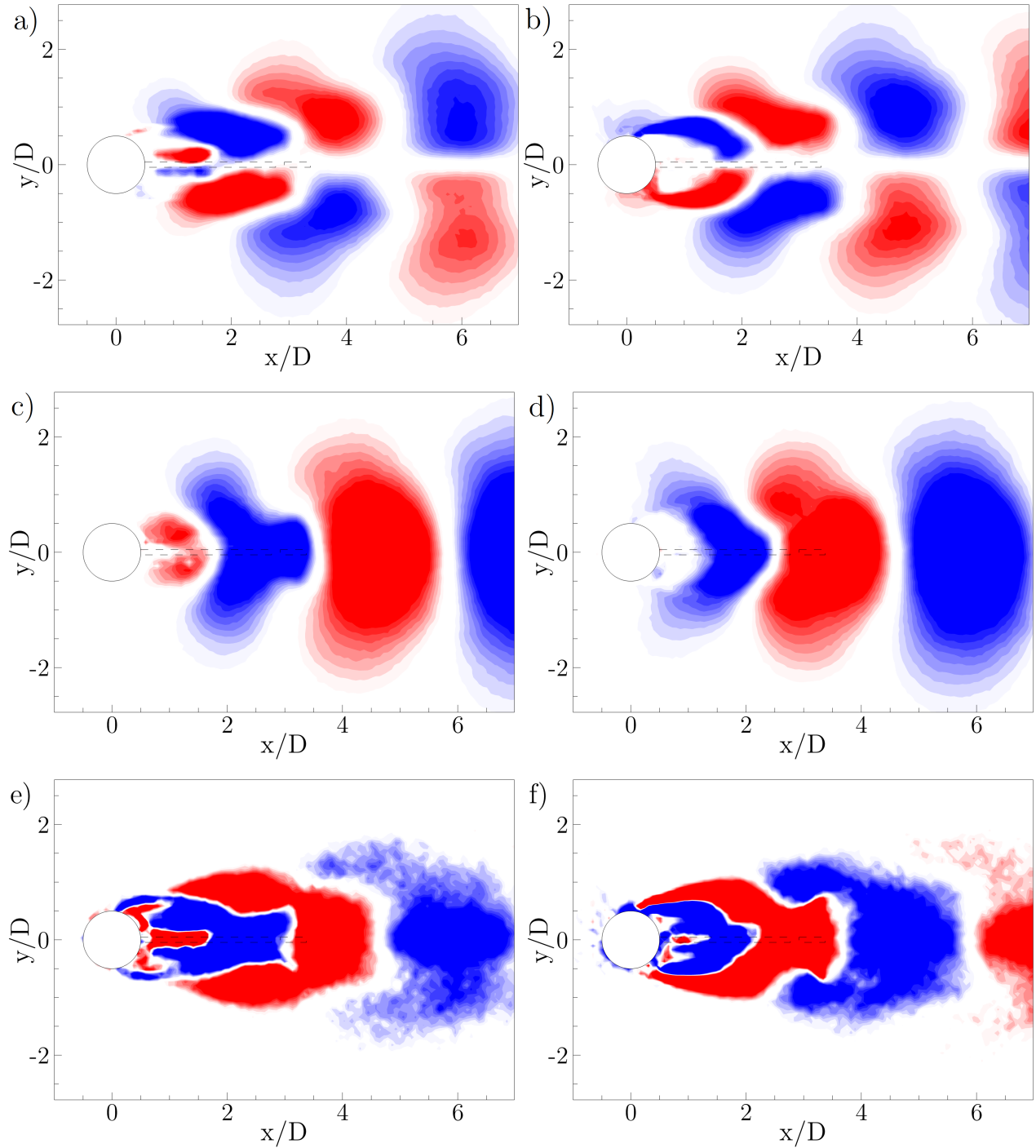


Figure 146: FSI-PfS-2a: POD analysis of the two-dimensional flow fields in the midplane ($z/D = 0$)
 a) velocity component u , first mode; b) velocity component u , second mode; c) velocity component v , first mode; d) velocity component v , second mode; e) vorticity component ω_z , first mode; f) vorticity component ω_z , second mode.

FSI-PfS-2b - Structural results

In the next paragraphs the measurement results of the second test case of this series, i.e. FSI-PfS-2b, will be discussed. The configuration of FSI-PfS-2b is similar to FSI-PfS-2a. The only difference is the free rotational DOF of the front cylinder in FSI-PfS-2b. Therefore, this test case refers to the turbulent benchmarks of Gomes and Lienhart (2013) which also possesses this additional DOF of the front cylinder. The strong influence of this DOF is visible in the structural response for increasing inflow velocities up to $u_{\text{inflow}} = 2.3$ m/s in Figs. 147 and 148. In Fig. 147 the maximal and minimal amplitudes of the structure deformation are displayed while Fig. 148 presents the corresponding swiveling frequencies of the flexible plate¹⁵.

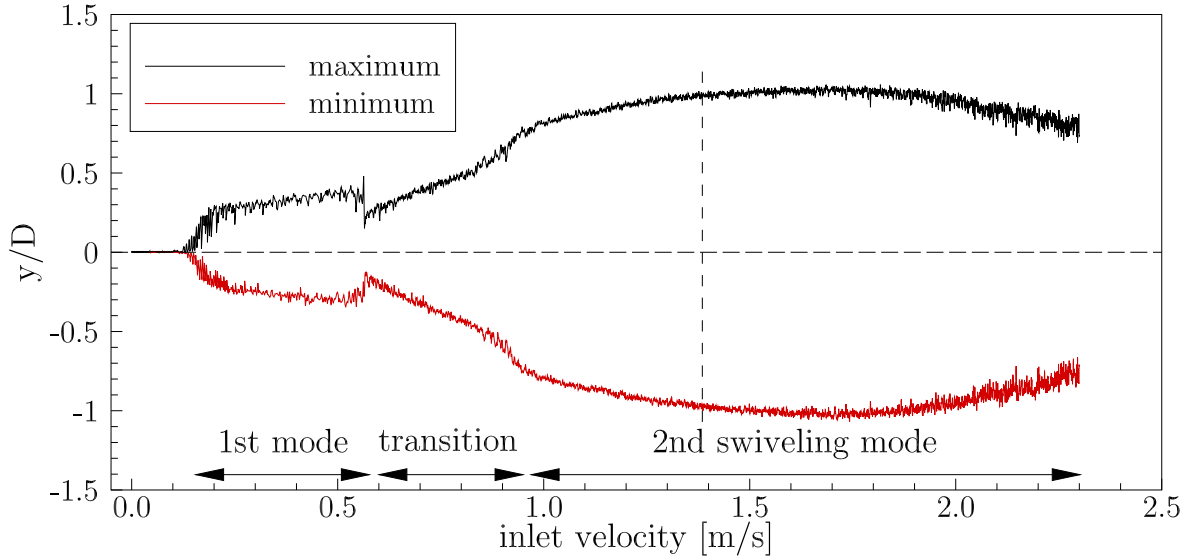


Figure 147: FSI-PfS-2b: Averaged maximal/minimal structural deflections as a function of the inflow velocity.

For this test case the FSI-coupling starts at an inflow velocity of about $u_{\text{inflow}} = 0.12$ m/s with tiny and aperiodic deformations until the velocity reaches a velocity of 0.2 m/s. By passing this critical inflow velocity the amplitudes of the structural motion rises and become quasi-periodic. Between the inflow velocities $u_{\text{inflow}} = 0.20$ to 0.55 m/s a small increase of the structural displacements from $(y/D)_{\text{max}} = \pm 0.25$ to ± 0.35 is observable. For low inflow velocities in this range the structure swivels in its first swiveling mode characterized by a rigid body motion (rotation of the whole structure, no elastic deformations of the flexible plate are observable). By increasing the inflow velocity still in the range between $u_{\text{inflow}} = 0.20$ to 0.55 m/s this mode is altered and small elastic deformations of the rubber plate appear. Large deformations of the para-rubber plate start at the end of this interval and mark the transition into the dominant second swiveling mode of this test case. With inflow velocities larger than $u_{\text{inflow}} = 0.55$ m/s the flow excitation results in nearly two-dimensional and almost periodic structural deflections with increasing peak amplitudes.

In the range between $u_{\text{inflow}} = 0.55$ m/s and 0.90 m/s these peak amplitudes rise linearly.

¹⁵Mean of 10 measurement series.

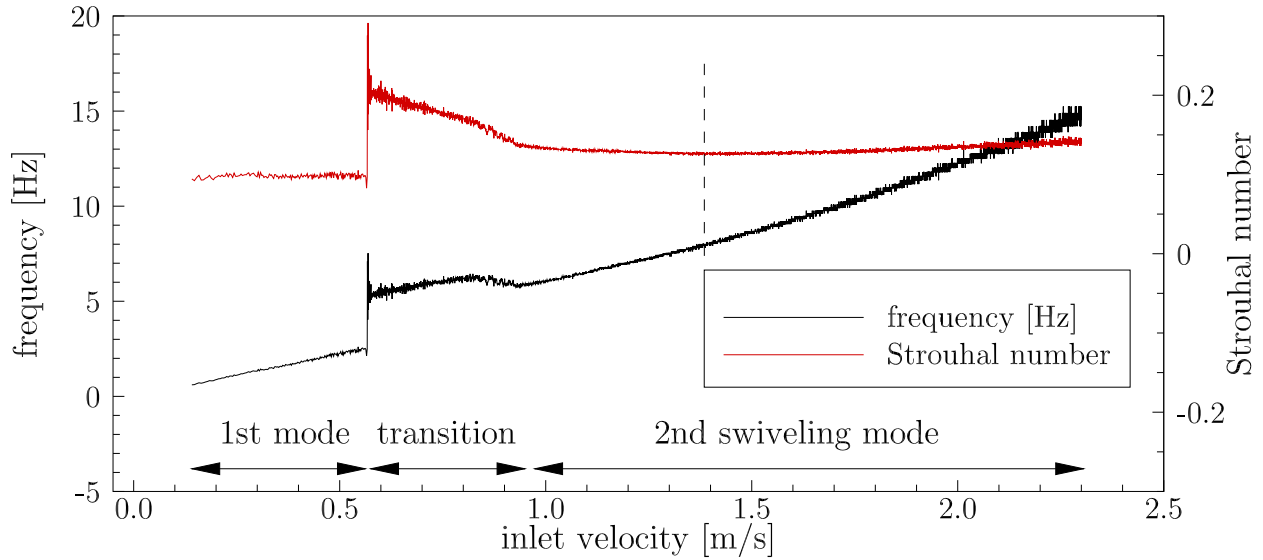


Figure 148: FSI-PfS-2b: Averaged frequency and Strouhal number as a function of the inflow velocity.

At about $u_{\text{inflow}} = 0.95$ m/s another change in the structural response is registered. This inflow velocity marks the end of the transition phase between the first and the second swiveling mode. The second mode is reached at about $u_{\text{inflow}} = 0.95$ m/s and is found to be dominant until the end of the measurement series. The maximal and minimal amplitudes ($(y/D)_{\text{max}} = 1.01$, $(y/D)_{\text{min}} = -1.01$) of the structure deformation are reached at the inflow velocity of $u_{\text{inflow}} = 1.65$ m/s. With a further increase of the inflow velocity the peak displacements decline and lead to higher variations in the structural deformations and the swiveling frequency. It can be assumed that the increasing inertia of the outer bulk flow limits the structural deflections for these high inflow velocities. The generated vortices in shear layer are hindered to drift further into to the bulk flow while the increased vortex shedding frequency produces faster oscillating pressure forces on the flexible rubber plate. This combined effect may reduce the structural deflections for high inflow velocities.

The snapshots in Fig. 149 illustrate the different deformation behavior of this test case in comparison to FSI-PfS-2a (Fig. 138). Here, large deflections are reached at lower inflow velocities and the entire profile of the deformed structure appears rounder in the middle section due to the simultaneously rotating front body.

The swiveling frequencies f and its dimensionless equivalent, the Strouhal number St , are presented in Fig. 148 as a function of the increasing inflow velocity. As already mentioned for the displacements, after the non-periodic settling phase a cyclic rigid body motion (no elastic deformations of the para-rubber plate are noticeable) starts at the inflow velocity of $u_{\text{inflow}} = 0.2$ m/s with a swiveling frequency of $f = 0.87$ Hz ($St = 0.096$). A further increase of the inflow velocity results in a linear rise ($\delta f / \delta u = 4.74$ Hz/(m s⁻¹)) of the swiveling frequency to a value of $f = 2.53$ Hz ($St = 0.099$) at $u_{\text{inflow}} = 0.55$ m/s and small deformations of the para-rubber plate. Based on the mode transition from this swiveling state to the large deformations of the rubber plate in the second mode a doubling of the frequency to $f = 5.31$ Hz ($St = 0.193$) takes place. Similar to the other test cases again this swiveling frequency at the transition from

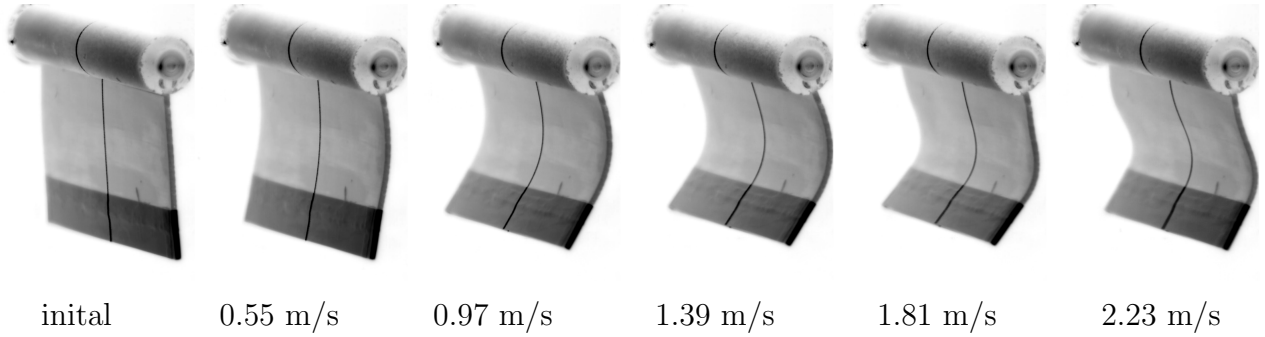


Figure 149: Characteristic moments of the structure deformation at several inflow velocities for FSI-PfS-2b.

the first to the second mode is close to the second natural frequency $f_{2b,2} = 5.15$ Hz of the structure (entire structure rotationally mounted). The transition phase to the second bending mode is characterized by large variations of the swiveling frequencies as visible in Fig. 148 for the inflow velocity between $u_{\text{inflow}} = 0.55$ m/s and 0.90 m/s.

Remarkable is that the oscillation frequency $f = 5.89$ Hz at the end of the transition phase $u_{\text{inflow}} = 0.95$ m/s is close the third natural frequency of the structure with $f_{2b,3} = 5.98$ Hz. After this phase the frequencies rise almost linearly to $f = 9.36$ Hz at $u_{\text{inflow}} = 1.65$ m/s and possess a relative low variation. With inflow velocities beyond $u_{\text{inflow}} = 1.65$ m/s the structural frequencies stronger fluctuate but still increase to $f = 14.91$ Hz at the end of the measurement series at $u_{\text{inflow}} = 2.30$ m/s.

Based on these investigations the final test case velocity $u_{\text{inflow}} = 1.385$ m/s is chosen. The time histories of the front body angle (extracted out of the measured structure profiles) and the structural deflection for a point near the extremity of the attached steel weight ($x/D = 3.13$) are shown in Fig. 150 for this inflow velocity. These time-dependent signals are quasi-periodic and show only mild amplitude variations over several structure cycles. With an average maximum peak $(y/D)_{\text{max}} = 0.895$ and an average minimum peak $(y/D)_{\text{min}} = -0.891$, the standard deviations of all positive and negative peaks over all 1460 recorded periods are calculated to be $\sigma_{\text{max}} = 0.029$ (3.24%) and $\sigma_{\text{min}} = 0.032$ (3.59%), respectively.

The mean swiveling frequency at this final inflow velocity is found to be $f_{\text{avg}} = 8.16$ Hz ($St = 0.130$) and its standard deviation $\sigma_f = 0.077$ Hz (0.94%). The front angle variation is represented by an average maximum deflection of $\phi_{\text{max}} = 21.5$ deg and an average minimum deflection of $\phi_{\text{min}} = -22.3$ deg. The standard deviation of all positive and negative angular peak deflections is calculated to be $\sigma_{\phi, \text{max}} = 1.04$ (4.83%) and $\sigma_{\phi, \text{min}} = 0.99$ (4.44%). Remarkable is the almost constant phase difference of 80 deg between the angular motion of the front cylinder and the deflection of the trailing edge at the steel weight (angle before displacement).

The phase-averaged structure results are presented in Figs. 151 and 152. The nearly sinusoidal oscillation shown in Fig. 151 consists of 98 phase-averaged data points calculated out of the recorded 1460 periods. Similar to FSI-PfS-2a the xy -path of the measurement point within the reference period is characterized by the form of an "8". Covering the whole structure within the mean time-phase interval, Fig. 152 illustrates the large deflections of the rubber plate in

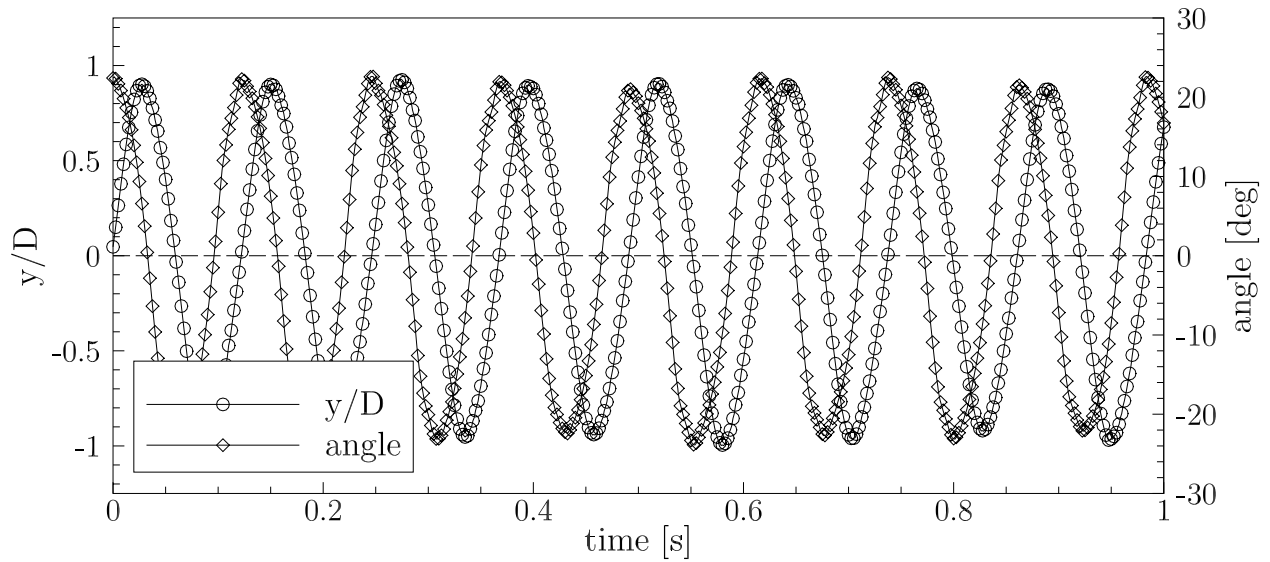


Figure 150: FSI-PfS-2b: Experimental structural results: Time history of the structural deflections y/D (extract) for the measurement point at $x/D = 3.13$ at $z/D = 0$ and the angle of rotation of the front cylinder.

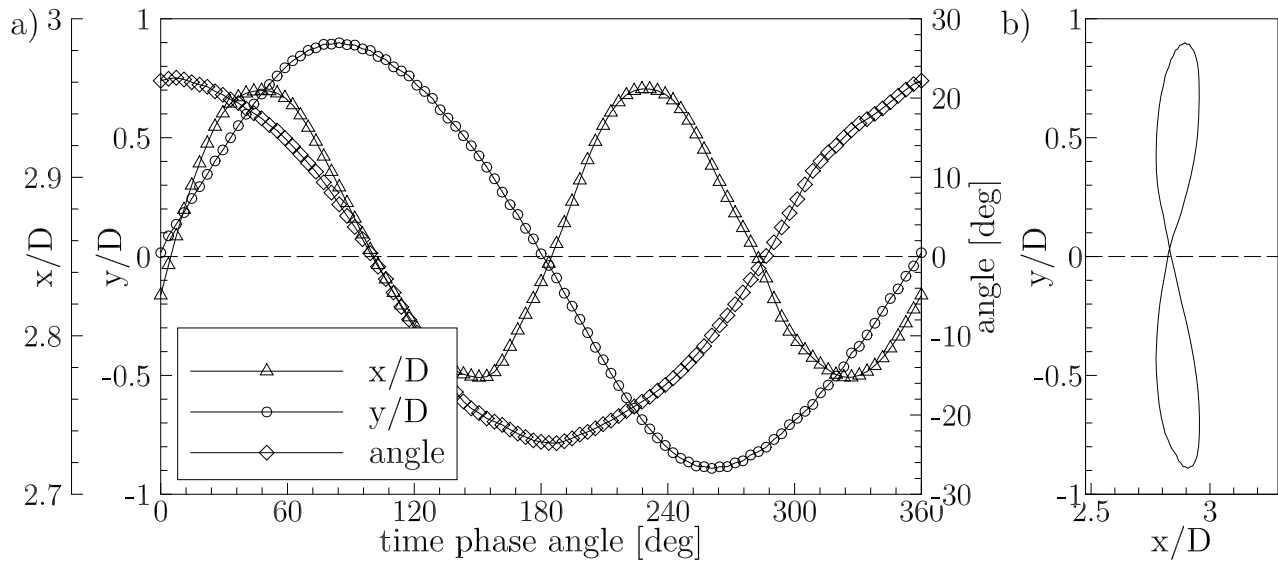


Figure 151: FSI-PfS-2b: Experimental structural results: a) phase-averaged reference period for the structural deflections y/D and the angle of rotation of the front cylinder and b) phase-averaged xy -phase-plane of the structural deflections, both at the measurement point $x/D = 3.13$ in the midplane of the channel at $z/D = 0$.

the second swiveling mode.

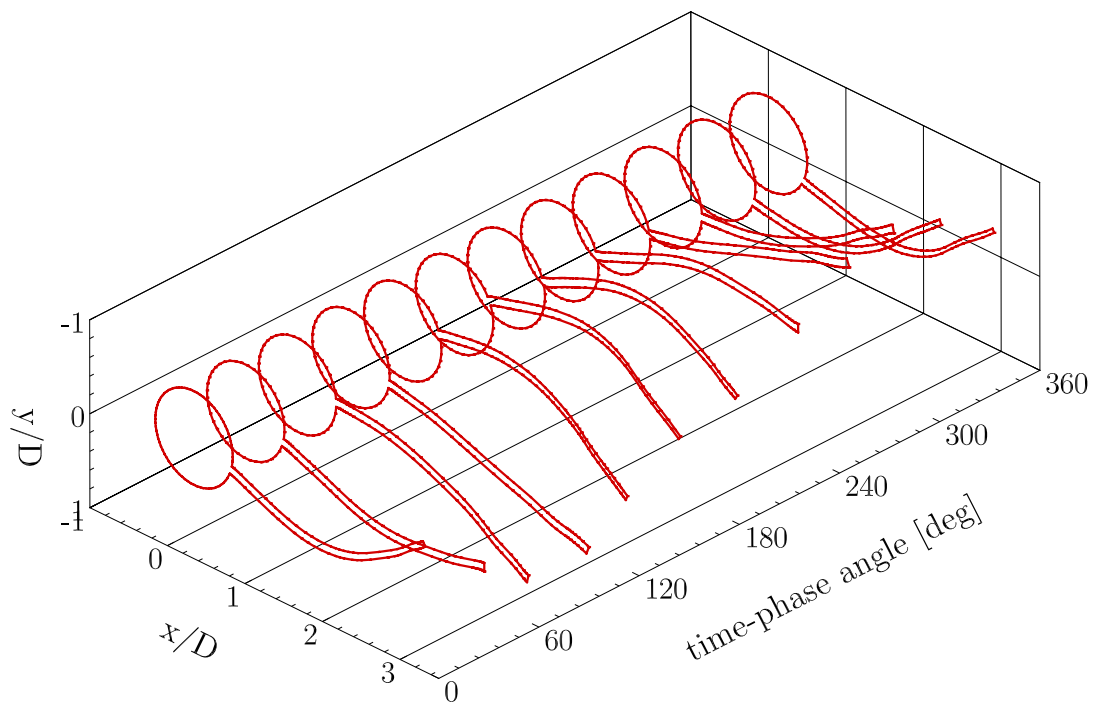


Figure 152: FSI-PfS-2b: Structural results: Structure contour for the reference period.

FSI-PfS-2b - Flow results

By averaging over all 1100 PIV measurements without applying a phase-reconstruction method the flow is almost symmetric. The mean field in terms of the velocity magnitude is given in Fig. 153a. Comparing the results of the FSI-PfS-2b configuration with the fixed configuration (see Section 8.1.1, Fig. 76) the additional DOF of the front cylinder obviously has an enormous effect on the mean flow. Now, the wake is increased to about five cylinder diameters in y -direction as a consequence of the large area of influence of the structure. Similar to the other test cases flow structures such as the acceleration areas, the shear layers and the stagnation point are again visible in the time-averaged result. The influence of the rotational DOF of the front cylinder is also noticeable in the mean Reynolds shear stress distribution depicted in Fig. 153b. The motion of the whole structure generates strong unsteady flow effects in its vicinity. In the far-wake area a V-shaped stress distribution is apparent. Here, the additional momentum related to the large structural deflections in y -direction results in additional unsteady flow effects and correspondingly in a broaden wake area.

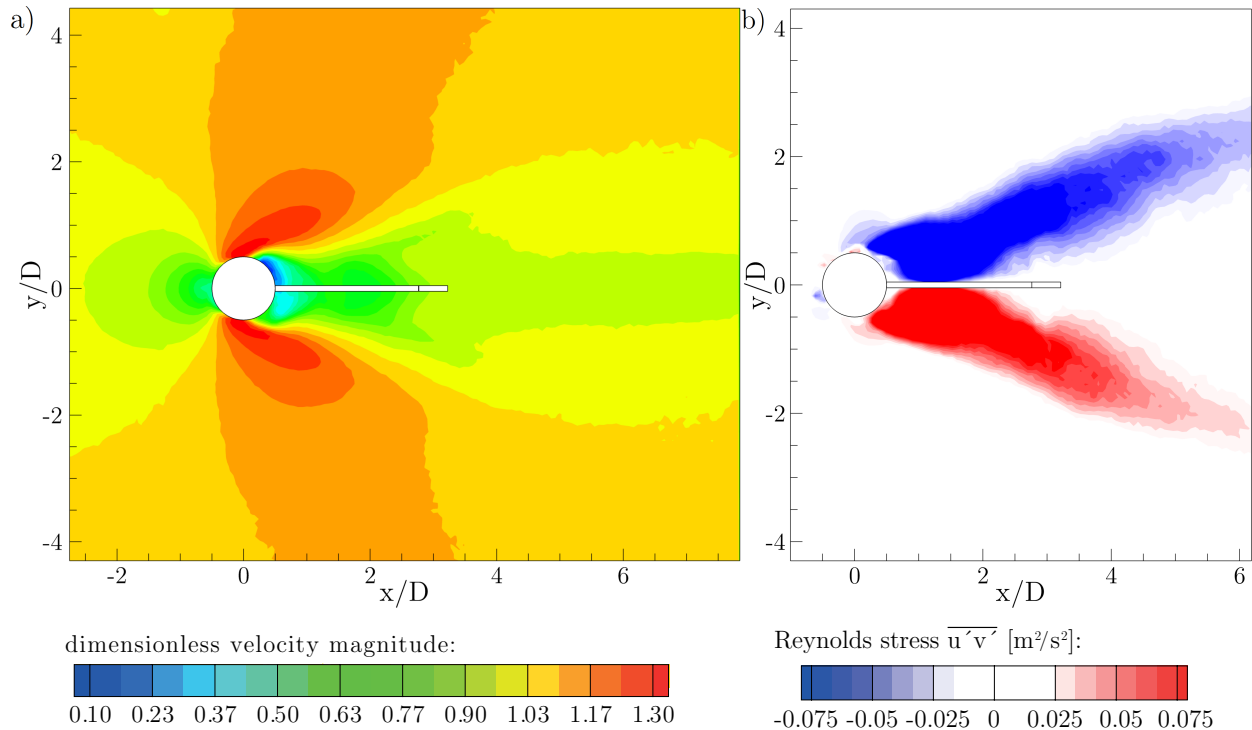


Figure 153: FSI-PfS-2b: Time-averaged PIV results of FSI-PfS-2b at $z/D = 0$ for a) dimensionless velocity magnitude and b) Reynolds shear stress $\overline{u'v'}$.

In the time series of the six time phase angles (16, 78, 141, 204, 266, 326 deg) the phase-averaged quasi-periodic FSI problem of this test case is illustrated in Fig. 154. In the first picture at the phase angle of 16 deg the rubber plate is strongly deformed, while the trailing edge is near the neutral axis of the structure. With a value of $\phi = 21.8$ deg the angle of the front cylinder is almost at its maximal excitation. The large vortex which is shedding on the upper cylinder surface at about 60 deg before this state is convected downstream and leads to increased pressure forces on the upper side of the rubber plate. At the next phase angle of 78 deg the trailing edge reaches its maximum deflection within the period while the middle

part of the plate already moves in the opposite direction. The angle of the front-body decreases to $\phi = 9.0$ deg. The vortex on the lower side of structure is shed shortly after this time phase angle as visible in the next moment at 141 deg (front-body angle $\phi = -17.6$ deg). In the meantime another vortex on the upper side is formed and continuously grows in size. Parts of the structure already have passed the neutral axis at $y/D = 0$ and deform further in negative y -direction. Within the phase interval between 141 deg and 204 deg the entire structure passes the zero-line $y/D = 0$ and reaches a similar but inverted state of the flow and structure motion to the first half of the period. Meanwhile, the front cylinder reaches its minimal excitation and starts to rotate again counterclockwise.

As already observed in FSI-PfS-2a a small secondary trailing-edge vortex is generated while the structures moves through the wake area. This secondary vortex follows the larger front-body vortex and is also convected downstream where both vortices merge. This process is hardly visible in the flow results because of the coarse resolution of the PIV-system and the systematic error of the phase-averaging method producing a blurred uncertainty as already discussed (see Section 10.1.1). In comparison to the other two-dimensional test cases the coupling between the fluid and the structure in FSI-PfS-2b produces a strongly affected flow field in terms of increased vortex sizes and broaden wake. Furthermore, the rotation of the front cylinder produces an angular displacement of the stagnation point as a function of the cylinder angle. Here, this angular displacement move contrariwise to the angular displacement of the front cylinder within the reference period. That means that if the front cylinder angle is on its maximum, the corresponding stagnation point is found on the opposite side of the front cylinder.

The POD analysis for the first two POD modes is presented in Fig. 155. In comparison to the previously discussed two-dimensional test cases the additional rotational degree of freedom results in a broaden energy distribution in the wake of the moving structure. Due to the increased covered area of the swiveling structure also the energy distribution is strongly influenced by the unsteady flow effects. While in the test cases without the additional rotational degree of freedom of the front cylinder, the area influenced by the FSI coupling starts approximately at $x/D \approx 1.5$, now the area involved starts at $x/D \approx 0$. Similar to FSI-PfS-2a both POD modes (first mode: $k_{\text{abs},1\text{st}} = 845.05 \text{ m}^2/\text{s}^2$, $k_{\text{rel},1\text{st}} = 36.55\%$ and second mode: $k_{\text{abs},2\text{nd}} = 667.97 \text{ m}^2/\text{s}^2$, $k_{\text{rel},2\text{nd}} = 28.89\%$)(36.55%) are related to the unsteady effects especially to the vortex formation. Due to the deflected fluid mass the influenced area ranges far beyond the maximum and minimum deflection of the structure. Remarkable is the fact that the combined energy content of these two modes represent 65% of the entire kinetic energy $k_{\text{abs},\text{all}} = 2312.05 \text{ m}^2/\text{s}^2$ ($k_{\text{rel},\text{all}} = 100\%$) of this test case. In comparison to the energy levels of FSI-PfS-1x ($\approx 1000 \text{ m}^2/\text{s}^2$) and 2a ($\approx 1450 \text{ m}^2/\text{s}^2$) this is an enormous increase (factor 2.3 and 1.6, respectively) in the unsteady flow energy which is directly related to the release of the rotational degree of the front cylinder.

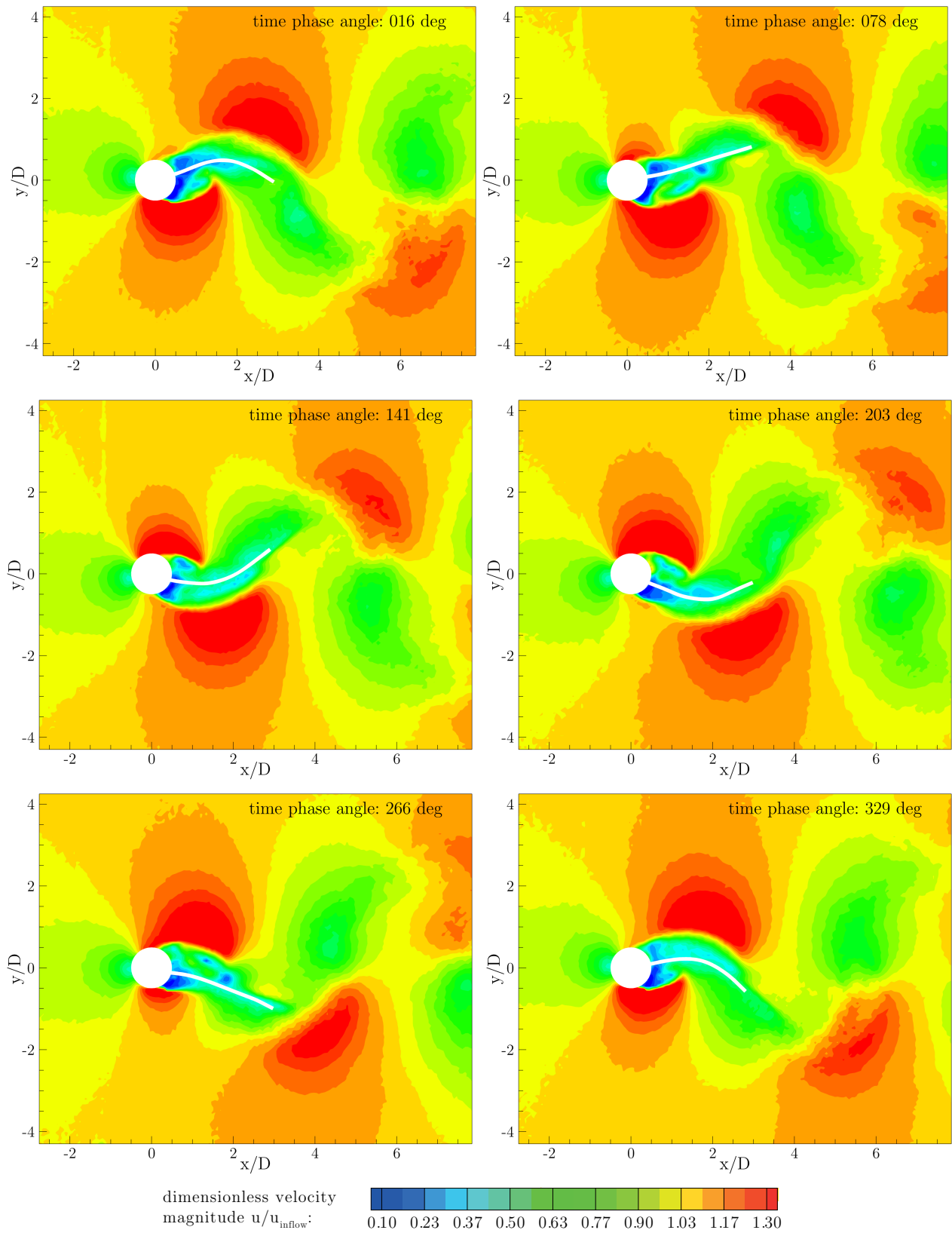


Figure 154: FSI-PfS-2b: Experimental phase-averaged flow and structural results for the reference period.

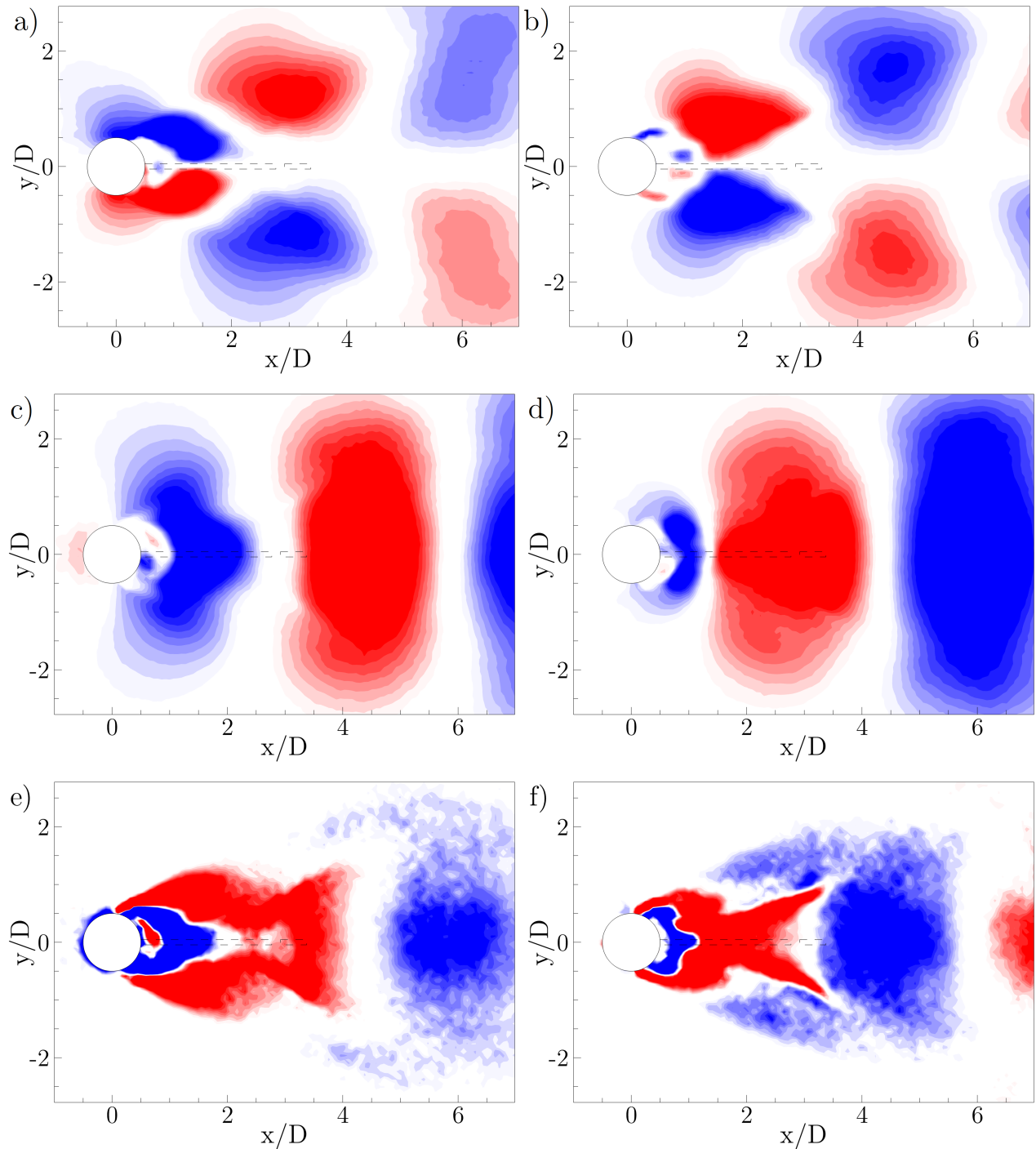


Figure 155: FSI-PfS-2b: POD analysis of the two-dimensional flow fields in the midplane ($z/D = 0$) of FSI-PfS-2b a) velocity component u , first mode; b) velocity component u , second mode; c) velocity component v , first mode; d) velocity component v , second mode; e) vorticity component ω_z , first mode; f) vorticity component ω_z , second mode.

FSI-PfS-2b - Comparison with FSI-PfS-2a

To illustrate the influence of the rotational DOF of the front cylinder in FSI-PfS-2b, the most significant changes compared to the fixed configuration of FSI-PfS-2a are described in the following paragraph. In Fig. 156 the structural deflections of both test cases at the measurement point $x/D = 3.13$ are compared. While the x/D -displacements are only shifted upstream by about -0.25 from case 2a to case 2b, the extrema of the y/D -deflections are increased by about $+0.25$ ($+38\%$).

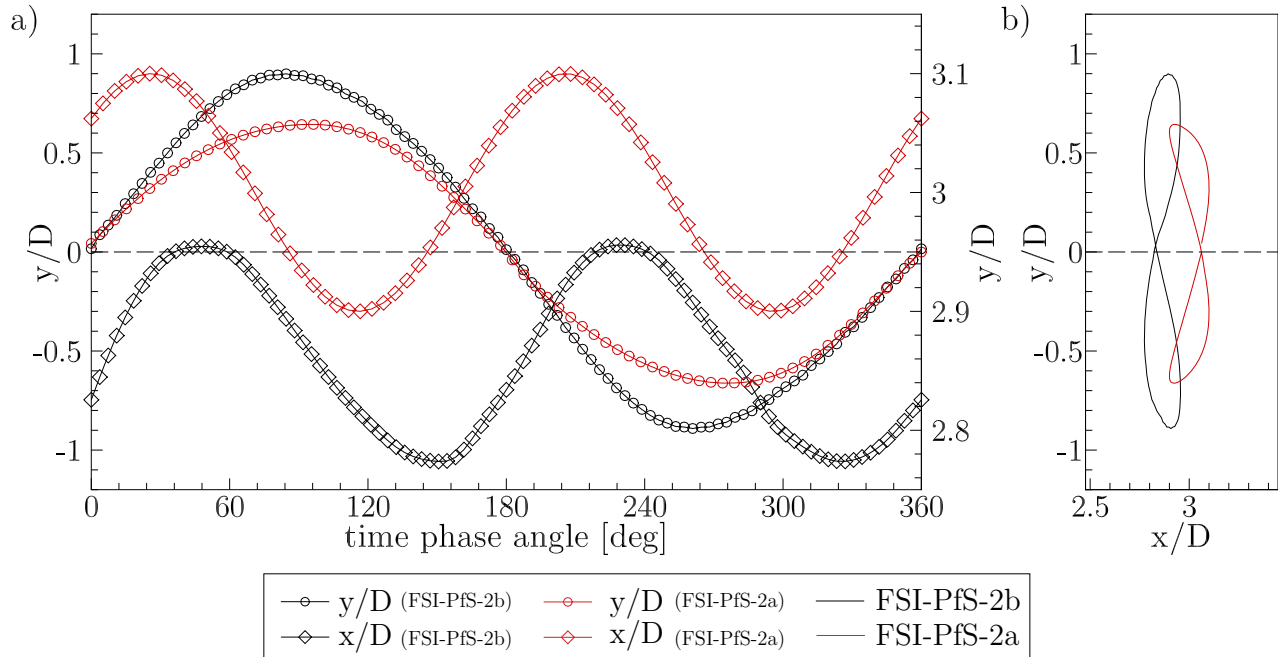


Figure 156: Comparison of the experimental structural results of FSI-PfS-2b (black) and FSI-PfS-2a (red) at $x/D = 3.13$: a) phase-averaged reference period for the structural deflections x/D and y/D and b) phase-averaged xy -phase-plane of the structural deflections.

This change is also evident in the comparison of the xy -trajectories presented in Fig. 156b. Here, both test cases form an "8". However, the extrema in FSI-PfS-2a are positioned in negative x/D -direction from its neutral point ($x/D = 3.06$, $y/D = 0$), while they are located in positive y/D -direction in FSI-PfS-2b (neutral point at $x/D = 2.84$, $y/D = 0$). Therefore, the motion path of the case 2a forms a left-opened sickle-shaped "8", while case 2b is represented by a slightly right-opened sickle-shaped "8". Furthermore, the swiveling frequency is altered from 11.25 Hz in FSI-PfS-2a to 8.16 Hz in FSI-PfS-2b representing a change of about -27.5% . The influence on the flow field is most obvious by comparing their mean flow fields in Fig. 142a (FSI-PfS-2a) and Fig. 153a (FSI-PfS-2b). Here, the increased y -expansion of the wake (three to five cylinder diameters) downstream of the structural configuration of FSI-PfS-2b is observable. This change is also visible in the phase-averaged flow fields since the shed vortices are larger in size and are convected further into the bulk flow. Despite these differences both test cases deflect in the second swiveling mode with only mild cycle-to-cycle fluctuations regarding the deflections and the frequency.

FSI-PfS-2b - Comparison with test case of Gomes and Lienhart

Referring to the literature review of this thesis in Section 1.2 the FSI-benchmarks of Gomes (2012) and Gomes and Lienhart (2013) are mentioned. Since the configuration of FSI-PfS-2b is quite similar to the set-up "F2M-CH.C" of Gomes (2012) and Gomes and Lienhart (2013), a direct comparison of both cases is carried out in the following paragraph. The set-up "F2M-CH.C" of Gomes and Lienhart (2013) is illustrated in Fig. 18 and consists of a rotationally mounted front cylinder with an attached steel sheet and weight. The dimensions of both structures are equal concerning the length and width due to the usage of the same test facility. However, the thickness of the flexible steel sheet in "F2M-CH.C" measures only 0.04 mm, in contrast to the 2 mm thick para-rubber plate in FSI-PfS-2b. While in "F2M-CH.C" the intersection of the steel sheet with the steel weight forms a step, the intersection in FSI-PfS-2b is smooth. The mount of the front cylinder, the attached steel weight, the applied fluid (water) and the flow measurement technique are again almost identical. The test cases F2M-CH.C and FSI-PfS-2b differ in the flexible plate material (steel to para-rubber), the plate thickness (0.04 mm to 2 mm), the inflow velocity (0.680 m/s to 1.385 m/s), the resulting Reynolds number ($Re = 15,400$ to $Re = 30,470$), the technique to measure the structural deformations and the generation of the phase-averaged results.

In general, the structural deformations are similar since both cases deflect in the second swiveling mode. Figure 157 presents the quantitative comparison of both test cases concerning the deflections (measurement points: $x/D = 3.22$ for F2M-CH.C and $x/D = 3.13$ for FSI-PfS-2b) and the angle of rotation of the front cylinder.

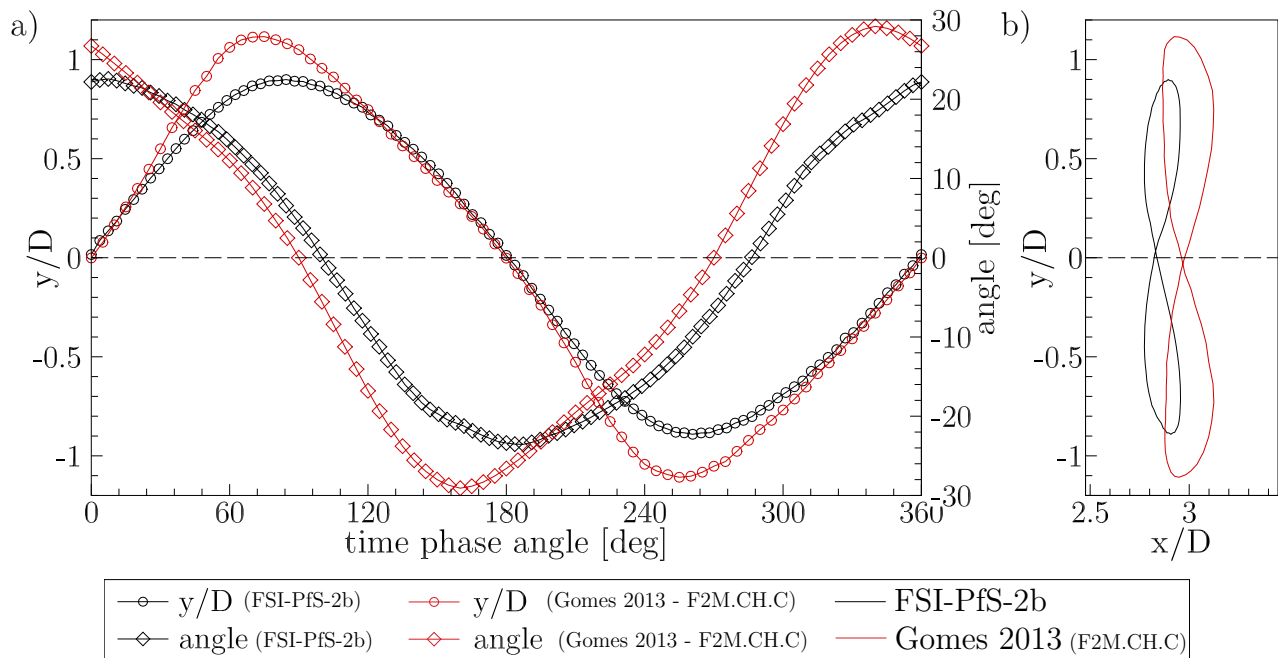


Figure 157: Comparison of the experimental structural results of FSI-PfS-2b (black) and F2M.CH.C by Gomes (2012) and Gomes and Lienhart (2013) (red): a) phase-averaged reference period for the structural deflections y/D and the angle of rotation of the front body and b) phase-averaged xy -phase-plane of the structural deflections.

The structural deflections y/D and the angular displacements are shown in Fig. 157a¹⁶. Both corresponding curves show strong qualitative similarities despite their different set-ups. The differences of "F2M-CH.C" to FSI-PfS-2b are found in the extrema of the y -deflections ($y/D \approx \pm 1.2$ to $y/D \approx \pm 0.9$) and the angular displacements ($\phi \approx \pm 29.2$ deg to $\phi \approx \pm 22.0$ deg). That means that the present case FSI-PfS-2b reveals milder displacements than the case of Gomes (2012) and Gomes and Lienhart (2013). The deviations in the xy -motion path (Fig. 157b) of both test cases refer to these differences. Another distinction is the low swiveling frequency of about 4.45 Hz in the case of "F2M-CH.C" compared to the frequency of about 8.16 Hz in FSI-PfS-2b. This difference refers mainly to the twice as fast inflow velocity of FSI-PfS-2b in comparison to "F2M-CH.C". As expected, the Strouhal numbers are similar with about $St = 0.14$ (F2M-CH.C) and $St = 0.13$ (FSI-PfS-2b), respectively. In the flow fields qualitatively the same flow structures (as mentioned in the description of the flow results of FSI-PfS-2b) are present in both cases. Due to the increased structural deflections in "F2M-CH.C" the wake area is further broadened to about seven cylinder diameters in contrast to the wake of FSI-PfS-2b which extends about five cylinder diameters in y -direction. The effect of the angular displaced stagnation point in front of the cylinder is also observed in "F2M-CH.C". Furthermore, the small vortex generated by the rear-end of the structure is found in both benchmarks.

The comparison of both configurations shows that the present test case FSI-PfS-2b reveals strong similarities to "F2M-CH.C" concerning the structural deflections and the resulting flow fields. Nevertheless, it is clear that the numerical computation of FSI-PfS-2b is rather easier than for the case "F2M-CH.C". The reasons are as follows: First, the significantly thicker rubber plate instead of the steel sheet avoids the step in the structure at the bond of the flexible plate with the steel weight. That strongly simplifies the grid generation of this case. Second, the very thin steel sheet had turned out to be a critical issue for the FEM simulation. Third, due to the milder displacements of the structure in the case of FSI-PfS-2b, the adjustments of the moving grid are much simpler than for the case "F2M-CH.C". However, the additional rotational DOF of the front cylinder complicates the simulation in both cases. But for this purpose this thesis also includes the case FSI-PfS-2a, which operates with a fixed front cylinder. Thus also this difficulty can be avoided if required.

¹⁶As a consequence of the applied structural measurement techniques in each case, slightly different measurement points are used. By recalculating the measurement data of Gomes and Lienhart (2013) at $x/D = 3.22$ to the same point as used in the present thesis at $x/D = 3.13$, both results should rather align.

FSI-PfS-2x - Conclusions

Contrary to FSI-PfS-1x the second set of FSI test cases (FSI-PfS-2x) is focused on large two-dimensional structural deformations. While the first series of test cases FSI-PfS-1x is focused on different elastic materials to examine their influence on the FSI coupling, the second test case series FSI-PfS-2x employs the same material and an additional steel weight attached to the rubber plate. However, by applying two different test-case configurations, the influence of the rotational DOF of the front body on the structural response is examined.

The detailed measurements concerning the finally chosen inflow velocity for both benchmark cases revealed quasi-periodic and nearly symmetric structural deflections for both test cases. Due to the restriction to two-dimensional structural deformations owing to the steel weight and despite the turbulent flow, the cycle-to-cycle fluctuations of the deflections are only mild similar to the benchmark cases presented by Gomes and Lienhart (2013). In general, the deflections of both configurations are large ($0.65 < y/D < 1$) compared to the first set of test cases FSI-PfS-1x. Here, the additional steel weight at the end of the structure increases the inertia of the system that leads to larger deflections and the modified swiveling behavior. The release of the rotational DOF of the front cylinder in FSI-PfS-2b increases once more the structural deflections due to its expanded range of influence. Furthermore, the special configuration of FSI-PfS-2b allows a rigid-body motion (i.e. a front cylinder rotation with a nearly rigid plate attached) for the lowest inflow velocities. The first swiveling mode is also present for low inflow velocities and the corresponding excitation frequencies are smaller than the second natural frequency of the structure. Nevertheless, the second swiveling mode of the structure is dominant in both test cases. The transition between the first and second mode again comes along with a doubling of the vortex shedding frequency of the fluid and the corresponding swiveling frequency of the structure in both test cases. The resulting frequency after the transition phase exceeds also the second eigenfrequency of the structure. A summary of the integral measurement results is given in Table 19.

Referring to the FSI excitation sources (see Section 3) it is assumed that the instability-induced excitation (IIE) is responsible for the excitations in the first swiveling mode for low inflow velocities. With increased inflow velocities, i.e., the investigation at the final inflow velocity of $u_{\text{inflow}} = 1.385$ m/s, the flow excitation is large enough to modify the whole system state and indicate a movement-induced excitation mode (MIE). This statement is supported by the eigenfrequency analysis of both test cases. For the chosen inflow velocity the swiveling frequencies are above the first and second eigenfrequencies of the structure. Furthermore, the POD analysis indicates a strongly coupled system with a large influence of the structural motion on the surrounding flow field. Again, the first and second POD modes contain 51% (2a) or 65% (2b) of the entire unsteady flow energy. Remarkable is the absolute energy content including all POD modes for both test cases (Fig. 158). While the kinetic energy stored in FSI-PfS-2a is calculated to 1451.67 m²/s², the value of FSI-PfS-2b is much higher with 2312.05 m²/s². Since this quantity is only an indication for the energy content in the midplane and furthermore directly depending on the amount of used vectors, it only offers a qualitative insight. Despite this issue the indication is obvious that the release of the rotational DOF

Test case	FSI-PfS-2a	FSI-PfS-2b
behavior	2D	2D
bending modes	1st mode, 2nd mode	1st mode, 2nd mode
bending shapes)', '8')', '8'
bending stiffness K_B	0.00878	0.00878
u_{inflow} [m/s]	1.385 m/s	1.385 m/s
symmetry	✓	✓
f [Hz]	11.25	8.16
$\sigma(f)$	$\pm 1.60\%$	$\pm 0.94\%$
St	0.179	0.130
$(y/D)_{\text{max}}$	0.667	0.895
$(y/D)_{\text{min}}$	-0.630	-0.891
$\sigma(y/D)_{\text{max}}$	$\pm 3.45\%$	$\pm 3.24\%$
$\sigma(y/D)_{\text{min}}$	$\pm 6.35\%$	$\pm 3.59\%$
POD energy content	1451.67 m ² /s ²	2312.05 m ² /s ²

Table 19: Summary of FSI-PfS-2x.

changes the coupling between the fluid and structure in a strong manner. In comparison to FSI-PfS-2a the structural motion of FSI-PfS-2b with its increased area of influence involves much more kinetic energy. This energy transfer from the bulk flow to the unsteady flow in the wake of the structure correspondingly results in much larger energy-containing areas or major flow structures (i.e., bigger shed vortices).

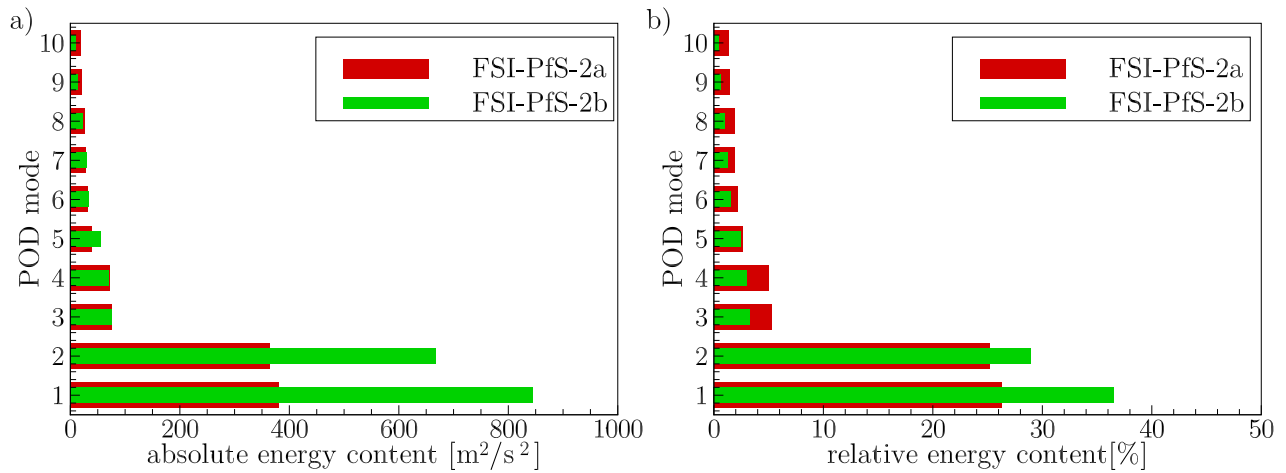


Figure 158: FSI-PfS-2x: POD results.